In-Situ Studies of Crystallization Processes and Other Aspects of Polymorphism

by

PHILIP ANDREW WILLIAMS

Thesis Submitted for

DOCTOR OF PHILOSOPHY

SCHOOL OF CHEMISTRY

CARDIFF UNIVERSITY

June 2014

DECLARATION

This work has not been submitted in substance for any other degree or award at this or any other university or place of learning, nor is being submitted concurrently in candidature for any degree or other award.

Signed …… (candidate) Date ……

STATEMENT 1

This thesis is being submitted in partial fulfillment of the requirements for the degree of ……(insert MCh, MD, MPhil, PhD etc, as appropriate)

Signed …… (candidate) Date ……

STATEMENT 2

This thesis is the result of my own independent work/investigation, except where otherwise stated.
Other sources are acknowledged by explicit references. The views expressed are my own.

Signed …… (candidate) Date ……

STATEMENT 3

I hereby give consent for my thesis, if accepted, to be available for photocopying and for inter-library loan, and for the title and summary to be made available to outside organisations.

Signed …… (candidate) Date ……

Abstract

The work presented in this thesis represents the study of the polymorphism exhibited by several molecular, organic solid-state systems. *In-situ* techniques are used to explore aspects of the polymorphism and crystallization behaviour displayed by these systems. The crystal structures of new polymorphs and other solid phases are determined directly from powder X-ray diffraction data.

Chapter 1 provides background information on the phenomenon of polymorphism and the importance of its study. In addition, the range of *in-situ* techniques that have been used to study crystallization and solid-state systems is described.

Chapter 2 gives details on the experimental techniques used in the work presented in this thesis. These include powder X-ray diffraction (including the methodology behind structure determination from powder X-ray diffraction data), solid-state nuclear magnetic resonance (NMR) spectroscopy, X-ray photoelectron spectroscopy, thermal analysis techniques and dynamic vapour sorption.

Chapter 3 explores the polymorphism of *m*-aminobenzoic acid, resulting in the discovery and characterization of three new polymorphs. The crystallization of *m*-aminobenzoic acid from solution is studied *via in-situ* solid-state NMR spectroscopy and this *in-situ* technique is expanded to allow the evolution of both the solid and liquid phases during the crystallization process to be studied.

Chapter 4 investigates the crystallization behaviour of triphenylphosphine oxide and methyldiphenylphosphine oxide from solution using *in-situ* solid-state NMR spectroscopy. Evidence is found for transient, unknown solid phases formed during the crystallization process.

Chapter 5 reports new insights into the crystallization behaviour of polymorph II of the drug *rac*-ibuprofen. Differential scanning calorimetry and *in-situ* powder X-ray diffraction experiments demonstrate that previous assumptions about the crystallization behaviour of this polymorph were incorrect.

Finally, Chapter 6 explores the crystalline phases of the amino acid L-phenylalanine. A new polymorph and two hydrate phases are discovered and their hydration/dehydration behaviour characterized.

Acknowledgements

Firstly, I would like to give my thanks to my supervisor, Professor Kenneth D. M. Harris for all of his support, guidance and advice over the course of this work. I would like to thank him for the opportunities he has given been me throughout this time and the research he has allowed me to be a part of. I would also like to give very special thanks to Dr. Colan Hughes for all of his excellent advice, help and support.

Furthermore, I truly give thanks to the other members of the research group both past and present, Dr. Colan Hughes, Dr. Vasileios Charalampopoulos, Gregory Edwards-Gau, Yuncheng Yan, Victoria Keast, Dr. Benjamin Palmer and Dr. Keat Lim for always being ready to provide help or advice. It has been very enjoyable working with all of you.

I would like to give my thanks to the UK 850 MHz Solid-State NMR Facility (funded by EPSRC and BBSRC, as well as the University of Warwick including via part funding through Birmingham Science City Advanced Materials Projects 1 and 2 supported by Advantage West Midlands and the European Regional Development Fund) for use of their 850 MHz solid-state NMR spectrometer and Dr. Dinu Iuga for his assistance while at the facility. I would also like to thank Professor Simon Gaisford and Asma Buanz from University College London for their help with performing TGA and DVS experiments.

Thanks to my friends (with special mention to Phil, Freya and Vic) and family for their encouragement over the last few years.

Finally and most of all I would like to give my thanks to my parents. Without you none of this would have been possible. Thank you both so much.

Table of Contents

Chapter 1: Introduction

1.1 - Polymorphism

The subject of polymorphism is both highly relevant and highly important to many areas of science today. Polymorphism is the ability for a solid system to exist in more than one crystalline form, with each form having identical chemical composition. In general, these crystalline forms have differing physical properties, such as melting point or solubility, and differing thermodynamic stability. Due to these differences in stability, polymorphic transformations, in which one polymorph transforms into another, may be observed. In some cases, however, kinetic factors may prevent the transformation of a thermodynamically less stable form into a more stable form. In this case, the less stable form is referred to as metastable. A famous example of this situation is the allotropism of carbon (Figure 1.1). Under ambient conditions, α-graphite is more stable than diamond; however, kinetic factors prevent facile transformation, allowing the metastable allotrope, diamond, to exist under ambient conditions.

It should be noted that while allotropism is often referred to as polymorphism of a pure element, different allotropes may contain different molecular configurations of the

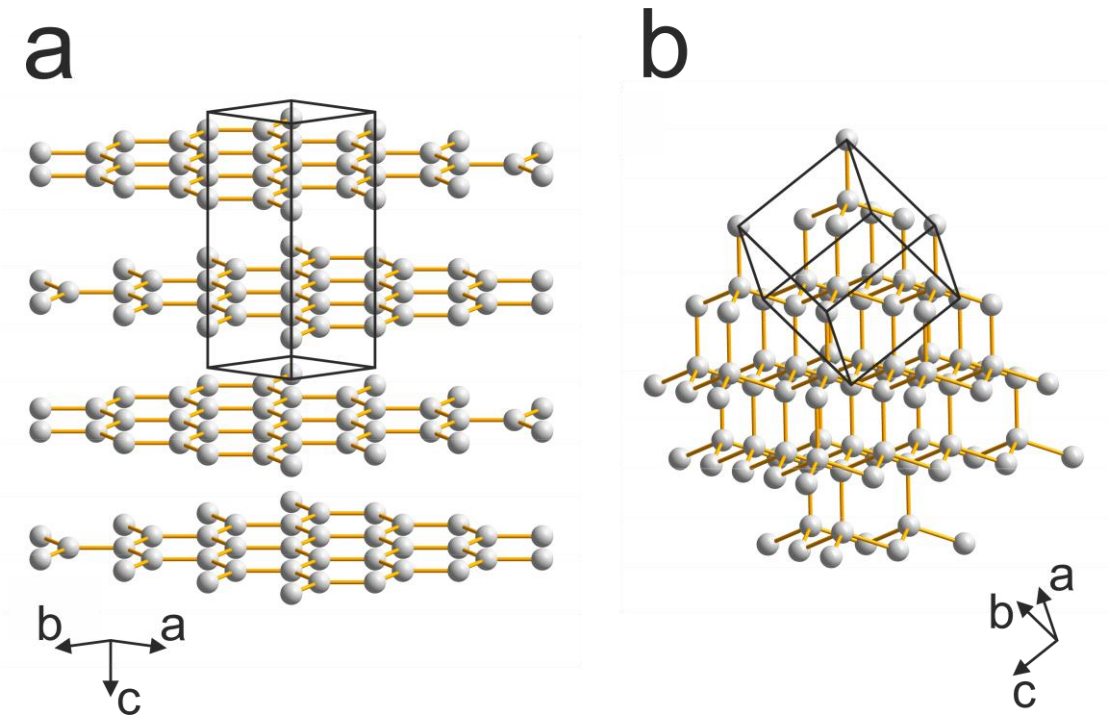

Figure 1.1: *Crystal structures of (a) α-graphite and (b) diamond.*

element. In the case of α-graphite and diamond, the carbon atoms obviously have different covalent bonding schemes. This situation can also be seen in the case of sulphur. While three allotropes, α-orthorhombic, β-monoclinic and γ-monoclinic sulphur contain S_8 molecules and have identical molecular composition, others contain *cyclo*-S_n rings of other sizes or *catena*-S_n polymer chains. In contrast, in the case of polymorphism, the molecular structure must be the same in each crystal structure (i.e., crystal structures containing isomers of a given molecule cannot be classed as polymorphs). The term polymorphism is only applied when the multiple crystalline forms have identical chemical composition. Thus, a hydrate or other solvate of a compound is not a polymorph of that compound. Prototropic tautomerism (changes in protonation state within the molecule) are, however, included within the definition of polymorphism, allowing situations where, for example, the molecules in one polymorph of a compound may be zwitterionic, while those in a second polymorph may be non-zwitterionic.

Polymorphism is a fairly common phenomenon, though highly polymorphic systems (containing more than three polymorphs) are rare. A famous example of a highly polymorphic compound is 5-methyl-2-[(2-nitrophenyl)amino]-3-thiophene-carbonitrile (Figure 1.2),[1-3] known more commonly as ROY (named for the varying red, orange and yellow colours of the different polymorphs). ROY has ten known

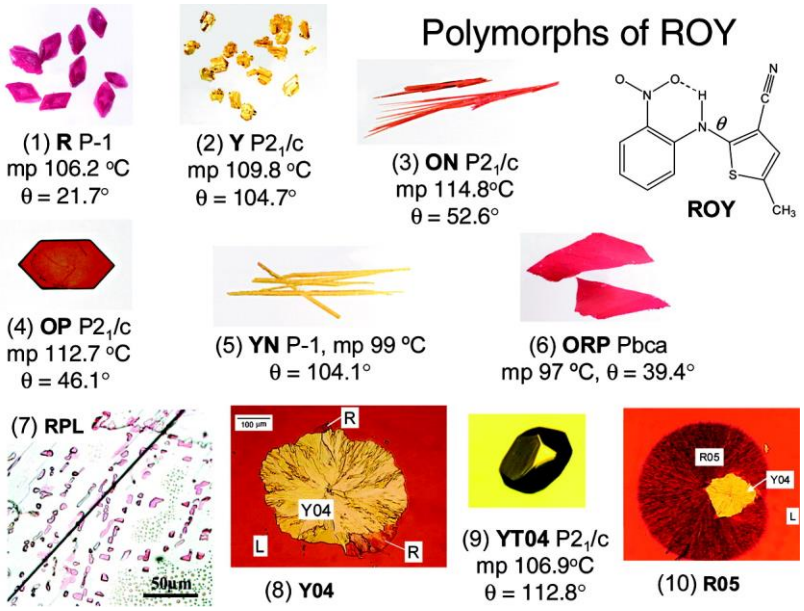

Figure 1.2: *The polymorphs of 5-methyl-2-[(2-nitrophenyl)amino]-3-thiophene-carbonitrile (ROY). Reprinted with permission from L. Yu, Acc. Chem. Res.,* ***43****, 1257-1266 (2010). Copyright 2010 American Chemical Society.*

polymorphs, though only seven of the polymorphs have known crystal structures.

Polymorphic forms may be related in one of two different ways: monotropically or enantiotropically. In terms of thermodynamic definitions, an enantiotropic system is one where the thermodynamic transition point (the point on a plot of free energy against temperature at which the curves for each polymorph intersect, representing the temperature at which the two polymorphs co-exist in equilibrium) is at a temperature below the melting point of the lower melting polymorph. Similarly, a monotropic system is one for which the thermodynamic transition point is at a temperature higher than the melting point of the lower melting polymorph. These two types of relationship are illustrated in Figure 1.3. If two forms are related monotropically, the transformation of one to the other is irreversible (i.e., polymorph A can transform into polymorph B but

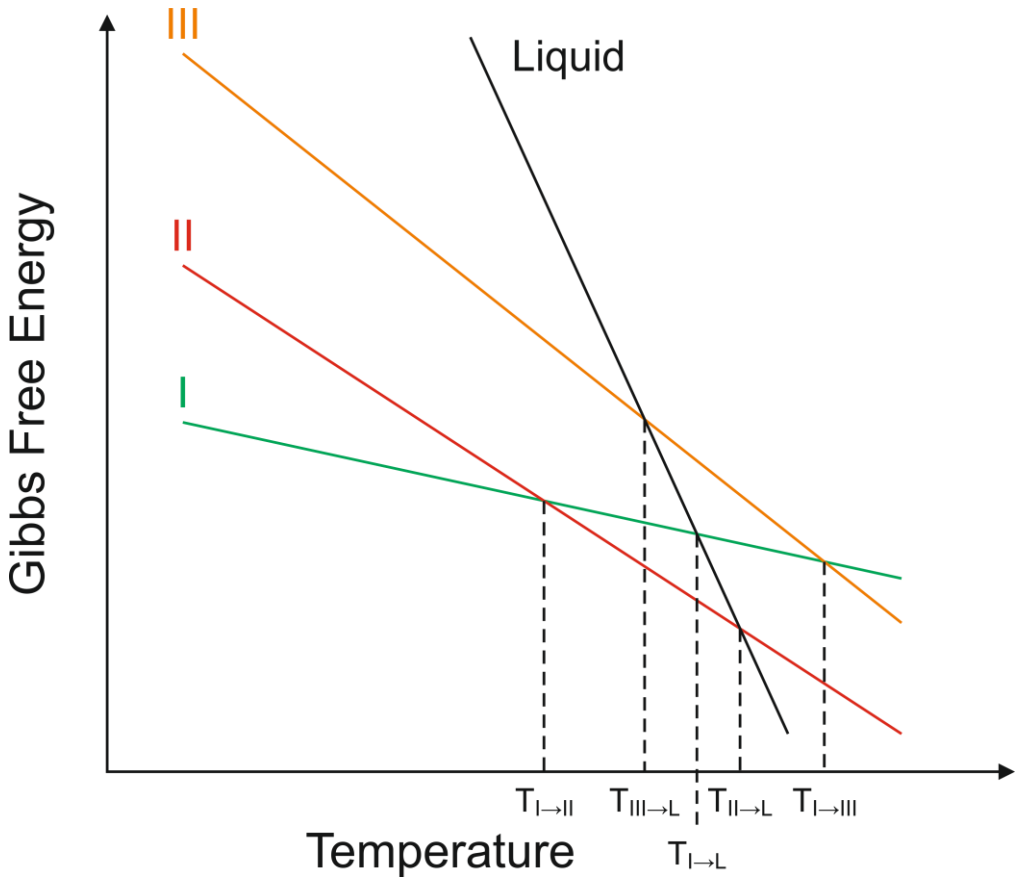

Figure 1.3: *Plot showing how the Gibbs free energy of three polymorphs (termed I, II and III) and the liquid phase of a compound may vary with temperature. Labelled are the melting points of the three polymorphs ($T_{I\rightarrow L}$, $T_{II\rightarrow L}$, $T_{III\rightarrow L}$), the temperature of the transformation from I to II ($T_{I\rightarrow II}$) and the temperature of the transformation of I to III ($T_{I\rightarrow III}$). I and II demonstrate an enantiotropic relationship as $T_{I\rightarrow II}$ is below the melting point of the two polymorphs. III demonstrates a monotropic relationship to the other polymorphs as any transformation lies above the melting point of III.*

polymorph B will never transform into polymorph A). If two forms are enantiotropically related, the transformation between the two is reversible (i.e., polymorph A can transform into polymorph B and polymorph B can transform back into polymorph A).

This situation can be demonstrated with the example of glycine (Figure 1.4).[4-6] Of

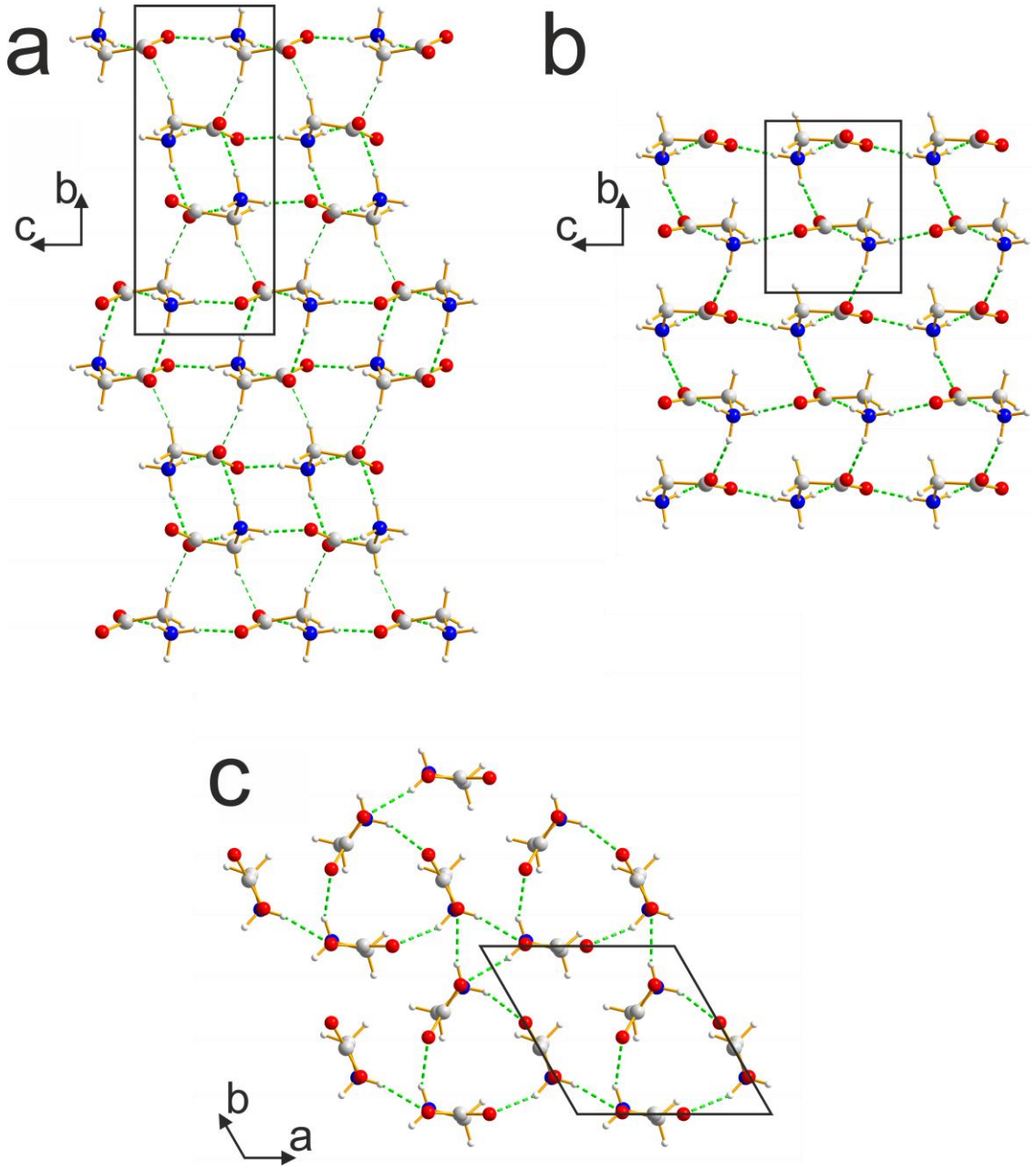

Figure 1.4: *The crystal structures of (a) α-glycine, (b) β-glycine and (c) γ-glycine. Carbon atoms are shown in grey, hydrogen atoms in white, nitrogen atoms in blue and oxygen atoms in red. Hydrogen bonds are shown as green dashed lines. (a) Also includes a weak hydrogen bond formed between a hydrogen on the α-carbon and an oxygen from a neighbouring carboxylate group.*

the three polymorphs of glycine found under ambient conditions (α, β and γ), α and γ are enantiotropically related. The polymorph γ is the most stable at room temperature; however, at high temperature this relationship is reversed, with a transition temperature of *ca*. 165 °C for the transformation of γ→α. The β-polymorph, however, is monotropically related to both α and γ.

1.1.1 - Importance of the Study of Polymorphism

From the development of pharmaceuticals to the fundamental understanding of the solid state, polymorphism is a vital area of study. First, we consider the role that polymorphism plays in the pharmaceutical industry. As previously stated, different polymorphs have differing physical properties. As a consequence, the solubility of any particular drug will differ depending on the polymorph, which can have massive consequence in terms of formulation and dosage. The most infamous example of the problems caused by polymorphism in pharmaceuticals is the case of ritonavir [Figure 1.5(a)].[7] Ritonavir, a protease inhibitor for the treatment of HIV, was developed by Abbott Laboratories and formulated as both a liquid and a gel capsule. Ritonavir is not bioavailable from the solid state and so both the liquid formulation and gel capsules contained a solution in mixed ethanol/water. Approximately two years after manufacture had begun, ritonavir was found to crystallize as a new phase within the capsules. This phase was found to be a previously unknown polymorph with a much greater stability than that of the previously known form. The solubility of this new

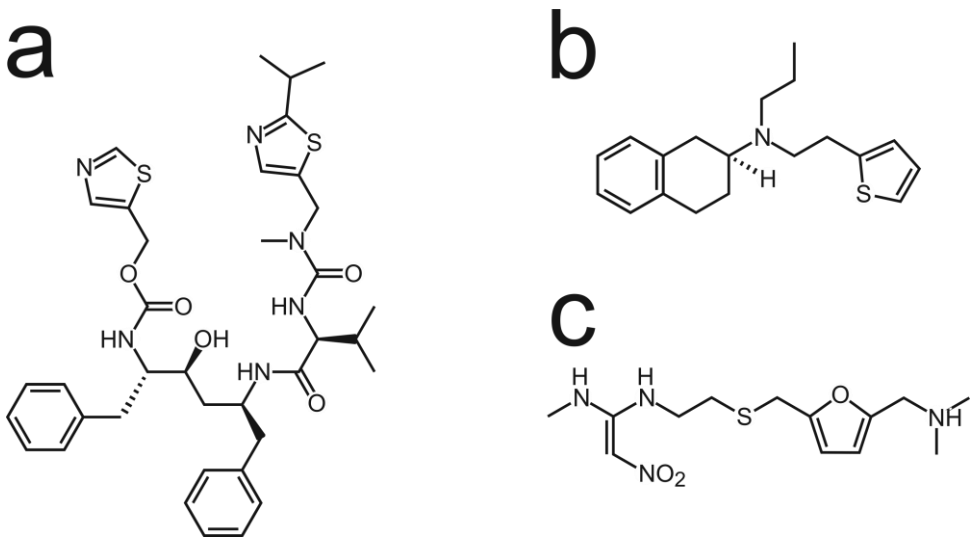

Figure 1.5: *The molecular structures of (a) ritonavir, (b) rotigotine and (c) ranitidine hydrochloride.*

polymorph is much lower than that of the previously known form; the formulated solution was not saturated with respect to the previously known form I, but was 400% supersaturated with respect to the new form II. Traces of form II were able to cause crystallization of the unusable form II and, thus, once the production facility became contaminated with form II, manufacture of ritonavir had to be stopped. A reformulation of ritonavir was necessary before production and sale could be restarted.

A second example[8-10] of problems caused by the discovery of previously unknown polymorphism of a pharmaceutical is the case of rotigotine [Figure 1.5(b)], a drug used in the treatment of Parkinson's disease and restless leg syndrome. Under the name Neupro®, it was formulated as a transdermal patch containing rotigotine dispersed in an adhesive coating. It was found, however, that rotigotine was crystallizing on the surface of these patches, preventing absorption and therefore making them unsuitable for use. These crystals were found to be a new polymorph, which resulted in Neupro® patches being withdrawn from sale in the United States until reformulation was completed.

Polymorphism can also influence the patenting of pharmaceuticals. An example concerns the drug ranitidine hydrochloride[11,12] [Zantac, Figure 1.5(c)], a histamine H_2-receptor antagonist used to reduce stomach acid production. Ranitidine hydrochloride was first patented by Glaxo in 1978 and a method for production was given. After scale up to a plant process, one batch of the ranitidine hydrochloride produced was found to have a different powder XRD pattern and IR spectrum from that described in the patent. This material was found to be a new polymorph and named Form 2, with the original form named Form 1. A new patent was granted for a process to produce Form 2 (claiming that Form 2 had preferable drying characteristics). Prior to expiry of the patent for Form 1 (allowing marketing of generics), several companies, including Novopharm, attempted to produce Form 1 but failed to do so, instead producing Form 2. These companies attempted to invalidate the second patent by claiming that the method used by Glaxo in the first patent inherently produced Form 2 and that the second patent did not accurately describe the method used by Glaxo to produce Form 2 (omitting an azeotroping process that allows for easier granulation of the product). Glaxo successfully argued that the attempts by Novopharm had been contaminated by seed crystals of Form 2 and went on to provide independent evidence of the production of Form 1 by the method established in the first patent. Novopharm later went on to find a method for reliable production of Form 1 and filed a new application to market this

product. Glaxo challenged this application, claiming that the product produced by Novopharm would contain a mixture of Form 1 and Form 2 and so would infringe on the second patent. Novopharm provided powder XRD patterns demonstrating no detectable amounts of Form 2 in their product and so were allowed to market the product.

Common pharmaceuticals that are known to be polymorphic include paracetamol,[13-15] aspirin[16-20] and ibuprofen.[21,22] Highly polymorphic pharmaceuticals include the non-steroidal anti-inflammatory drug (NSAID) flufenamic acid,[23] the anticonvulsant carbamazepine[24] and the antimicrobial sulfathiazole.[25,26]

1.2 - Crystallization

The crystallization of a solid from a supersaturated solution may be described in terms of three major steps: pre-nucleation, the nucleation event and post-nucleation. At the pre-nucleation stage, the solution is supersaturated with respect to the solubility of the crystalline solid. The solution is therefore thermodynamically unstable and crystallization will occur at some point (assuming that there is no insurmountable kinetic barrier to the crystallization process). Initially, aggregation occurs between solute molecules. The formation of an aggregate of a certain critical size (the smallest size at which a particle is stable with respect to dissolution) corresponds to the nucleation step. The size of stable crystal nuclei may range from as few as ten molecules, to tens of thousands of molecules (nuclei of ice contain 80-100 molecules of water).[27] After the crystal nuclei have formed, crystal growth occurs. Crystal growth is often faster along certain crystallographic axes, corresponding, for example, to the direction of hydrogen bonded chains within a crystal structure. This unequal growth rate results in the formation of a distinctive crystal morphology (e.g., hexagonal plates, extended needles, etc.).

Crystal nucleation may be either primary or secondary. Primary nucleation occurs in the absence of crystals, while secondary nucleation is induced by the presence of other crystal nuclei. Primary nucleation may be subdivided into homogeneous and heterogeneous types. Homogeneous nucleation occurs spontaneously within the solution phase, while heterogeneous nucleation is induced by foreign particles or surfaces, or more generally *via* the intervention of another phase in contact with the solution.

It has been suggested[28] that polymorphism during crystallization from solution may in part result from competition between multiple different aggregates. Each of these aggregates would contain structural elements present in the final crystalline form. A series of equilibria would be established between the free molecules, the various molecular aggregates and the final crystals. Once nucleation has occurred, the solution equilibria will be displaced to favour the fastest growing crystal nuclei. The fastest nucleating and growing crystals may not be the most thermodynamically stable crystal structure under these conditions and so can result in a metastable, kinetic product of crystallization.

1.3 - *In-Situ* Methods

In-situ methods have been widely exploited in solid-state chemistry. Many different experimental techniques have been used in these studies, including spectroscopic methods, scattering methods and the definition could, perhaps, be extended to thermal and gravimetric methods. The obvious advantage of an *in-situ* method is the ability to observe the solid forms directly as a function of time during the occurrence of some type of transformation, without removing it from the conditions under which the transformation occurs. This can allow insight into the presence, for example, of transient intermediate phases during crystallization processes or forms which are simply not stable under ambient conditions and so could never be removed for *ex-situ* analysis.

In-situ studies using scattering methods have shown some success, especially in the field of inorganic chemistry. Much work has been undertaken using both conventional (or angular dispersive) X-ray diffraction (XRD) and energy dispersive XRD.[29] In general, however, greater success has been found using energy XRD as this uses a polychromatic X-ray beam (from a synchrotron source) which is of higher intensity than the monochromatic beams used in conventional XRD, allowing use of larger and more elaborate *in-situ* vessels (as absorption of the X-ray beam is less problematic due to the higher intensity). The study of the formation of the microporous gallophosphate ULM-5[30] is an excellent example where both conventional and energy dispersive XRD have been combined to fully understand the processes occurring during crystallization. Through use of both techniques, two new intermediates were found during the crystallization of ULM-5 and the conditions that favour one over the other

were discovered. A second example is the use of powder XRD to study the solid-state reaction of $CaCO_3$ and TiO_2 to form $CaTiO_3$, a dielectric material.[31] By taking repeated powder XRD patterns while heating a mixture of the starting materials, it was found that mechanical activation greatly enhanced the rate of reaction and allowed the production of a phase-pure product.

In-situ studies using neutron diffraction methods have also been used extensively. There are, of course, both advantages and disadvantages of using neutron diffraction in comparison to XRD for *in-situ* studies. Among the advantages is the ability to select a material for the reaction vessel with a low neutron absorption cross-section, rendering the vessel essentially invisible during the diffraction measurements. As a consequence, larger reaction vessels can be used, including autoclaves, cryostats or pressure vessels. In addition, due to the fact that neutrons are scattered by the atomic nucleus, rather than the electrons as in the case of XRD (the theory behind XRD is described in Chapter 2), light elements that are normally difficult to observe *via* XRD are easily observed *via* neutron diffraction. This aspect may be highly advantageous in, for example, studies involving water (such as the crystallization of hydrates). Disadvantages of the use of neutron diffraction include the low flux of neutrons produced by neutron sources (compared to X-ray sources) combined with the inability to collimate neutron beams, necessitating large sample volumes and long acquisition times. As a consequence, both short-lived intermediates and intermediates only produced in small amounts during the *in-situ* study may not be observable by neutron scattering methods.

For diffraction to occur, the scattering from a material must be coherent and elastic, which is an important factor in neutron diffraction studies of samples containing hydrogen. The high natural abundance (99.98%)[32] ^1H isotope of hydrogen scatters mostly incoherently, however, the ^2H (deuterium) isotope, scatters mostly coherently. Thus, in order to acquire high quality neutron diffraction data, deuterated samples must be used. Unfortunately, deuteration may be limited by difficulties in synthesis (e.g., it may be impossible to produce deuterated versions of a naturally occurring mineral sample) or it may be prohibitively expensive. An early example[33] of *in-situ* neutron diffraction is the study of the intercalation of ammonia into tantalum disulphide (specifically, the polymorph 2*H*-TaS_2). Through use of neutron diffraction, it was found that the intercalation occurs with two different reaction periods, first a slow nucleation process, followed by faster growth.

For spectroscopic methods, many experimental techniques have been used for *in-situ* studies, ranging from Fourier transform infra-red (FTIR) and Raman spectroscopy, to X-ray absorption spectroscopy (XAS) and nuclear magnetic resonance (NMR) spectroscopy. Raman spectroscopy has been used, *in situ*, to study the solvent-mediated polymorphic transformation of L-glutamic acid.[34] During this experiment, Raman spectroscopy was used to monitor the polymorphic form present, while attenuated full reflection Fourier transform infrared (ATR-FTIR) spectroscopy was used to study the concentration in the solution phase. In addition, focused beam reflectance measurement (FBRM) and an optical imaging technique were used to track the chord length and morphology of the crystals, respectively. This combination of techniques allowed the characterization of the nucleation and growth of the two polymorphic forms (the metastable α form and stable β form), and also allowed the study of the dissolution of the metastable polymorph. Raman spectroscopy has been coupled with dynamic vapour sorption (DVS) measurements for a tandem *in-situ* study of the hydration of an active pharmaceutical ingredient.[35] Raman spectroscopy has also been used to great effect for the in-line monitoring of pharmaceutical production processes.[36]

Solid-state NMR spectroscopy has many advantages in relation to *in-situ* studies of crystallization but the most important advantage compared to other spectroscopic techniques is the ability to selectively observe *only* the solid state, completely excluding the solution state from the measurement. Certain challenges must, however, be met when attempting *in-situ* solid-state NMR studies of crystallization, the most practical of which is finding a method of sealing a liquid sample within a solid-state NMR rotor spinning under magic-angle conditions (typically with a spinning frequency of 8 to 12 kHz). Details on how this challenge may be overcome are given in Chapter 2. In addition, the system being studied must involve suitable nuclei for solid-state NMR spectroscopy. Examples include ^{13}C and ^{31}P (though due to the low natural abundance of ^{13}C, a labelled sample may be required). This technique has previously been used successfully to study crystallization of the amino acid glycine from solution. Glycine has five known polymorphs[37-41] termed α, β, γ, δ and ε (though only α, β and γ have been found under ambient conditions, with δ and ε formed only under high pressure). Under ambient conditions, γ is the most stable form, followed by α and then β. Crystallization of glycine from H_2O (with natural isotopic abundance) generally gives the α-form. However, when crystallized from D_2O, formation of the γ-form is favoured. This apparent isotope effect on the resultant polymorph of the crystallization was

studied by *in-situ* solid-state NMR.[42] It was found that during crystallization from H_2O, α-glycine is quickly formed followed by no further change in the solid-state (within *ca*. 14 hours). When crystallizing from D_2O, α-glycine is again formed initially, but then transforms over the course of several hours into the γ form. This observation demonstrates that the difference when crystallizing from the H_2O and D_2O is not in the initial nucleation process (the α polymorph is produced initially in crystallization from both H_2O and D_2O) but instead the fact that D_2O catalyses the polymorphic transformation of α-glycine to γ-glycine. The *in-situ* NMR technique was also applied to study crystallization of β-glycine from a water/methanol mixture.[43] It was found that after adding methanol to an aqueous solution of glycine, the resultant anti-solvent crystallization initially produces β-glycine, which then quickly transforms into the more stable α-polymorph. *In-situ* solid-state NMR has also been applied to inorganic systems, such as crystallization of zeolite A from a gel.[44] This *in-situ* measurement involved both ^{27}Al and ^{29}Si direct-excitation measurements (under magic-angle spinning of 2.1 kHz) to chart the progress of the crystallization.

Thermal analysis techniques may be considered as a type of *in-situ* study, including such techniques as thermogravimetric analysis (TGA) and differential scanning calorimetry (DSC). DSC has been combined with small and wide angle X-ray scattering (SAXS and WAXS, respectively) in the study of the polymorphic transition of the lipid trilaurin[45] (the triglyceride of lauric acid). Trilaurin with a 4% addition of cholesterol was measured by DSC after tempering at varying temperature. During the DSC measurement, SAXS and WAXS patterns were acquired simultaneously. A synchrotron radiation source was used to minimize the amount of time required to acquire the X-ray scattering data (a heating rate of 1 °C/min was used to acquire the data with each set of X-ray scattering data acquired over approximately one minute).

As previously stated, each *in-situ* technique has particular advantages and disadvantages that must be assessed when designing an experimental protocol. When the system to be studied involves fast changes and quick evolution, a method that allows for maximal time resolution is essential. In these cases, a spectroscopic method such as IR, Raman or NMR may be preferred. To allow for optimal time resolution during an *in-situ* NMR study, two of the three following conditions must generally be met: the sample must have fast relaxation behaviour, the nucleus to be studied must either have high natural abundance or be artificially enriched, or a high field instrument must be

used. When the studied process is slower but maximal structural information is desired, *in-situ* powder XRD or powder neutron diffraction may be considered as the best choice. Through use of either of these methods, the crystal structures of intermediate solid phases may be determined. It should also be noted that *in-situ* NMR spectroscopy studies the *entire* sample, while other spectroscopic and diffraction techniques generally only interrogate a small part of the sample (e.g., the location of the incident beam in XRD).

1.4 - Aims of this Project

One of the aims of this project has been to develop *in-situ* techniques and to use them in combination with *ex-situ* techniques to gain the maximum insight possible from solid-state systems, including the further development of the *in-situ* NMR technique previously used in the study of the crystallization of glycine, as mentioned above. These *in-situ* studies have been combined with *ex-situ* analysis and structure determination from powder XRD data. Other *in-situ* techniques used in this project include *in-situ* powder XRD. The systems studied involve simple organic molecules, with similarity to active pharmaceutical compounds (and, in the case of ibuprofen, a very widely used drug).

The aminobenzoic acids are a class of simple organic compound used as feedstocks in the production of many important molecules. All three isomers, *o*-aminobenzoic acid, *m*-aminobenzoic acid and *p*-aminobenzoic acid exhibit polymorphism. As the aminobenzoic acids contain both an acidic carboxylic acid group and a basic amine group, the possibility exists for the molecules to form zwitterions. *o*-Aminobenzoic acid (*o*-ABA) has three known polymorphs designated I,[46] II[47] and III.[48] Forms II and III both contain non-zwitterionic molecules of *o*-ABA, while Form I, interestingly, contains both zwitterionic and non-zwitterionic molecules of *o*-ABA. Prior to this work, *m*-aminobenzoic acid (*m*-ABA, Figure 1.6) was known to have two polymorphs, Forms I and II.[49] Form I of *m*-ABA was known to contain only zwitterionic molecules of *m*-ABA,[50] while Form II contains only non-zwitterionic molecules of *m*-ABA. Only the crystal structure of Form II[51] was known prior to the current work, presumably due to the inability to grow single crystals of sufficient size and quality to solve the crystal structure of Form I using single-crystal X-ray diffraction. *p*-Aminobenzoic acid is known to have two polymorphs, α[52] and β.[53] Both

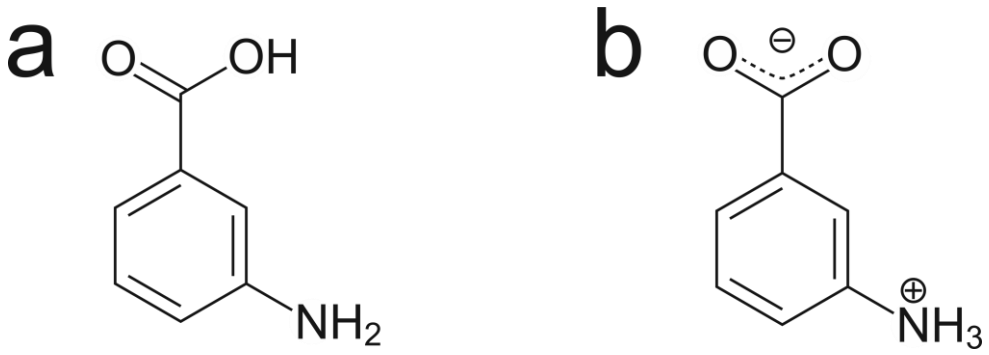

Figure 1.6: *The molecular structure of m-aminobenzoic acid as (a) the non-zwitterionic tautomer and (b) the zwitterionic tautomer.*

polymorphs contain only non-zwitterionic molecules of *p*-ABA. It was previously believed that there were four polymorphs of *p*-ABA.[54] However, it was discovered that two of these materials are actually solvates with acetone and 1,4-dioxane.[55] Within this project, the polymorphism of *m*-aminobenzoic acid has been studied, revealing the abundant polymorphism of this system.

The second system studied in this project is triphenylphosphine oxide [TPPO, Figure 1.7(a)]. TPPO is commonly encountered in the field of organic chemistry. It is produced as a by-product from several synthesis reactions including the Mitsunobu reaction, Staudinger reaction and Wittig reaction. TPPO is also used as a ligand and as a crystallization aid.[56] Both TPPO and its cocrystals tend to form large blocky crystals. TPPO is known to have four polymorphs: monoclinic I,[57] orthorhombic,[58] monoclinic II[59] and monoclinic III. While crystal structures have been reported for all four polymorphs, only two (monoclinic I and orthorhombic) have known and repeatable methods of production. Monoclinic II was found serendipitously during the attempted crystallization of a metal complex and the structural information on monoclinic III in the CSD database was provided only as a "private communication" with no information

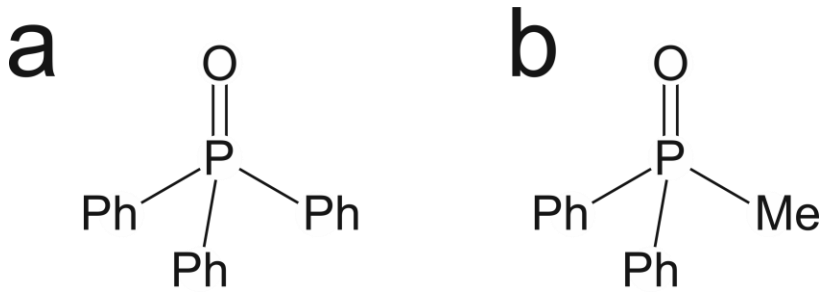

Figure 1.7: *The molecular structures of (a) triphenylphosphine oxide and (b) methyldiphenylphosphine oxide.*

on the method of production. During this work, the crystallization of TPPO has been studied *via in-situ* solid-state ^{31}P NMR, revealing the presence of new transient solid phases.

The related compound, methyldiphenylphosphine oxide [MDPPO, Figure 1.7(b)], was not previously known to be polymorphic and had a single known crystal structure.[60] As in the case of TPPO, MDPPO finds use as a ligand and also in a variety of organic syntheses.[61-63] The crystallization of MDPPO is also studied in this work by *in-situ* ^{31}P NMR and evidence for new transient phases found. This suggests that MDPPO may indeed be polymorphic.

Ibuprofen (Figure 1.8), as previously mentioned, is a widely used non-steroidal anti-inflammatory drug. Ibuprofen is most commonly used as the racemic free acid (*rac*-ibuprofen) which has recently been discovered to be polymorphic[22] and the crystal structure of the new polymorph has been determined from powder XRD data.[64] Ibuprofen is most commonly found as Form I, the most stable form at room temperature. Molten *rac*-ibuprofen (Form I melting point: 349 K) can easily be supercooled and is found to undergo a glass transition at approximately 228 K. Form II is reported[22] to be produced when molten *rac*-ibuprofen is quench cooled to a temperature at least 60 K below the glass transition point, before annealing for several hours at 258 K. Form II of *rac*-ibuprofen has a melting point of 290 K, a value 59 K below that of Form I. During this work, DSC and *in-situ* powder XRD were used to explore the conditions required to produce Form II of *rac*-ibuprofen, to discover whether the quench to a temperature below the glass transition is essential.

L-Phenylalanine (L-Phe, Figure 1.9) is one of the 20 directly genetically encoded amino acids. Industrially, L-Phe is used in the production of the artificial sweetener aspartame [*N*-(L-α-aspartyl)-L-phenylalanine, 1-methyl ester]. L-Phe is known, industrially, in both an anhydrous solid form[65] and a hydrous solid form.[66] In this context, crystallization as the anhydrate is preferred, as the hydrate exhibits a long

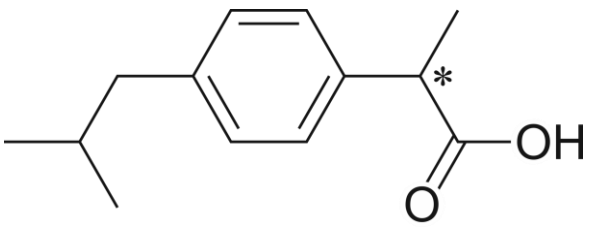

Figure 1.8: *The molecular structure of ibuprofen.*

needle-like morphology that makes processing very difficult.[66] Within the literature, there has been confusion over the existence of polymorphism within the L-Phe system. There are multiple entries within the Cambridge Structural Database (CSD) for anhydrous L-Phe. However, only one of these entries contains atomic coordinates (this structure was actually determined using D-Phe), corresponding to the commonly found anhydrous form of L-Phe.[65] Work[67] studying the crystallization product of L-Phe from water and a mixed water/ethanol solvent by solid-state ^{13}C NMR found that different crystalline forms were obtained from each solvent. During this project, crystallization experiments have been carried out to produce new hydrate phases and the hydration behaviour has been analysed using dynamic vapour sorption (DVS) measurements which, combined with *in-situ* powder XRD, have led to the discovery of a new polymorph of anhydrous L-Phe.

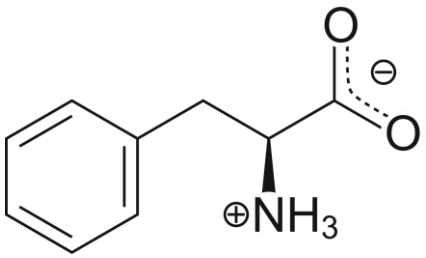

Figure 1.9: *The molecular structure of L-phenylalanine.*

Chapter 2: Experimental Methods

2.1 - X-Ray Diffraction

X-ray diffraction (XRD) is a very powerful and widely used technique for the analysis of materials. It is generally non-destructive (though sensitive samples can suffer radiation damage and some sample containment techniques may result in an unrecoverable sample) and can provide a large amount of information about the sample. The vast majority of crystal structures are solved using single-crystal XRD, where three-dimensional diffraction data for a crystal is recorded. Powder XRD, on the other hand, tends to be used for more analytical purposes: determining the identity of a crystalline sample, analysis of crystalline domain size and *in-situ* study of crystallizations and transformations. However, advances over the past 20 years now allow crystal structures to be determined directly from powder XRD data and the procedures used in such work are discussed more in Section 2.2.

X-ray waves are scattered by the electrons within atoms. Each atom within a crystal will scatter X-ray waves in all directions. A regularly spaced array of scatterers (such as the atoms within a crystal) will result in a regularly spaced array of diffracted waves. In most directions, destructive interference causes the X-ray waves to be "cancelled out", however, in specific directions, constructive interference will occur and a diffraction spot will be produced. For constructive interference to occur (and, thus for a diffraction maximum to be observed), the diffracted waves must be in phase with one another and so the path difference between X-ray waves must be an integer multiple of the wavelength.

Bragg demonstrated[68] that the angular distribution of diffraction maxima in a diffraction pattern can be rationalized by treating the scattered X-rays as if they are reflected from planes passing through points of the crystal lattice (Figure 2.1). This reflection is analogous to that of light from a mirror, thus, the incident angle of the X-ray is equal to the angle of reflection. As mentioned above, for two waves "reflected" from parallel planes to be in phase, the path difference between the two (AB + BC) must be an integer multiple of the wavelength (Equation 2.1).

$$AB + BC = n\lambda . \qquad (2.1)$$

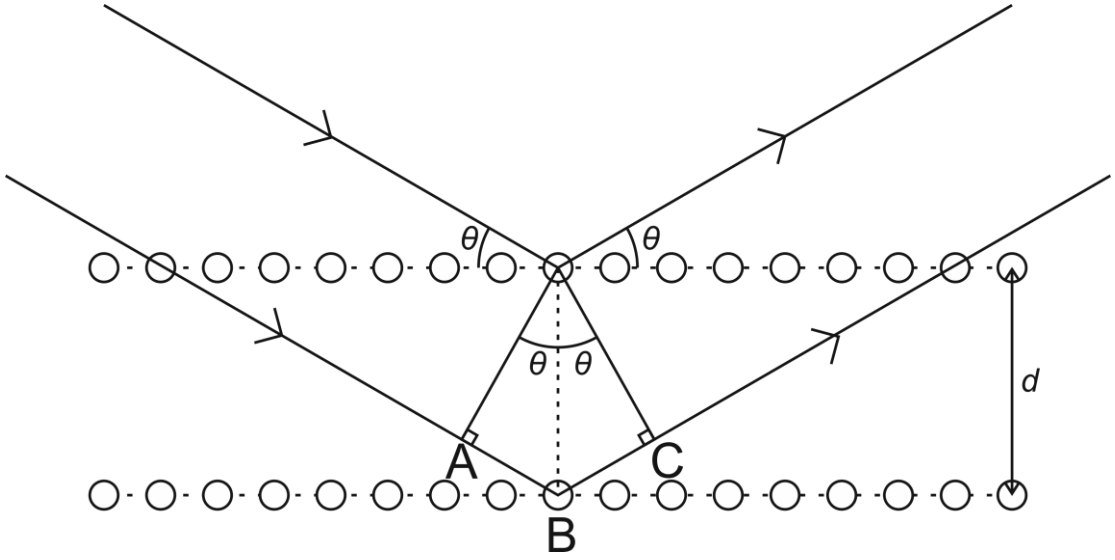

Figure 2.1: *Derivation of Bragg's Law from the scattering of X-rays from parallel lattice planes within a crystal structure.*

As seen in Figure 2.1:

$$AB = BC = d\sin\theta, \tag{2.2}$$

which, combined with Equation 2.1 results in Bragg's Law:

$$n\lambda = 2d_{hkl}\sin\theta, \tag{2.3}$$

where n is the order of the diffraction maximum, λ is the wavelength of incident radiation, d_{hkl} is the spacing between a particular set of lattice planes defined by the Miller indices hkl and θ is the angle between the incident X-ray beam and the lattice plane (corresponding to half the diffraction angle 2θ).

The intensity, I_{hkl}, of the Bragg reflection with Miller indices hkl, is proportional to the square of the magnitude of the structure factor, F_{hkl}:

$$I_{hkl} \propto \left|F_{hkl}\right|^2. \tag{2.4}$$

The structure factor, F_{hkl}, is defined by the following equation:

$$F_{hkl} = \sum_{j=1}^{n} f_j N_j e^{2\pi i\left(hx_j + ky_j + lz_j\right)} \exp\left(\frac{-B_j \sin^2\theta}{\lambda^2}\right), \tag{2.5}$$

where the summation is over all atoms in the unit cell, f_j is the atomic scattering factor for the jth atom, N_j is the site occupancy for the jth atom, x_j, y_j and z_j are the atomic

coordinates for the *j*th atom and B_j is the isotropic displacement factor (B_{iso}) for the *j*th atom, a measure of atomic displacement (which may be caused by a variety of effects both temperature dependent and temperature independent, including thermal vibration of atoms, dynamic disorder and static disorder). B_{iso} may be related to the also commonly used U_{iso}:

$$U_{iso} = \frac{B_{iso}}{8\pi^2} \tag{2.6}$$

The use of U_{iso} allows the determination of physically relevant properties as

$$U_{iso} = \left\langle u^2 \right\rangle, \tag{2.7}$$

where *u* is the atomic displacement and $\langle\ \rangle$ represents averaging over space and time. Thus, the square root of U_{iso} gives a root mean square value for the atomic displacement.

Each atomic scattering factor can be calculated through the equation:

$$f = c + \sum_{i=1}^{4} a_i \exp\left(\frac{-b_i \sin^2\theta}{\lambda^2}\right), \tag{2.8}$$

where a_i, b_i and *c* are a set of coefficients determined from a fit to a simulated atomic scattering curve[69] (calculated, depending on the atom or ion concerned, by a number of methods including relativistic Hartree-Fock and Dirac-Slater wavefunctions) and in this way depend on the electronic structure of the atom. Scattering of X-rays by an atom increases with atomic number (i.e., as the number of electrons within the atom increases). Consequently, elements with higher atomic number scatter X-rays more strongly than elements of lower atomic number. Hydrogen atoms, with only a single electron, can therefore be difficult to observe amongst the scattering produced by heavier atoms (even against carbon, oxygen and nitrogen, as commonly found in simple organic molecules). As described later, locating hydrogen atoms during structure determination from X-ray diffraction data can be difficult for this reason. Other methods may be required for accurate determination of hydrogen atom positions and for this purpose neutron diffraction is often performed. The scattering of neutrons from an atom does not depend upon the electrons but instead on the nuclear structure and so there is no overall increase in scattering power with increasing atomic number as seen for X-ray diffraction.

2.1.1 - Powder X-Ray Diffraction

A powder sample is ideally made up of a large number of randomly oriented crystallites. In the ideal situation, there is a random distribution of crystallite orientations within the powder. Due to this random distribution, unlike the diffraction "spots" produced in the case of single-crystal XRD, powder XRD produces diffraction cones. As a consequence of the fact that diffraction data are effectively compressed into one dimension in powder XRD (compared to the three dimensions in single-crystal XRD), there is usually significant overlap of diffraction peaks in the powder XRD pattern. This is especially true for materials with large unit cells and/or low symmetry (as found for most molecular solids), where there is a very high density of peaks in the powder XRD pattern. The process for structure solution from powder XRD data is further explained in Section 2.2.

As may be expected, actual powder samples may not conform to the ideal situation mentioned above and will not have an entirely random distribution of crystallite orientations. Crystallites will have a particular morphology, including shapes such as plates or needles. Due to this, crystallites will often lay preferentially in certain orientations, for example, plates stacking flat on top of one another other or needles aligning along the same direction (Figure 2.2). The non-random distribution of orientations causes the measured relative peak intensities to differ from their intrinsic values and so can cause difficulty during structure determination. This preferred orientation effect, when severe, can prevent structure solution from powder XRD data and so, therefore, effort must be made to reduce or remove it. Preferred orientation is less pronounced in samples contained within glass capillaries than those held flat between pieces of tape within a foil type sample holder. Preferred orientation may be reduced further by mixing the sample with an amorphous phase (amorphous to avoid observing diffraction peaks from the second phase).

Two geometries were used during the course of this project, Bragg-Brentano reflection and θ-2θ transmission. Transmission geometry was utilized with a foil-type sample holder, with samples either held flat between two pieces of tape or contained within sealed glass capillaries. Transmission geometry has the advantages of superior line shapes, reduced preferred orientation and higher instrumental resolution over reflection geometry making the data more suitable for structure determination.

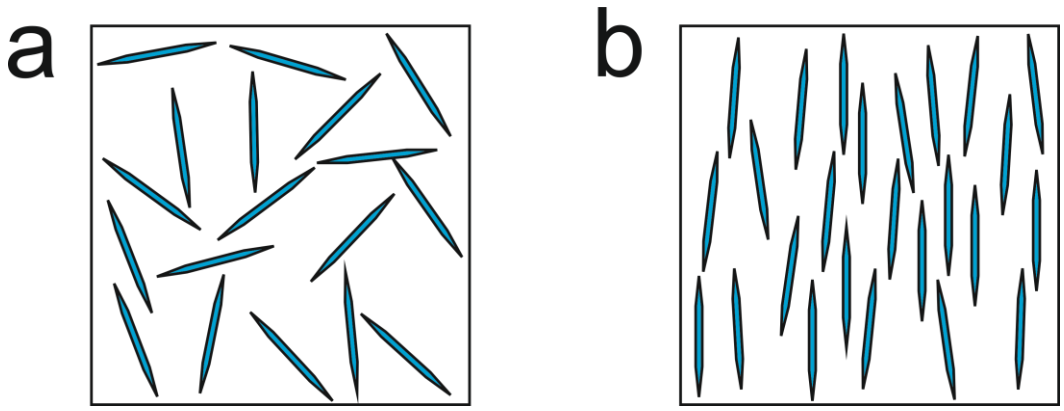

Figure 2.2: *Schematic demonstrating (a) a powder consisting of randomly oriented crystallites and (b) a powder in which the crystallites exhibit substantial preferred orientation.*

Reflection geometry was used for variable temperature powder XRD measurements under vacuum using a Phenix cryostat.

2.1.2 - X-Ray Sources

X-rays for use in diffraction experiments may be generated in different ways. Laboratory sources are based on an X-ray tube, in which electrons are emitted from a heated filament cathode and are accelerated through a high voltage towards a metal target anode. The electrons striking the anode cause excitation and emission of core electrons from the *K* shell (1*s* orbital). Electrons from either the *L* or *M* shell (specifically, the 2*p* or 3*p* orbitals respectively) relax to the *K* shell, producing either Kα or Kβ radiation, respectively. In laboratory experiments, Cu $K\alpha_1$ radiation is typically used for powder diffraction (the Kα radiation is actually made up of two components, $K\alpha_1$ and $K\alpha_2$ due to the difference in energy between the spin states of the 2*p* orbital). The $K\alpha_1$ radiation is specifically selected through use of a single-crystal monochromator made of a material such as germanium.

X-rays may also be generated by a synchrotron. In a synchrotron, a beam of electrons is accelerated through use of a linear accelerator before injection into a large storage ring, around which the electrons travel at constant energy. At specific points, the beam of electrons is bent, causing an acceleration resulting in the emission of X-rays. These X-rays are of very high intensity, are highly collimated, are tuneable (i.e., all X-ray wavelengths are available and any specific wavelength may be selected through use of an appropriate monochromator), are highly polarized and the radiation is pulsed.

Instrumental line broadening effects are reduced when using synchrotron radiation, resulting in high-intensity and high-resolution data.

2.2 - Structure Determination from Powder X-Ray Diffraction Data

As mentioned previously, the powder XRD pattern is related to the crystal structure through the structure factor (Equations 2.2 and 2.4), allowing the powder XRD pattern corresponding to a known crystal structure to be calculated easily. However, the reverse process, the determination of a crystal structure from a diffraction pattern is much more complicated. The crystal structure may be represented in the case of XRD by the electron density $\rho(\mathbf{r})$ within the unit cell. Atoms will obviously be represented by maxima within an electron density map of the unit cell.

By defining the structure factor for a diffraction maximum as $F(\boldsymbol{H})$, where $\boldsymbol{H}$ is the scattering vector in reciprocal space, $\boldsymbol{H} = h\boldsymbol{a}^* + k\boldsymbol{b}^* + l\boldsymbol{c}^*$, and $\boldsymbol{a}^*$, $\boldsymbol{b}^*$ and $\boldsymbol{c}^*$ are the reciprocal lattice vectors, it is related to the electron density as follows:

$$F(\boldsymbol{H}) = \left|F(\boldsymbol{H})\right| \exp[i\alpha(\boldsymbol{H})] = \int \rho(\boldsymbol{r}) \exp(2\pi i\, \boldsymbol{H} \cdot \boldsymbol{r}) d\boldsymbol{r}\,, \tag{2.9}$$

where the structure factor $F(\boldsymbol{H})$ has magnitude $\left|F(\boldsymbol{H})\right|$ and phase $\alpha(\boldsymbol{H})$, and $\boldsymbol{r}$ is the vector $\boldsymbol{r} = x\boldsymbol{a} + y\boldsymbol{b} + z\boldsymbol{c}$ in direct space, with lattice vectors $\boldsymbol{a}$, $\boldsymbol{b}$, $\boldsymbol{c}$ (defining the periodicity of the crystal structure). The integration is performed over all vectors $\mathbf{r}$ in the unit cell.

Through inverse Fourier transformation, the electron density is given by:

$$\rho(\boldsymbol{r}) = \frac{1}{V} \sum_{\boldsymbol{H}} \left|F(\boldsymbol{H})\right| \exp[i\alpha(\boldsymbol{H}) - 2\pi i\, \boldsymbol{H} \cdot \boldsymbol{r}]. \tag{2.10}$$

The magnitude of the structure factor can be determined experimentally from X-ray diffraction data but the phase cannot. As a consequence, the electron density cannot be automatically determined from an X-ray diffraction data and this represents the "phase problem" at the heart of crystal structure solution. Multiple methods now exist for overcoming the phase problem and allowing crystal structure solution from X-ray diffraction data. Among these are direct methods,[70,71] the Patterson method,[72] the charge-flipping method[73-75] and, most importantly in the context of this thesis, the direct space strategy.[76]

Structure determination begins with the indexing of a powder diffraction pattern. This is an essential first step and often the point at which failure occurs. The position of peaks within the powder XRD pattern are determined and entered into an indexing program. This program then uses an algorithm to search for relationships between the entered peak positions, in an attempt to determine the unit cell dimensions and metric symmetry (e.g., cubic, monoclinic, etc.). By identifying the systematic absences, along with density considerations, the space group of the structure may then be assigned. If additional information is required, solid-state NMR spectroscopy can be used to determine the number of crystallographically distinct molecules within the unit cell.

After indexing, the powder pattern must undergo profile fitting using, for example, the Le Bail method[77] (as performed in this work) or the Pawley method.[78] The aim of profile fitting is to fit the complete powder XRD profile via refinement of variables that describe the peak positions (determined by the unit cell parameters and the zero-point shift parameter), the background intensity distribution, the peak widths, the peak shapes and the peak intensities. The input values of the unit cell parameters are those obtained in the indexing stage, with the refined values resulting from this fitting representing a more accurate set of unit cell parameters. It must be emphasized that no structural model (other than the unit cell parameters used to determine peak position) is used in profile fitting and that the intensities of the peaks represent a set of variables that are refined to give an optimal fit to the experimental powder XRD pattern without reference to any structural model. The aim of profile fitting is not to determine the crystal structure but to obtain reliable values for the previously mentioned variables that describe the powder XRD pattern in preparation for the subsequent steps of the structure determination process.

The goodness of fit (between the calculated and experimental powder XRD patterns) is most commonly measured by the weighted and unweighted profile R-factors, R_{wp} and R_p, respectively, defined as:

$$R_{wp} = 100 \times \sqrt{\frac{\sum_i w_i \left(y_i - y_{ci}\right)^2}{\sum_i w_i y_i^2}} \tag{2.11}$$

$$R_{wp} = 100 \times \frac{\sum_i \left|y_i - y_{ci}\right|}{\sum_i \left|y_i\right|} \tag{2.12}$$

where, y_i is the intensity of the ith point in the experimental powder pattern, y_{ci} is the ith point in the calculated powder pattern and w_i is a weighting factor for the ith point defined as $w_i = 1/y_i$.

The peak shape depends on several instrumental and sample dependent effects. Instrumental effects on peak broadening include the measurement geometry, the distribution of wavelengths within the incident radiation (monochromated radiation produces narrower peaks than non-monochromated radiation), the type of detector used and the degree of collimation of the X-ray beam. The sample dependent effects include broadening caused by particle size, stress and strain within the particles and disorder or stacking faults. The overall peak shape can be defined using a number of functions, the most comprehensive of which used in this project is a pseudo-Voigt function as described by Thompson, Cox and Hastings[79] convoluted with a correction for peak asymmetry caused by axial divergence as described by Finger, Cox and Jephcoat.[80] Axial divergence is an instrumental effect that causes asymmetric line broadening at low angles.

After refinement of the unit cell and profile parameters in the profile-fitting procedure, structure solution *via* the direct space technique is carried out. The direct space strategy involves the creation of trial structures built from chemical knowledge. Knowledge of the molecules present in the crystal structure allows these molecules to be placed as fragments into the structure solution. By treating molecules as a single fragment, rather than treating each individual atom as a freely moving entity, the complexity of the structure solution process is greatly reduced. Each molecular fragment can be described by a set of variables, three positional variables x, y, z, three orientational variables ϕ, χ, ψ, and, depending on the molecule, a number of torsional angle variables τ_1 τ_2 … τ_n. During a direct space calculation, a powder XRD pattern is simulated for each trial structure and is compared against the experimental powder XRD pattern by determining the R_{wp} value (the weighted powder R-factor). As in the case of Le Bail fitting and Rietveld refinement, the lower the value of R_{wp}, the better the quality of the fit between calculated and experimental powder XRD patterns.

The program used for direct-space structure solution in this project, EAGER,[81-86] uses a genetic algorithm (GA) for exploring the R_{wp} hypersurface. The GA applies an evolutionary technique by carrying out mating and mutation operations on a population

of trial structures. In an analogous way to evolution in the natural world, the "genetic code" of the trial structures is the previously described positional, orientational and torsional structural parameters. These parameters are changed by mating and mutation operations and the "fittest" structures are defined as those with lowest R_{wp}. The mutation operation will randomize a set number of parameters (the number of parameters to be randomized is defined before beginning the calculation), e.g., a trial structure with a set of parameters (three positional, three orientational and two torsional angle): $x, y, z, \varphi, \chi, \psi, \tau_1, \tau_2$ may mutate, randomizing four parameters to give a new trial structure with parameters: $x, Y, z, \varphi, X, \Psi, \tau_1, T_2$, where the values of four parameters are the same as the previous structure and the values of the other four are new and random. The mating operation will mix the parameters of two parent structures to form two daughter structures, e.g., parent trial structures with parameters: $x, y, z, \phi, \chi, \psi, \tau_1, \tau_2$ and $X, Y, Z, \Phi, X, \Psi, T_1, T_2$ will mate to produce two daughter structures with possible parameters: $x, Y, Z, \Phi, \chi, \Psi, \tau_1, T_2$ and $X, y, z, \phi, X, \psi, T_1, \tau_2$ (other combinations of the parameters from the parent structures are possible).

The GA is usually carried out on multiple processors in parallel, allowing multiple independent populations. A graphical representation of the GA process is shown in Figure 2.3. In generation M there will be a population of N_p trial structures. In generation 0, i.e., the starting point for the calculation, the initial population of trial structures is constructed through randomization of the structural parameters, i.e., the molecules within each trial structure will have random positions and orientations within the unit cell and random values of torsional angles. From the population in generation M, the mating operations are carried out, i.e., N_m pairs of structures are selected (where N_m is the defined number of mating operations per generation) and for each pair, two daughter structures created through the mixing of the structural parameters of the parent structures, as described above. These daughter structures are added to the initial population to produce an intermediate population of $N_p + 2N_m$ trial structures.

From this intermediate population, mutation operations are carried out, i.e., N_x mutant structures (where N_x is the defined number of mutation operations) are created from the trial structures of the intermediate population through randomization of one or more (the number of randomized parameters is set within the input file) of the structural parameters of the mutant structures. These mutant structures are passed along to the next generation, i.e., generation $M + 1$. In addition, from the intermediate population,

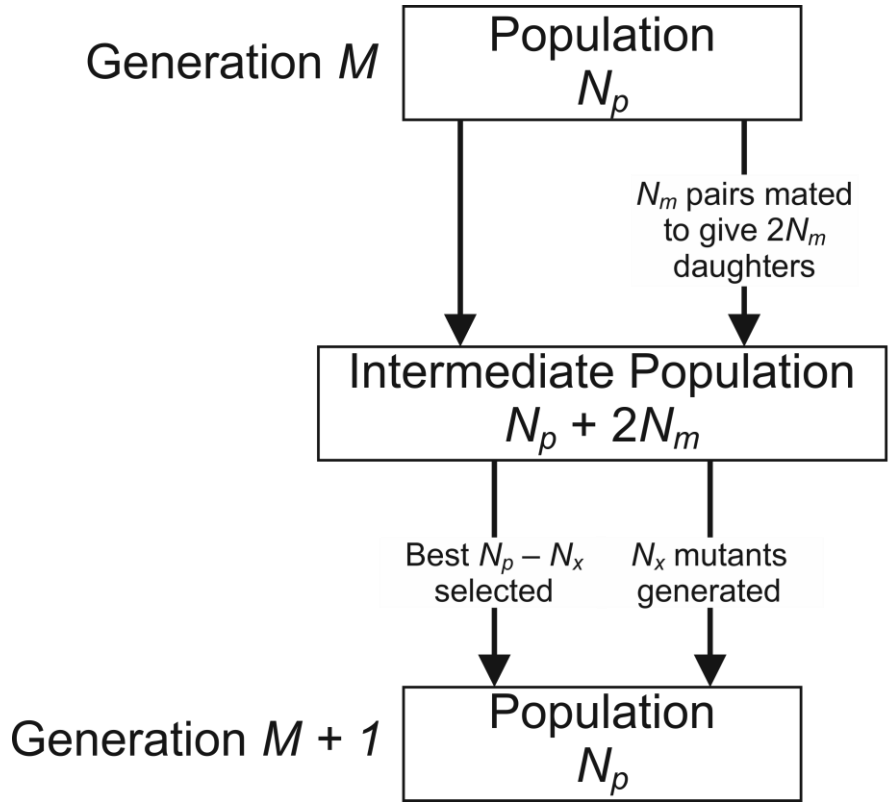

Figure 2.3: *Schematic of the genetic algorithm (GA) process used during structure solution with the program EAGER.*

the ($N_p - N_x$) best trial structures (where "best" is defined as those with the lowest R_{wp}) are selected and passed along to the next generation, $M + 1$. The structure solution is judged to have been successful when multiple independent populations from parallel GA calculations have reached the same, chemically sensible structure with a good fit to the powder XRD pattern. This structure then becomes the starting point for the final step in structure determination, Rietveld refinement.[87]

Rietveld refinement involves fitting the simulated powder pattern for a structure to an experimental powder pattern. However, unlike Le Bail fitting, during Rietveld refinement the intensities of the diffraction peaks are fully simulated from the structure. Rietveld refinement allows the movement of each individual atom within the crystal structure and so allows improvement upon the structure produced by the direct space GA structure solution. Usually, however, soft restraints are imposed during the refinement, based on chemical knowledge. Bond lengths and angles within molecules are set to be close to known values (though still allowed to vary near to these values) and planar parts of molecules (such as aromatic rings) are restrained to remain close to planarity. In addition, Rietveld refinement allows the refinement of the isotropic

displacement parameters mentioned previously. In terms of displacement parameters, constraints are set to cause all atoms within a molecule (or multiple similar molecules) to have a common value of the isotropic displacement. The value of U_{iso} for hydrogen atoms is usually fixed at a value of 1.2 times that of the atom to which it is bonded. Site occupancy can also be refined during Rietveld refinement. This allows disorder to be taken into account and the refinement of populations contributing to the disordered sites.

2.3 - Solid-State Nuclear Magnetic Resonance Spectroscopy

Nuclear magnetic resonance (NMR) spectroscopy[88] is a widely used and highly informative technique for the study of the chemical environment of a target nucleus. In the process of crystal structure determination from powder XRD data, solid-state NMR can provide information that may be greatly beneficial (for example, identification of the number of molecules within the asymmetric unit). It may also be used to investigate molecular motion and disorder within crystalline structures. In addition, solid-state NMR can be used to study amorphous and highly disordered phases, gaining information on internuclear distances and bond angles which may not be possible through other techniques.

In liquid-state NMR spectroscopy, fast motion of the molecules allows for complete orientational averaging, i.e., the sample is isotropic. In solid-state NMR, however, there is generally significantly less molecular motion (on the time scale of NMR spectroscopy) and so the sample is anisotropic. Chemical shift depends on the orientation of the crystal with respect to the external magnetic field. Solid-state NMR is generally performed on powder samples containing a large number of randomly oriented crystallites. Each crystallite orientation, due to the chemical shift anisotropy, will have a different chemical shift and so the peaks within a solid-state NMR spectrum become broadened. In addition, the peaks are broadened by dipolar coupling of both heteronuclear (e.g., ^{1}H-^{13}C dipolar coupling) and homonuclear varieties (e.g., ^{1}H-^{1}H dipolar coupling). To reduce the line widths observed in solid-state NMR, two techniques are used: (i) magic-angle spinning and (ii) high-power decoupling (most commonly applied to the ^{1}H nuclei).

When performing magic-angle spinning, the solid-state NMR sample (contained within a sample rotor) is spun about an axis forming an angle of 54.74° (the “magic

angle") with respect to the applied magnetic field, B_0. The anisotropic part of the spin Hamiltonian (excluding large quadrupoles) is averaged to zero by spinning at this angle. By calculating a value for θ_R (the angle between the spinning axis of the rotor and the external magnetic field) that satisfies the expression:

$$\tfrac{1}{2}(3\cos^2\theta_R - 1) = 0\,, \tag{2.13}$$

we find the magic-angle of approximately 54.74°. Provided that the spinning frequency is significantly greater than the static line width caused by the anisotropy, the peak will be narrowed.

The interactions that cause this broadening may be homogeneous or inhomogeneous. For inhomogeneous interactions (such as chemical shift anisotropy), a single crystal would give sharp peaks and so the broadening found in a powder sample is due to the range of orientations present. In this case, for full line sharpening, the spinning frequency only needs to be greater than the static line width for a single crystallite, not greater than the static line width for the entire powder. However, in addition to line sharpening, a set of spinning sidebands are produced. These are peaks spaced at intervals of the spinning frequency from the centreband at isotropic chemical shift. While these additional peaks can complicate the NMR spectrum (thus, higher spinning frequencies where the spinning sidebands are weaker and spaced further apart may be advantageous), additional information on the chemical shift anisotropy can be extracted from the spinning-sideband manifold. For homogeneous interactions (such as homonuclear ^{1}H-^{1}H dipolar coupling), broad lines are still observed in single crystals due to the variety in the size and orientation of internuclear distances. In this case, very high spinning frequencies are required to exceed the static line width of the crystallite and produce a high-resolution spectrum (thus, solid-state ^{1}H NMR requires very high spinning frequencies).

Solid-state NMR spectra are often recorded using the cross-polarization[89] (CP) technique, particularly to observe spins of low natural abundance, such as ^{13}C. Cross-polarization involves the transference of magnetization from a nucleus of high Larmor frequency (such as ^{1}H) to nuclei of low Larmor frequency (X). By transferring magnetization from ^{1}H to X, two advantages are achieved: (i) a signal enhancement is achieved with a maximum value determined by the ratio of the Larmor frequencies of the ^{1}H and X nuclei, i.e., $\omega_0(^1\mathrm{H})/\omega_0(\mathrm{X})$ (equivalent to the ratio of the gyromagnetic

ratios γ^H/γ^X where γ^H and γ^X are the gyromagnetic ratios of ^{1}H and X, respectively), and (ii) because the magnetization originates from ^{1}H, signal recovery by relaxation is dependent on $T_1(^1H)$ rather than $T_1(X)$. With respect to (i), the maximum signal enhancement for a $^1H \rightarrow ^{13}C$ CP experiment compared to a ^{13}C direct excitation experiment is approximately fourfold [as $\omega_0(^1H)/\omega_0(^{13}C) \approx 4$]. With respect to (ii), values of $T_1(^1H)$ are generally smaller than values of $T_1(X)$, allowing shorter recycle delays to be used in a CP experiment than would be the case in a direct-excitation experiment.

The pulse sequence for this technique is shown in Figure 2.4. Initially a 90° pulse is applied to the ^{1}H channel of the spectrometer, before applying a spin-lock pulse to the ^{1}H channel and a contact pulse to the X channel (where X is the second nucleus in the CP experiment). The spin-lock and contact pulses are set in such a way as to allow transference of magnetization between ^{1}H and X nuclei. This transference relies on dipolar coupling between the ^{1}H and X nuclei and, thus, cross-polarization cannot occur in the solution state (as dipolar coupling is averaged out by motion in solution). After

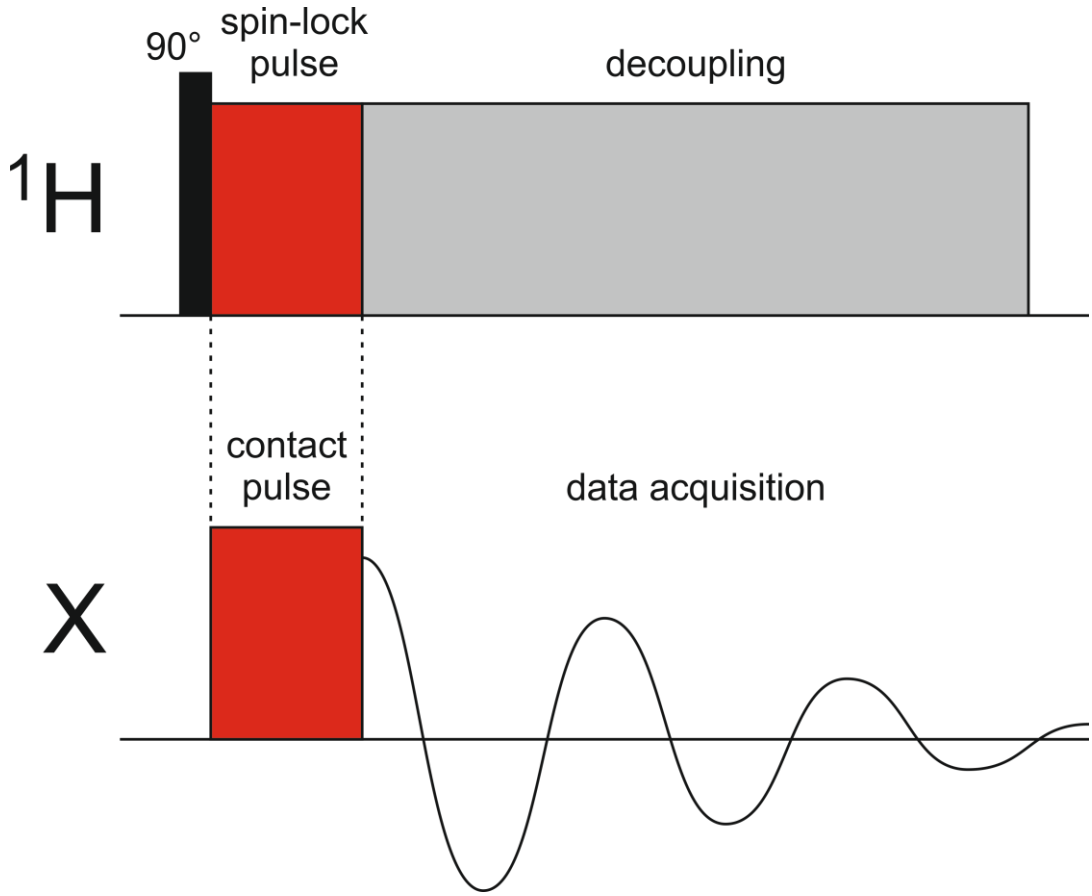

Figure 2.4: *Pulse sequence for the simple cross-polarization magic-angle spinning NMR experiment.*

the contact pulse, signal is collected for the X nuclei while performing ^{1}H decoupling to remove heteronuclear dipolar coupling (as this is not completely averaged by magic-angle spinning at typical spinning frequencies). This decoupling may be performed either by continuous irradiation of the ^{1}H nuclei, or as used in this thesis, a sequence of pulses such as SPINAL64.[90]

After being perturbed from equilibrium by a pulse, the spins of the nuclei will revert back to their equilibrium situation in a process known as relaxation. The main processes involved in relaxation are spin-lattice relaxation (also known as longitudinal relaxation) and spin-spin relaxation (also known as transverse relaxation). Spin-lattice relaxation describes the process of regaining the equilibrium of the *z* component of the spin magnetization vector. Generally, for solid samples, this process is describable as a single exponential with a relaxation time constant T_1. Knowledge of T_1 is essential when performing experiments where repeated pulses are utilized (i.e., the vast majority of solid-state experiments). Sufficient time must be allowed between each pulse (the time between pulses is known as the pulse delay or recycle delay) for spin-lattice relaxation to complete. If the recycle delay is too short and spin-lattice relaxation is incomplete when the next pulse occurs, the amount of signal acquired will be reduced. However, if the recycle delay is longer than needed, spectrometer time is wasted. To ensure that the information gained from signal intensities is quantitative, a recycle delay of $5T_1$ is used (a delay of this length results in recovery of 99.3% of the signal). If quantitative intensity information is not required, the recycle delay can be reduced below the value of $5T_1$ which, while reducing the signal gained in each repetition, allows more repetitions to be performed within a given period of time and can therefore lead to an increase in signal to noise (the optimum recycle delay to produce the maximum signal to noise is $1.26T_1$). However, when working under compromised relaxation conditions, one or more "dummy" acquisitions (pulses where the resultant data are not saved) may be undertaken before acquisition of the actual data. This ensures that the diminution in signal caused by the insufficient recycle delay occurs *prior* to the collection of data and, thus, changes in relative intensity between acquired spectra remain quantitative (provided that there are no changes in the value of T_1).

Spin-spin relaxation describes the process of regaining the equilibrium of the *xy* component of the spin magnetization vector (zero at equilibrium). The typical relaxation time constant for spin-spin relaxation is given the symbol T_2. In solids, T_2 is generally

much shorter than T_1 (with values of T_2 for protons in a rigid solid typically on the order of tens of microseconds). The value of T_2 is related to the width of peaks in the spectrum. A driving force for relaxation is molecular motion within the sample. Solids containing molecules with mobile groups (e.g., methyl groups will generally undergo facile rotation about the axis of the $–CH_3$ bond) will have shorter values of T_1 than completely rigid molecules.

2.4 - *In-Situ* Solid-State NMR Studies of Crystallization

As mentioned in Chapter 1, solid-state NMR can be used to study the evolution in solid phases present during the crystallization process. This allows the detection of transient, unstable crystalline forms that would not be identified by *ex-situ* analysis of the final crystallization product. The crystallization process is carried out within a solid-state NMR rotor and, therefore, the crystallization solution must be prepared within the rotor.

To prepare the crystallization solution, the solute and solvent are measured by mass into the bottom of a 4 mm zirconia solid-state NMR rotor. The rotor is spun in a centrifuge for a few seconds to ensure that the sample is at the bottom of the rotor. The rotor is then sealed using a plastic insert (made of either PTFE or Kel-F®, depending on the solvent used), as shown in Figure 2.5, to ensure that the crystallization solution does not escape from the rotor when it is placed under magic-angle spinning. Following sealing, the rotor is placed within the NMR spectrometer and spun under magic-angle

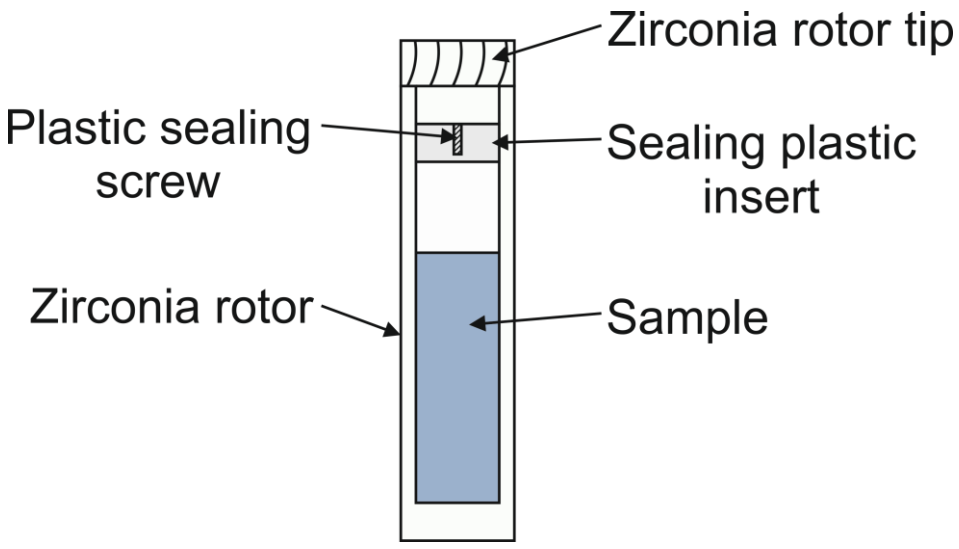

Figure 2.5: *Schematic showing the sealed solid-state NMR rotor used to carry out in-situ solid-state NMR studies of crystallization.*

conditions (usually at 8 to 12 kHz). The spectrometer is tuned at the temperature that will later be used for data acquisition. The sample is then warmed to an upper temperature for a set period of time (usually 1 hr), to allow for complete dissolution, before cooling to the crystallization temperature. After reaching this temperature, acquisition of NMR spectra is begun.

The NMR spectra may either be acquired as solely solid-state measurements (using CP, as previously described) or as interleaved solid-state and liquid-state measurements (using direct-excitation) the so-called CLASSIC (**C**ombined **L**iquid- **A**nd **S**olid-**S**tate **I**n-situ **C**rystallization) NMR method, developed during the work described in Chapter 3. As stated in Section 2.3, CP cannot occur in the liquid state, so by using a CP pulse sequence, the solid-state can be *selectively* observed, and the liquid state is "invisible". This means that NMR spectroscopy can be used to selectively monitor both solid and liquid phases during crystallization using the *same* instrument, simply by changing the pulse sequence used. During these measurements, good time resolution is obviously critical to the success of the experiment. The time resolution is dependent on both the number of individual scans required to produce each spectrum and the recycle delay between the acquisition of each scan. Solution-state measurements tend to use a short recycle delay (1 to 3 seconds) while those of solid-state measurements vary depending on the longitudinal ^{1}H relaxation time (T_1) of the solid phase in question; a longer relaxation time requires a longer recycle delay to gather signal during the acquisition. Measurements of nuclei of low natural abundance (e.g., ^{13}C) require a greater number of scans to achieve sufficient signal to noise within each individual spectrum. A natural-abundance ^{13}C sample with a long relaxation time will therefore be very challenging to achieve suitable time resolution to observe crystallization. To improve matters, the *in-situ* experiments carried out during this project were performed using the UK 850 MHz Solid-State NMR Facility located at the University of Warwick. The high field of this spectrometer increases the signal-to-noise ratio and so allows for greater time resolution. Spectral resolution is also increased at high field, allowing for separation of peaks which may overlap at lower field strength.

2.5 - X-Ray Photoelectron Spectroscopy

X-ray photoelectron spectroscopy (XPS)[91] involves the study of core electron binding energies through their emission by absorption of X-ray radiation. The elemental

composition, oxidation state and charge within a sample can all be studied. In XPS (Figure 2.6), a sample, held under vacuum, is illuminated with a beam of X-rays (normally using monochromatic Al Kα X-rays). The X-ray photons cause excitation of the electrons from core atomic orbitals and XPS is focused on studying the kinetic energies of those electrons ejected from the material by this process. The kinetic energy and intensity of the emitted electrons are measured by a detector allowing determination of the binding energy:

$$E_B = E_{h\nu} - (E_K + \phi), \tag{2.14}$$

where E_B is the binding energy of the electron, $E_{h\nu}$ is the energy of the incident X-ray photon, E_K is the kinetic energy of the emitted electron and ϕ is the work function of the spectrometer. The electrons emitted from the sample must escape to the vacuum in order to be detected. While the X-ray photons may penetrate deeply into the sample, electrons emitted below the surface will not be detected. These electrons interact readily with atoms within sample and may undergo inelastic collisions or become trapped either through recombination with an ion or within an excited state of an atom. This causes XPS to only be sensitive to the surface of the sample and not to the bulk, causing surface contamination effects to be highly problematic.

Atomic binding energies are sensitive to the electronic structure of the species in question. This means that XPS is able to distinguish, for example, between the neutral

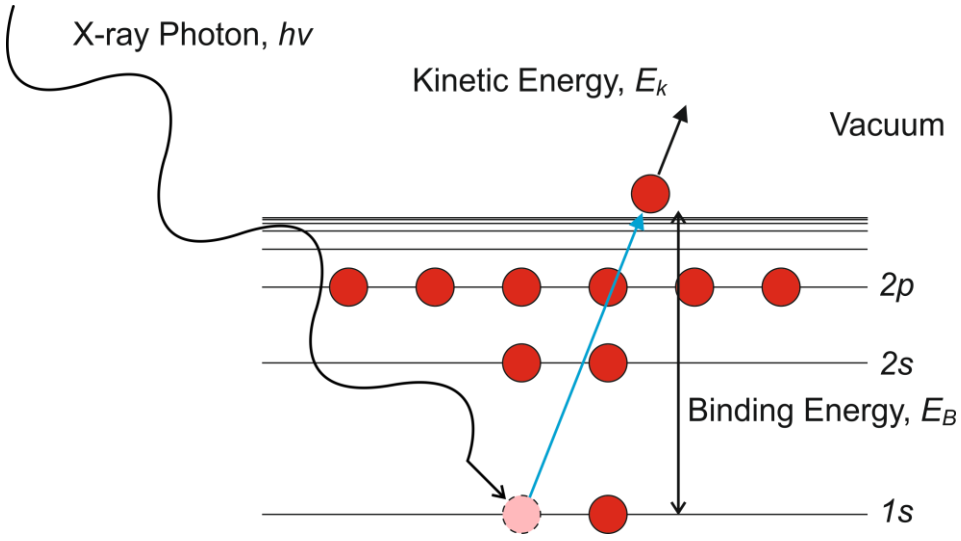

Figure 2.6: *Schematic of X-ray photoelectron spectroscopy. An incident X-ray photon causes excitation and expulsion of a core electron causing it to be ejected from the surface with kinetic energy* E_k.

nitrogen within an amine $–NH_2$ group and the charged nitrogen within an ammonium $–NH_3^+$ group and so allow differentiation between the uncharged, non-zwitterionic and zwitterionic forms of amino acids or between a co-crystal and a salt.

2.6 - Differential Scanning Calorimetry

Differential scanning calorimetry (DSC)[92] is a technique for studying the thermal properties of a sample. The sample (of known mass on the order of a few milligrams) is held within a sealed aluminium pan, which is placed on a plinth within the calorimeter. An empty reference pan is placed on a second plinth. The calorimeter then measures the difference in heat flow into the sample pan compared to the reference pan. Measuring this heat flow allows calculation of the heat capacity of the sample and the enthalpy and entropy change of any phase transitions, for example a polymorphic transformation, melting or crystallization. This arrangement of a heat flux "turret-type" differential scanning calorimeter is shown in Figure 2.7.

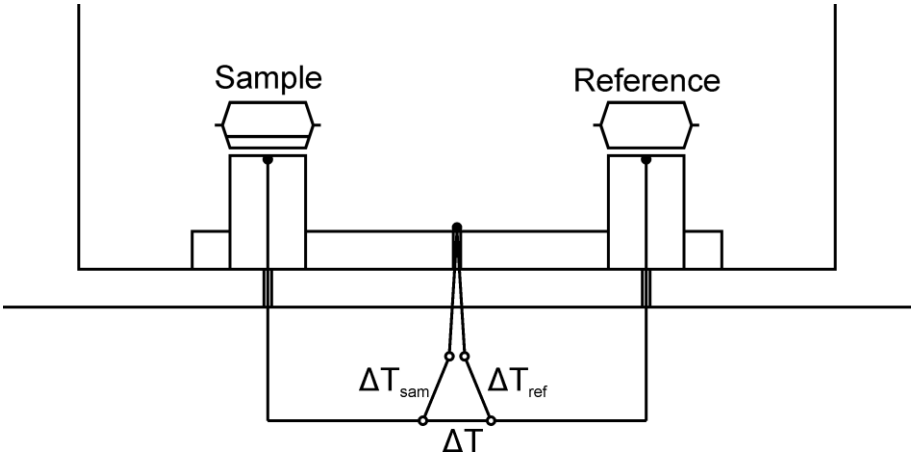

Figure 2.7: *Schematic of a heat flux, turret differential scanning calorimeter. Temperatures are measured by the thermocouples indicated by black circles.*

Examples of different features that may be observed in DSC data are shown in Figure 2.8. This example shows, on heating, a glass transition (i.e., the transformation of a glass to a supercooled liquid or rubber state), a phase transformation (e.g., the transformation of one polymorph to another) and finally a melting peak. On cooling, a crystallization peak is observed.

In DSC data, the peak value of thermal events is often found to vary depending on heating/cooling rate and the sample used. As shown in Figure 2.9, it is possible to calculate an onset temperature for the event by finding the point where the tangent of

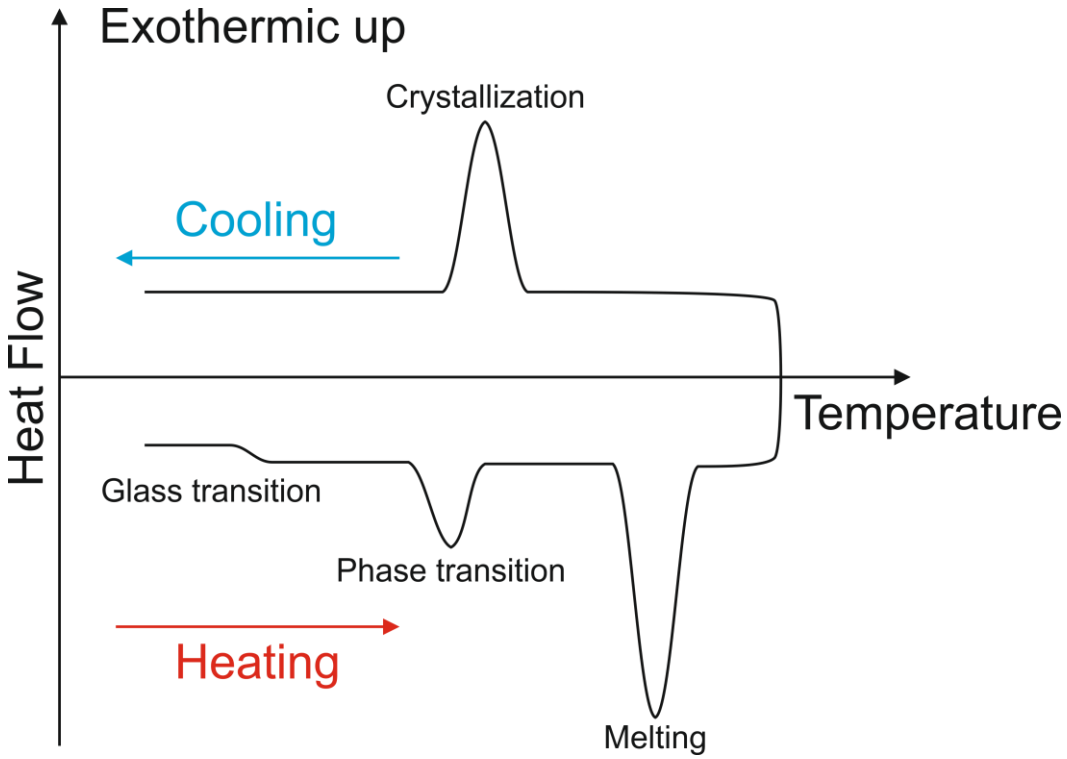

Figure 2.8: *Schematic demonstrating various thermal events that may be observed using differential scanning calorimetry (DSC). Exothermic events are shown plotted upwards.*

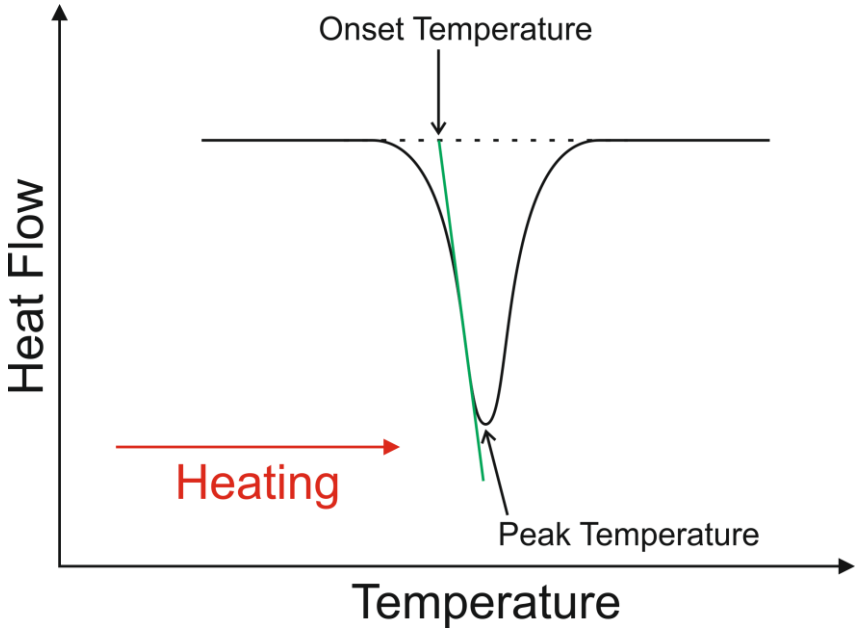

Figure 2.9: *Schematic demonstrating the calculation of the onset temperature of a transformation in differential scanning calorimetry (DSC) data.*

the peak crosses the interpolated baseline. The onset temperature does not generally depend on heat/cooling rates or sample and so is a more reliable value to report.

2.7 - Thermogravimetric Analysis

Thermogravimetric analysis (TGA) measures the change in mass of a sample upon heating. A sample is contained within an aluminium pan and its mass is measured as it is subjected to increasing temperature. As volatile components of the sample are lost, the mass of the sample decreases. Analysis of this decrease in mass allows the determination of, for example, the stoichiometry of a solvate structure. From the observed mass decrease associated with the desolvation event on heating, the number of moles of solvent can be determined and related to the number of moles of starting material.

An example TGA plot is shown in Figure 2.10. In this example, two partial losses of mass are observed and may be assigned as two desolvation processes; for example, a dihydrate transforming to a monohydrate followed by transformation to the anhydrous form. At higher temperature, a large decrease in mass corresponding to the decomposition of the sample is observed.

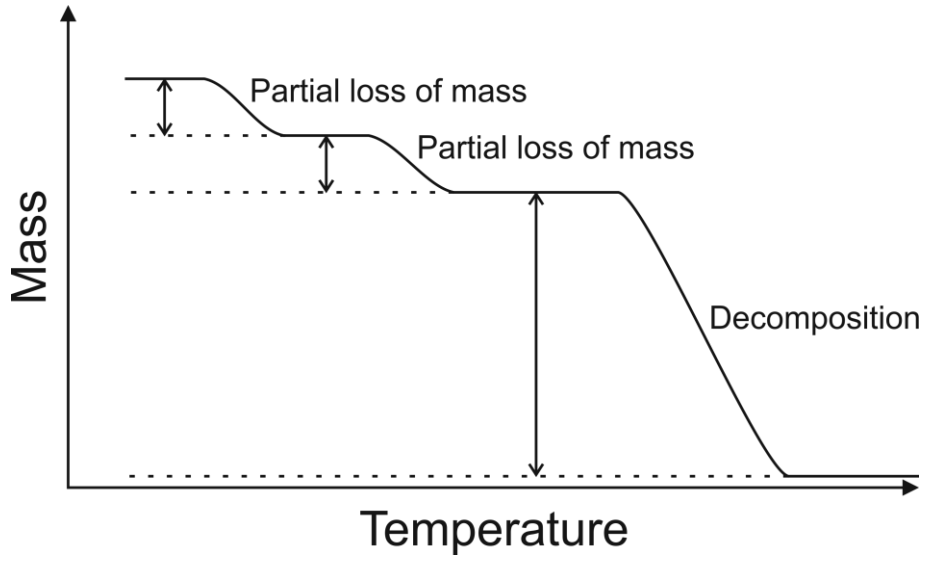

Figure 2.10: *Schematic demonstrating the change in mass that may be observed in thermogravimetric analysis (TGA) data.*

2.8 - Dynamic Vapour Sorption

Dynamic vapour sorption (DVS) is a gravimetric method for studying the hydration and dehydration of samples through varying humidity. A sample of known mass is subjected to increasing followed by decreasing relative humidity (each in a stepwise fashion) and the change in mass measured. The humidity is increased in a stepwise fashion, with time allowed for equilibration of the sample to the new humidity level. As in the case of TGA, observed changes in mass can offer insight on the number of molecules of water involved in each step of hydration/dehydration processes. An example DVS plot is shown in Figure 2.11.

DVS is widely used within the pharmaceutical[93] and food science industries.[94] The propensity and mechanisms for water absorption and loss from samples are critically important when considering formulation, processing and storage of pharmaceuticals. Hygroscopicity may be seen as an undesirable characteristic in a drug compound as water absorption may cause "stickiness" of the sample, complicating processing, including the pressing of tablets. Some medications, such as sodium valproate,[95] deliquesce on exposure to humidity.

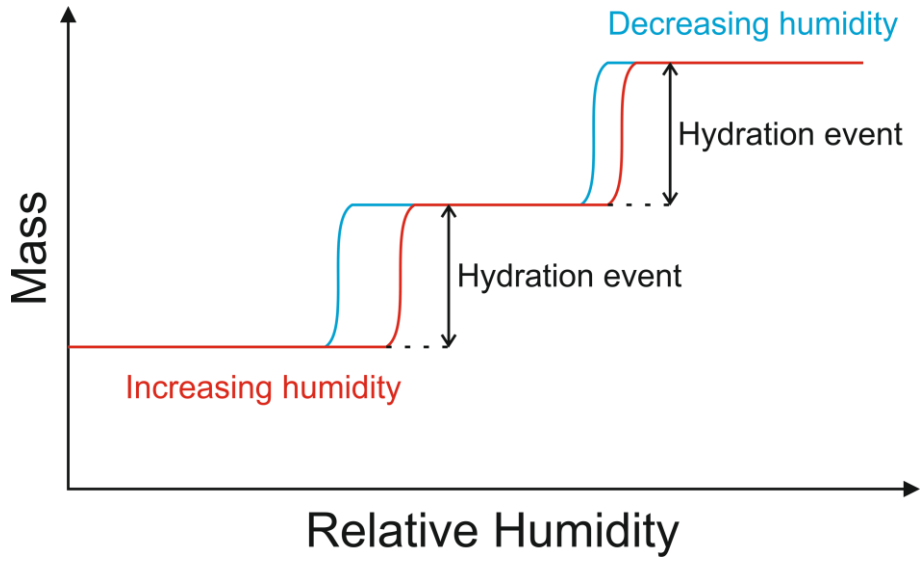

Figure 2.11: *Schematic demonstrating a typical dynamic vapour sorption (DVS) measurement. Shown are two hydration/dehydration events with hysteresis, i.e., the relative humidity value for the event is different depending on whether the humidity is increasing or decreasing.*

Chapter 3: Discovery of a New System Exhibiting Abundant Polymorphism: *m*-Aminobenzoic Acid

3.1 - Introduction

m-Aminobenzoic acid (*m*-ABA) is a simple molecular organic solid, part of the aminobenzoic acid family. All three isomers are known to be polymorphic: *o*-aminobenzoic acid (*o*-ABA) has three known polymorphs,[47,48,96] *m*-ABA had two known polymorphs[97] prior to the present work and *p*-aminobenzoic acid (*p*-ABA) has two known polymorphs.[52,53] *m*-ABA has a wide range of applications and it is used as a fundamental organic building block in the synthesis of drugs such as analgesics and antihypertensives.[98] The literature reports the use of *m*-ABA in the chemical passivation of metals including iron,[99] steel[99] and aluminium.[100]

m-ABA contains both an acidic (carboxylic acid) group and a basic (amine) group, allowing the molecule to potentially exist in non-zwitterionic and/or zwitterionic forms (Figure 3.1): a case of prototropic tautomerism. In solution, the tautomer of *m*-ABA present is found to vary between solvents. *m*-ABA is known to be present as the non-zwitterionic tautomer in DMSO,[101] 1,4-dioxane[102] and chloroform,[103] almost entirely as the non-zwitterionic tautomer in methanol (with a proportion of non-zwitterions greater than 98%),[104] and predominantly as the zwitterionic tautomer in water (proportion of zwitterions ranging from 50% to 78%).[104,105]

Prior to the present work, there were two known polymorphs of *m*-ABA, denoted Form I and Form II. These two forms were identified by infrared spectroscopy in 1971,[97] and the *m*-ABA molecules assigned as zwitterionic in Form I and non-

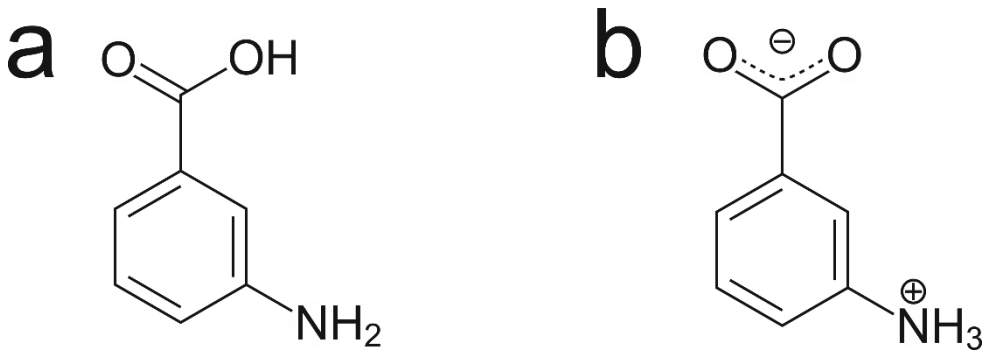

Figure 3.1: *Molecular structure of m-ABA as (a) the non-zwitterionic tautomer and (b) the zwitterionic tautomer.*

zwitterionic in Form II. The crystal structure of Form II was subsequently determined by single-crystal XRD,[51] confirming that the molecules in Form II are non-zwitterionic (with head-to-head dimers formed by hydrogen-bonding of *m*-ABA molecules through the carboxylic acid group). XPS studies[50] on *o*-ABA, *p*-ABA and *m*-ABA also confirmed the presence of zwitterionic *m*-ABA molecules in Form I and non-zwitterionic molecules in Form II. Form I has no known crystal structure, presumably due to difficulty in growing single crystals of sufficient size and quality for single-crystal XRD. Previous work found that, under ambient conditions, Form I is more stable than Form II, with DSC measurements demonstrating that the relationship between the forms is enantiotropic; Form I converts to Form II at 157.25 °C.[49]

The initial aim of this work was to determine the crystal structure of Form I of *m*-ABA directly from powder XRD data. However, structure determination of Form I from powder XRD data proved to be intractable due to challenges encountered in the indexing stage of the structure determination process. The resulting discovery of abundant polymorphism in *m*-ABA led to the study of the system by *in-situ* solid-state ^{13}C NMR and the development of the **C**ombined **L**iquid- **A**nd **S**olid-**S**tate **I**n-situ **C**rystallization NMR (CLASSIC NMR) method.

3.2 - Experimental Methods

m-ABA was purchased from Sigma-Aldrich (purity >98%) and powder XRD of this sample revealed that it was a new polymorph, denoted Form III. Samples of Form I were prepared through fast evaporation of solvent from a solution in either methanol or ethanol, or by cooling a supersaturated solution in dimethyl sulphoxide (DMSO). Form II was prepared by heating Form III of *m*-ABA until melting was observed to begin; the sample was then removed from the heat source before melting had completed and allowed to cool to ambient temperature. Form III was prepared by slow evaporation of a solution in methanol (evaporation occurring overnight) or by anti-solvent crystallization induced by addition of water to a solution of *m*-ABA in either DMSO or methanol. Form IV was prepared by sublimation of *m*-ABA at 140 °C onto a glass “cold finger” held at ambient temperature.

Form V was prepared by the complete melting of *m*-ABA to form thin films followed by rapid cooling to ambient temperature (or lower temperature by using an ice bath). Crystallization of bulk *m*-ABA produced Form II, with crystallization of Form V

favoured by cooling a thin film of the melt. Thin films of *m*-ABA melt were prepared by melting a small amount of Form III of *m*-ABA in a flat bottomed "boat" constructed out of aluminium foil. This foil boat was heated on a hotplate until complete melting was observed, at which point the boat was removed from the heat source. Rapid cooling was induced by placing the boat onto the surface of a water/ice mixture. Heating of *m*-ABA to melting was carried out in a glove box under an atmosphere of nitrogen. Melting *m*-ABA in the presence of air was found to cause the sample to rapidly change colour (becoming purple), presumably as a consequence of the sample undergoing a chemical reaction in the presence of oxygen.

Powder XRD measurements, both for fingerprinting purposes and for structure determination, were carried out using a Bruker D8 diffractometer operating in transmission mode (CuKα_1 radiation, germanium monochromated). Samples were either held flat between two pieces of tape or, if preferred orientation was suspected, packed into a glass capillary. As described later, the powder XRD patterns of Forms III, IV and V were indexed using algorithms contained within the CRYSFIRE powder indexing suite,[106] prior to profile fitting using the Le Bail technique[77] using the program GSAS with EXPGUI.[107,108] Structure solution was carried out using the direct-space genetic algorithm technique within the program EAGER, followed by final Rietveld refinement using the program GSAS with EXPGUI.

XPS measurements were carried out on samples of the five polymorphs of *m*-ABA using a Kratos Axis Ultra DLD system with an Al Kα X-ray source operating at 120 W. Data were collected with pass energies of 160 eV for survey spectra and 20 eV for high-resolution scans. The system was operated in hybrid mode, using a combination of magnetic immersion and electrostatic lenses and data were acquired over a surface area of *ca*. 300 to 700 μm^2. A magnetically confined charge compensation system was used to minimize charging of the sample surface and all spectra were acquired with a 90° take off angle. A high vacuum with base pressure 10^{-9} Torr was maintained during data acquisition.

Solid-state ^{13}C NMR measurements on all five polymorphs were carried out using a Chemagnetics Infinity Plus spectrometer (^1H Larmor frequency, 300.2 MHz, ^{13}C Larmor frequency, 75.48 MHz; 4 mm rotor; MAS frequency 12 kHz; ramped $^1H \rightarrow ^{13}C$ CP[109] with contact time, 2 ms; TPPM ^1H decoupling). A range of recycle delays were

required due to the differing ^{1}H spin-lattice relaxation times (T_1) of the polymorphs but, in each case, the recycle delay was at least five times the value of T_1. More information on values of T_1 is given in Section 3.3.

All DSC measurements were carried out using a TA Instruments Q100 differential scanning calorimeter. All samples were contained within hermetically sealed aluminium pans. A range of heating and cooling rates were used between 1 °C/min and 20 °C/min.

Solubility measurements were carried out by mixing a known mass of *m*-ABA (of a specific polymorph) with a known mass of solvent and sealing within a glass sample vial. A range of mass ratios were prepared. The samples were held at 20 °C for several days with frequent agitation to allow for maximal dissolution. Visual inspection of each sample was used to make a qualitative judgment of dissolution (i.e., if the sample had dissolved or not). By carrying out further studies using narrower ranges of mass ratios in the region corresponding to complete dissolution, the solubility of each sample was measured.

3.3 - Discovery and Characterization of New Polymorphs of *m*-ABA

A sample of *m*-ABA (>98% purity) was purchased from Sigma-Aldrich. The powder XRD pattern of this sample did not match that of either known form of *m*-ABA and was, therefore, established to be a monophasic sample of a new polymorph of *m*-ABA, hereafter designated Form III. Form III was found to be produced from slow crystallization from methanol (the crystallization taking from *ca*. 18 hours to several days). Faster crystallization from methanol, for example, induced by flowing a stream of nitrogen gas across the surface of the solution, was found to favour crystallization of Form I. Concomitant crystallization of Form I and Form III was commonly observed from methanol.

DSC measurements were carried out on the sample of Form III (further details of the thermal analysis experiments are given later). The powder XRD pattern of the sample collected from the DSC pan after heating to 200 °C and cooling to ambient temperature was found to differ from both the two previously known forms and the new Form III. This phase was found to be a monophasic sample of a new polymorph and designated Form IV. Further experiments led to the discovery that Form IV is most reliably produced from the sublimation of *m*-ABA onto a surface.

In an attempt to replicate the conditions of the DSC measurement in the laboratory, a fifth polymorph, Form V of *m*-ABA, was discovered. Form V is found to crystallize from thin films of molten *m*-ABA. Crystallization of bulk molten *m*-ABA is found to produce Form II and indeed, attempts to crystallize thin films of *m*-ABA often result in concomitant crystallization of Forms II and V. Rapid cooling of the melt was found to favour the crystallization of Form V.

The powder XRD patterns of all five polymorphs of *m*-ABA are shown in Figure 3.2. The crystal structures of Forms III, IV and V were determined directly from powder XRD data. Further details on the structure determination process are given in Section 3.4. Attempts to index the powder XRD pattern of Form I were unsuccessful, almost certainly due to the inability to accurately pick peaks for indexing in the region $24° \leq 2\theta \leq 30°$, in which there is a high degree of peak overlap. Synchrotron powder XRD data were collected on Form I *m*-ABA at the Diamond Light Source. However, no

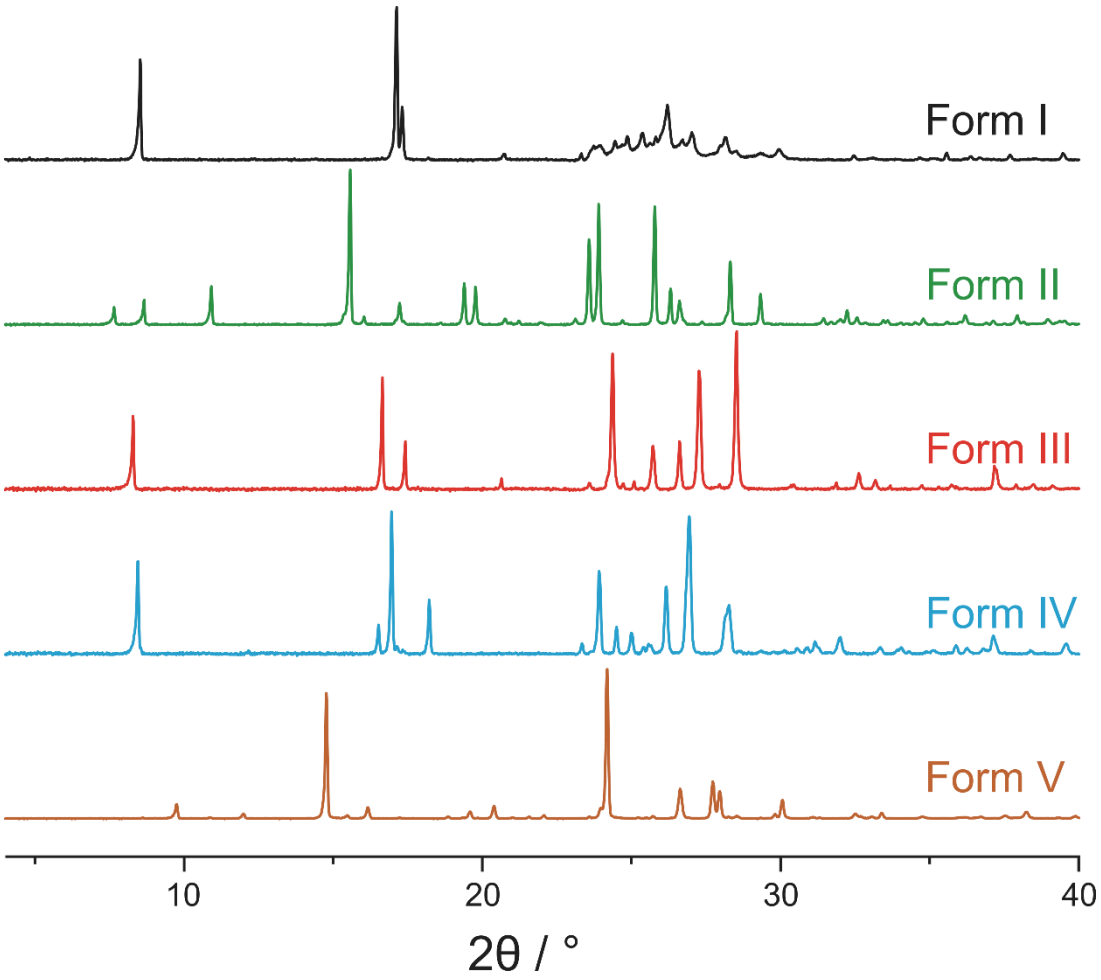

Figure 3.2: *Powder XRD patterns recorded for samples of the five polymorphs of m-ABA.*

improvement of the peak resolution in the problematic region was observed, suggesting that the peak overlap is sample dependent and not a problem of instrument resolution.

As previously mentioned, *m*-ABA is known to exist in two tautomeric forms, zwitterionic in Form I and non-zwitterionic in Form II. To establish the tautomeric form present in each of the new polymorphs, XPS measurements were carried out (Figure 3.3). In particular, the N(1s) region is diagnostic to the tautomeric state of the *m*-ABA molecule. Forms I, III and IV have an N(1s) peak at 402 eV, while Forms II and V have an N(1s) peak at 399.5 eV. A higher binding energy for the N(1s) electrons suggests that the nitrogen carries a positive charge. The higher binding energy peaks for Forms I, III and IV suggest that these forms contain a charged ammonium group and hence the *m*-ABA molecules are zwitterionic, whilst the lower binding energy peaks for Forms II and V suggest that they contain an uncharged amine group and hence the *m*-ABA molecules are non-zwitterionic. These results agree with the previous literature[50] assigning the *m*-ABA molecules in Form I as zwitterionic and those in Form II as non-zwitterionic. The assignments of Forms III and IV as containing the zwitterionic tautomer and Form V as containing the non-zwitterionic tautomer were used in the final Rietveld refinement.

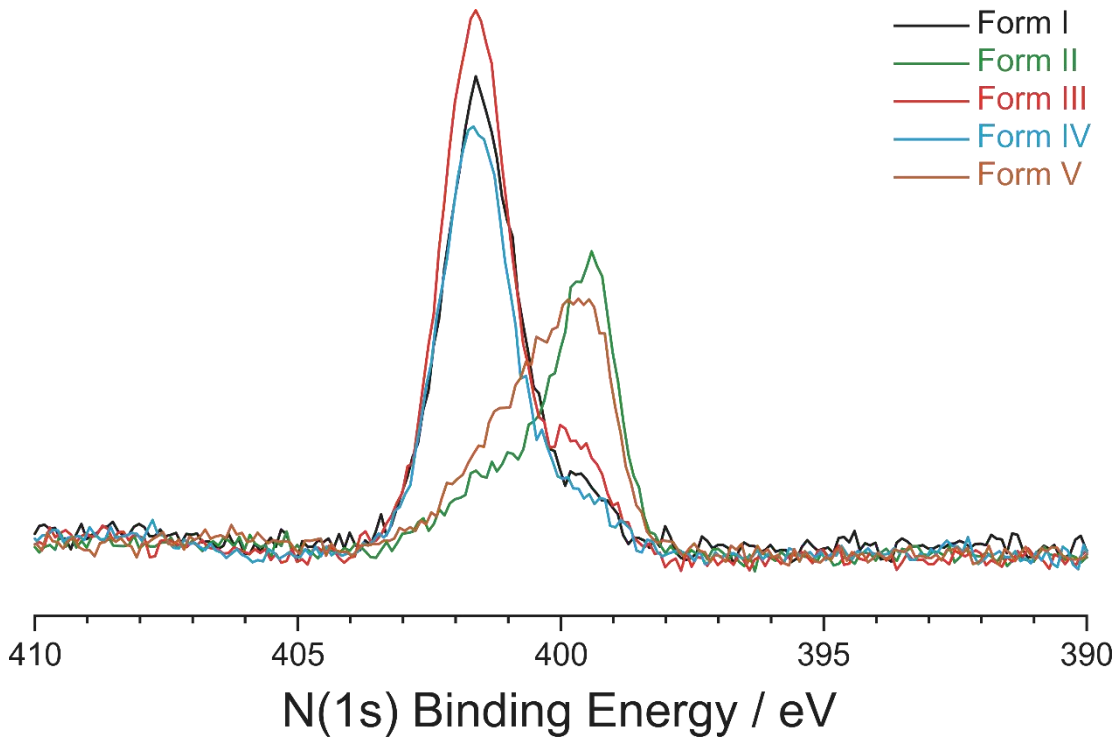

Figure 3.3: *N(1s) XPS spectra for the five polymorphs of m-ABA showing a clear distinction between the zwitterionic (Form I, Form III and Form IV) and non-zwitterionic (Form II and Form V) forms.*

Solid-state ^{13}C NMR data were acquired for all five polymorphs of *m*-ABA (Figure 3.4). From the spectra it is possible to determine the number of molecules within the asymmetric unit in the crystal structure. Each molecule of *m*-ABA contains seven unique carbon environments and so should display, at most, seven resonances in a ^{13}C NMR spectrum (provided there is no coupling). Forms I, II and IV all have more than seven peaks in their solid-state ^{13}C spectra and so must contain at least two molecules in the asymmetric unit. Forms III and V, on the other hand, have less than seven peaks and so show no evidence of more than one molecule in the asymmetric unit. It should be noted that this result does not provide conclusive evidence that there are not two or more molecules present, as multiple independent resonances may be "accidentally" unresolved.

The ^{1}H spin-lattice relaxation time (T_1) is found to vary between the polymorphs as follows: Form I, 0.6 s; Form II, 190 s; Form III, 1.7 s; Form IV, 0.5 s; and Form V, 7.2 s. From these values, it can be seen that the T_1 values for the zwitterionic polymorphs are significantly shorter than those of the non-zwitterionic polymorphs and, in particular, Form II. This relaxation is driven by molecular motion within the crystal structure and so the faster relaxation of the zwitterionic forms may be attributed to

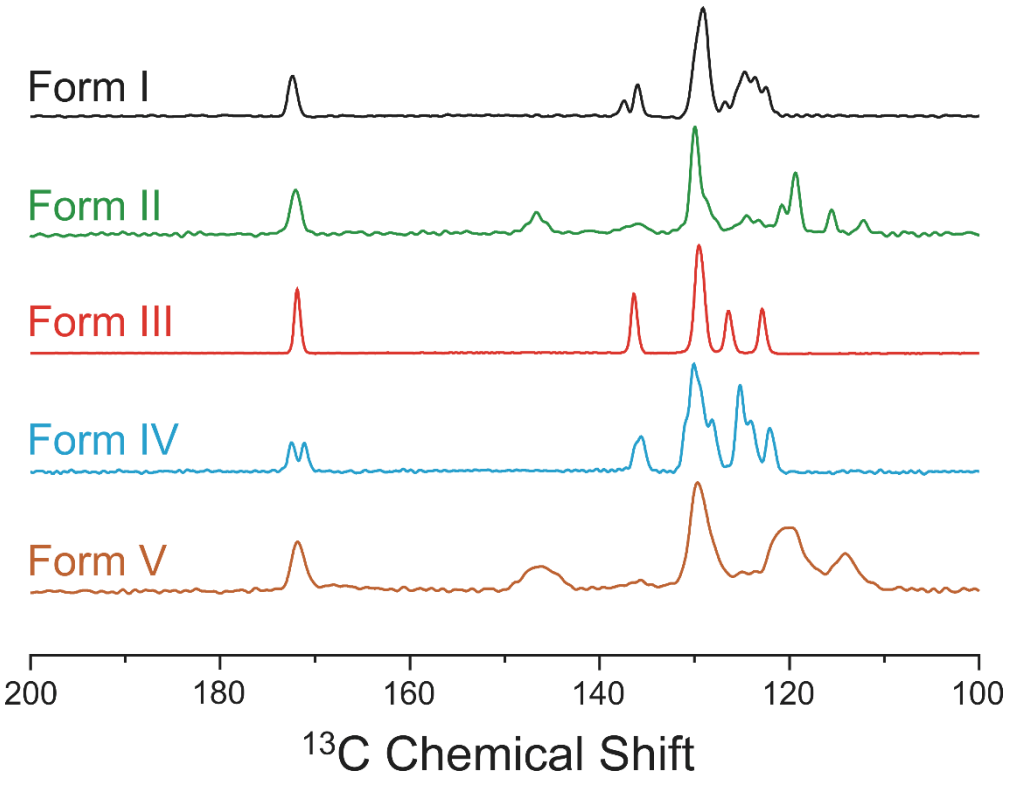

Figure 3.4: *High-resolution solid-state ^{13}C NMR spectra of the five polymorphs of m-ABA.*

rotation of the ammonium group. Forms II and V instead contain an amine group which may not be as free to rotate. The result that Form V has much shorter T_1 than Form II may be ascribed to the presence of dynamic disorder and this is further discussed in the structural description below.

3.3.1 - Structural Description

The crystal structures of Form III, Form IV and Form V of *m*-ABA were determined directly from powder XRD data and their structural parameters are given (along with those of the previously determined Form II) in Table 3.1.

	Form II	Form III	Form IV	Form V
Space Group	$P2_1/c$	$P2_1/a$	$P\bar{1}$	$P2_1/a$
a / Å	5.047(1)	21.3393(6)	3.80003(7)	14.7870(7)
b / Å	23.06(1)	7.29604(16)	11.55389(32)	4.95659(18)
c / Å	11.790(5)	3.77733(8)	14.6333(4)	9.0814(4)
α / °	90	90	110.5047(14)	90
β / °	105.47(3)	94.8240(12)	100.0115(35)	95.2119(21)
γ / °	90	90	96.5930(14)	90
V / Å^3	1322.45(87)	586.018(33)	595.108(35)	662.85(7)

Table 3.1: *Structural parameters for the polymorphs of m-ABA with known structures (Form II previously known;[51] Form III, Form IV and Form V determined during this work).*

In the crystal structure of Form III (Figure 3.5), the asymmetric unit contains a single molecule of *m*-ABA present as the zwitterionic tautomer. The structure can be described in terms of bilayers of *m*-ABA molecules, with the plane of the bilayer parallel to the (100) plane. In the internal region of a given bilayer, adjacent *m*-ABA molecules are engaged in N–H···O hydrogen bonding with the aryl rings projected either above or below the mean plane of this hydrogen-bonded region, forming the upper and lower surfaces of the bilayer. The upper and lower surfaces of adjacent

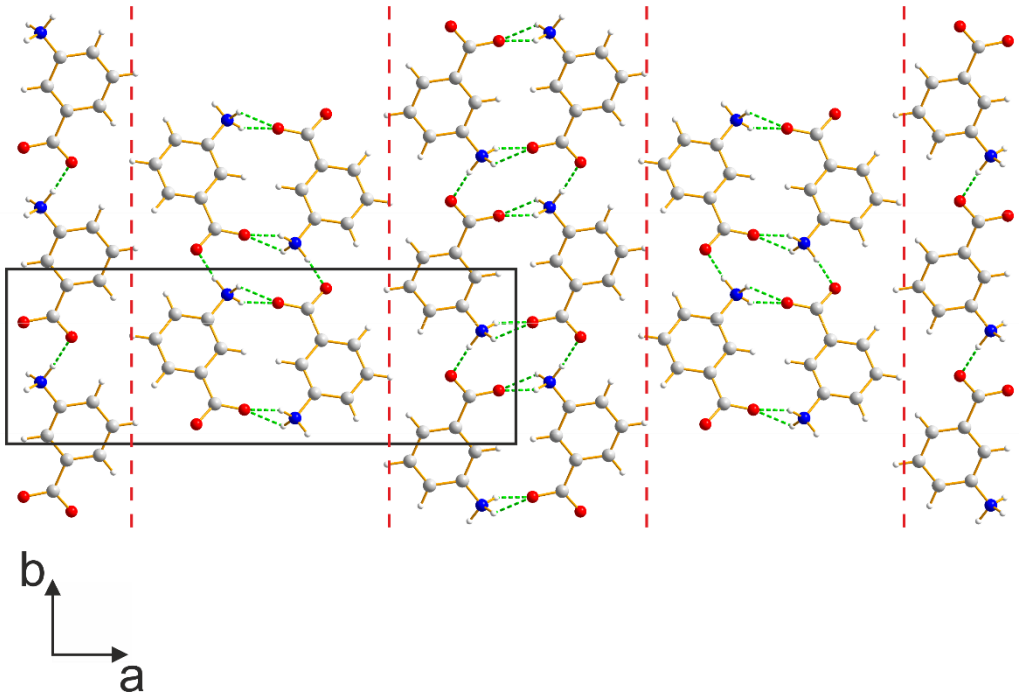

Figure 3.5: *Crystal structure of Form III of m-ABA. Shown is the view along the c-axis, allowing the bilayer nature of the structure to be seen. Carbon atoms are shown in grey, hydrogen atoms in white, oxygen atoms in red and nitrogen in blue. Hydrogen bonds are represented by green dashed lines. Red dashed lines indicate the interface between adjacent bilayers.*

bilayers (formed of the aryl rings) are in contact with each other *via* van der Waals interactions. Each ammonium group is within close proximity of four carboxylate groups of adjacent *m*-ABA molecules. On the basis of geometric criteria, restraints were used to produce the most favourable hydrogen-bonding arrangement, as shown in Figure 3.6. This arrangement results in two fairly linear hydrogen bonds to oxygen atoms of two neighbouring molecules (N–H···O angles: 161.9°, 158.0°), with the third hydrogen involved in a bifurcated hydrogen bond to two oxygen atoms (each oxygen atom belonging to a different *m*-ABA molecule). However, it should be noted that rotation of the ammonium group about the C–N bond allows formation of other, geometrically less optimal sets of N–H···O hydrogen bonds. This would suggest that the energy barrier to rotation of the ammonium group is likely relatively low. Within the bilayer, the planes of all the aryl groups are aligned parallel to each other. In the periodic repeat along the *a*-axis, there are two symmetry related bilayers (related by the *a*-glide operation), which differ in the orientation of the constituent *m*-ABA molecules.

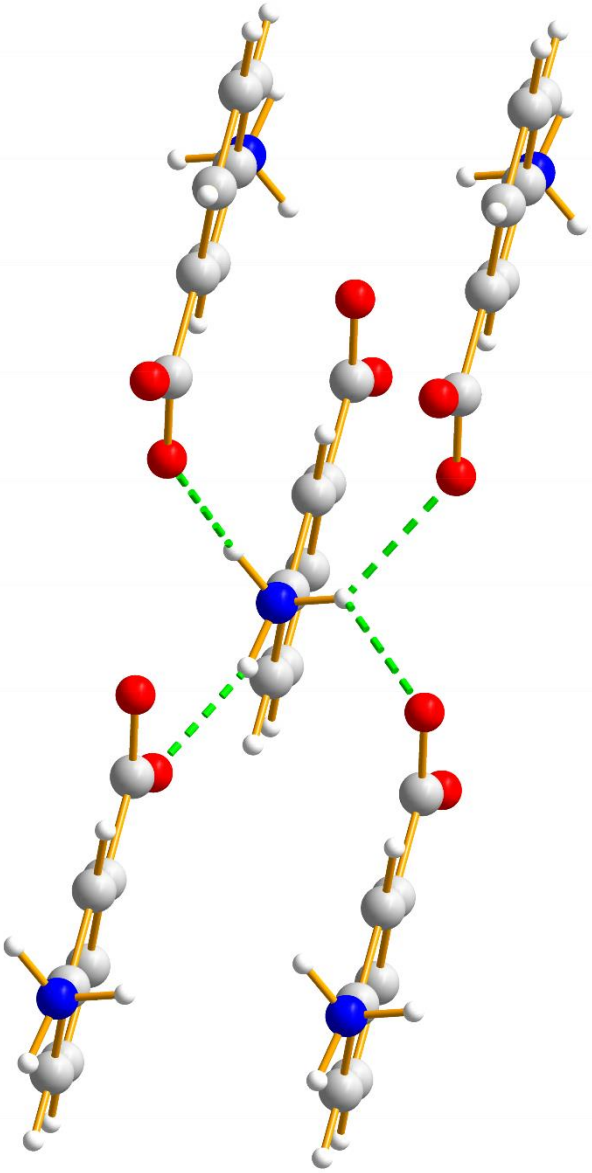

Figure 3.6: *Hydrogen-bonding interactions in the crystal structure of Form III of m-ABA between the ammonium group and oxygen atoms of four neighbouring molecules. All the molecules shown are in the same bilayer, illustrating that the planes of the molecules in a given bilayer are parallel to each other.*

In the crystal structure of Form IV (Figure 3.7), there are two independent molecules of *m*-ABA within the asymmetric unit, both of which are present as the zwitterionic tautomer. Although the crystal symmetry of Form IV (triclinic, space group: $P\bar{1}$) differs from Form III (monoclinic, space group: $P2_1/a$), the two structures share several common features. The structure of Form IV, as in the case of Form III, contains bilayers of *m*-ABA molecules, though with the bilayer plane parallel to the $(01\bar{1})$ plane. Within the bilayer, there are two different orientations of the aryl rings

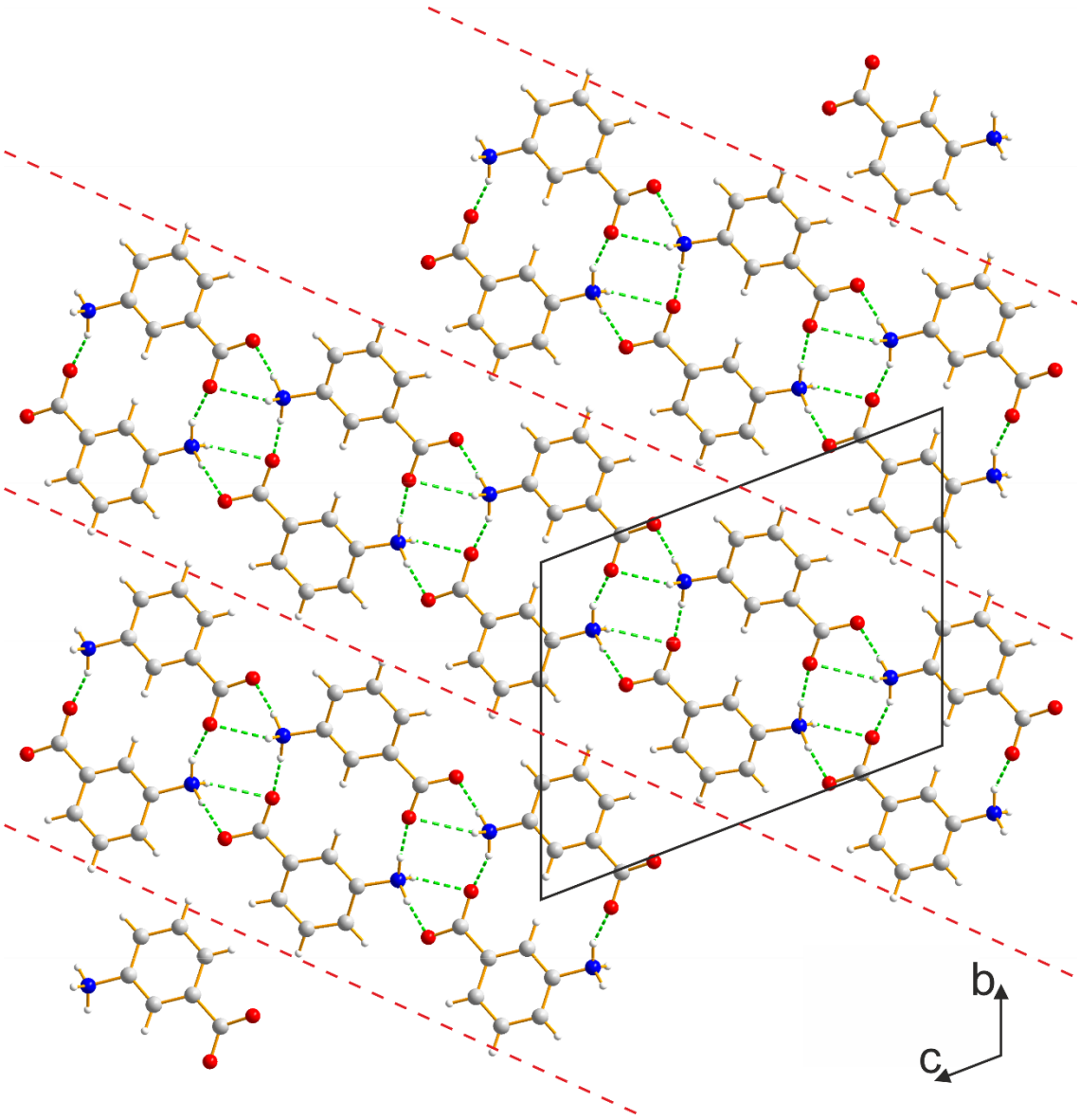

Figure 3.7: *Crystal structure of Form IV of m-ABA. Shown is the view along the a-axis, allowing the bilayer nature of the structure to be seen. Hydrogen bonds are represented by green dashed lines. Red dashed lines indicate the interface between adjacent bilayers.*

(from the two independent molecules of *m*-ABA in the structure), differing substantially from the structure of Form III (in which there is only one orientation of the aryl rings within the bilayer). Similar to the structure of Form III, adjacent molecules within the bilayer are engaged in N–H···O hydrogen bonds between ammonium and carboxylate groups, with the aryl ring again projected above and below the mean plane of the hydrogen-bonded region (forming the upper and lower surfaces of the bilayer). Adjacent bilayers (related by translation) are in contact *via* van der Waals interactions between the aryl rings. The ammonium group of each independent molecule of *m*-ABA is in close proximity to four carboxylate groups of neighbouring molecules (as observed in

Form III). Again, restraints were used during structure refinement to produce the most geometrically favourable hydrogen bonding arrangement around the ammonium group (Figure 3.8). As in the case of Form III, rotation of the ammonium group leads to the formation of other, less geometrically favourable hydrogen-bonding arrangements, again suggesting that the barrier to rotation is probably low.

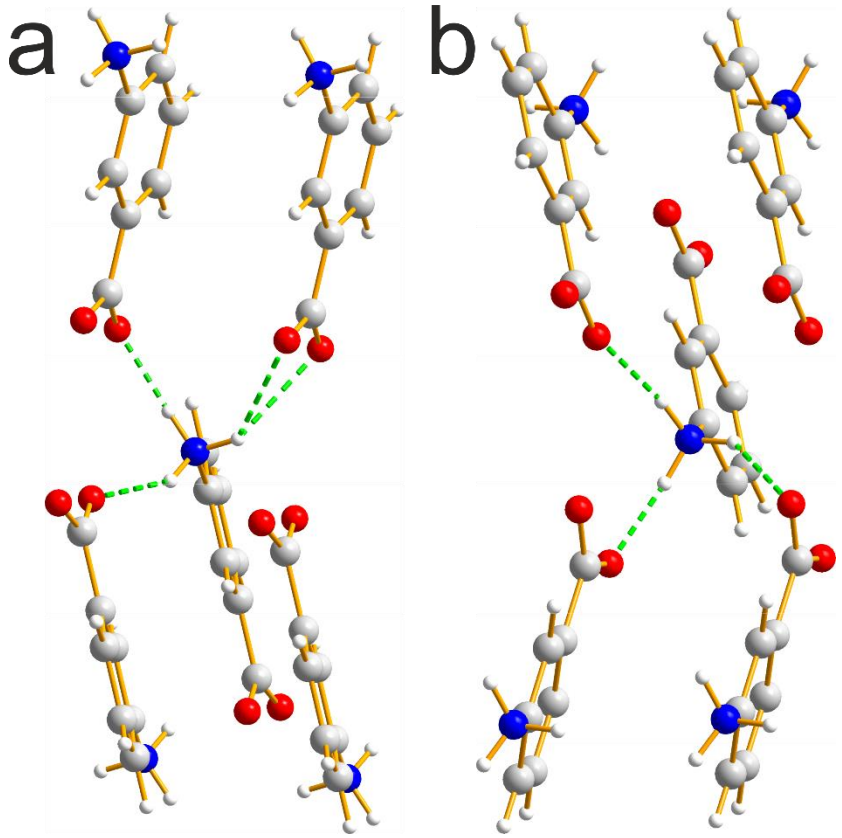

Figure 3.8: *Hydrogen-bonding interactions in the crystal structure of Form IV of m-ABA. (a) Shown between the ammonium group of one molecule in the asymmetric unit and oxygen atoms of three neighbouring molecules. (b) Shown between the ammonium group of the other molecule in the asymmetric unit and oxygen atoms of three neighbouring molecules. In each panel, all the molecules shown are in the same bilayer, illustrating that the planes of the molecules in a given bilayer exhibit two distinct orientations.*

The crystal structure of Form V contains a single molecule of *m*-ABA in the asymmetric unit as the non-zwitterionic tautomer. The hydrogen-bonding arrangement must, therefore, be different from those in Form III and Form IV. In Form V, the carboxylic acid groups of the *m*-ABA molecules form hydrogen-bonded dimers, $R_2^2(8)$ in graph set notation,[110-112] an arrangement that cannot occur when *m*-ABA is present as the zwitterionic tautomer. Detailed consideration of the Rietveld refinement, including the inspection of difference Fourier maps, indicated that the structure of Form V in fact

exhibits disorder in terms of two orientations of the *m*-ABA molecule in the average crystal structure. These two orientations are related by a 180° flip about an axis passing along the $HO_2C–C_{aryl}$ bond and, therefore, have different positions for the amine group and the hydrogen and oxygen atoms of the carboxylic acid group but share the same positions for the six carbon atoms of the aryl ring and three of the four hydrogen atoms attached to the aryl ring (excluding the hydrogen atom in the meta position with respect to both the amine and carboxylic acid groups). The refined occupancies of the two molecular orientations are 0.602(5) and 0.398(5), and their relative positions in the refined structure are shown in Figure 3.9.

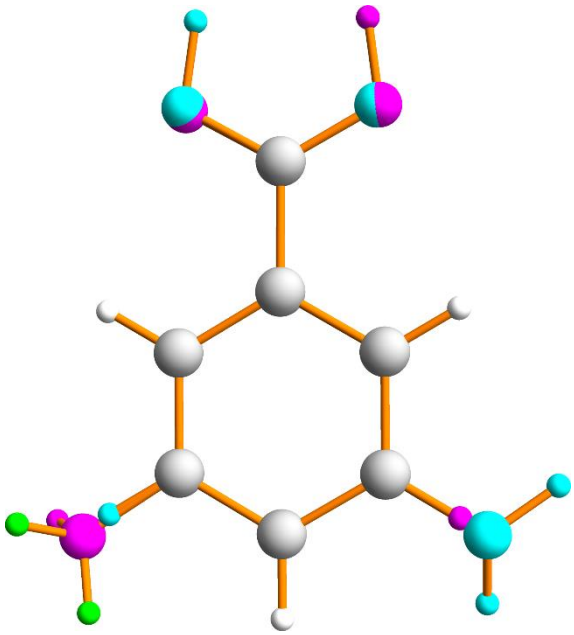

Figure 3.9: *Molecules of the two disordered components in the crystal structure of Form V of m-ABA. Atoms unique to the higher occupancy component are shown in cyan, atoms unique to the lower occupancy component in magenta (with the two positions of the disordered hydrogen atom shown in green), and atoms common to both components are shown in grey (carbon) and white (hydrogen).*

It must be noted that a crystal structure from XRD data gives an averaged representation of the actual structure taken over all unit cells present in the crystal and averaged over time. In the case of Form V of *m*-ABA, the average structure has disorder involving two molecular orientations although, from XRD data alone, the exact spatial distribution of the two molecular orientations cannot be determined directly. Consequently, two possible scenarios arise, both of which are compatible with a molecule disordered over two orientations (denoted **A** and **B** with respective orientations x_A and $1 – x_A$): (i) a structure in which there are ordered domains containing

only orientation **A** (with such domains representing a fraction x_A of the crystal) and ordered domains containing *only* orientation **B** (with such domains representing a fraction $1 - x_A$ of the crystal), or (ii) a structure in which each individual molecule throughout the crystal has a statistical probability of having orientation **A** (with probability x_A) or orientation **B** (with probability x_B). In case (i), the molecular orientations in each individual domain are ordered and the disorder in the average structure arises from averaging over all the different domains. In case (ii), the disorder exists at the molecular level and, in principle, the orientation of any given molecule may be uncorrelated with the orientations of its neighbours. Consequently, in case (i), the molecules in a given domain have a well-defined set of interactions with their neighbours (analogous to an ordered crystal structure) whereas, in case (ii), a range of different local intermolecular environments may exist depending on the orientation of a given molecule and the orientations of its neighbours. In certain cases, disorder of the type described in case (ii) may be ruled out if it transpires that an individual molecule in orientation **A** surrounded by molecules in orientation **B** (or vice versa) would give rise to unfavourable intermolecular interactions between neighbouring molecules.

In the case of Form V of *m*-ABA, intermolecular hydrogen bonds of reasonable geometry can form in each of the following situations (in which the molecular orientation with occupancy of 0.602 is defined as **A** and the molecular orientation with occupancy of 0.398 is defined as **B**): (1) an ordered domain containing only molecular orientation **A**, (2) an ordered domain containing only molecular orientation **B**, (3) a molecule in orientation **A** surrounded by neighbouring molecules in orientation **B**, and (4) a molecule in orientation **B** surrounded by molecules in orientation **A**. Situations (3) and (4) represent the type of disorder described in case (ii) above. In addition, in situations (3) and (4), there are no unfavourable interactions of the type which would categorically rule out a disordered model of the type observed in case (ii). Thus, from the knowledge of the average crystal structure determined from powder XRD in this work, it cannot be established whether the disorder in the average crystal structure of Form V of *m*-ABA represents disorder between two ordered domains (each containing only one molecular orientation), statistical orientational disorder of individual molecules, or a model of disorder that lies somewhere between these two extremes. However, as mentioned earlier, the $T_1(^1H)$ relaxation time of Form V (7.2 s) is substantially shorter than that of Form II (190 s). The substantially faster relaxation of Form V could be explained by the occurrence of a dynamic process in which the

m-ABA molecules interconvert between the two orientations over time. As T_1 relaxation is driven by molecular motion, *m*-ABA molecules swapping between the two orientations would be expected to result in a shorter T_1 than in the case with no dynamic interconversion (i.e., static disorder). The coordinated interconversion of an entire domain between the two molecular orientations would be significantly less likely than the same interconversion occurring on a molecular level, suggesting that case (ii), as described above, is perhaps the more likely hypothesis. In addition, the peaks in the solid-state ^{13}C NMR spectrum of Form V appear to be broadened. This broadening indicates a range of chemical environments and, thus, would be most readily explained by the molecular disorder described in case (ii) [or for the presence of very small domains in case (i)].

To further illustrate the intermolecular hydrogen-bonding arrangement that would arise in the types of structure described previously, an ordered domain containing only molecular orientation **A** [i.e., situation (1), Figure 3.10(a)] has neighbouring molecules linked by N–H···O hydrogen bonds, involving one N–H bond of each amine group and the carboxyl oxygen of each carboxylic acid group. An ordered domain containing only molecular orientation **B** [i.e., situation (2), Figure 3.10(b)] has pairs of molecules linked by both intermolecular N–H···O and N–H···N hydrogen bonds. It should be noted that there is additional disorder in terms of the position of the hydrogen atom engaged in the N–H···N hydrogen bond due to the presence of a crystallographic inversion centre at the midpoint of the N···N distance. Due to this inversion centre, the averaged crystal structure has equal populations of the N–H···N and N···H–N hydrogen-bonding arrangements linking the two nitrogen atoms. The positions of the hydrogen atoms in the amine and carboxylic acid groups are the specific hydrogen positions considered to give the most favourable sets of intermolecular hydrogen bonds and restraints were used during Rietveld refinement to maintain this arrangement.

As mentioned earlier, the structure of Form V bears some similarity to the previously reported structure of Form II. Form II of *m*-ABA also contains non-zwitterionic molecules in $R_2^2(8)$ dimers. However, Form II has two independent molecules in the asymmetric unit whereas Form V has one independent molecule. In addition, there are differences in the hydrogen bonding of the amine group. In Form II, N–H···N hydrogen bonds form between the two independent *m*-ABA molecules to

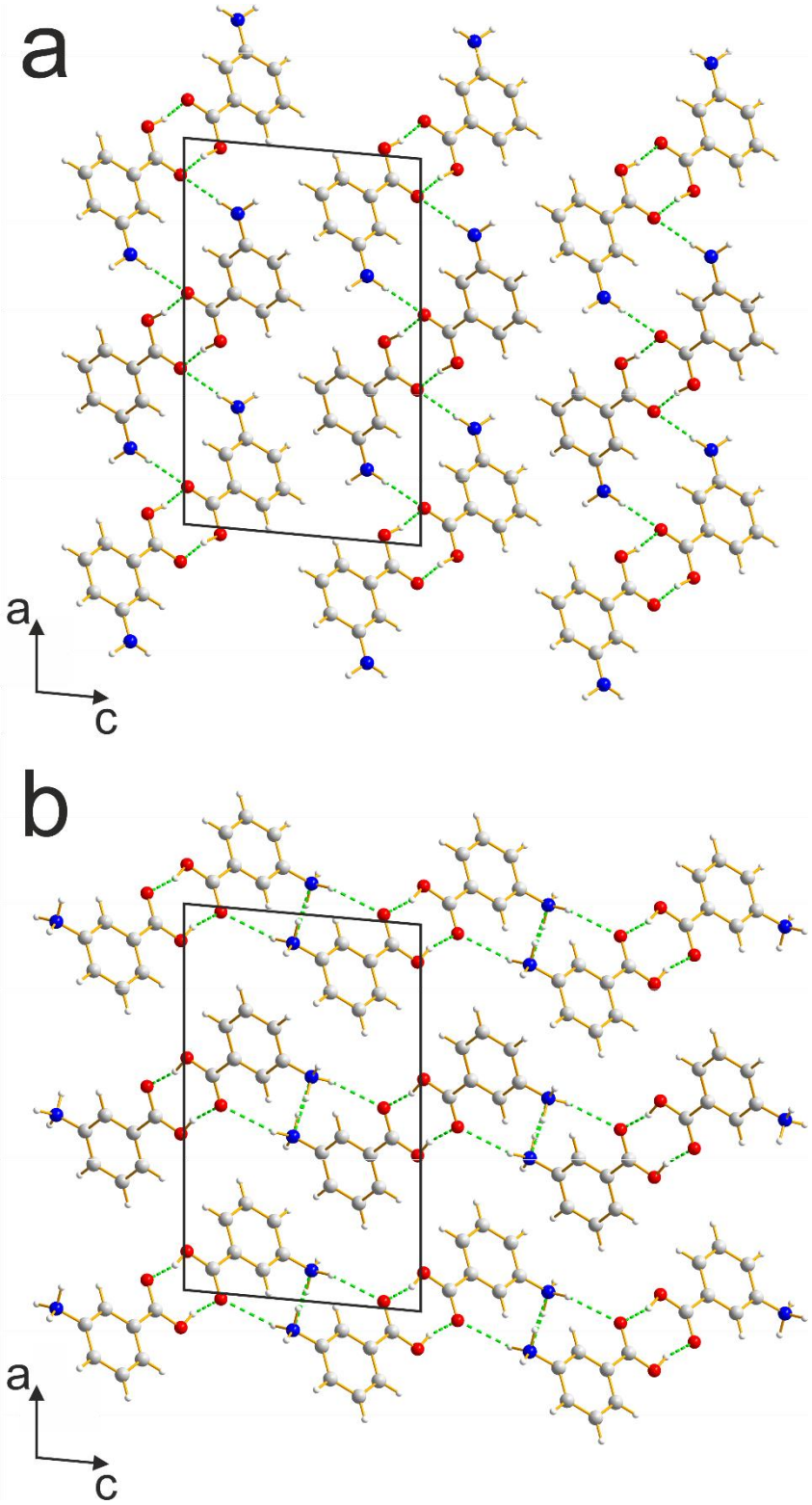

Figure 3.10: *Crystal structure of Form V of m-ABA viewed along the b-axis (green dashed lines indicate hydrogen bonds) for (a) ordered domains containing the molecular orientation of higher occupancy (i.e.,* ***A****) and (b) ordered domains containing the molecular orientation of lower occupancy (i.e.,* ***B****). Note that the aryl rings have the same positions and orientations in panels a and b, but the hydrogen bonding arrangements are different.*

create a "zigzagged" N–H···N–H···N–H···N–H hydrogen-bonded chain parallel to the *a*-axis. Formation of N–H···O hydrogen bonds also occurs between the amine groups within this chain and the carboxylic acid dimers, such that an amine group of one independent molecule is hydrogen bonded to two other amine groups (each belonging to the second type of independent *m*-ABA molecule, acting as a hydrogen-bond donor to one and a hydrogen-bond acceptor to the other) and to an oxygen in a carboxylic acid group.

3.3.2 - Stability

A range of experiments and observations have led to insights concerning the relative stabilities of the five polymorphs of *m*-ABA. Under dry conditions at ambient temperature and pressure, Form II and Form V (the two non-zwitterionic polymorphs) are observed to be unstable. Form V transforms to Form II over *ca.* 2 days and Form II transforms to Form I over *ca*. 7 days. Form I, Form III and Form IV are found to be stable under dry ambient conditions over several months. However, when in contact with a saturated solution of *m*-ABA in methanol (i.e., as a slurry), Form I and Form IV are found to transform over *ca*. 12 hours to produce Form III. In the present work, the relative stabilities of Form I and Form IV were unable to be determined, as slurry experiments involving these two polymorphs result in the formation of Form III. From this set of observations, Form III is assigned as the most stable of the known polymorphs of *m*-ABA under ambient conditions.

The solubility of Form III was measured at 20 °C in acetonitrile, ethyl acetate and methanol to allow comparison with the corresponding solubility data previously reported by Svärd *et al*.[49] for Form I and Form II. The solubility data for these three polymorphs are given in Table 3.2.

	Solubility (mg/g)		
Solvent	Form I	Form II	Form III
Acetonitrile	7.15 ± 0.006	23.39 ± 0.05	4.65 ± 0.05
Ethyl acetate	8.78 ± 0.27	29.61 ± 0.11	4.95 ± 0.05
Methanol	51.73 ± 0.38		50.3 ± 0.4

Table 3.2*: Solubilities of Form I, Form II and Form III of m-ABA in acetonitrile, ethyl acetate and methanol, quoted as mass of solute (mg) per unit mass of solvent (g).*

For each of the solvents studied, the solubility of Form III is lower than that of Form I and Form II. Lower solubility among a set of polymorphs is indicative of higher thermodynamic stability, suggesting that Form III is indeed the most stable polymorph of *m*-ABA discovered thus far.

DSC measurements have previously been reported[49] for Forms I and II and indicate that, on heating, Form II undergoes only melting at 178 °C and no other transformation. Form I, on the other hand, is reported to either undergo a transformation to Form II at 157 °C, or undergo melting at 172 °C. Forms I and II therefore have an enantiotropic relationship. During this work, DSC measurements were performed on the three new polymorphs of *m*-ABA in order to characterize their thermal properties.

Form III (Figure 3.11) is found to undergo an endothermic phase transition at 154 °C on heating. No reverse transition is found on subsequent cooling and the product phase can be identified by powder XRD as Form I. As Form III is the most stable polymorph at ambient temperature and an endothermic phase transition is observed to

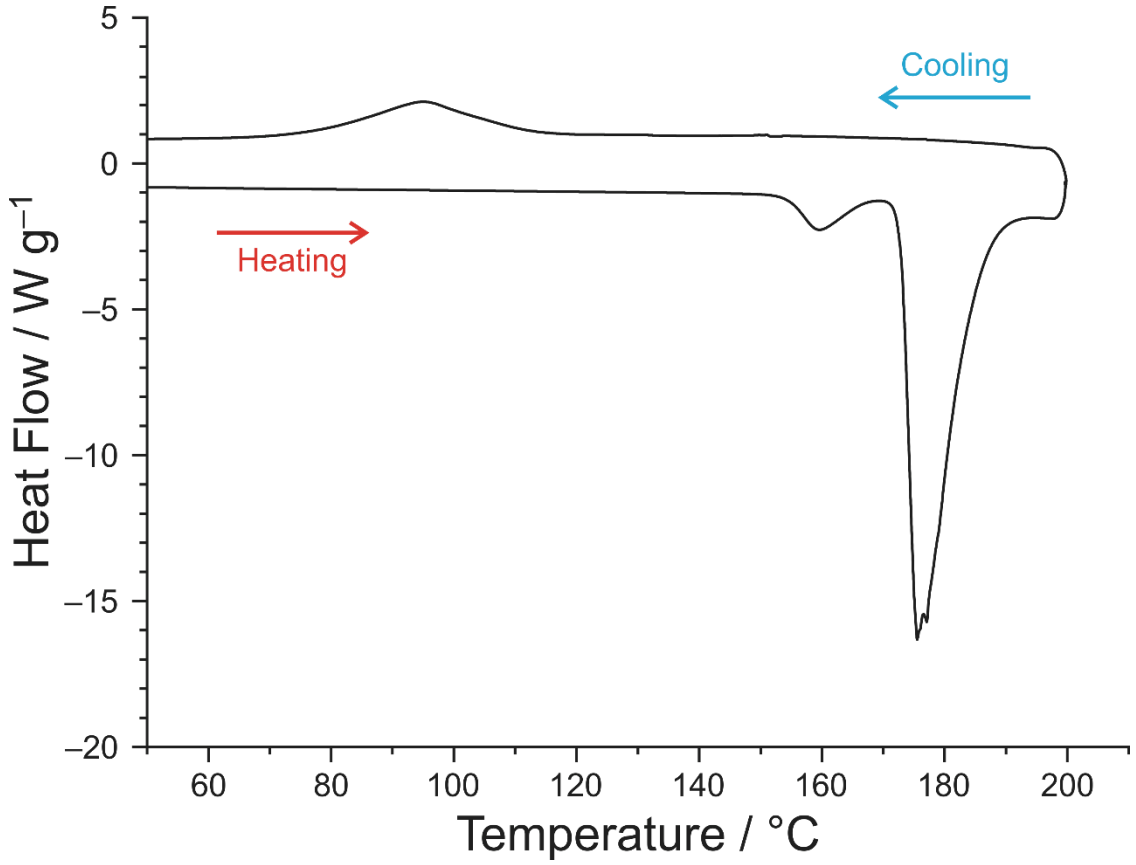

Figure 3.11: *DSC data for Form III of m-ABA recorded with a heating/cooling rate of 20 °C min^{-1}. Exotherms are plotted upwards.*

produce Form I upon heating, the relationship between Form I and Form III is assigned as enantiotropic, with Form III having higher stability below the transformation temperature (including ambient temperature). The fact that the reverse transformation from Form I to Form III is not observed on cooling during the DSC measurement is likely attributable to kinetic factors.

Form IV (Figure 3.12) undergoes an endothermic phase transition at 169 °C on heating, which is not reversible on cooling. The resultant phase following this transformation is found by powder XRD to be Form II. Form V (Figure 3.13) is observed to undergo melting at 167 °C. However, the melting endotherm in the DSC thermogram is broad. In addition, there appears to be a hint of an additional peak at a temperature just below melting but, unfortunately, this peak could not be separated from the melting endotherm.

The density rule is a useful rule-of-thumb for judging the relative stability within polymorphic systems, with higher density associated with higher stability (though there are known counter examples). The densities of the four polymorphs of *m*-ABA with

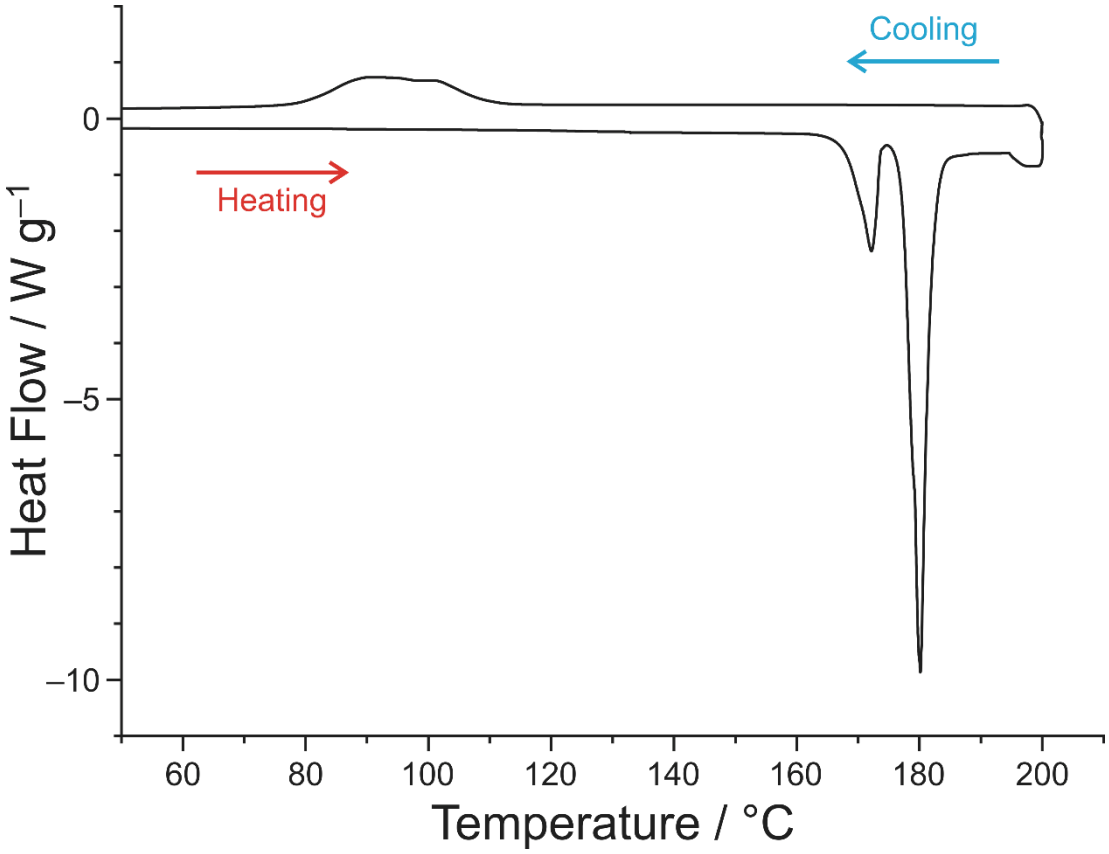

Figure 3.12: *DSC data for Form IV of m-ABA recorded with a heating/cooling rate of 10 °C min^{-1}. Exotherms are plotted upwards.*

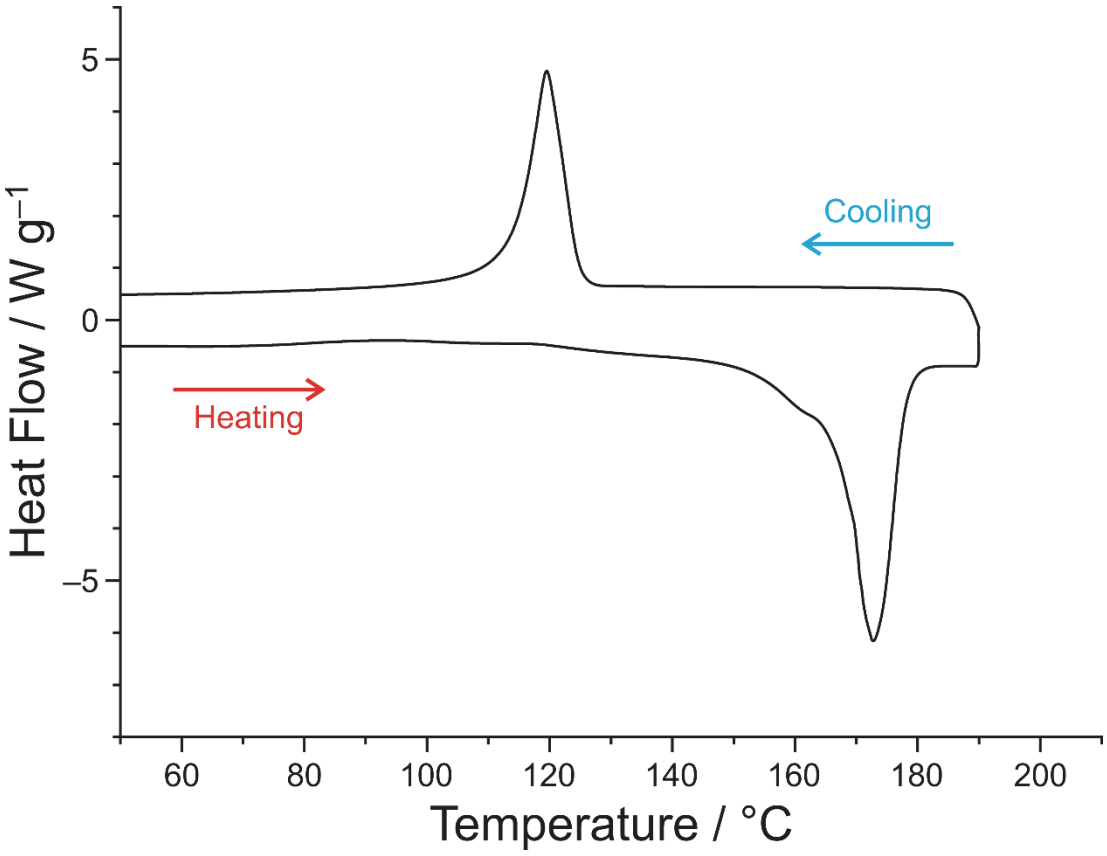

Figure 3.13: *DSC data for Form V of m-ABA recorded with a heating/cooling rate of 10 °C min^{-1}. Exotherms are plotted upwards.*

known structures (noting that Form I has no known structure) are as follows: Form II, 1.378 g cm^{-3}; Form III, 1.553 g cm^{-3}; Form IV, 1.522 g cm^{-3}; and Form V, 1.372 g cm^{-3}. Thus, the two zwitterionic forms with known structure (Form III and Form IV) are significantly denser than the two non-zwitterionic forms (Form II and Form V). It is noteworthy that the polymorph of *m*-ABA assigned experimentally as the most stable at ambient temperature (Form III) is also the densest.

3.4 - Details of Structure Determination

3.4.1 - Structure Determination of Form III of m-ABA

The powder XRD pattern of Form III of *m*-ABA was indexed using the program TREOR[113] within the CRYSFIRE program suite,[106] as a monoclinic cell with metric symmetry: a = 21.38 Å, b = 7.30 Å, c = 3.78 Å, β = 94.8° (V = 587.7 Å^3). From systematic absences, the space group was assigned as $P2_1/a$ and from density arguments the asymmetric unit was determined to contain a single molecule (Z' = 1). Le Bail fitting was performed on the powder XRD pattern, using the program GSAS,[107] achieving a

high quality of fit [Figure 3.14(a), R_{wp} = 2.45%, R_p = 1.77%] and the refined unit cell and profile parameters were used in the structure solution calculations.

The program EAGER was used to carry out structure solution with 16 independent GA calculations performed. The evolution involved 100 generations for a population of 100 structures, with 40 mating operations and 30 mutation operations carried out per generation. The *m*-ABA molecule (used in the structure solution without hydrogen atoms) was represented by seven structural variables: three positional variables, three orientational variables and a single torsional variable (around the aromatic to carboxylate group bond). After 100 generations, the same good quality fit was found in each of the 16 calculations and so was used as the starting point for Rietveld refinement.

Rietveld refinement was carried out using the program GSAS.[107] Standard restraints were applied to bond lengths and angles and planar restraints were used to maintain the planarity of the aromatic ring and carboxylate group. These restraints were relaxed during the refinement procedure. Hydrogen atoms were added to the *m*-ABA molecule as defined by standard geometries. Intermolecular bond-length restraints were used to orient the ammonium group so as to give the optimum hydrogen bonding environment. A global U_{iso} value was refined for all non-hydrogen atoms, with the value U_{iso} for the hydrogen atoms set to be 1.2 times that of the non-hydrogen atoms. The March-Dollase function[114,115] was used to allow for preferred orientation within the sample. The final Rietveld refinement gave a high quality fit to the powder XRD data [Figure 3.14(b), R_{wp} = 2.45% and R_p = 1.80%] with the following refined parameters: a = 21.3393(6) Å, b = 7.29604(16) Å, c = 3.77733(8) Å, β = 94.8240(12)°; V = 586.018(33) Å^3 (2θ range, 4 to 70°; 3867 profile points; 74 refined variables).

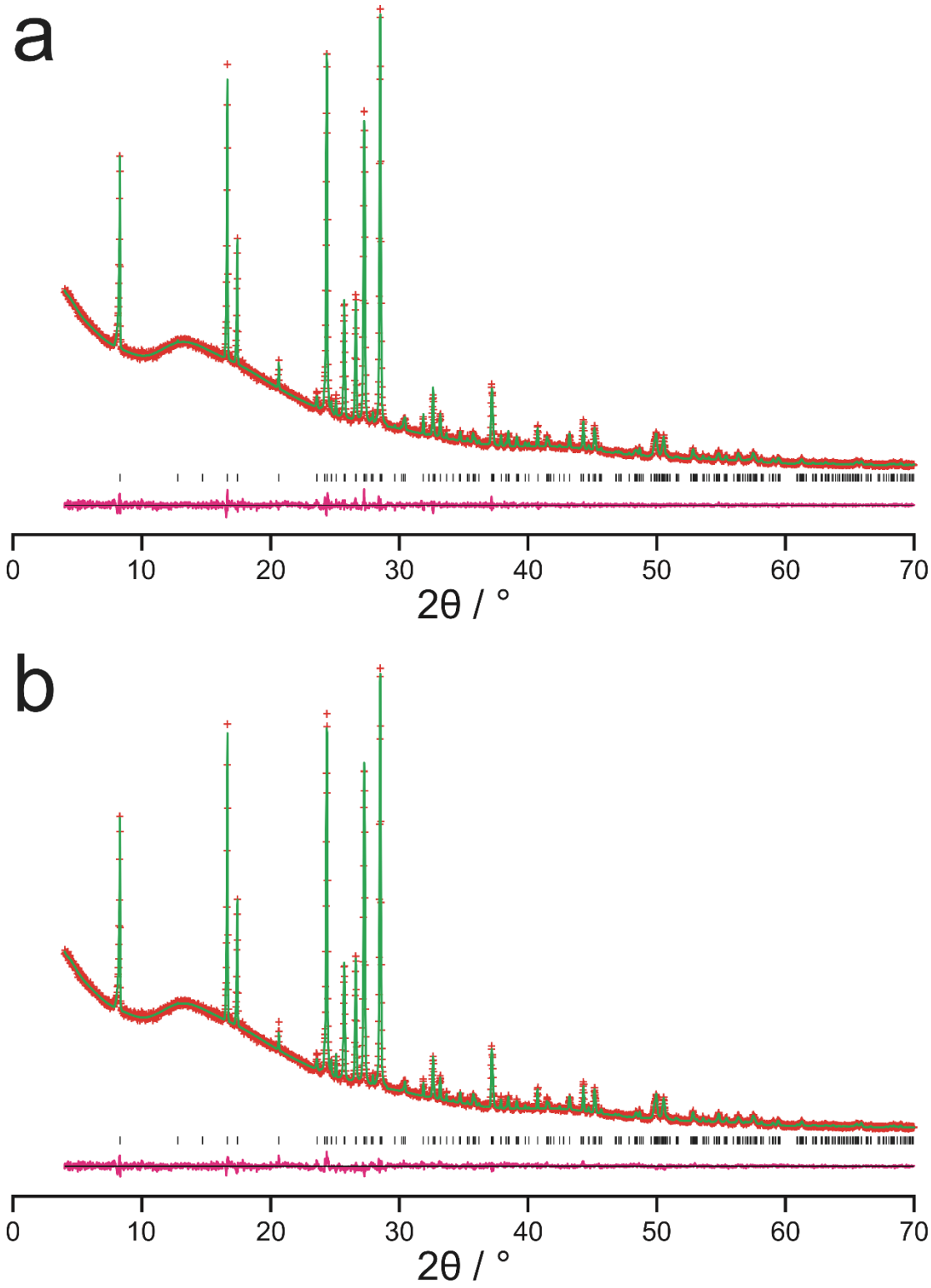

Figure 3.14: *(a) Le Bail fit and (b) Rietveld fit for the powder XRD pattern of Form III of m-ABA. The experimental data is shown as red crosses, the calculated fit as a green line and the difference between the two as a magenta line. Peak positions are displayed as black tick marks.*

3.4.2 - Structure Determination of Form IV of m-ABA

The powder XRD pattern of Form IV of *m*-ABA was indexed using the program ITO,[116] again within the CRYSFIRE suite[106] with a triclinic cell with metric symmetry: a = 3.82 Å, b = 11.60 Å, c = 14.69 Å, α = 110.5°, β = 92.8°, γ = 96.6° (V = 602.5 Å^3). From density arguments, the unit cell must contain four molecules of *m*-ABA (Z = 4). The space group was assigned as $P\bar{1}$ with two molecules in the asymmetric unit (Z' = 2). Le Bail fitting was carried out on the powder XRD pattern of Form IV, giving a high quality of fit [Figure 3.15(a), R_{wp} = 2.82%, R_p = 2.10%].

The program EAGER was used to carry out structure solution with 16 independent GA calculations performed. The evolution involved 100 generations for a population of 100 structures, with 40 mating operations and 30 mutation operations carried out per generation. Each *m*-ABA molecule (used in the structure solution without hydrogen atoms) was represented by seven structural variables: three positional variables, three orientational variables and a single torsional variable (around the aromatic to carboxylate group bond), amounting to a total of 14 structural variables. After 100 generations, the same good quality fit was found in each of the 16 calculations and so was used as the starting point for Rietveld refinement.

Rietveld refinement was carried out using the program GSAS.[107] Standard restraints were applied to bond lengths and angles and planar restraints were used to maintain the planarity of the aromatic ring and carboxylate group. These restraints were relaxed during the refinement procedure. Hydrogen atoms were added to the *m*-ABA molecules as defined by standard geometries. Intermolecular bond-length restraints were used to orient the ammonium group so as to give the optimum hydrogen bonding environment. A global U_{iso} value was refined for all non-hydrogen atoms with the value of U_{iso} for the hydrogen atoms set to be 1.2 times that of the non-hydrogen atoms. The March-Dollase function[114,115] was used to allow for preferred orientation within the sample. The final Rietveld refinement gave a high quality fit to the powder XRD data [Figure 3.15(b), R_{wp} = 2.86% and R_p = 2.17%] with the following refined parameters: a = 3.80003(7) Å, b = 11.55389(32) Å, c = 14.6333(4) Å, α = 110.5047(14)°, β = 92.7424(16)°, γ = 96.5930(14)°; V = 595.108(35) Å^3 (2θ range, 4 to 70°; 3867 profile points; 125 refined variables).

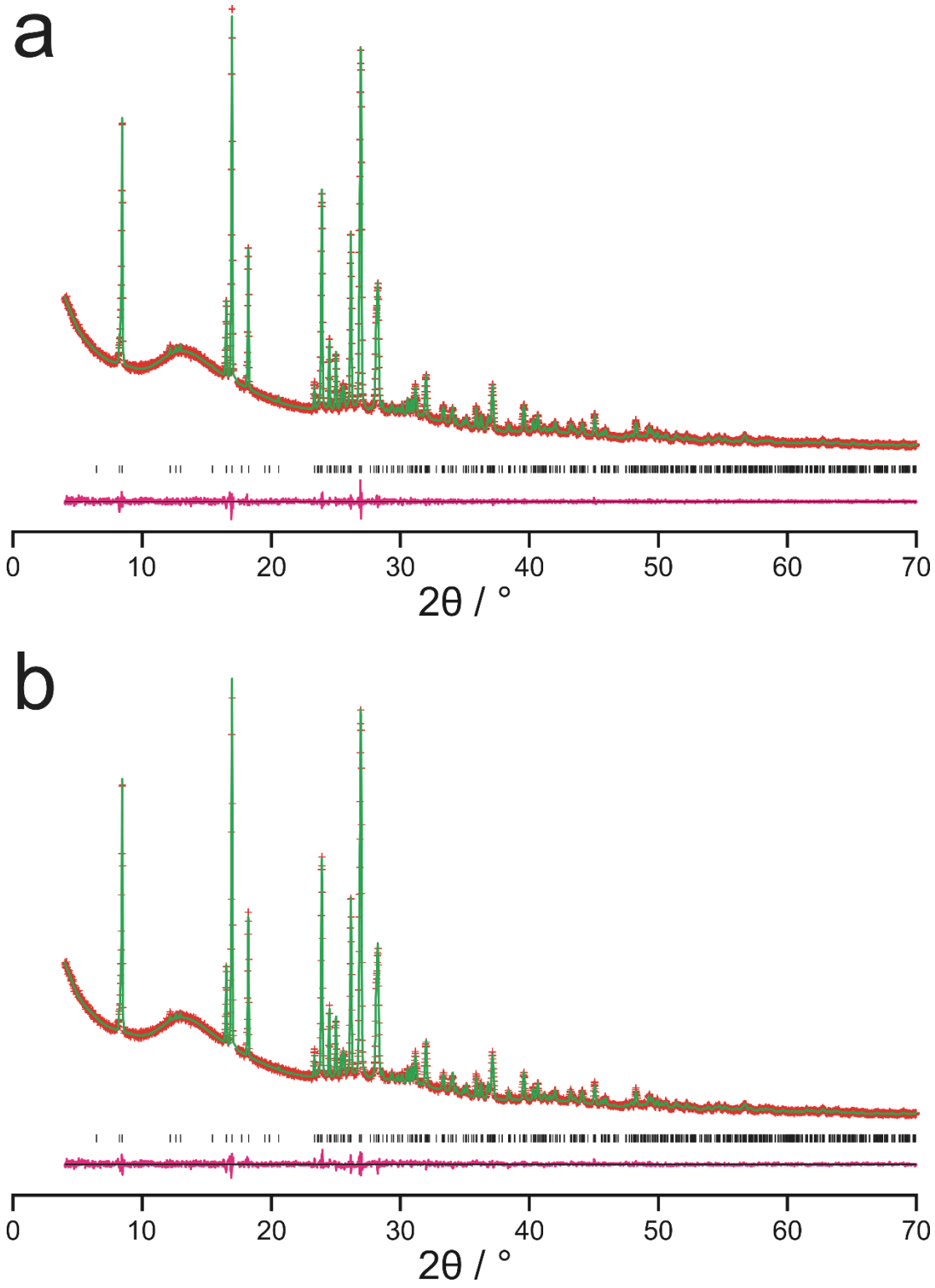

Figure 3.15: *(a) Le Bail fit and (b) Rietveld fit for the powder XRD pattern of Form IV of m-ABA. The experimental data is shown as red crosses, the calculated fit as a green line and the difference between the two as a magenta line. Peak positions are displayed as black tick marks.*

3.4.3 - Structure Determination of Form V of m-ABA

The powder XRD pattern of Form V of *m*-ABA was indexed using the program TREOR,[113] again within the CRYSFIRE suite[106] with a monoclinic cell with metric symmetry: $a = 14.76$ Å, $b = 4.95$ Å, $c = 9.09$ Å, $\beta = 95.2°$ ($V = 662.1$ Å^3). From systematic absences, the space group was assigned as $P2_1/a$ and from density arguments the asymmetric unit was determined to contain a single molecule ($Z' = 1$). Le Bail fitting was carried out on the powder XRD pattern of Form V, giving a high quality of fit [Figure 3.16(a), $R_{wp} = 2.45\%$, $R_p = 1.83\%$] and the refined unit cell and profile parameters were used in the structure solution calculations.

The program EAGER was used to carry out structure solution with eight independent GA calculations performed. The evolution involved 100 generations for a population of 100 structures, with 40 mating operations and 30 mutation operations carried out per generation. The *m*-ABA molecule (used in the structure solution without hydrogen atoms) was represented by seven structural variables: three positional variables, three orientational variables and a single torsional variable (around the aromatic to carboxylic acid group bond). After 100 generations, the same good quality fit was found in each of the eight calculations and so was used as the starting point for Rietveld refinement.

Rietveld refinement was carried out as described for the other forms of *m*-ABA. However, a small impurity of Form II of *m*-ABA was present within the sample and was included as an impurity phase during Rietveld refinement. Standard restraints were applied to bond lengths and angles and planar restraints used to maintain the planarity of the aromatic ring and carboxylic acid group. Difference Fourier plots created during the refinement procedure strongly suggested the presence of positional disorder of the amine group with the two positions related by 180° flip of the molecule about the $HO_2C–C_{aryl}$ bond. The carboxylic acid group was also disordered over two orientations corresponding to the same 180° flip of the molecule about the $HO_2C–C_{aryl}$ bond (with the two orientations of the carboxylic acid group having the same occupancies as the two sites occupied by the amine group). The relative occupancies of the two orientations was refined. Hydrogen atoms were added to the molecule according to standard geometries and the orientation of the amine group was chosen such that the most reasonable set of intermolecular hydrogen bonds was formed, based on consideration of

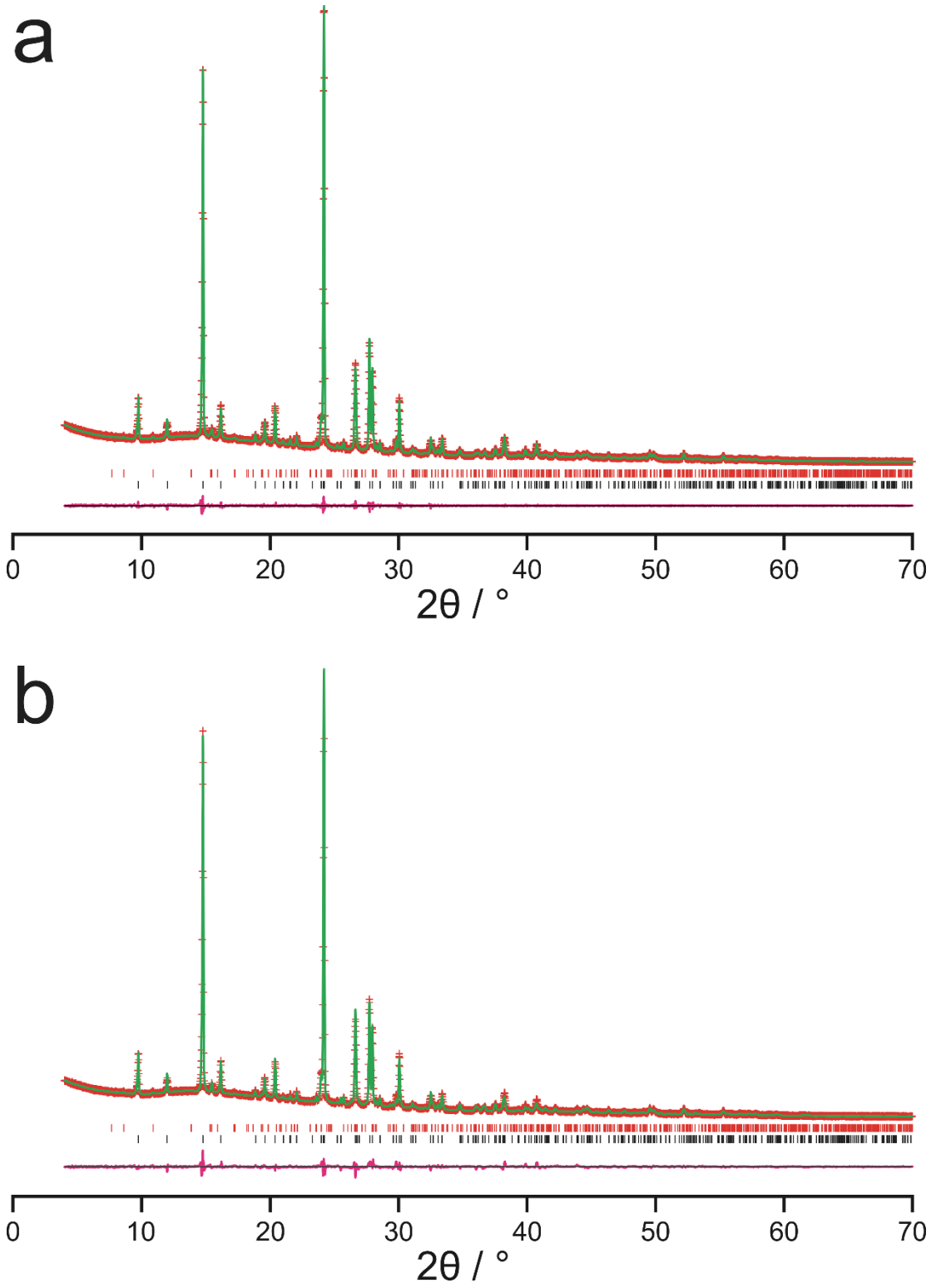

Figure 3.16: *(a) Le Bail fit and (b) Rietveld fit for the powder XRD pattern of Form V of m-ABA. The experimental data is shown as red crosses, the calculated fit as a green line and the difference between the two as a magenta line. Peak positions of Form V are displayed as black tick marks and those of an impurity phase of Form II of m-ABA are displayed as red tick marks.*

the disorder model with domains containing only the molecular orientation of higher occupancy and domains containing only the molecular orientation of lower occupancy [i.e., case (i) discussed above]. Disorder was also included in the positioning of the hydrogen-bonded hydrogen within the amine group of the lower occupancy orientation (due to the presence of a crystallographic inversion centre at the midpoint of the hydrogen bond). A global U_{iso} value was refined for the non-hydrogen atoms with the value of U_{iso} for the hydrogen atoms set to be 1.2 times that of the non-hydrogen atoms. The March-Dollase function[114,115] was used to allow for preferred orientation within the sample. The final Rietveld refinement gave a high quality fit to the powder XRD data (Figure 3.16(b), R_{wp} = 4.08% and R_p = 2.79%) with the following refined parameters: a = 14.7870(7) Å, b = 4.95659(18) Å, c = 9.0814(4) Å, β = 95.2119(21)°; V = 662.85(7) Å^3 (2θ range, 4 to 70°; 3867 profile points; 114 refined variables).

3.5 - *In-Situ* Solid-State NMR Study of the Crystallization of *m*-ABA from Methanol

The abundant polymorphism discovered within the *m*-ABA system made the crystallization of *m*-ABA from a solvent a prime target of study using the previously developed *in-situ* solid-state NMR technique[42,43] (expanded upon in Chapters 1 and 2). Through use of solid-state ^{13}C NMR, the identity of the solid phase present during the crystallization process can be determined, excluding any signal from the liquid phase. This strategy allows the formation and polymorphic evolution of the solid phase to be monitored as a factor of time during the crystallization process. The crystallization of *m*-ABA from methanol was studied using this technique.

As mentioned earlier in this chapter, crystallization of *m*-ABA from methanol in the laboratory can result in the formation of either Form I or Form III (or both concomitantly). Rapid crystallization was found, in the laboratory, to favour the crystallization of Form I, while slower crystallization was found to favour the formation of Form III.

3.5.1 - Methodology of In-Situ Solid-State NMR Study

This *in-situ* NMR study was carried out using a Bruker AVANCE III NMR spectrometer at the UK 850 MHz Solid-State NMR Facility at the University of Warwick (^{13}C Larmor frequency, 213.82 MHz; 4 mm HXY probe in double-resonance

mode). A sample of *m*-ABA with natural isotopic abundance was used. To prepare the crystallization solution, Form III of *m*-ABA (5.5 mg) and methanol (40.8 mg) were measured by mass into the bottom of a zirconia NMR rotor. The rotor was spun in a centrifuge for a few seconds to ensure that the sample was at the bottom of the rotor, before sealing with Kel-F® inserts, as described in Section 2.4. The rotor was spun within the spectrometer under MAS conditions (12 kHz), before heating to 85 °C for one hour to allow for complete dissolution. The rotor was then cooled to 33 °C, before commencing the repeated acquisition of solid-state NMR spectra. Each spectrum involved the acquisition of 256 scans, with a pulse delay of 9 s, leading to a total time to acquire each spectrum of 38.4 mins, representing the time resolution of the *in-situ* study of the crystallization process. To record the solid-state ^{13}C spectra, ramped $^{1}H \rightarrow ^{13}C$ CP was employed (CP contact time, 1.5 ms) with ^{1}H decoupling using SPINAL-64 (nutation frequency, 91 kHz).

3.5.2 - Results and Discussion

The evolution of the solid-state data over the course of the *in-situ* experiment is shown in Figure 3.17. The presence of solid is observed in the first CP-MAS spectrum,

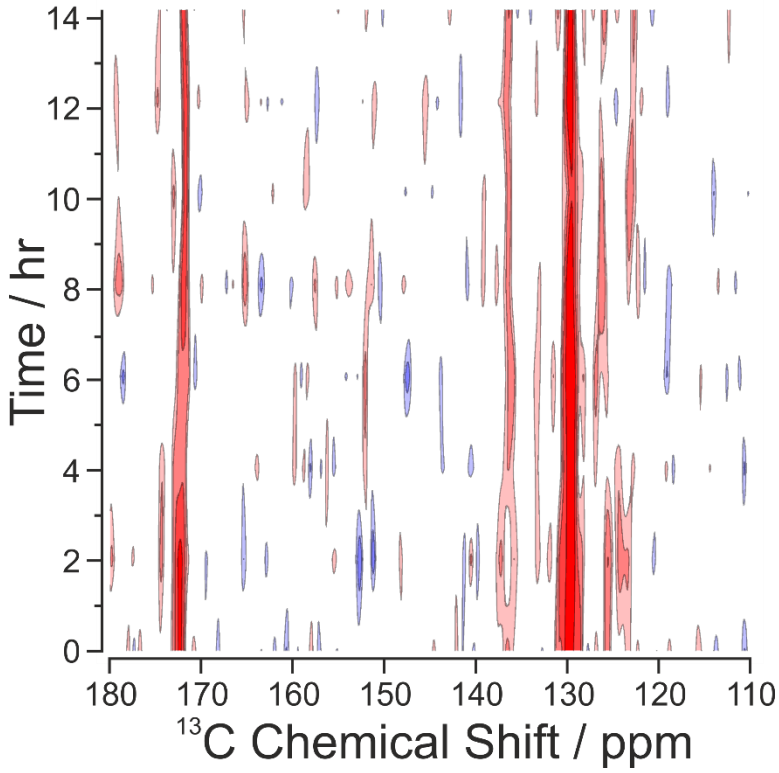

Figure 3.17: *Solid-state $^{1}H \rightarrow ^{13}C$ CP-MAS NMR spectra acquired during the crystallization of m-ABA from methanol.*

indicating that the initial crystallization of *m*-ABA occurred before measurement was started (during the cooling process). Through comparison of the spectrum with those of the five polymorphs shown in Figure 3.4, the initial product of the crystallization is identified as Form I of *m*-ABA. This phase is present without change until *ca*. 5 hrs after the start of the measurement. Over the next 4 hours, a change in the chemical shift of the carboxylic acid peak is observed (Figure 3.18), along with a change in the distribution of the peaks in the 140 to 120 ppm region. By comparing the spectra acquired after completion of the transformation (after *ca*. 9 hrs) with those in Figure 3.4, the solid sample after the transformation is identified as a monophasic sample of Form III. Thus, Form I has undergone a transformation to Form III of *m*-ABA during the crystallization process.

Thus, the initial product of crystallization from methanol in the *in-situ* NMR experiment is Form I but, over time and in contact with methanol, a transformation to the more stable Form III occurs. These results give further explanation to the observations found during laboratory crystallization experiments. Experiments in which

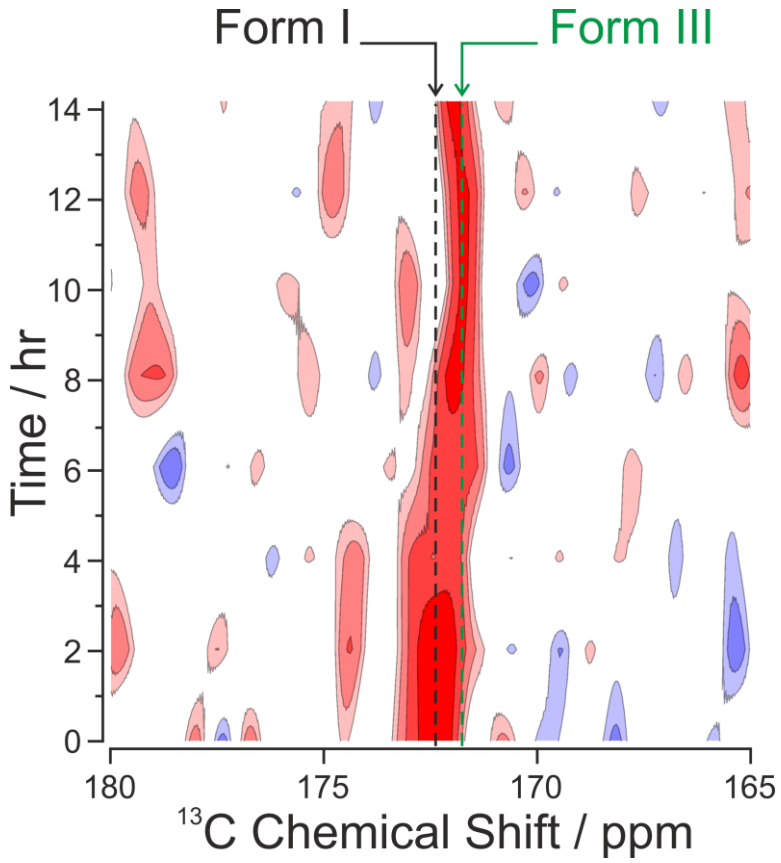

Figure 3.18: *Solid-state $^{1}H \rightarrow ^{13}C$ CP-MAS NMR spectra acquired during the crystallization of m-ABA from methanol showing the peak due to the carboxylate carbon of the m-ABA molecule.*

crystallization from methanol is rapid would be expected to result in Form I of *m*-ABA (as seen in the laboratory), whereas slower crystallization experiments, in which the crystallized product is in contact with methanol for an extended length of time, would be expected to result in Form III of *m*-ABA (again, mirroring the laboratory experiments).

3.6 - *In-Situ* CLASSIC NMR Study of the Crystallization of *m*-ABA from DMSO

During the course of this study, the *in-situ* NMR technique for studying crystallization processes was expanded to include solution-state NMR, leading to the CLASSIC NMR (**C**ombined **L**iquid- **A**nd **S**olid-**S**tate **I**n-situ **C**rystallization NMR) technique, expanded upon in Chapter 2. By monitoring both the solid-state and solution state ^{13}C NMR spectra over the course of the experiment, the evolution of both the solid-state and the solution-state can be studied essentially simultaneously. Thus, the complimentary changes that occur in the solid and liquid phases as crystallization proceeds can be studied. From the solid-state NMR spectra, the amount and polymorphic identity of the solid phase present is established as a function of time. Concomitantly, the solution becomes more dilute as crystallization proceeds, resulting in changes in solution-state speciation and the modes of molecular aggregation, which are revealed in the liquid-state NMR spectra. As mentioned in Chapter 2, spectra are acquired in an alternating manner by cycling solid-state CP-MAS and liquid-state direct-excitation pulse sequences.

Before carrying out the CLASSIC NMR study of crystallization of *m*-ABA from DMSO, extensive tests of the crystallization process (involving dissolution at elevated temperature and inducing crystallization by cooling to ambient temperature) were carried out under normal laboratory conditions. In some cases, however, the viscous, supersaturated solution obtained on cooling to ambient temperature remained kinetically stable and no crystallization was observed within the timescale (up to several days) of the experiments. In such cases, crystallization could not even be induced by agitation, shock or further cooling (to *ca*. –5 °C).

3.6.1 - Methodology of CLASSIC NMR Experiment

The CLASSIC NMR experiment was carried out using a Bruker AVANCE III NMR spectrometer at the UK 850 MHz Solid-State NMR Facility at the University of

Warwick (^{13}C Larmor frequency, 213.82 MHz; 4 mm HXY probe in double-resonance mode). The crystallization solution was prepared at ambient temperature by adding solid *m*-ABA Form III (24.8 mg) into the bottom of a zirconia NMR rotor followed by DMSO (23.2 mg), added by pipette. The rotor was spun in a centrifuge for a few seconds to ensure that the sample was at the bottom of the rotor, before sealing with the Kel-F® inserts, as described in Section 2.4. The sample was spun under MAS (at 12 kHz), before heating to 120 °C for one hour to allow complete dissolution of the sample, followed by cooling to 33 °C over *ca*. 15 mins. The CLASSIC NMR strategy was then applied over 15 hrs. To record the solid-state ^{13}C NMR spectra, ramped ^{1}H→^{13}C CP was employed (CP contact time, 1.5 ms) with ^{1}H decoupling using SPINAL-64 (nutation frequency, 91 kHz). To observe the liquid-state ^{13}C NMR spectra, the direct-excitation ^{13}C NMR pulse sequence was used, with a single 90° ^{13}C pulse and no ^{1}H decoupling. The time to acquire each spectrum was 38.4 mins for CP-MAS and 6.4 mins for ^{13}C direct-excitation. The effective time resolution for the CLASSIC NMR study (the time to acquire both a solid-state and liquid-state spectrum) was therefore 44.8 mins. A correction was applied (by another member of the research group) to the peak positions in the liquid-state ^{13}C spectra to account for a general drift in chemical shift caused by the cooling of the shims within the spectrometer during measurement.

3.6.2 - Results

The evolution of the solid-state ^{13}C NMR spectra, over the course of the experiment, is shown in Figure 3.19. The first solid-state signal emerged *ca*. 2 hours after commencing the experiment, signifying the start of crystallization. From comparison of the ^{13}C chemical shifts with those in Figure 3.4 (by summing all the solid-state ^{13}C NMR spectra acquired over the experiment as shown in Figure 3.20), this solid phase is assigned as Form I of *m*-ABA. The intensity of the peaks in the solid-state spectrum then increased monotonically with time (Figure 3.21), indicating that the amount of solid increased and, therefore, that the crystallization process continued until levelling off at *ca*. 8 hrs. No further changes occur in the solid-state spectra for the remainder of the experiment, i.e., no polymorphic transformation occurs and the final product of the crystallization is Form I of *m*-ABA. This observation is in agreement with the results determined in the laboratory.

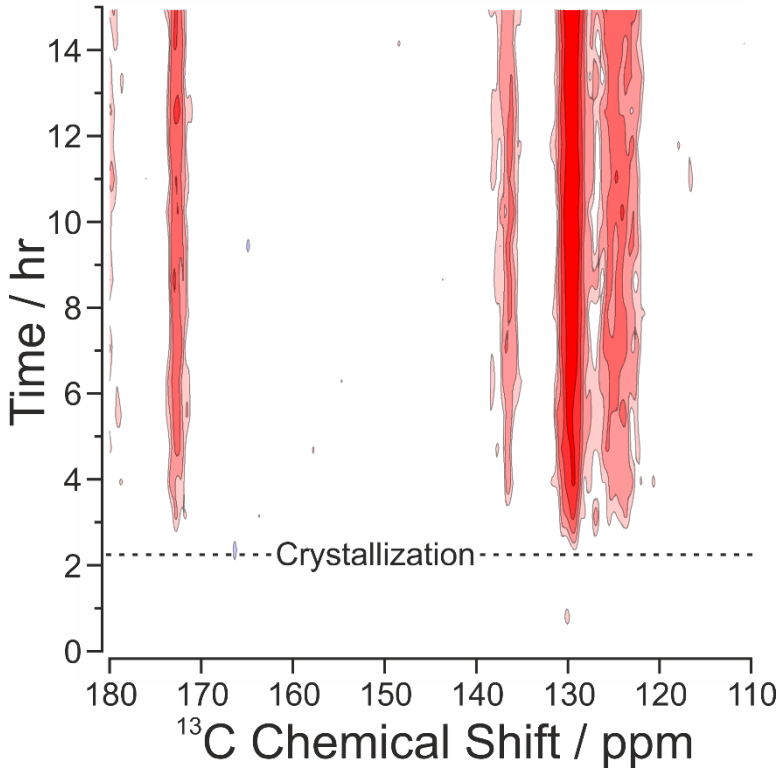

Figure 3.19: *Solid-state $^{1}H \rightarrow ^{13}C$ CP-MAS component of the CLASSIC ^{13}C NMR data acquired during the crystallization of m-ABA from DMSO.*

The liquid-state ^{13}C NMR spectra contain seven sharp peaks for each of the seven ^{13}C environments in the *m*-ABA molecule, with only J-coupling to directly attached protons resolved. The summed integral over the peaks in each liquid-state spectrum allows the proportion of *m*-ABA in solution to be measured as a function of time (Figure 3.21). This proportion is found to remain level until that point at which the first

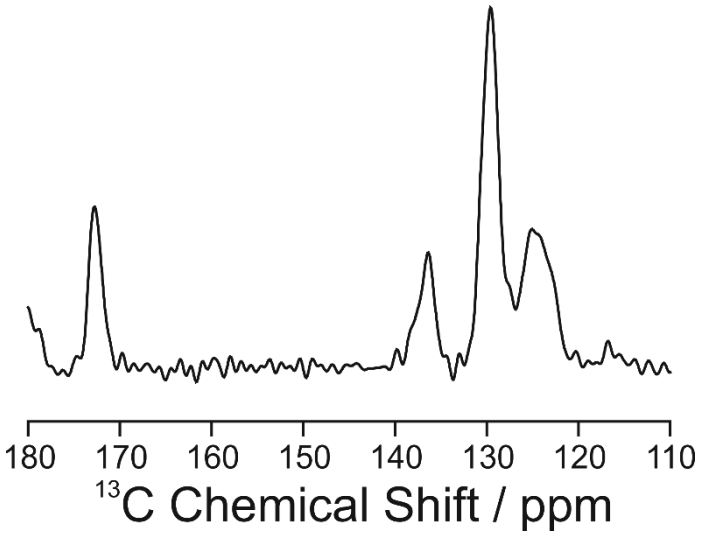

Figure 3.20: *Sum of all solid-state $^{1}H \rightarrow ^{13}C$ CP-MAS NMR spectra acquired during the crystallization of m-ABA from DMSO using CLASSIC NMR.*

solid signal is observed in the solid-state ^{13}C NMR spectra (i.e., the point at which crystallization has begun). Thereafter, the summed integral decreased with time, before reaching a constant value at *ca*. 8 hrs. That the concentration of *m*-ABA in solution is not observed to decrease until Form I is observed in the solid-state spectra rules out the possibility of crystallization of Form II prior to Form I. Due to the long T_1 relaxation time of Form II of *m*-ABA, it would not be observable in the CP-MAS ^{13}C spectra (T_1 of 190 s compared to a pulse delay of 9 s). Crystallization of Form II prior to that of Form I would, however, be manifest in a decrease in the total integral of the liquid-NMR spectra.

The results from the solid-state and liquid-state measurements are, therefore, in good agreement on the start point and end point of the crystallization process.

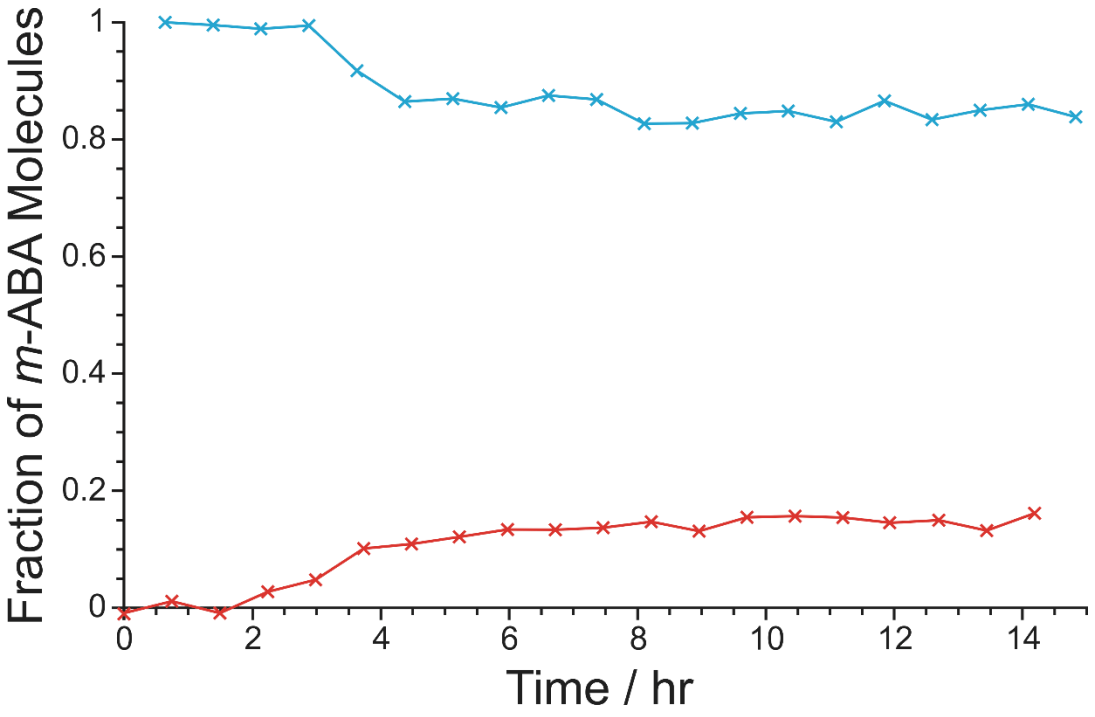

Figure 3.21: *Fraction of m-ABA molecules in the liquid (blue) and solid (red) phases as a function of time, established from the integrals of the liquid-state and solid-state components of the CLASSIC ^{13}C NMR data, respectively. To determine the fraction of molecules in the liquid state, the integrals of the liquid-state NMR spectra were normalized relative to the integral of the first spectrum recorded (at this stage of the experiment, it is known that all m-ABA molecules are in the liquid state). To determine the fraction of molecules in the solid state, the integrals of the solid-state NMR spectra were normalized by setting the fraction (F_S^{eq}) of m-ABA molecules in the solid state at the end of the experiment as $F_S^{eq} = 1 - F_L^{eq}$, where F_L^{eq} is the fraction of m-ABA molecules in the liquid state at the end of the experiment.*

Crystallization began 2 hrs after measurement was started with crystal growth continuing for the next 6 hrs. After these 8 hours, no further evolution in the total amounts of *m*-ABA in the liquid and solution was observed suggesting that, by this stage, the system comprised an equilibrium saturated solution.

A more detailed interpretation of the changes in the liquid-state ^{13}C NMR spectrum during crystallization can now be developed. Figure 3.22 shows the ^{13}C chemical shift $\delta_i(t)$ for each site (i) in *m*-ABA as a function of time, relative to the corresponding initial value δ_i^{start}. Initially, the system is a supersaturated solution (with concentration *ca*. 1.4 times the solubility of Form III of *m*-ABA at 33 °C). It should be noted that the solubility of Form I is higher than that of Form III at ambient temperature. This fact may account for any discrepancy between the total decrease in the integral of the liquid-state ^{13}C NMR spectrum during the crystallization process (Figure 3.21) and the total amount of solute that is predicted to crystallize based on the

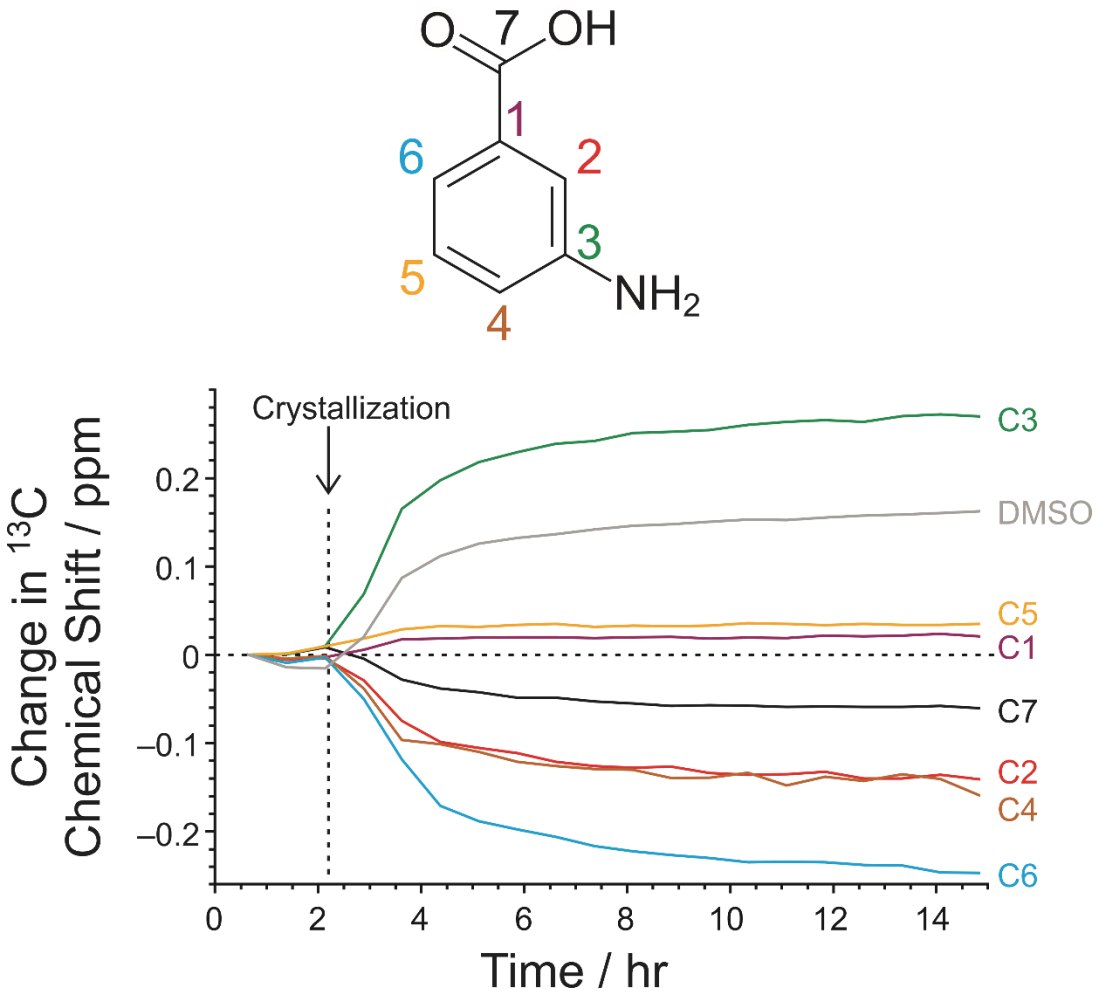

Figure 3.22: *Evolution of ^{13}C chemical shifts in the liquid-state component of the CLASSIC NMR data, for crystallization of m-ABA from DMSO.*

degree of supersaturation, with respect to Form III, of the initial crystallization solution. After crystallization begins, the supersaturation decreases with time. By the end of the crystallization process, the system is an equilibrium saturated solution with chemical shifts denoted δ_i^{eq}(DMSO). To rationalize the changes that occur in the solution state as crystallization proceeds, it is instructive to consider the values of $\Delta\delta_i^{classic} = \Delta\delta_i^{start} - \Delta\delta_i^{eq}$(DMSO), representing the difference in chemical shift between the initial solution (with maximum supersaturation) and the final solution (at equilibrium saturation). Values of $\Delta\delta_i^{classic}$ determined from the data in Figure 3.22 are given in Table 3.3.

As an independent comparison, the liquid-state ^{13}C NMR spectra for saturated solutions of *m*-ABA (Form III) in water, methanol, 1,4-dioxane and DMSO were recorded at 33 °C (recalling[101-105] that *m*-ABA is predominantly zwitterionic in water, almost entirely non-zwitterionic in methanol and non-zwitterionic in 1,4-dioxane and DMSO). For each ^{13}C site *i* in *m*-ABA, the *difference* in chemical shift in a given solvent relevant to DMSO is denoted $\Delta\delta_i^{solvent} = \Delta\delta_i^{eq}$(solvent) – $\Delta\delta_i^{eq}$(DMSO), where

	$\Delta\delta_i^{classic}$	$\Delta\delta_i^{water}$ [a]	$\Delta\delta_i^{methanol}$ [a]	$\Delta\delta_i^{1,4\text{-dioxane}}$ [a]
C3	–0.27	–11.48	–0.27	–0.13
C5	–0.03	0.34	–0.30	–0.32
C1	–0.02	3.47	0.01	–0.34
C7	0.06	3.65	1.07	–1.10
C2	0.14	5.09	0.94	0.06
C4	0.16	4.44	0.84	–0.43
C6	0.25	7.27	1.19	0.39
r^2 [b]		0.88	0.71	0.05

Table 3.3: *Values of $\Delta\delta_i^{classic}$ measured from the liquid-state component of the CLASSIC ^{13}C NMR data for crystallization of m-ABA from DMSO and values of $\Delta\delta_i^{solvent}$ determined from ex-situ liquid-state ^{13}C NMR data. [a] For saturated solutions in water, methanol, 1,4-dioxane and DMSO. [b] Correlation coefficients (r^2) between values of $\Delta\delta_i^{classic}$ and values of $\Delta\delta_i^{solvent}$ for each solvent.*

$\Delta\delta_i^{eq}$(solvent) is the chemical shift in the saturated solution at 33 °C and $\Delta\delta_i^{eq}$(DMSO) is the chemical shift in the saturated DMSO solution at 33 °C. Comparison (Table 3.3) of values of $\Delta\delta_i^{classic}$ and $\Delta\delta_i^{solvent}$ gives a very high correlation coefficient for water (0.88), a moderately high correlation coefficient for methanol (0.71) and a very low correlation coefficient for 1,4-dioxane (0.05). Recalling that the definitions of $\Delta\delta_i^{classic}$ and $\Delta\delta_i^{solvent}$ have the same reference point [i.e., chemical shifts δ_i^{eq}(DMSO) for a saturated solution of *m*-ABA in DMSO], the high correlation coefficients for water and methanol suggest that the speciation and intermolecular environment of *m*-ABA molecules in the supersaturated DMSO solution at the start of the CLASSIC NMR experiment (reflected in the values of $\Delta\delta_i^{start}$ and hence in the values of $\Delta\delta_i^{classic}$) may bear some resemblance to those of *m*-ABA molecules in saturated solutions in water and methanol [reflected in the values of δ_i^{eq}(solvent) and hence in the values of $\Delta\delta_i^{solvent}$]. Based on the high correlation coefficients observed between values of $\Delta\delta_i^{classic}$ and values of $\Delta\delta_i^{water}$ and $\Delta\delta_i^{methanol}$, two hypotheses are now developed concerning the nature of the supersaturated solution of *m*-ABA in DMSO at the start of the CLASSIC NMR experiment.

First, the key difference (reflected in the values of $\Delta\delta_i^{water}$) between saturated solutions of *m*-ABA in water and DMSO is that *m*-ABA is predominantly zwitterionic in saturated water solution but non-zwitterionic in saturated DMSO solution. Thus, one hypothesis is that, at sufficiently high supersaturation of *m*-ABA in DMSO, the proportion of *m*-ABA molecules present as zwitterions is significantly higher than that in an equilibrium saturated solution of *m*-ABA in DMSO. The fact that the magnitudes $|\Delta\delta_i^{classic}|$ are less than $|\Delta\delta_i^{water}|$ suggests that the proportion of zwitterionic *m*-ABA molecules in the supersaturated solution at the start of crystallization from DMSO is less than that in the saturated solution of *m*-ABA in water (50 to 78% zwitterionic tautomer in water[104,105]).

Second, a key difference (reflected in the values of $\Delta\delta_i^{methanol}$) between saturated solutions of *m*-ABA in methanol and DMSO is the presence of a hydrogen-bond donor in methanol (while DMSO can only act as a hydrogen-bond acceptor). In saturated methanol solution, *m*-ABA is almost entirely non-zwitterionic and the amine group is likely to act as an acceptor in O–H···N hydrogen bonds. Thus, a second hypothesis is that, in the supersaturated solution of *m*-ABA in DMSO at the start of the crystallization experiment, there is an increase in the proportion of non-zwitterionic *m*-ABA molecules

present in aggregates containing intermolecular hydrogen bonds with the amine group acting as the acceptor. As DMSO has no hydrogen-bond donors, the amine group of non-zwitterionic *m*-ABA can be a hydrogen-bond acceptor only with amine groups or carboxylic acid groups of other *m*-ABA molecules as the donor.

Thus, the changes ($\Delta\delta_i^{classic}$) in ^{13}C chemical shifts observed in the crystallization process are consistent with the supersaturated solution of *m*-ABA in DMSO at the start of crystallization having a higher proportion of zwitterionic *m*-ABA molecules and/or a higher proportion of non-zwitterionic *m*-ABA molecules present in hydrogen-bonded aggregates, relative to a saturated solution of *m*-ABA in DMSO. Both scenarios represent an increased degree of protonation of the amine group, leading to increased positive charge on the nitrogen atom, increasing the shielding of C3 and promoting the specific changes in ^{13}C chemical shifts observed.

Finally, it must be noted that the evolution of the ^{13}C chemical shift for the solvent DMSO as a function of time in the liquid-state component of the CLASSIC NMR data (Figure 3.22) is a direct consequence of the decrease in the concentration of *m*-ABA molecules and hence in the extent to which DMSO molecules are engaged as the acceptor in O–H···O or N–H···O hydrogen bonds with *m*-ABA molecules.

The crystal structure of Form I of *m*-ABA has not yet been determined, although the N(1s) XPS studies carried out in the present work (Figure 3.3) indicate that the *m*-ABA molecules are zwitterionic. Thus, it is expected that the ammonium and carboxylate groups will interact *via* intermolecular $O^-\cdots H–N^+$ hydrogen bonds in the crystal structure, as these are the only hydrogen-bond donor and acceptor groups present. From the analysis of the liquid-state component of the CLASSIC NMR data discussed above, it can be proposed that the supersaturated solution of *m*-ABA in DMSO at the start of the crystallization process contains (i) zwitterionic *m*-ABA molecules, which may or may not be present as aggregates containing $O^-\cdots H–N^+$ hydrogen bonds (although such aggregates must ultimately be formed at some stage on the crystallization pathway) and/or (ii) aggregates of non-zwitterionic *m*-ABA molecules linked by O–H···N hydrogen bonds.

Clearly, either situation is a plausible precursor to the $O^-\cdots H–N^+$ hydrogen bonds that are expected to exist between *m*-ABA zwitterions in the crystal structure of Form I. Although the current work cannot distinguish whether situation (i) or situation (ii) is

predominant, the results give clear insight into the nature of the speciation and interactions that exist in the supersaturated pre-nucleation solution of *m*-ABA in DMSO prior to the crystallization, relative to those in the saturated solution at the end of the crystallization process. While this rationalization of the evolution of the solution-state ^{13}C chemical shifts during crystallization are based on empirical observations of the differences in ^{13}C chemical shifts from *m*-ABA in different solvents in which the speciation of the *m*-ABA molecules is known independently, it should be noted that an alternative approach could be to compute the ^{13}C chemical shifts *via* DFT calculations on proposed solution-state clusters. Such *ab initio* calculations are now widely used in the field of NMR crystallography.[117-119]

3.7 - Conclusions

The discovery of three new polymorphs of *m*-ABA during this work has demonstrated the abundant polymorphism within this system. The fact that one of the three new polymorphs of *m*-ABA discovered in the present work (Form III) is more stable under ambient conditions than the two observed previously (Form I and Form II) emphasizes that the earliest discovered polymorphs of a given molecule do not necessarily include the most stable polymorph. Indeed, by extrapolating this argument, it cannot be stated that Form III is definitely the thermodynamically stable polymorph under ambient conditions, only that it has the highest relative stability among the polymorphs of *m*-ABA discovered so far. An interesting aspect of the polymorphism of *m*-ABA is the fact that the molecule is zwitterionic in some polymorphs and non-zwitterionic in others. Among the polymorphs of *o*-ABA and *p*-ABA, the zwitterionic tautomer appears less common than in the case of *m*-ABA. Thus with the exception of Form I of *o*-ABA (which contains both zwitterionic and non-zwitterionic molecules in a 1:1 ratio), all other polymorphs of *o*-ABA and *p*-ABA contain only non-zwitterionic molecules. Although none of the polymorphs of *m*-ABA contain both zwitterionic and non-zwitterionic molecules within the same crystal structure, the discovery in the current work of two new polymorphs of *m*-ABA containing zwitterionic molecules (Form III and Form IV) and one new polymorph containing non-zwitterionic molecules (Form V) suggests that the dividing line between these tautomeric forms is readily crossed in this system.

Use of *in-situ* solid-state NMR has demonstrated that during crystallization of *m*-ABA from methanol, Form I of *m*-ABA is formed initially, followed at a later point by transformation into the more stable Form III. The *in-situ* result therefore gives insight into the crystallization behaviour of *m*-ABA from methanol in a laboratory setting: faster crystallization results in Form I while slower crystallization results in Form III.

The CLASSIC NMR experiment extends the scope and capability of *in-situ* monitoring of crystallization processes, particularly as it provides complementary information on the time-evolution of both the solid phase and the liquid phase during crystallization. The CLASSIC NMR strategy, applied to the crystallization of *m*-ABA from DMSO, has given clear insights into the changes in the nature of speciation and interactions as the crystallization process occurs. In spite of the simplicity of the concept of "interleaving" the measurement of liquid-state and solid-state NMR spectra, it is surprising that this strategy has not been exploited more widely in other scientific fields, although a notable case is the SedNMR technique, which has been developed to monitor the kinetics of sedimentation and fibrillization processes in biological systems.[120] Another recent development to study heterogeneous biomaterials is the CMP[121] technique. However, in contrast to CLASSIC NMR, the CMP technique requires new and specialized probe design and has not been applied to systems containing free liquid nor to study time-dependent processes. Within the study of crystallization processes, the CLASSIC NMR technique reported here is unique as an *in-situ* NMR strategy for simultaneously mapping the time-evolution of both the liquid and solution phases. It is anticipated that the advantages of the CLASSIC NMR strategy will yield significant new insights on a wide range of other crystallization systems in the future.

Chapter 4: Discovery of New Solid Forms of Triphenylphosphine Oxide and Methyldiphenyl-phosphine Oxide by *In-Situ* Solid-State NMR

4.1 - Introduction

Triphenylphosphine oxide [TPPO, Figure 4.1(a)] is a very commonly encountered chemical. TPPO is regularly used as a ligand in metal coordination[122] and is a common by-product of several organic synthesis reactions including the Mitsunobu,[123] Staudinger[124] and Wittig[125,126] reactions. In addition, cocrystals of TPPO have been found to have favourable crystal growth and handling conditions,[56] allowing TPPO to be used as a crystallization aid. Nevertheless, questions remain over the polymorphism of TPPO. There are four reported polymorphs of TPPO (Figure 4.2): monoclinic I,[57] orthorhombic,[58] monoclinic II[59] and monoclinic III.[127] All four polymorphs have known crystal structures. Of these, only monoclinic I and orthorhombic have known and replicable methods of crystallization. Monoclinic II is reported[59] to have crystallized from a solution containing a metal complex. However, no further details on the solution, metal complex or crystallization conditions are given. No details are known of the method used to crystallize monoclinic III; the structure was submitted to the CSD as a private communication. The crystal structures of three polymorphs of TPPO hemihydrate[128-130] and the structure of a diethyl ether solvate[131] have also been reported.

TPPO is reported to crystallize concomitantly as the monoclinic I and orthorhombic polymorphs by evaporation of a solution in hexane.[57] The highly polymorphic nature of TPPO, combined with the ability to crystallize as two polymorphs concomitantly from certain solvents, made TPPO an interesting system to study crystallization *via in-situ* NMR. Previous solid-state ^{31}P NMR performed on

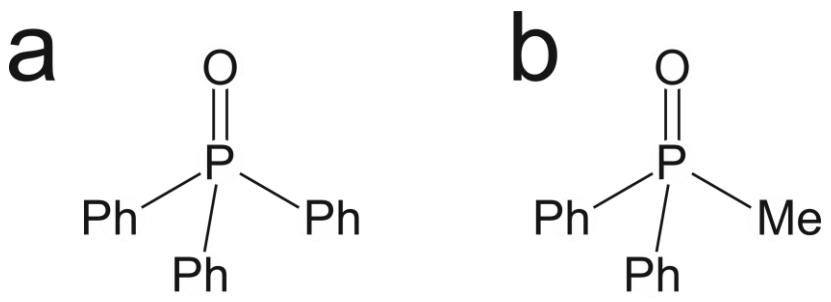

Figure 4.1: *Molecular structures of (a) triphenylphosphine oxide (TPPO) and (b) methyldiphenylphosphine oxide (MDPPO).*

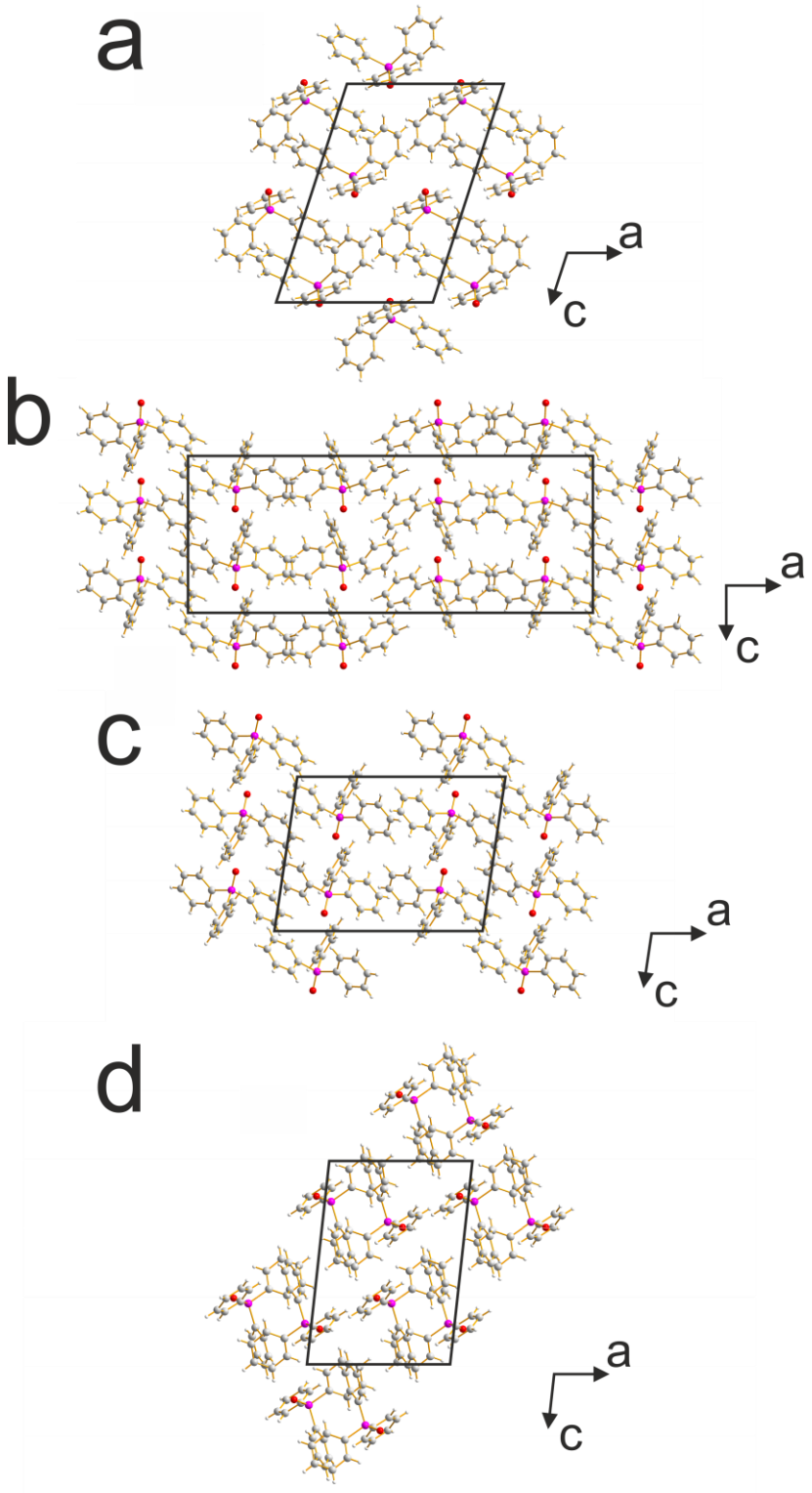

Figure 4.2: *Crystal structures of the four polymorphs of TPPO: (a) monoclinic I, (b) orthorhombic, (c) monoclinic II and (d) monoclinic III.*

TPPO assigned chemical shifts of 26.8 ppm for the monoclinic I polymorph and 28.5 ppm for the orthorhombic polymorph.[132]

Prior to this work, the related compound, methyldiphenylphosphine oxide (MDPPO) was not known to be polymorphic. There is a single reported crystal structure of MDPPO (Figure 4.3).[60] MDPPO finds use in a variety of organic syntheses[61-63] and, as in the case of TPPO, as a ligand. The fact that MDPPO has only one known crystal structure while the very closely related compound TPPO is highly polymorphic made the crystallization of MDPPO a prime target for study *via in-situ* solid-state NMR.

4.2 - Experimental Methods

TPPO was purchased from Sigma-Aldrich (purity >98%). This material was found by powder XRD to be a monophasic sample of the monoclinic I polymorph of TPPO. A sample of orthorhombic TPPO was prepared by heating monoclinic I to melting, before cooling to ambient temperature.

Initial *in-situ* solid-state ^{31}P NMR studies on the crystallization of TPPO from solution were carried out using a 300 MHz Chemagnetics Infinity Plus spectrometer (^{31}P Larmor frequency, 121.5 MHz; 4 mm rotor; MAS frequency 8 kHz; ramped ^{1}H→^{31}P CP[109] with contact time, 1.5 ms; TPPM ^{1}H decoupling). Crystallization of TPPO from ethanol/hexane (1:1 by mass, 31.9 mg TPPO in 14.3 mg ethanol and

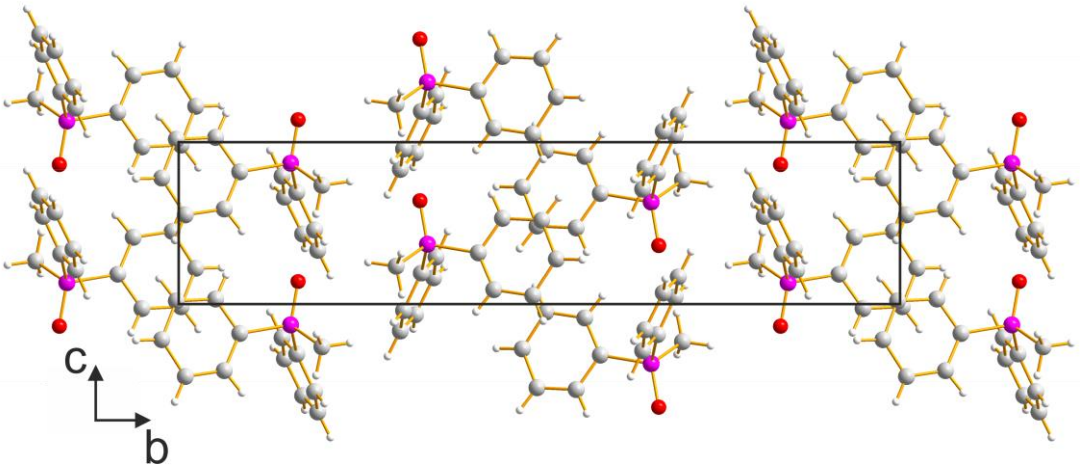

Figure 4.3: *The reported crystal structure of MDPPO, viewed along the* a*-axis. The crystal structure is disordered with one phenyl ring occupying three possible orientations. For clarity, only a single orientation of this phenyl ring is shown.*

14.7 mg hexane) and ethanol/cyclohexane (1:3 by mass, 19.5 mg TPPO in 6.7 mg ethanol and 21.4 mg cyclohexane) by mass were investigated. In each case, 16 scans were acquired for each spectrum using a pulse delay of 120 s, resulting in each spectrum taking 32 mins to record (representing the maximum time resolution).

A CLASSIC NMR study of crystallization of TPPO from solution in ethanol/cyclohexane, 1:3 by mass, and acquisition of solid-state ^{31}P NMR spectra for powder samples of the monoclinic I and orthorhombic polymorphs of TPPO were carried out using a Bruker AVANCE III spectrometer at the UK 850 MHz Solid-State NMR Facility at the University of Warwick (^{31}P Larmor frequency, 344.17 MHz; 4 mm HXY probe in double-resonance mode). A sample of TPPO with natural isotopic abundances was used. The monoclinic I polymorph of TPPO (15.0 mg), ethanol (6.1 mg) and cyclohexane (19.7 mg) were measured by mass into the bottom of a zirconia NMR rotor. The rotor was spun in a centrifuge for a few seconds to ensure the sample was at the bottom, before sealing with PTFE inserts, as described in Section 2.4. The rotor was spun within the spectrometer under MAS conditions (12 kHz), before heating to 75 °C for one hour to allow for complete dissolution of the sample. The rotor was then cooled to 20 °C, before application of the CLASSIC NMR procedure over *ca*. 22 hrs. In this case, the procedure was modified such that the sequence of acquisition was: direct-excitation liquid-state ^{31}P NMR spectrum, direct-excitation liquid-state ^{1}H NMR spectrum, solid-state ^{1}H→^{31}P CP-MAS spectrum. Each solid-state spectrum involved the acquisition of 16 scans, with a pulse delay of 120 s and each liquid-state spectrum (for each of ^{31}P and ^{1}H) involved 16 scans with a pulse delay of 3 s, leading to a total time to acquire each spectrum of 33.6 mins, representing the maximum time resolution of the experiment. To record the solid-state spectra, ramped ^{1}H→^{31}P CP was employed (CP contact time, 1.5 ms) with ^{1}H decoupling using SPINAL-64 (nutation frequency, 91 kHz).

MDPPO was purchased from Sigma-Aldrich (purity > 98%). The sample was found by powder XRD to be the known crystalline phase of MDPPO. The *in-situ* solid-state NMR study of the crystallization of MDPPO from toluene was carried out using a Bruker AVANCE III spectrometer at the UK 850 MHz Solid-State NMR Facility at the University of Warwick (^{31}P Larmor frequency, 344.17 MHz; 4 mm HXY probe in double-resonance mode). MDPPO (5.1 mg, natural isotopic abundance) and toluene (34.9 mg) were measured by mass into the bottom of a zirconia NMR rotor. The rotor

was spun in a centrifuge for a few seconds to ensure the sample was at the bottom, before sealing with Kel-F® inserts, as described in Section 2.4. The rotor was spun within the spectrometer under MAS conditions (12 kHz), before heating to 80 °C for one hour to allow for complete dissolution of the sample. The rotor was then cooled to 20 °C, before acquisition of repeated solid-state ^{31}P NMR spectra. Each spectrum involved the acquisition of 16 scans, with a pulse delay of 9 s, leading to a total time to acquire each spectrum of 38.4 mins, representing the maximum time resolution of the experiment. To record the solid-state spectra, ramped ^{1}H→^{31}P CP was employed (CP contact time, 1.5 ms) with ^{1}H decoupling using SPINAL-64 (nutation frequency, 91 kHz).

Powder XRD measurements on TPPO and MDPPO were performed using a Bruker D8 diffractometer operating in transmission mode (CuKα_1). Fingerprinting of solid samples was carried out with the sample held between two pieces of tape (foil-type sample holder).

4.2.1 - Crystallization within a Glass Capillary

Crystallization of TPPO from ethanol/cyclohexane (1:3 by mass) was carried out within glass capillaries to allow powder XRD data to be recorded for the crystallization products without removal from the mother liquor (with a schematic representation of this process shown in Figure 4.4). TPPO (*ca*. 0.305 g), ethanol (*ca*. 0.125 g) and cyclohexane (*ca*. 0.385 g) were measured into a glass, liquid-state NMR tube of 5 mm external diameter. The tube was sealed using a plastic NMR tube cap and Nescofilm® before being submerged (leaving only the top 1/3 uncovered) in silicone oil and heated to 60 °C. The tube was held at this temperature with frequent agitation until all solid TPPO present was observed to dissolve in the mixed solvent. Five to six glass capillaries of external diameter 0.7 mm were cut to a length (from sealed bottom to open top) of *ca*. 15 mm. The NMR tube containing the solution was unsealed and the cut glass capillaries were added such that the open tops of the capillaries were pointing upwards. The NMR tube was resealed and maintained at 60 °C while vigorously agitating the solution until the glass capillaries were observed to have filled with solution and sunk to the bottom of the tube. The tube was unsealed, the solvent emptied and the glass capillaries recovered as quickly as possible. The exterior of each glass capillary was cleaned with a small amount of ethanol/cyclohexane (1:3 by mass)

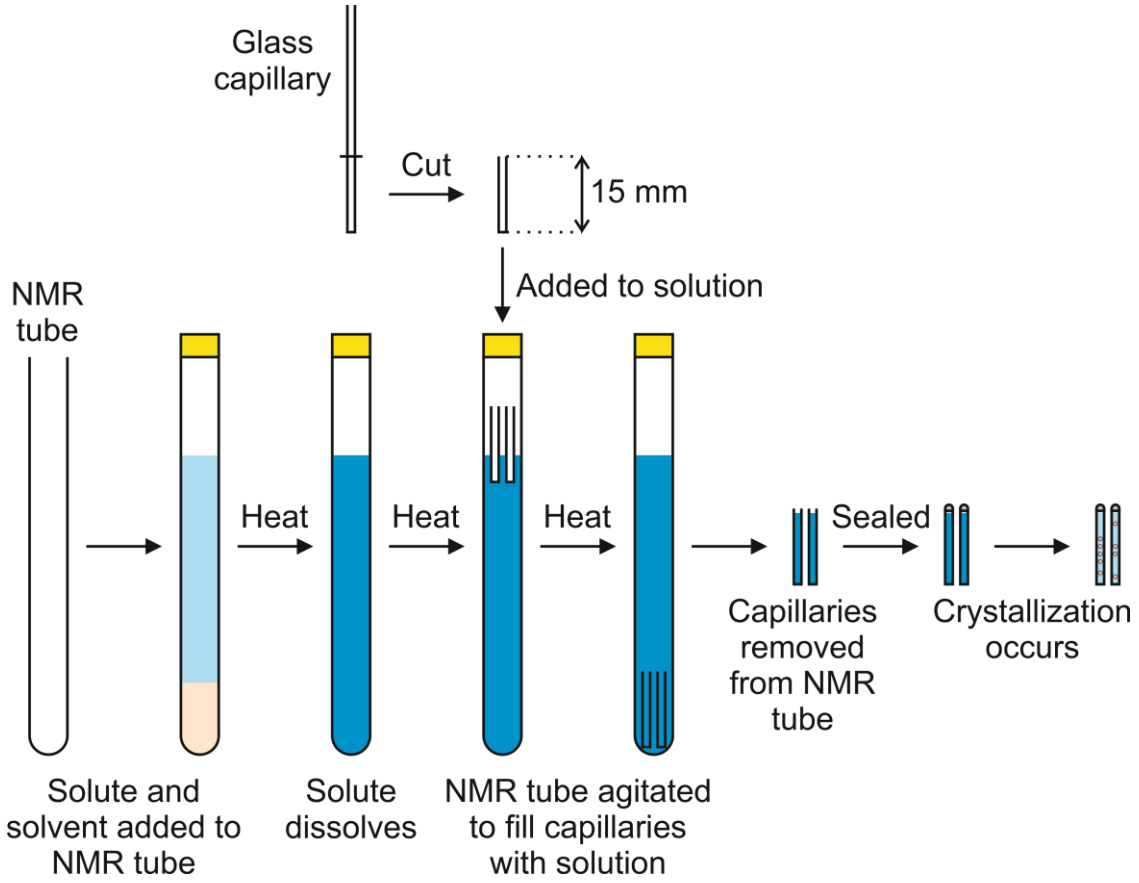

Figure 4.4: *Schematic showing the method used to carry out crystallization within glass capillaries.*

absorbed into a facial tissue, before sealing the open end of each capillary with either quick setting epoxy resin or superglue. Once the resin/glue had finished setting, powder XRD data were recorded for the capillaries containing crystalline material.

4.3 - Results

4.3.1 - Triphenylphosphine Oxide

Crystallization experiments were carried out on TPPO in the laboratory. Pure orthorhombic TPPO was found to be reliably produced by heating monoclinic I to the melting point, allowing partial melting to occur and cooling to ambient temperature. Crystallization of TPPO from ethanol *via* evaporation of the solvent was found to produce the monoclinic I polymorph of TPPO. It is reported[57] that slow evaporation of a solution of TPPO in hexane results in the concomitant crystallization of both the monoclinic I and orthorhombic polymorphs of TPPO. Crystallization of TPPO from cyclohexane *via* evaporation was found to produce only orthorhombic TPPO.

The solubility of TPPO is considerably higher in ethanol than in hexane or cyclohexane. In an attempt to find a solvent mixture giving rise to concomitant crystallization of the monoclinic I and orthorhombic polymorphs and in which TPPO has a high solubility (allowing the system to be studied by *in-situ* NMR), the mixed solvent systems ethanol/hexane (1:1 by mass) and ethanol/cyclohexane (1:3 by mass) were tested. Evaporation of solutions of TPPO in both of these mixed solvents was found to result in concomitant crystallization of monoclinic I and orthorhombic TPPO.

The solid-state ^{31}P NMR spectra for the monoclinic I and orthorhombic polymorphs of TPPO are shown in Figure 4.5. Both monoclinic I and orthorhombic contain one molecule of TPPO in the asymmetric unit and so the NMR spectrum of each polymorph contains a single ^{31}P peak (at 26.4 ppm for monoclinic I and 28.5 ppm for orthorhombic). The most intense peak in each spectrum is not, in fact, the isotropic peak but the first spinning sideband to higher chemical shift.

Initial *in-situ* solid-state ^{31}P NMR studies on the crystallization of TPPO were performed using a 300 MHz solid-state NMR spectrometer as described in the experimental section. Crystallization of TPPO was carried out from mixed

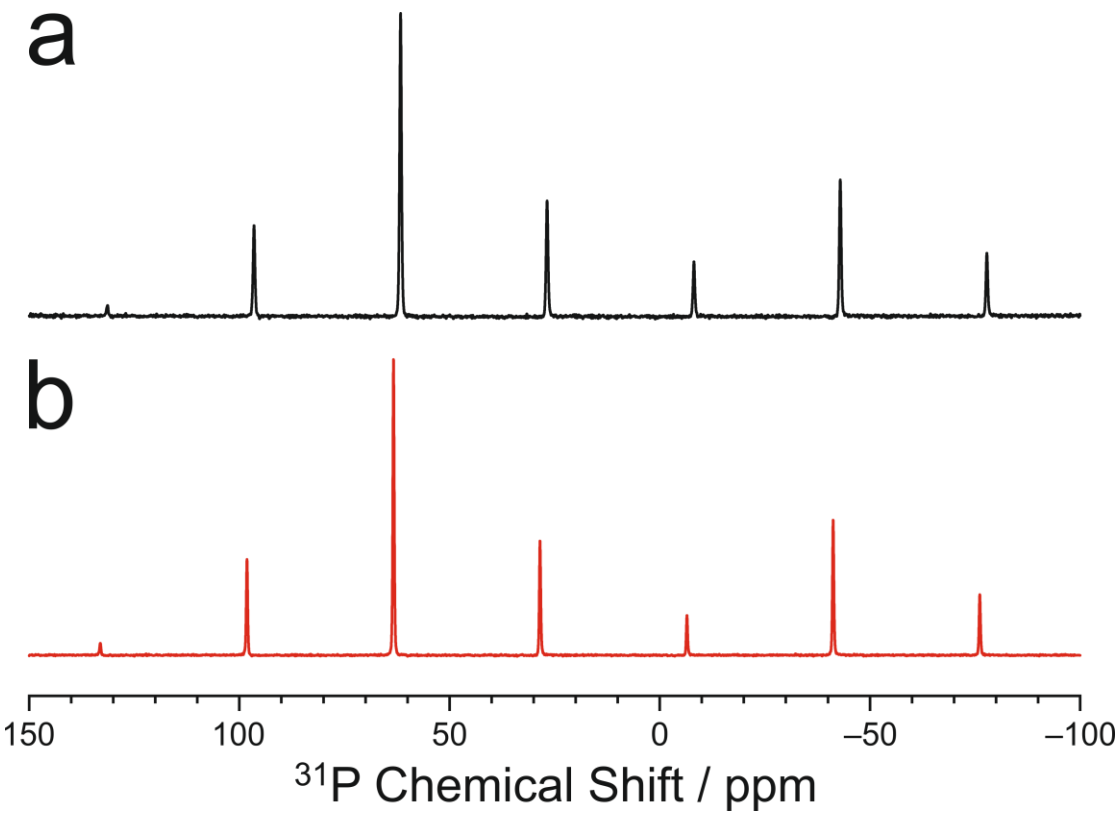

Figure 4.5: *Solid-state $^{1}H \rightarrow ^{31}P$ CP-MAS NMR spectra for (a) the monoclinic I polymorph of TPPO and (b) the orthorhombic polymorph of TPPO.*

ethanol/hexane (both 1:1 and 1:3 by mass) and from ethanol/cyclohexane (1:3 by mass). The signal-to-noise ratio observed during these experiments was insufficient to allow for suitable time resolution to study changes in the solid phase over time. However, by summation of all spectra acquired in each experiment, the solid phases present during the crystallization process can be identified. As shown in Figures 4.6 and 4.7, no phases are present that represent either the monoclinic I or orthorhombic polymorphs of TPPO. Powder XRD conducted on the products of the crystallization in these two experiments demonstrated the presence of both monoclinic I and orthorhombic phases of TPPO. The unknown phases must, therefore, undergo a transformation to form the known phases. Thus, the unknown phases appear to be unstable upon removal from the NMR rotor.

To increase the signal-to-noise ratio and to gain both time resolution and spectral resolution, the *in-situ* solid-state ^{31}P NMR study of the crystallization of TPPO from ethanol/cyclohexane (1:3 by mass) was repeated at the UK 850 MHz solid-state NMR facility. In this experiment, the CLASSIC NMR method was applied, allowing acquisition of three sets of NMR spectra (liquid-state ^{31}P NMR spectra, liquid-state ^{1}H NMR spectra and solid-state ^{31}P NMR spectra), with the aim of monitoring the

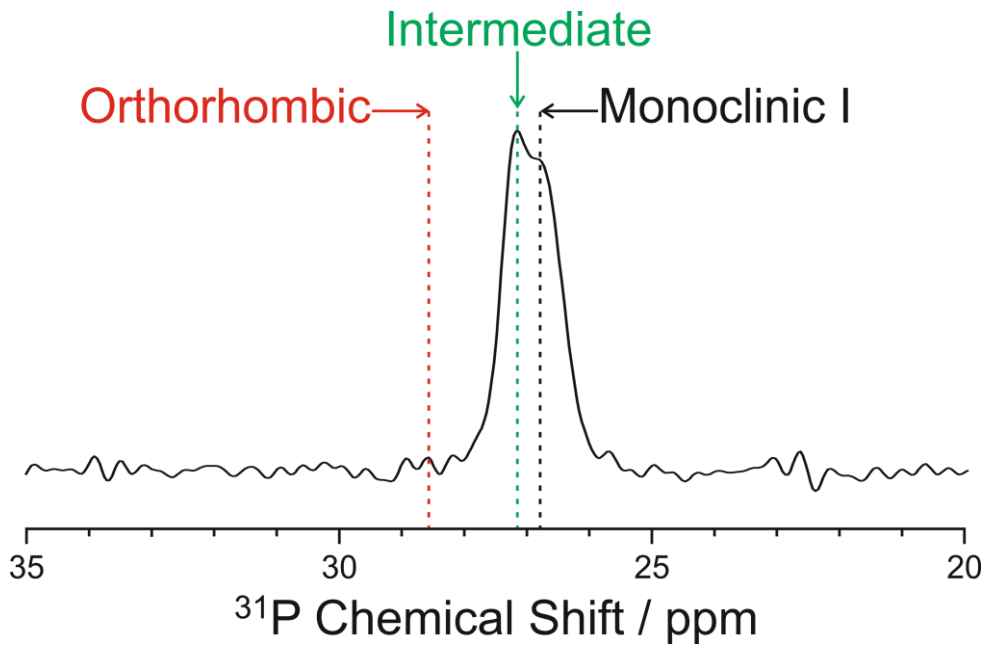

Figure 4.6: *Sum of the* in-situ *solid-state $^{1}H \rightarrow ^{31}P$ CP-MAS NMR spectra acquired during the crystallization of TPPO from ethanol/hexane (1:1 by mass). The positions of the peaks due to the monoclinic I and orthorhombic polymorphs of TPPO and the position of the unknown intermediate phase are marked.*

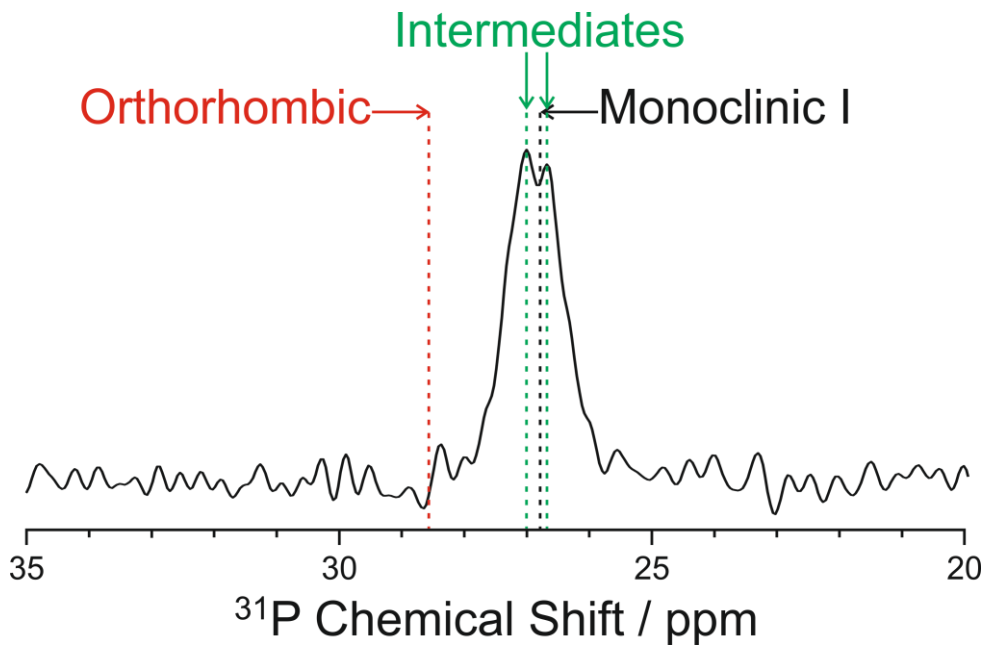

Figure 4.7: *Sum of the* in-situ *solid-state* $^{1}H \rightarrow ^{31}P$ *CP-MAS NMR spectra acquired during the crystallization of TPPO from ethanol/cyclohexane (1:3 by mass). The positions of the peaks due to the monoclinic I and orthorhombic polymorphs of TPPO and the position of the unknown intermediate phase are marked.*

evolution in both the solid-state and liquid-state over the course of the crystallization process.

The evolution in the solid-state ^{31}P NMR spectrum over time is shown in Figure 4.8. A signal is observed in the first recorded solid-state spectrum and, thus, crystallization must have begun before or during the recording of the first spectrum. A single peak is observed at 63.30 ppm (phase A). Two additional peaks are observed at 61.58 and 61.34 ppm (phase B and phase C, respectively) and grow over time (appearing at the intensity contour level used in the plot shown in Figure 4.8 at *ca*. 6 hrs). The intensity of the peak due to phase A is found to decrease monotonically with time until *ca*. 17.5 hrs, while the intensity of the peaks due to phase B and phase C are found to increase over the same 17.5 hrs. After *ca*. 17.5 hrs, no further signal is observed for phase A. Phase A has therefore completely transformed into phase B and phase C. The sum of the solid-state ^{31}P spectra recorded over the last *ca*. 6.1 hrs of the experiment is shown in Figure 4.9, clearly demonstrating the existence of the two separate peaks belonging to phase B and phase C.

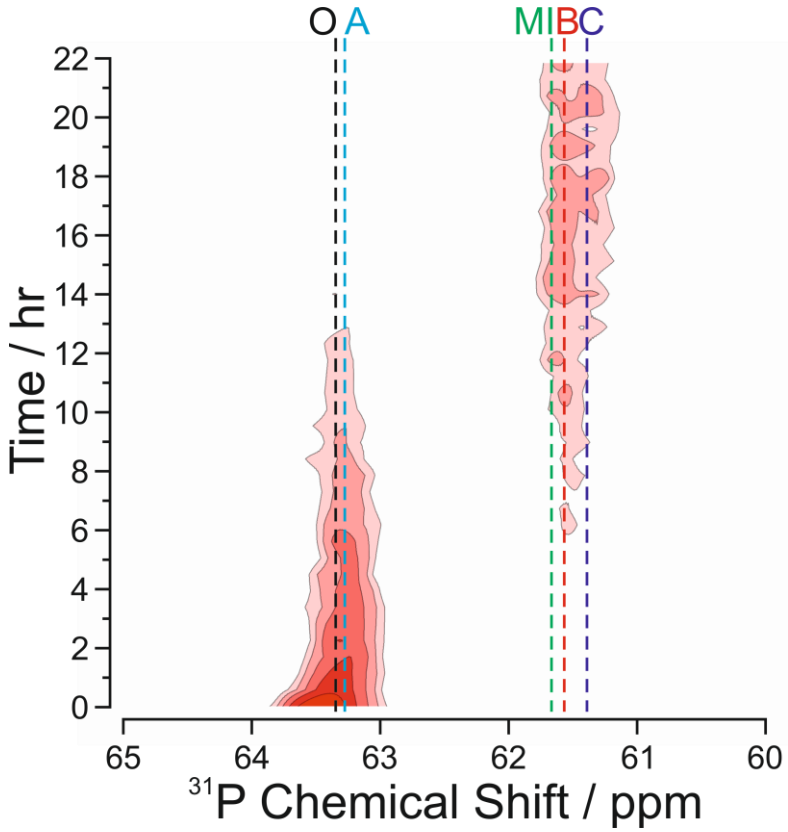

Figure 4.8: *In-situ solid-state $^{1}H \rightarrow ^{31}P$ CP-MAS NMR spectra acquired during the crystallization of TPPO from a mixed ethanol/cyclohexane (1:3 by mass) solvent. The region corresponding to the first spinning sidebands to higher chemical shift of the isotropic peaks is shown. Dashed lines indicate the positions expected for peaks due to the orthorhombic polymorph of TPPO (O), monoclinic I polymorph of TPPO (MI) and the positions of the three unknown phases (A, B and C).*

The liquid-state ^{31}P NMR spectrum was found to contain a single ^{31}P resonance corresponding to TPPO dissolved in the mixed solvent. The integrated intensity of the peak due to phase A, along with the total integrated intensity of the peaks belonging to phase B and phase C (which are positioned too close to accurately calculate separate integrated intensities) and the integrated intensity of the liquid-phase peak are shown in Figure 4.10. The intensities are normalized such that the maximum value in each case is set to 1. The intensity of the peak for phase A is found to decrease from the beginning of the experiment until *ca*. 17.5 hrs, indicating that the amount of this phase decreases with time until it is completely lost at *ca*. 17.5 hrs. Concurrently, the intensities of the solid-state peaks for phase B and phase C are found to increase over the same period, indicating an increase in the amounts of these two phases. In addition, the intensity of the liquid-state peak decreases throughout the experiment. Thus, over the course of the

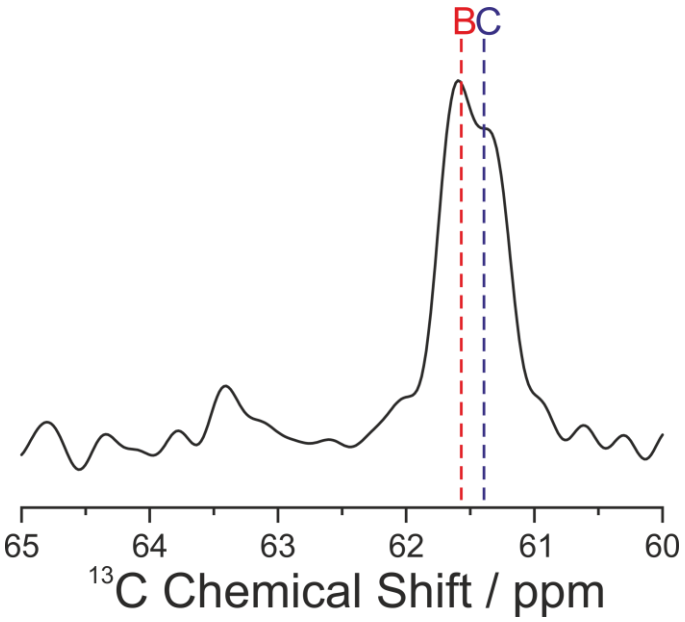

Figure 4.9: *Sum of the last 11 solid-state $^{1}H \rightarrow ^{31}P$ CP-MAS NMR spectra (last ca. 6.1 hrs) acquired during the crystallization process,*

experiment, there is both a transformation of phase A to phase B and phase C as well as a continuation of crystallization from solution.

Unfortunately, analysis of the changes in the chemical shifts of the peaks in the liquid-state ^{1}H NMR spectrum (in a similar manner to that performed for the liquid-state ^{13}C chemical shifts during the CLASSIC NMR study of *m*-ABA in Chapter 3) could not be performed due to changes in the shimming over the course of the experiment. When the sample is heated in the spectrometer to allow dissolution, the shims (which are used to ensure magnetic field homogeneity over the sample) are also heated and subsequently cool over the course of the experiment. This cooling causes a change in shimming resulting in changes in peak shape and, therefore, changes in the peak position calculated by the peak picking procedure, thus, masking changes in chemical shift caused by changes in solute concentration.

It must be noted that the peaks in the solid-state spectra here assigned to phases A, B and C, do not match the peak positions belonging to either monoclinic I or orthorhombic TPPO. It could be argued that a small error in referencing could allow the peak assigned as phase A to match the peak due to orthorhombic TPPO and/or would allow the peaks assigned to phase B or phase C to match the peak due to monoclinic I. However, the difference in chemical shift between orthorhombic and monoclinic I (1.70 ppm) does not match the difference between phase A and phase B (1.72 ppm) or the

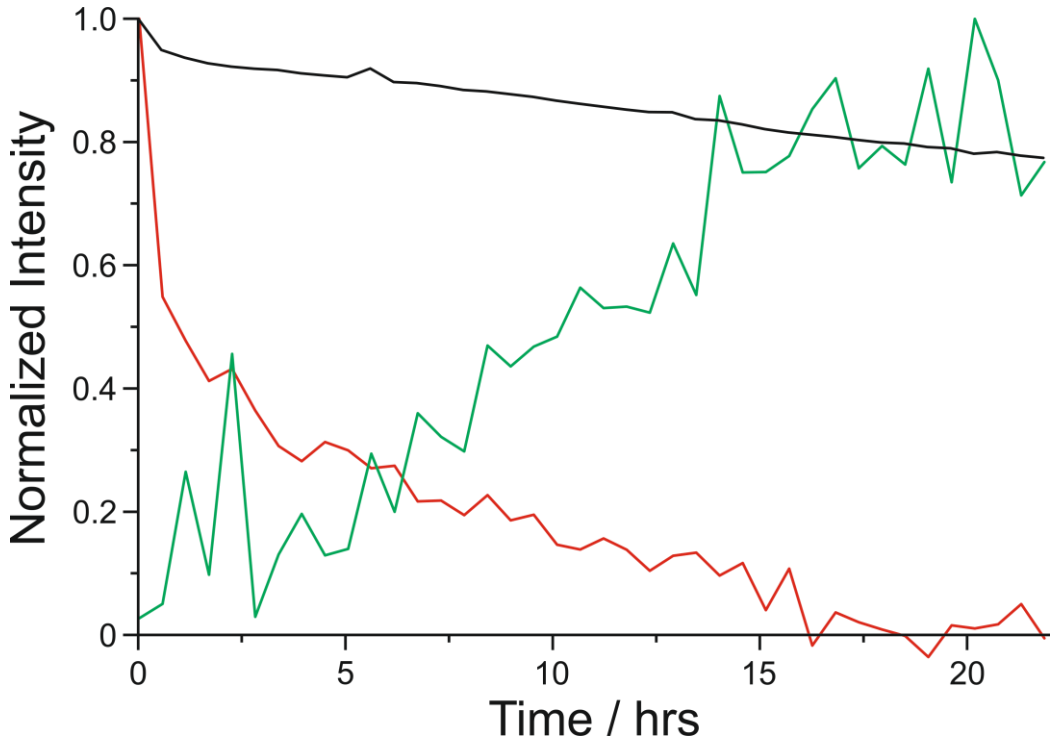

Figure 4.10: *Evolution in the integrated intensities of the TPPO peak in the liquid-state ^{31}P NMR spectra (black), the peak at 63.3 ppm in the solid-state ^{31}P spectra (red) and the integrated intensity of the combination of the peaks at 61.58 and 61.34 ppm in the solid-state ^{31}P spectra (green). The intensities have been normalized such that the maximum value in each case is set to 1.*

difference between phase A and phase C (1.96 ppm). Therefore, even if one of these three unknown phases is, in actuality, monoclinic I or orthorhombic TPPO, there remain two other unknown phases.

In addition, the behaviour of phase A in this *in-situ* study does not appear to match that expected for orthorhombic TPPO. Due to the common concomitant crystallization of orthorhombic and monoclinic I polymorphs of TPPO, it would be expected that the two polymorphs are close in relative stability. Thus, orthorhombic TPPO would not be expected to undergo the fairly rapid transformation that phase A is observed to undergo during this experiment. Due to the inability to reproduce the crystallization of the monoclinic II or monoclinic III polymorphs of TPPO (and therefore to record solid-state ^{31}P NMR spectra for well-characterized powder samples of these polymorphs), it cannot be ruled out that these polymorphs are present during this *in-situ* experiment. Nevertheless, the results from this CLASSIC NMR study give evidence for a possible three new solid forms of TPPO. Solvates of TPPO are obviously

also a possible identity for the phases observed here; however, so far, no ethanol solvate or cyclohexane solvate of TPPO have been reported.

In an attempt to replicate the conditions of the *in-situ* crystallization and record powder XRD data on the new phases observed, crystallization of TPPO from ethanol/cyclohexane (1:3 by mass) was carried out within glass capillaries, using the method described in Section 4.2.1. The majority of attempts were found by XRD to produce only monoclinic I and orthorhombic polymorphs. However, two capillaries in a single crystallization batch were found to contain a polycrystalline sample that was revealed by powder XRD to match none of the known polymorphs of TPPO (Figure 4.11).

This new powder XRD pattern was indexed successfully (using the program KOHL[133] within the CRYSFIRE program suite[106]) with orthorhombic metric symmetry and unit cell dimensions: a = 13.09 Å, b = 22.66 Å, c = 12.08 Å, V = 3583 Å^3. Le Bail fitting (using the program GSAS[107]) was also successful (using space group $P222$, Figure 4.12), resulting in a unit cell of dimensions: a = 13.09427(30) Å, b = 22.6553(5) Å, c = 12.0816(4) Å, V = 3584.04(22) Å^3 (R_{wp} = 1.82%, R_p = 1.29%; 2θ range, 4 to 70°; 3867 profile points). However, further crystal structure determination directly from this powder pattern was unsuccessful, presumably due to a high degree of preferred orientation introduced by carrying out the crystallization process within the glass capillary. Density arguments suggest that this phase may possibly be a solvate of TPPO. The densities of the polymorphs of TPPO range from 1.22 g cm^{-3} (monoclinic II) to 1.24 g cm^{-3} (monoclinic I). Assuming Z = 8 and assuming that the new phase contains only TPPO, the density would be 1.03 g cm^{-3}, significantly lower than of any of the known polymorphs of TPPO. A structure containing TPPO and ethanol in a 1:1 ratio, on the other hand, would have density 1.20 g cm^{-3}, much closer to those of the known polymorphs. For comparison, the density of the diethyl ether solvate of TPPO is 1.13 g cm^{-3} and the density of TPPO hemihydrate ranges from 1.25 g cm^{-3} to 1.29 g cm^{-3}.

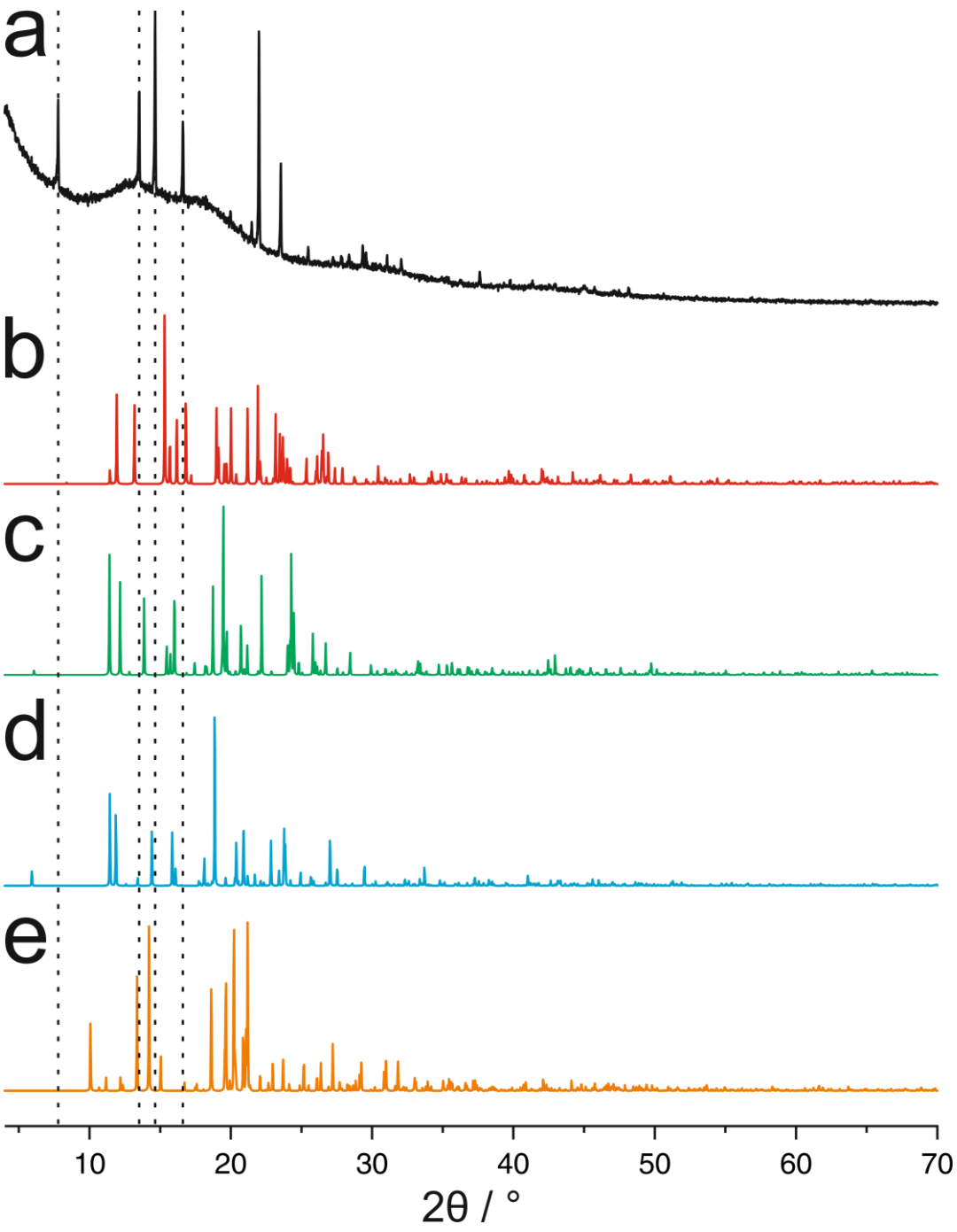

Figure 4.11: *(a) Experimental powder XRD pattern of TPPO crystallized from a mixed ethanol/cyclohexane (1:1 by mass) solvent within glass capillaries. Simulated powder XRD patterns of (b) monoclinic I phase of TPPO, (c) orthorhombic phase of TPPO, (d) monoclinic II phase of TPPO and (e) monoclinic III phase of TPPO. The positions of the first four peaks in the experimental powder XRD pattern of the crystallized sample are shown by dashed lines.*

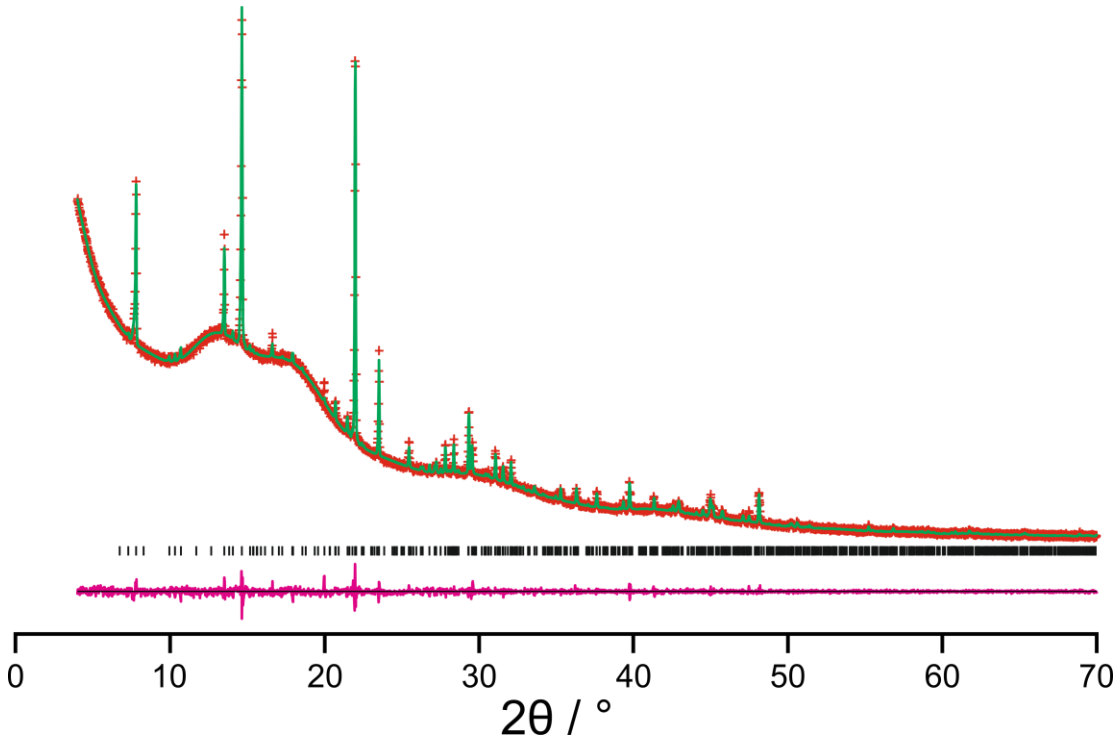

Figure 4.12: *Le Bail fit for the powder XRD pattern of the new phase of TPPO crystallized from ethanol/cyclohexane (1:3 by mass) within a glass capillary. The experimental data are shown as red crosses, the calculated fit as a green line and the difference between the two as a magenta line. Peak positions are displayed as black tick marks.*

3.4.2 - Methyldiphenylphosphine Oxide

Laboratory experiments were performed to investigate the crystallization of MDPPO from toluene, both through evaporation of the solvent and through cooling a saturated solution. Powder XRD confirmed that the crystallization products of these experiments are monophasic samples of the known crystalline phase of MDPPO.

The solid-state ^{31}P NMR spectrum recorded for the single known form of MDPPO has a single ^{31}P resonance at 30.78 ppm (Figure 4.13), corresponding to the single molecule of MDPPO in the asymmetric unit. As shown in Figure 4.13, the most intense peak in the spectrum is not the isotropic peak, but is the first order spinning sideband at higher chemical shift (65.57 ppm). Small peaks from impurity phases also appear at 33.84 ppm and 29.54 ppm (though whether these peaks represent impurity compounds or other crystalline phases of MDPPO is unknown). The $T_1(^1\text{H})$ of MDPPO is found to be less than 1 s. The evolution in the solid-state ^{31}P NMR spectra over the course of the crystallization of MDPPO from toluene is shown in Figure 4.14, focused on the first-

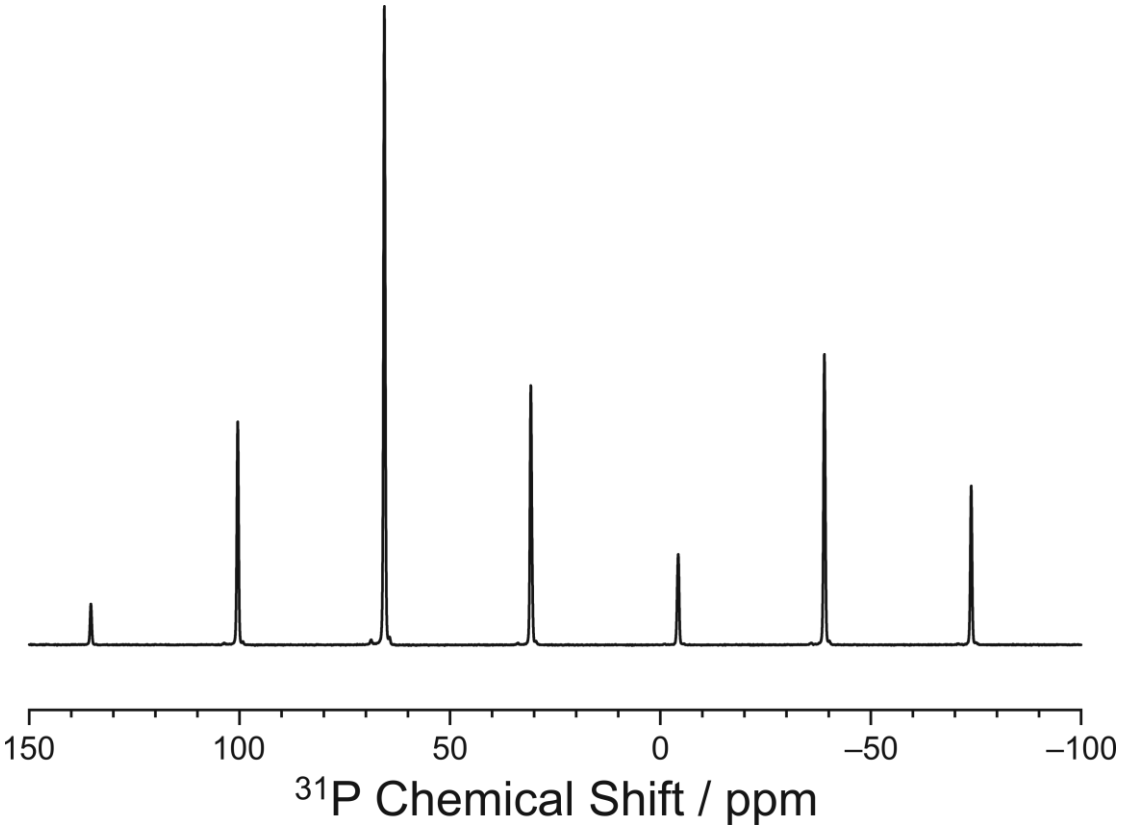

Figure 4.13: *Solid-state $^{1}H \rightarrow ^{31}P$ CP-MAS NMR spectrum for the known phase of MDPPO. The isotropic peak is located at 30.78 ppm. Two small peaks due to impurity phases are present at 33.84 ppm and 29.54 ppm.*

order spinning sideband to higher chemical shift (as to it has the highest intensity). It is clear from Figure 4.14 that crystallization must have begun before or during the recording of the first spectrum. All spectra acquired throughout the crystallization process are dominated by the intense peak at 65.57 ppm, corresponding to the known phase of MDPPO. Significantly, however, two additional peaks of considerably lower intensity are also observed in the early stages of crystallization, with first-order spinning sidebands at 63.7 ppm and 64.5 ppm (corresponding to isotropic peaks at 28.8 ppm and 29.6 ppm, respectively).

Only one crystalline phase of MDPPO was known prior to this work. Thus, these two additional peaks must represent new solid forms of MDPPO produced at a very early stage of the crystallization process. The intensity of the peaks due to the new forms is highest in the first acquired spectrum, decreasing as a function of time. These two peaks are assigned as arising from two different solid phases, rather than a single solid phase with two distinct ^{31}P environments from the fact that the evolution of the two peaks is distinctly different, with significantly different rates of decay of peak

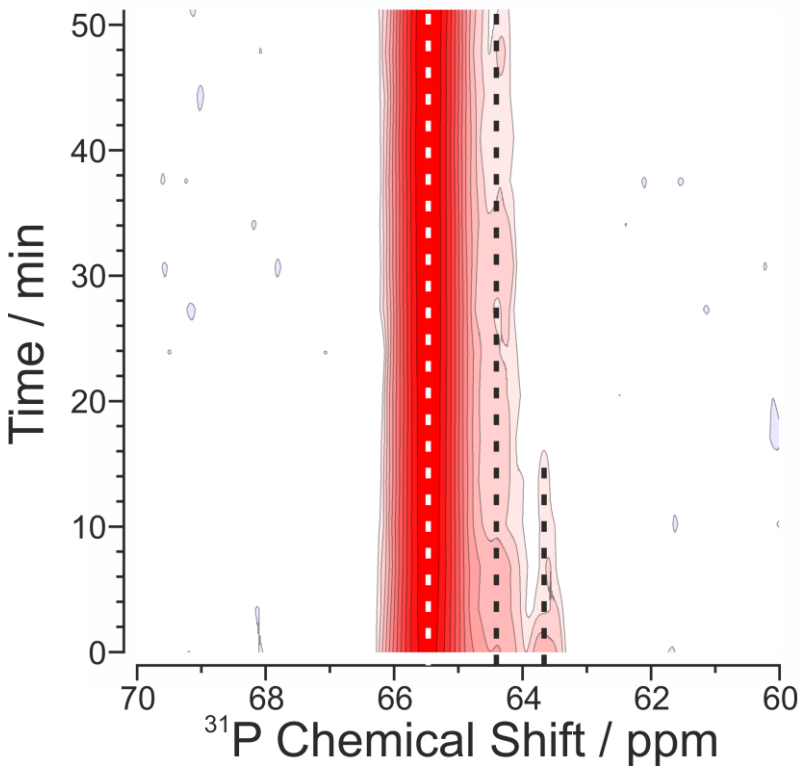

Figure 4.14: *In-situ solid-state $^{1}H \rightarrow ^{31}P$ CP-MAS NMR spectra acquired during the crystallization of MDPPO from toluene. The region corresponding to the first spinning sidebands to higher chemical shift of the isotropic peaks is shown.*

intensity. Thus, the peak at 63.7 ppm becomes indiscernible from the background after *ca*. 16 mins, while the peak at 64.5 ppm remains visible for *ca*. 6 hrs. From these *in-situ* ^{31}P solid-state NMR results, the possibility that these unknown phases represent toluene solvates of MDPPO cannot be ruled out. However, it must be noted that no toluene solvate of MDPPO has been reported previously.

The two new phases of MDPPO observed in the *in-situ* NMR experiment may be difficult to isolate *ex situ*. It is obvious that these phases are produced in small amounts during the early stages of the crystallization of MDPPPO from toluene. However, due to the overwhelming presence of the known phase of MDPPO, isolation of the new phases in these proportions would very likely present an insurmountable problem. Other crystallization procedures must therefore be researched in order to produce these two unknown forms.

4.4 - Conclusions

Through use of *in-situ* solid-state ^{31}P NMR, up to three new solid phases of TPPO have been discovered during the crystallization of TPPO from an ethanol/cyclohexane mixed solvent (1:3 by mass). If all three phases correspond to new polymorphs of TPPO, the total number of polymorphs for this compound would be raised to seven (only very rare cases such as ROY[3] have more known polymorphs). Crystallization of TPPO from ethanol/cyclohexane (1:3 by mass) within glass capillaries revealed a new crystalline phase by powder XRD. Structure determination of this phase was unsuccessful and work is continuing in an attempt to isolate and characterize this phase, though density arguments suggest that it may, in fact, be a solvate of TPPO.

The *in-situ* solid-state ^{31}P NMR study of the crystallization of MDPPO from toluene has demonstrated the existence of two unstable, transient phases during the crystallization process. These phases represent possible new polymorphs of MDPPO. Laboratory isolation of these phases is expected to be highly difficult under the conditions used in the *in-situ* NMR crystallization experiment due to the low proportion of the unknown phases relative to the known crystalline phase of MDPPO. Other crystallization conditions (such as a variation on solvent or temperature schedule used), will likely need to be explored but the conditions described here represent a starting point for further experimentation.

Both of these studies exemplify the ability of *in-situ* solid-state NMR studies of crystallization to discover previously unknown, transient phases formed during crystallization processes. In particular, the case of TPPO has demonstrated that extrapolation of the conditions used in the *in-situ* NMR crystallization experiment to the laboratory allows the characterization of previously unknown crystalline phases *via* powder XRD.

Chapter 5: New Insights into the Preparation of Form II of *rac*-Ibuprofen

5.1 - Introduction

As mentioned in Chapter 1, polymorphism is both widespread and of great importance within the pharmaceutical industry. Common pharmaceuticals, including aspirin[16-20] and paracetamol,[13-15] are known to be polymorphic and undiscovered polymorphism was disastrous in the case of the antiretroviral ritonavir.[7]

Ibuprofen (Figure 5.1) is listed by the World Health Organization (WHO) as one of the three essential non-opioid and non-steroidal anti-inflammatory medicines (NSAIMs).[134] Only the *S*-(+)-enantiomer of ibuprofen is biologically active.[135] *In vivo*, however, the *R*-(–)-enantiomer is converted to the *S*-(+)-enantiomer[135] and so ibuprofen is usually supplied as the racemate. *rac*-Ibuprofen melt can easily be supercooled and is reported to undergo a glass transition at –55 °C.[22] At ambient temperature, the solubility of ibuprofen in water is fairly poor while the aqueous solubilities of the sodium and lysinium salts of ibuprofen are much higher.[136] These salts are therefore marketed for fast-acting pain treatment and migraine relief as the higher solubility allows for faster absorption of the drug *in vivo*.[137]

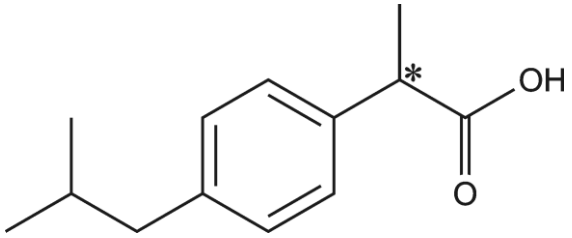

Figure 5.1: *Molecular structure of ibuprofen.*

The first crystal structure for *rac*-ibuprofen was solved[21] in 1974. It was not until 2008 that polymorphism was discovered in *rac*-ibuprofen.[22] Experiments performed on *rac*-ibuprofen melt demonstrated that a new polymorph, Form II (the previously determined structure is named Form I), could be prepared by undertaking a particular cooling regime. It was reported that, in order to produce Form II, it was essential to quench cool ibuprofen melt to a temperature at least 60 K below the glass transition and to hold for an hour before warming to 258 K, at which point crystal growth of Form II would occur. It was reported that nucleation of Form II was dependent on the initial

quench and mechanisms based on the formation of cracks within the glass were postulated. The melting point of Form II was reported as 290 K, substantially (59 K) lower than that of Form I, 349 K.

The process of quench cooling of a melt to below a glass transition to achieve crystallization replicates that observed in other systems such as *m*-toluidine,[138] *o*-benzylphenol[139] and 3,3'-dimethoxy-4,4'-bis(2,2-diphenylvinyl)biphenyl.[140] Similar to the case reported for Form II of *rac*-ibuprofen, the quench cooling of *m*-toluidine is the only known method for production of the β-polymorph.

The crystal structure[64] of Form II of *rac*-ibuprofen [Figure 5.2(b)] was determined directly from powder XRD data recorded using synchrotron radiation. The structure of Form II contains dimers of ibuprofen hydrogen bonded through the carboxylic acid groups, as in the case of Form I [Figure 5.2(a)]. In Form I, the hydrogen bonding occurs perpendicular to the chains of dimers within the structure and links ibuprofen molecules from two different chains. In Form II, however, the hydrogen bonding links ibuprofen molecules from within the same chain.

To explore this method of crystallization further, in the present work, both DSC and *in-situ* powder XRD were utilized to give insight on whether quenching to a temperature below the glass transition is truly necessary to the formation of Form II.

5.2 - Experimental Methods

Ibuprofen was purchased commercially as the racemic sodium salt from Fluka (purity 99.5%). This sample was converted into the free acid by dissolution in water followed by acidification with hydrochloric acid, leading to the precipitation of *rac*-ibuprofen (due to the low solubility of the free acid in water). Extraction of *rac*-ibuprofen was performed using chloroform, followed by washing with water to remove any remaining sodium salt. *rac*-Ibuprofen was finally recrystallized from chloroform by evaporation of the solvent.

To confirm the purity of the sample prepared by this procedure, solution-state ^{1}H NMR, gas chromatography, melting point analysis and powder XRD were performed. The solution-state ^{1}H NMR demonstrated the absence of any chloroform-soluble compound other than *rac*-ibuprofen, with gas chromatography confirming a purity of greater than 99%. Powder XRD showed that the only crystalline phase present was *rac*-

ibuprofen Form I and melting point analysis determined a melting onset temperature of 347.15(10) K and melting enthalpy of 25.96(45) kJ mol^{-1}, tallying well with reported literature values (Table 5.1).

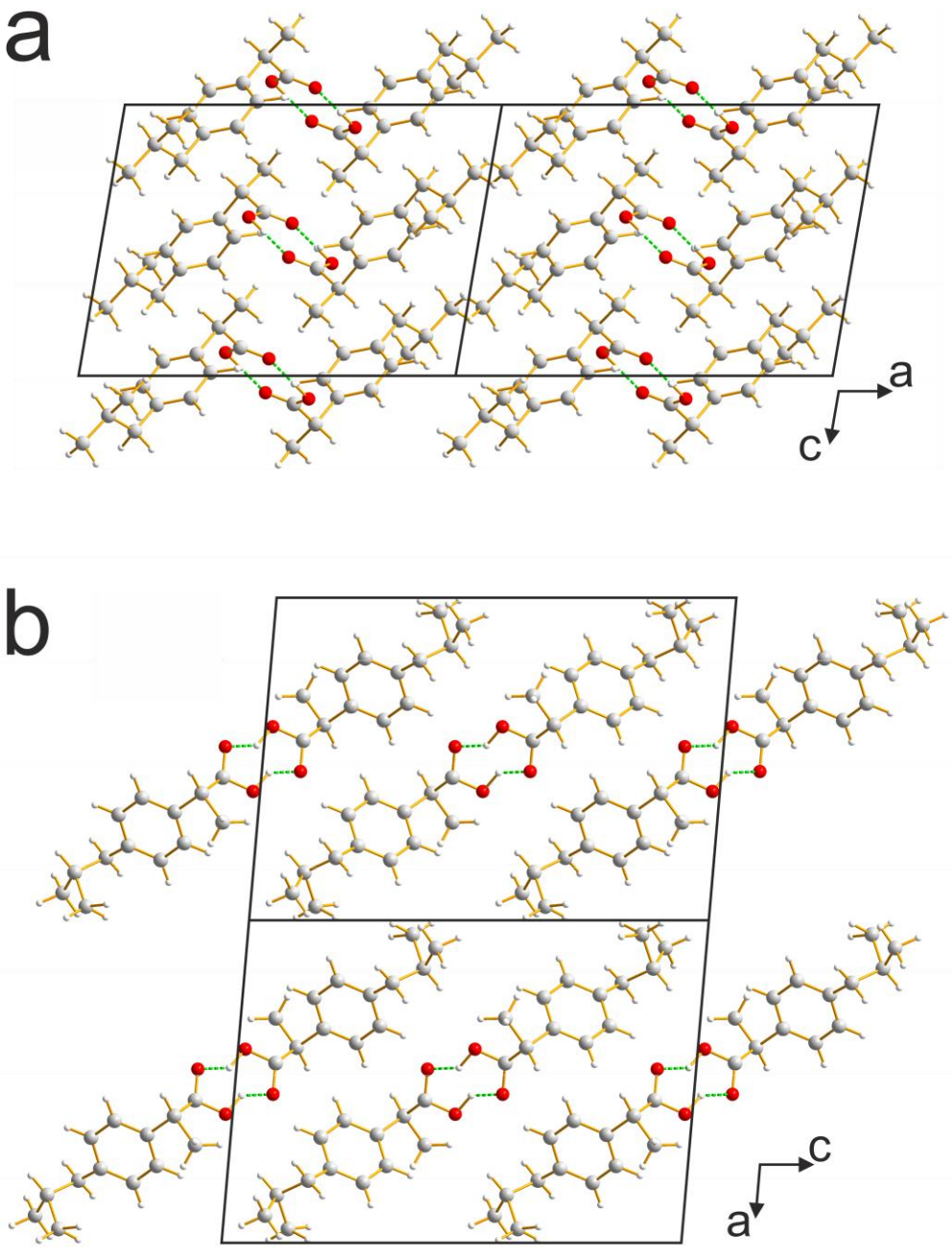

Figure 5.2: *Crystal structures of (a) Form I of rac-ibuprofen, and (b) Form II of rac-ibuprofen, each viewed along the 2_1 screw axis.*

Source	Onset Melting Point (K)	Melting Enthalpy (kJ mol^{-1})
This work	347.15 ± 0.20	25.96 ± 0.90[a]
Chow *et al.*[141]	344.8 ± 0.2	27.2 ± 0.4[a]
Seton *et al.*[142]	347.84	23.33[a]
Xu *et al.*[143]	348.35 ± 0.11	25.04 ± 0.10;[a] 26.65[b]
Dudognon *et al.*[22]	–	25.8 ± 0.5[a]

Table 5.1: *Onset melting point and melting enthalpy ([a] determined using DSC, [b] determined using adiabatic calorimetry) for Form I of rac-ibuprofen.*

All DSC measurements were performed using a TA Instruments Q100 differential scanning calorimeter. Samples were contained within hermetically sealed aluminium pans. A heating rate of 10 K min^{-1} and cooling rate of 20 K min^{-1} were used in all DSC experiments. Each DSC experiment was performed with the same general procedure. Initially, the sample was heated to 373 K to allow for melting of the sample, followed by cooling to a temperature lower than the glass transition (termed the quenching temperature). The sample was held at this quench temperature for a certain length of time before heating to a second temperature (the annealing temperature) and again holding for a certain length of time. Finally, the sample was heated again to 373 K, to allow observation of the melting of any crystalline sample present followed by cooling to room temperature. In some cases, the quenching step was removed and the molten sample was instead cooled directly to the annealing temperature. A variety of quenching and annealing temperatures were used, with full details given in Section 5.3.

In-situ powder XRD was carried out using a Bruker D8 diffractometer in reflection geometry (Cu Kα_1 radiation, germanium monochromated). An Oxford Cryostreams Phenix was used to control the temperature of the sample. The sample of *rac*-ibuprofen (of approximate mass 11 mg) was contained in an indentation on a copper disk held within a silver-coated copper sample cup. The sample of *rac*-ibuprofen was melted *ex situ* by heating the sample contained on the copper disk to 373 K using a bench-top hot plate, before transferring the disk to the diffractometer (with the sample cooling to ambient temperature during the transfer). At this point, the cryostat chamber was evacuated and cooled at a maximum rate of approximately 2 K min^{-1}. At each temperature to be studied, powder XRD patterns were repeatedly recorded over time. As mentioned in Chapter 1, the time-resolution of an *in-situ* study is limited in this case by the time to record a single powder XRD pattern. The total time to record a powder XRD pattern in this study was either 44 or 88 minutes, with these times, therefore,

representing the maximum time resolution. Powder XRD data were recorded over the angle range $4° \leq 2\theta \leq 43°$ (step size 0.016°). The data recorded with 2θ below 10° are not shown within the figures of this chapter as they are dominated by a high background scattering caused by the shielding of the cryostat chamber.

5.3 - Results and Discussion

5.3.1 - DSC Studies of the Crystallization of Form II of rac-Ibuprofen

As previously mentioned, the intention of this work was to explore the crystallization conditions for Form II of *rac*-ibuprofen in order to discover if the initial quench cool below the glass transition point is essential to its formation. To this end, DSC experiments constituting a range of conditions were performed, both including and excluding the initial low temperature quench. The full set of experiments and results in each case is summarized in Table 5.2, with a graphical representation of the temperature scheme used in the first experiment (a repeat of that conducted by Dudognon *et al.*[22]) shown in Figure 5.3. The results are given as percentages of the sample crystallized as Form II and a qualitative measurement for the presence of Form I.

	Quench		**Anneal**		**Result**	
	T / K	**Time / h**	**T / K**	**Time / h**	**Form II**	**Form I**
A	143	1	258	3	70%	Yes
B	143	0	258	3	100%	Yes
C	143	0	258	3	<5%	No
D	193	0	258	3	<5%	Yes
E			258	6	35%	Yes
F			258	3	0	Yes
G			258	3	<5%	Yes
H			258	1	0	No
I			258	1	<5%	No
J			243	3	0	Yes
K			243	3	0	Yes
L			273	12	0	No
M			273	3	0	No
N			273	3	0	No

Table 5.2: *Summary of DSC experiments conducted on rac-ibuprofen.*

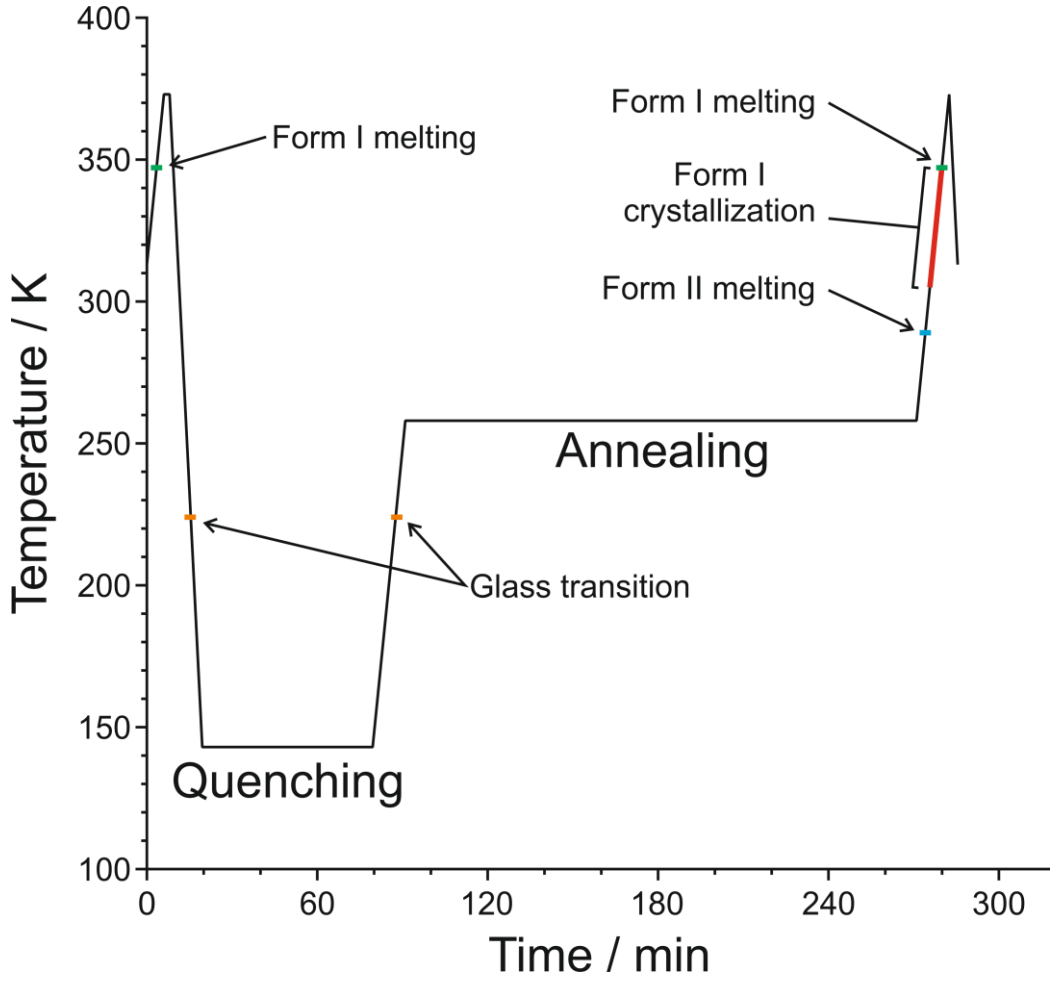

Figure 5.3: *Graphical representation of the procedure used in DSC Experiment A, repeating the experiment performed by Dudognon et al.*[22]

In each case, the crystalline content of Form II in the sample is measured through comparison of the melting enthalpy of the Form II peak detected during the final heating procedure with the value of the Form II melting enthalpy reported by Dudognon *et al.*[22] A similar approach to find the amount of Form I present during the final heating cannot be performed, as the melting endotherm of Form I is found to overlap with the exotherm caused by the crystallization of Form I. The presence of Form I can therefore only be determined in a qualitative manner, i.e., either a melting endotherm for Form I is observed or it is not observed.

The series of experiments was completed in order, beginning with experiment A, a repeat of the method described by Dudognon *et al.*,[22] i.e., a quench to 143 K for one hour, followed by an annealing for three hours at 258 K. The DSC thermogram for this experiment is shown in Figure 5.4. As shown in Table 5.2, this method resulted in crystallization of Form II (with approximately 70% of the sample crystallizing in this form). Form I was also observed during the final heating. It should be noted that, during

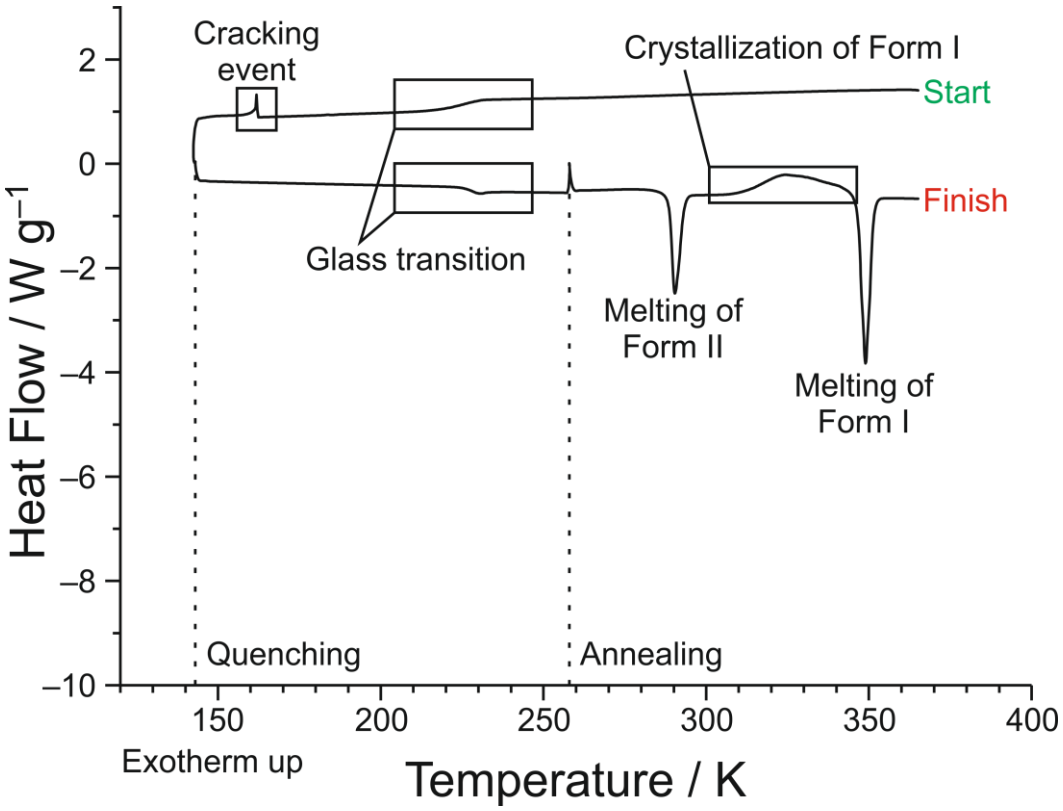

Figure 5.4: *DSC thermogram for experiment A. For clarity, the initial heating of the sample to 373 K and final cooling to 313 K have been excluded. Indicated are the quenching and annealing temperatures and the thermal events occurring during the DSC experiment, including a cracking event further expanded upon in the text.*

the DSC experiments involving quench cooling of the sample to 143 K, a spike in heat flow was observed in the DSC thermogram. This spike seems to correlate with the occurrence of cracking within the glassy sample described by Dudognon *et al.*[22] (and is marked in Figure 5.4 as a cracking event). During some attempts at cooling below the glass transition, some of the spikes in heat flow were followed by a loss in heat flow signal from the sample, which was found to be caused by the sealed DSC sample pan becoming dislodged from the plinth within the calorimeter. This observation demonstrates that the cracking events described by Dudognon *et al.*[22] and observed here are occasionally violent enough to cause a substantial movement of the sample pan.

To determine if crystallization of Form II is dependent on remaining at the quenching temperature for one hour, two experiments (B and C) were performed in which the *rac*-ibuprofen melt was cooled to the quenching temperature of 193 K followed by immediate heating to the annealing temperature (at which it was annealed for three hours). Form II was observed to have crystallized during both of these experiments. In B, the entire sample was estimated to have crystallized as Form II while

in C, less than 5% of the sample was estimated to have crystallized as Form II (Figure 5.5). Additionally, in B, a melting endotherm for Form I was observed during the final heating while this was missing in C. These two experiments, while showing inconsistency, indicate that it is possible to crystallize Form II without holding the sample for an extended length of time at the quenching temperature.

In experiment D, the sample was quenched at 193 K (i.e., 31 K below the glass transition), a quenching temperature higher than that reported[22] to be essential for nucleation of Form II. During the final heating run, an endotherm was observed for both Forms II and I. However, this endotherm corresponded to only a small amount of crystallized Form II (less than 5%). Nevertheless, this result demonstrates that crystallization of Form II can occur without quenching to a temperature more than 60 K below the glass transition.

Following this result, the entire quenching step was removed from the procedure. In experiment E, the sample of molten *rac*-ibuprofen was cooled directly to the

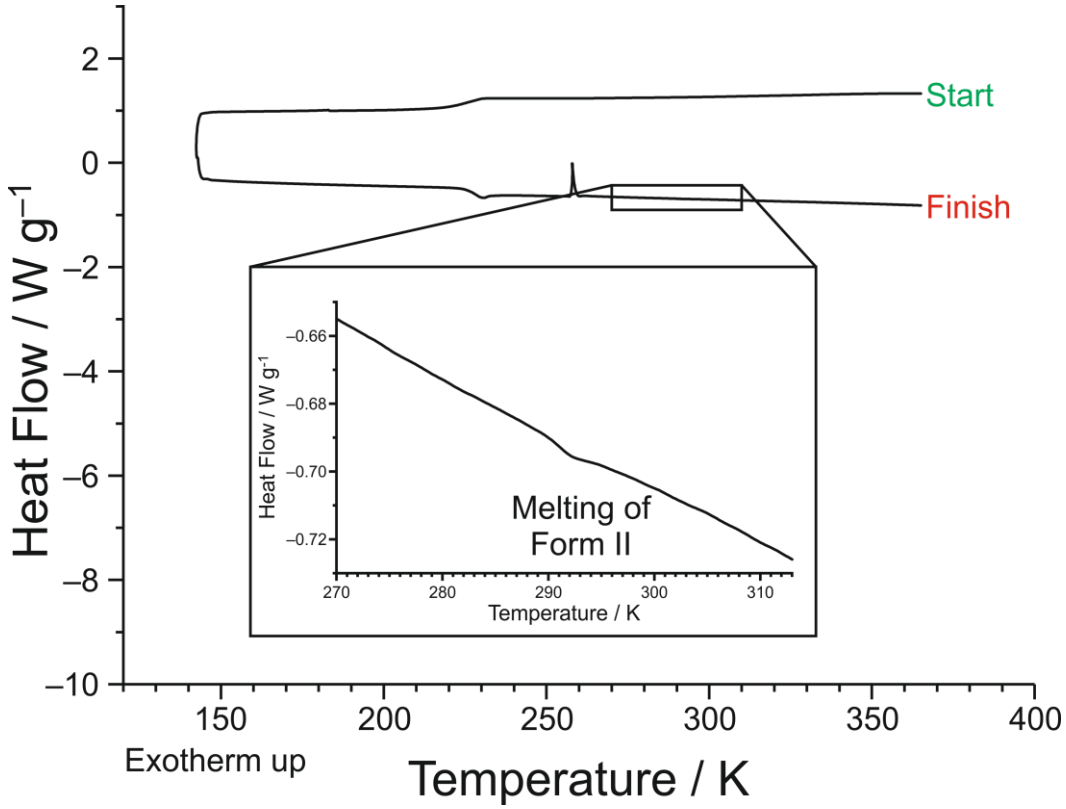

Figure 5.5: *DSC thermogram for experiment C. For clarity, the initial heating of the sample to 373 K and final cooling to 313 K have been excluded. The region of 270 to 310 K has been expanded to demonstrate the very small endotherm observed for the melting of Form II, in this case.*

annealing temperature (258 K) and maintained at this temperature for six hours. During the final heating run, endotherms for both Form II and Form I were observed (with roughly 35% of the sample crystallizing as Form II). This experiment conclusively demonstrates that quenching to low temperature is *not* essential for nucleation of Form II of *rac*-ibuprofen. The annealing step was then shortened to three hours (experiments F and G) and further to one hour (experiments H and I). A small amount of Form II (less than 5% of the total sample) was observed in one of the two experiments conducted at each annealing time (experiments G and I), indicating that the crystallization of Form II during these annealing times is somewhat inconsistent.

Further experiments were carried out to explore the effect of the annealing temperature on the crystallization of Form II in the absence of the initial low temperature quenching step. Using an annealing temperature of 243 K and annealing time of three hours (experiments J and K), no melting endotherm was observed for Form II during the final heating, while Form I was observed in both cases. Using an annealing temperature of 273 K and annealing times of three hours (experiments M and N) and a longer annealing time of twelve hours (experiment L), no evidence for the crystallization of Form II or Form I was found.

5.3.2 - In-Situ Powder XRD Studies of the Crystallization of Form II of rac-Ibuprofen

To further investigate the crystallization of Form II of *rac*-ibuprofen with no quenching step, *in-situ* powder XRD experiments were carried out. For comparison with the experimental powder patterns recorded during these experiments, the simulated powder XRD patterns of the two polymorphs of *rac*-ibuprofen are shown in Figure 5.6. As described in Section 5.2, Form I of *rac*-ibuprofen was heated until melting had completed, *ex situ*, before transfer to a laboratory powder X-ray diffractometer in reflection mode (during which time the sample cools to ambient temperature), where it was further cooled, under vacuum, to the desired annealing temperature.

Three *in-situ* powder XRD experiments were performed. In the first, the sample of liquid *rac*-ibuprofen was cooled to 258 K and held at this temperature for 43.0 hours while recording repeated powder XRD patterns. After this time, the sample was warmed to 273 K and held for a further 23.4 hours, again recording repeated powder XRD patterns. For the first 9.5 hours after reaching 258 K, no diffraction peaks were observed, indicating the absence of crystalline phases within the sample. At 9.5 hours,

peaks corresponding to the diffraction pattern of *rac*-ibuprofen Form II were observed. Subsequent measurements from 9.5 to 16.1 hours showed only a slight increase in the intensity of these peaks. Thereafter, there were no significant changes in the peak intensities throughout the remaining time at 258 K and Form II remained as the only crystalline phase present during this time. After 43.0 hours at 258 K, the sample was warmed to 273 K. After 2.9 hours at this new temperature, peaks attributed to the presence of Form I of *rac*-ibuprofen were observed to appear. These peaks were found to grow in intensity over time, with a subsequent decrease in the intensity of the peaks due to Form II. The disappearance of the peaks due to Form II was complete by

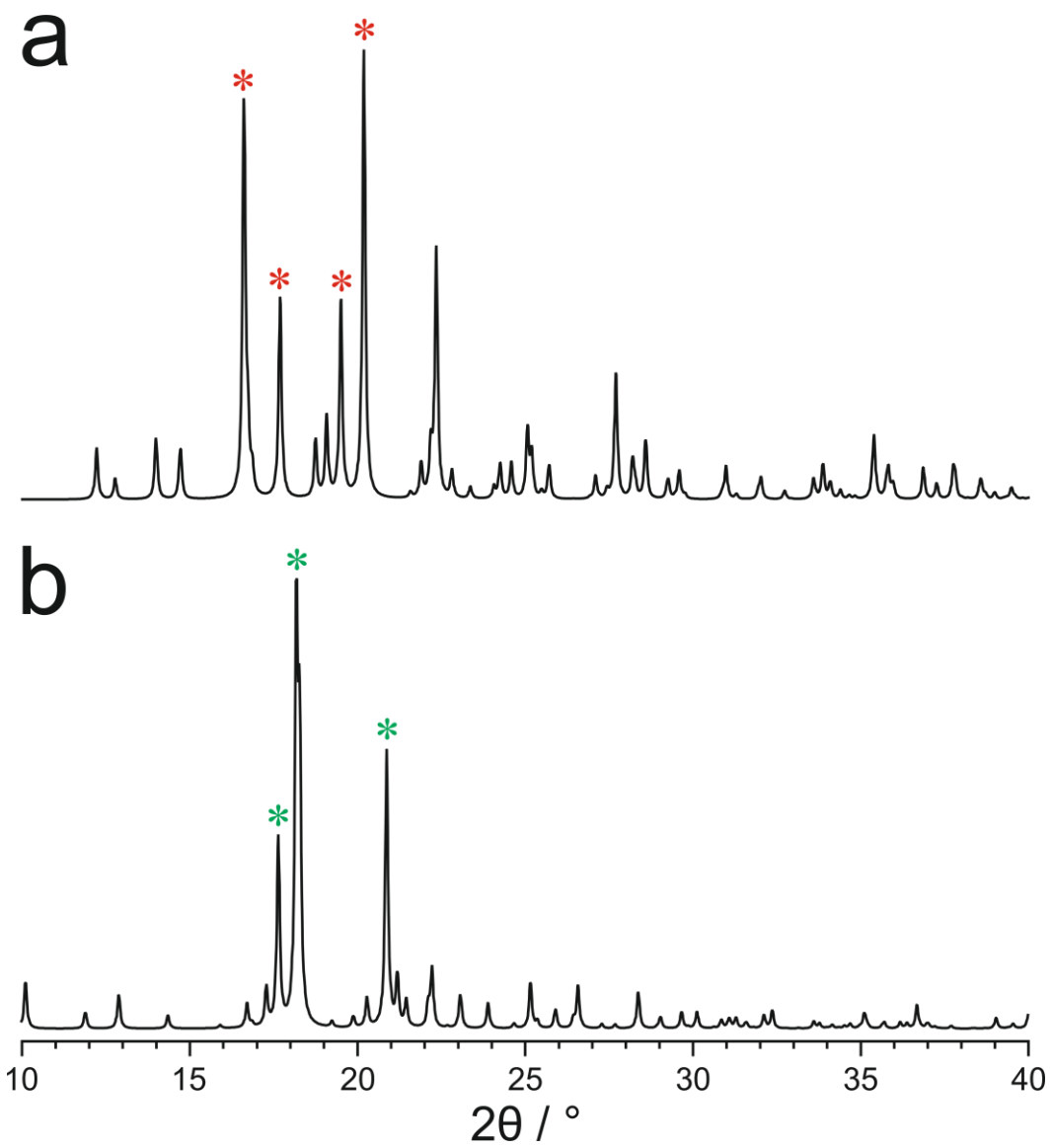

Figure 5.6: *Simulated powder XRD patterns for (a) Form I of rac-ibuprofen and (b) Form II of rac-ibuprofen, over the range 10° ≤ 2θ ≤ 40° (Cu Kα₁ radiation) using the published crystal structures. Marked with asterisks are distinctive peaks indicative of the form in question (red for Form I, green for Form II).*

8.7 hours after reaching 273 K, indicating that the transformation of Form II to Form I had completed. No further change in crystalline form was observed at 273 K. A schematic representation of this experiment is given in Figure 5.7 and selected *in-situ* powder XRD patterns are shown in Figure 5.8. The changes in the relative amounts of Form I and Form II were measured through integration of isolated peaks belonging to the two forms (the region 18.8° to 20.0° for Form I and the region 20.0° to 22.0° for Form II) and the results are displayed in Figure 5.9. The integrals during this measurement were normalized so that the maximum value for each polymorph was set to unity. The results from this experiment corroborate the findings of the DSC experiments, i.e., that crystallization of Form II can occur at 258 K with no prior low-temperature quenching step.

In the second *in-situ* powder XRD experiment, the sample of liquid *rac*-ibuprofen was cooled directly to 273 K and held at this temperature for 46.7 hours while recording repeated powder XRD patterns. Similar to the previous experiment, no diffraction peaks corresponding to crystalline phases were observed for the first 14.6 hours after cooling. After this time, however, peaks corresponding to Form II were observed, increasing in intensity until 17.5 hours. From 19.0 hours at 273 K, peaks corresponding to Form I were first observed, and then increased in intensity with a decrease in the intensity of

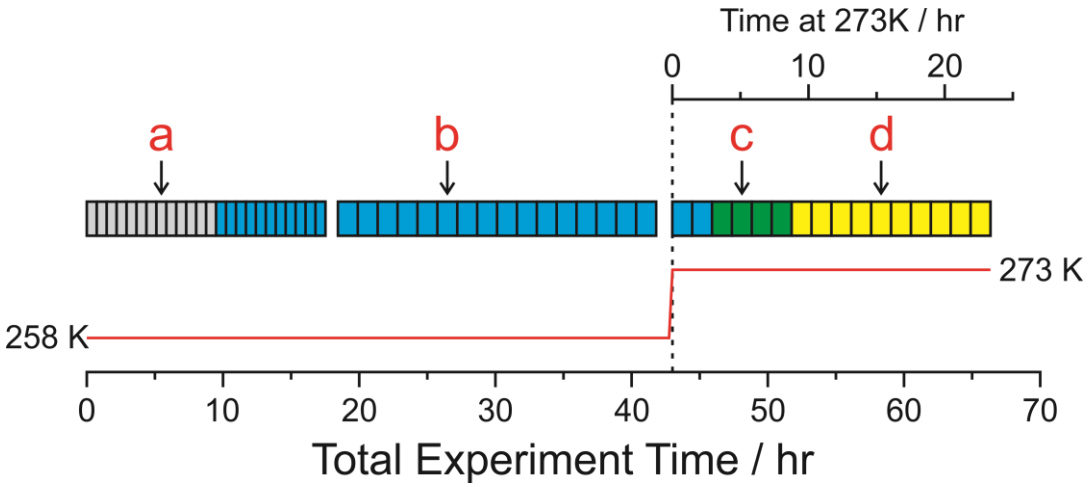

Figure 5.7: *Schematic representation of the phases found in the an in-situ powder XRD experiment studying the crystallization of rac-ibuprofen from the supercooled liquid, initially at 258 K, followed by 273 K. Shown in grey are the patterns where no crystalline phases are observed, blue where only Form II is observed, yellow where only Form I is observed and green where both Form I and Form II are observed. Marked with arrows and labelled a-d are the specific powder XRD patterns shown in Figure 5.8.*

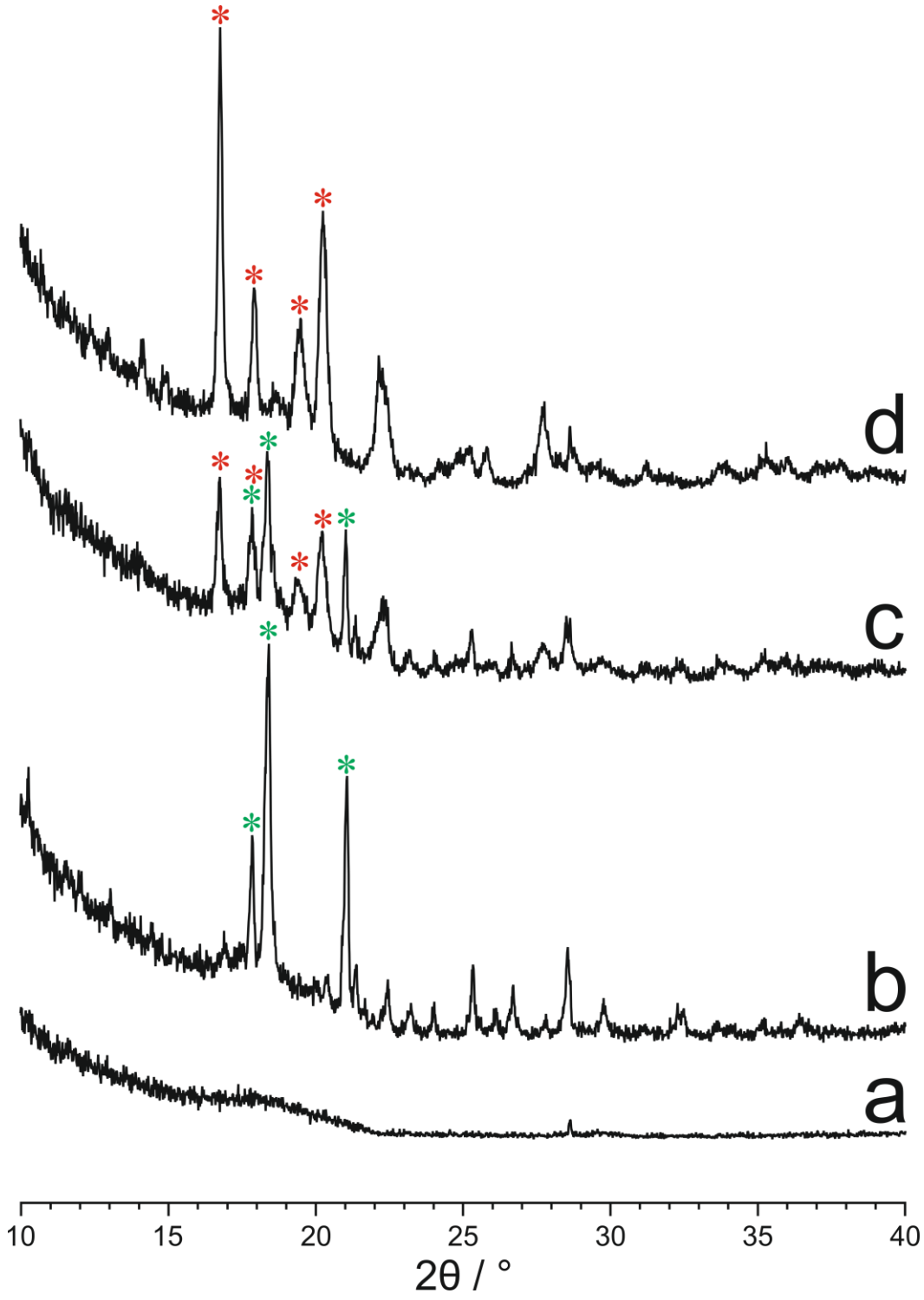

Figure 5.8: *In-situ powder XRD patterns collected during the crystallization of rac-ibuprofen from the supercooled liquid, initially at 258 K (for a period of 43.0 hours), and then at 273 K (for a period of 23.4 hours). Within the entire experiment, the specific time at which each powder XRD pattern (a-d) was recorded is shown in Figure 5.7 (labelled a-d).*

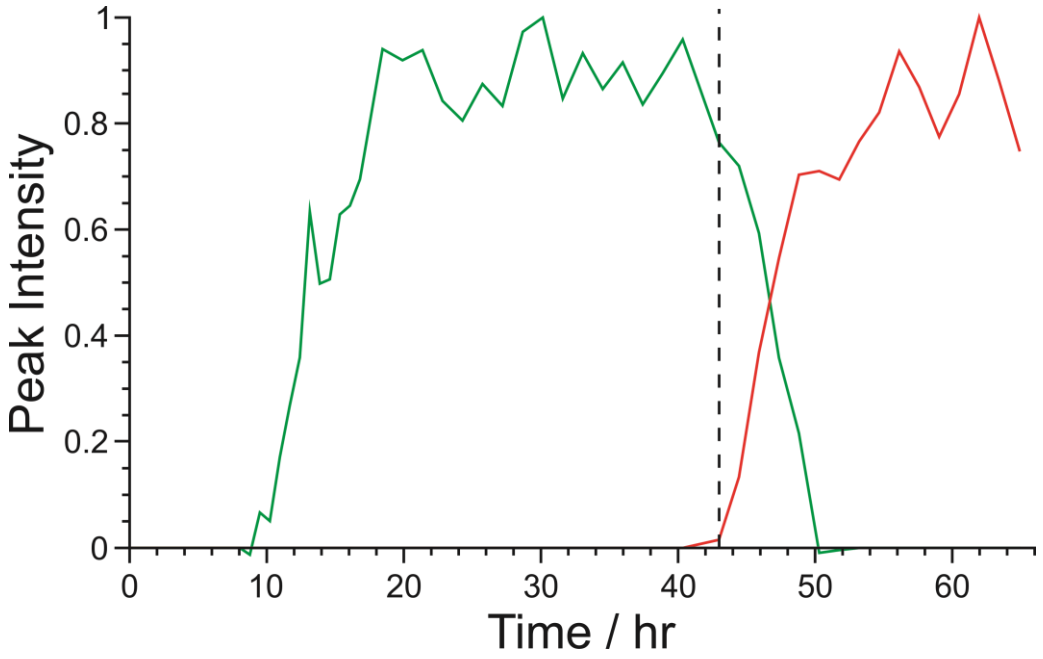

Figure 5.9: *Integrated peak intensities for the phases observed during the crystallization of rac-ibuprofen from the supercooled liquid, initially at 258 K, followed by 273 K. Form II is shown in green (intensity integrated over the 2θ range: 20.0° – 22.0°) and Form I in red (intensity integrated over the 2θ range: 18.8° – 22.0°). The integrals were normalized so that the maximum value of each polymorph is set to unity.*

the peaks due to Form II. By 27.7 hours, the peaks due to Form II disappeared completely. No further change in crystalline form was detected for the remainder of the experiment. A schematic representation of this experiment along with extracted *in-situ* powder XRD patterns is shown in Figure 5.10. As in the previous experiment, integrated peak intensities for isolated distinctive peaks (again, the region 18.8° to 20.0° for Form I and the region 20.0° to 22.0° for Form II) were calculated for the two forms during this measurement and are displayed in Figure 5.11. This experiment shows that crystallization of Form II can occur at 273 K. The fact that Form II was not observed in the DSC experiments involving annealing at 273 K may be attributed to the crystallization event being preceded by a significant lag time.

A third *in-situ* experiment was carried out, cooling the sample of *rac*-ibuprofen melt to 243 K, in order to assess whether, in a similar manner to the second experiment, crystallization of Form II occurs at this temperature after a suitably long time. The sample was held at 243 K for a total of 93 hours. However, no crystalline phases were observed to form at any stages of this experiment.

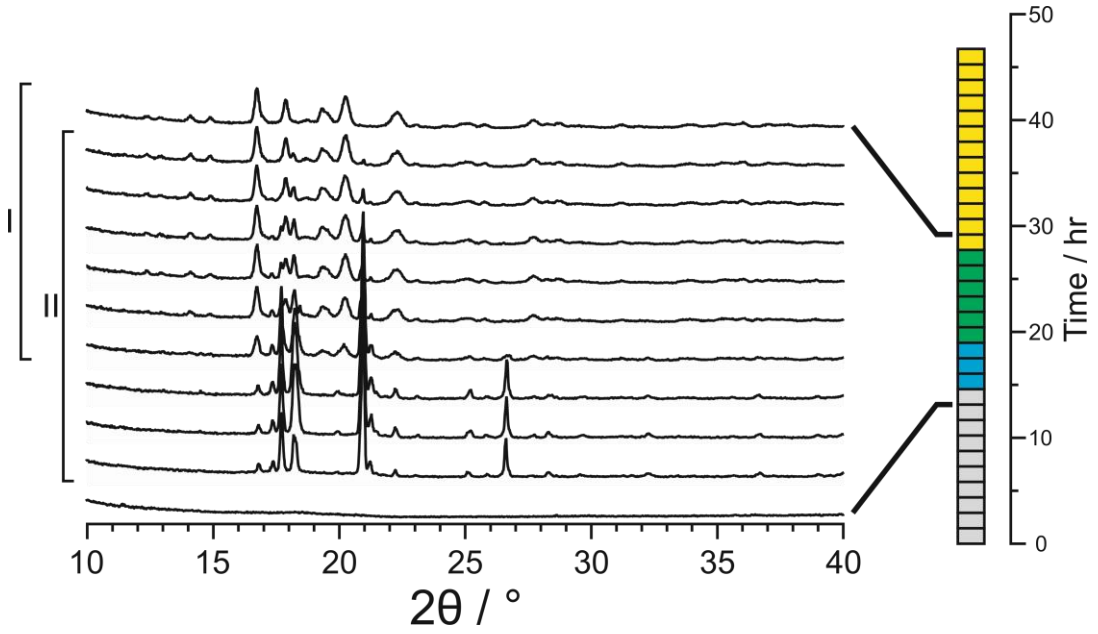

Figure 5.10: *In-situ powder XRD patterns collected during the crystallization of rac-ibuprofen from the supercooled liquid at 273 K. Shown are extracted powder XRD patterns recorded during the timeframe 13.1 to 29.2 hours. Shown on the right is a representation of the complete experiment, showing scans where no crystalline phases are observed in grey, scans where Form II is observed in blue, scans where Form I is observed in yellow and scans where both are observed in green.*

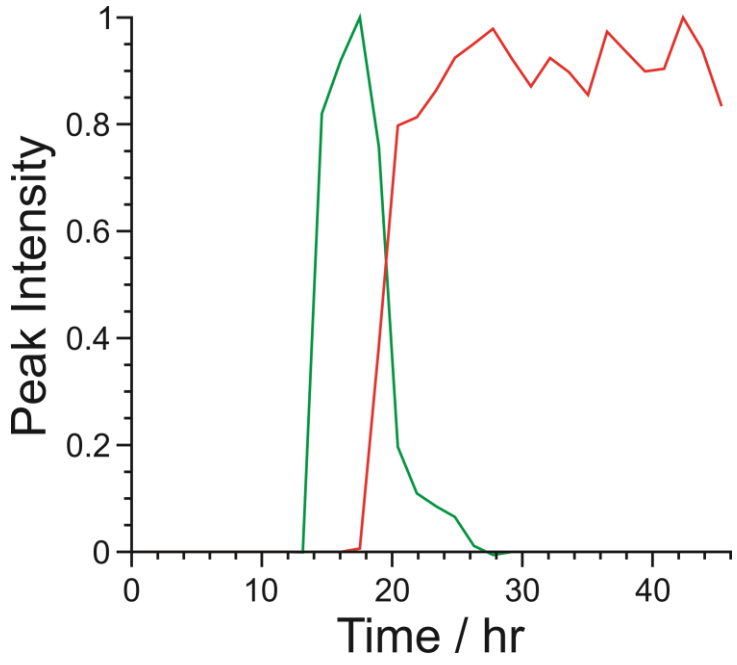

Figure 5.11: *Integrated peak intensities for the phases observed during the crystallization of rac-ibuprofen from the supercooled liquid at 273 K. Form II is shown in green (intensity integrated over the 2θ range: 20.0° – 22.0°) and Form I in red (intensity integrated over the 2θ range: 18.8° – 22.0°). The integrals were normalized so that the maximum value of each polymorph is set to unity.*

The DSC and *in-situ* powder XRD experiments, taken together, demonstrate that the low temperature quench described by Dudognon *et al.*[22] is *not* essential to the formation of Form II. The crystallization of Form II is observed at a maximum temperature of 258 K in the DSC experiments and 273 K in the *in-situ* powder XRD experiments. This difference may be accounted for in the long lag time observed before crystallization at 273 K during the *in-situ* measurements (14.6 hours). This is longer than the time held at 273 K during the DSC experiments (12 hours) and so it is possible that if held at 273 K for long enough in the DSC measurement, the crystallization of Form II may be observed. This would be complicated, unfortunately, by the transformation of Form II to Form I at 273 K. Additionally, the DSC results show some irreproducibility, with repeated experiments under the same conditions producing varying crystallization results, as is often the case in polymorphic systems. This demonstrates that a high degree of care must be taken when investigating crystallization from a super-cooled melt.

5.4 - Conclusions

Although pharmaceutical applications of Form II of *rac*-ibuprofen are necessarily limited by the fact that its melting point is below ambient temperature, the results reported here are nevertheless significant within the broader context of understanding the phase behaviour and polymorphism in the *rac*-ibuprofen system. Indeed, a significant observation from this work concerns the kinetic stability of supercooled liquid *rac*-ibuprofen, which had previously not been reported to undergo a transformation to a crystalline phase within the temperature range to which pharmaceuticals are typically subjected. In contrast, this work has demonstrated that maintaining supercooled liquid *rac*-ibuprofen at 273 K for less than a day is sufficient to lead to crystallization of Form II (followed, after a further period of time, by the formation of Form I *via* a solid-state polymorphic transformation). Importantly, this work has shown that low-temperature quenching of amorphous *rac*-ibuprofen is *not* a prerequisite for the crystallization of Form II. In more general terms, the observations reported here may also have relevance to other systems for which low-temperature quenching of supercooled liquid phases is used as a strategy to produce specific crystalline polymorphs (such as *m*-toluidine[138]).

Chapter 6: Expanding the Solid-State Landscape of L-Phenylalanine: Discovery of Polymorphism, New Hydrate Phases and Rationalization of Hydration/Dehydration Processes

6.1 - Introduction

Phenylalanine (Phe), shown in Figure 6.1, is one of the 20 directly genetically-encoded amino acids (those encoded directly in DNA by a codon). It is also one of the essential amino acids for humans, i.e., humans are unable to biosynthesize phenylalanine. As in the case of all amino acids other than glycine, Phe is chiral and exists as both an L- and a D-enantiomer.

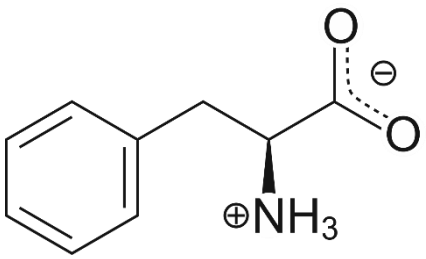

Figure 6.1: *Molecular structure of L-Phe.*

Phenylalanine is used industrially in the production of the artificial sweetener aspartame (Figure 6.2), the methyl ester of the dipeptide of L-aspartic acid and L-phenylalanine. Both an anhydrous solid form[65] and a hydrated solid form[66] of L-Phe have been reported. The crystal structure of enantiomerically pure Phe is known[65] (with further information given below), while, prior to this work, there was no known crystal structure for any L-Phe hydrate phase. During the production of L-Phe for use in aspartame synthesis, it is highly desirable to crystallize L-Phe as the anhydrous form,[66] due to the better separation and handling properties when compared to the hydrate. Patents exist on the methods for preferential crystallization of the anhydrous form.[144]

There has been much confusion surrounding the occurrence of polymorphism for phenylalanine. Multiple structure entries exist for enantiomerically pure phenylalanine in the CSD.[145] However, only one of these entries contains atomic coordinates[65] (in this case, determined for D-Phe, reference code SIMPEJ). The other entries (reference codes QQQAUJ, QQQAUJ01 and QQQAUJ02), all reported by the same author,[146,147] only provide sets of unit cell parameters (unrelated to those of SIMPEJ), with QQQAUJ02

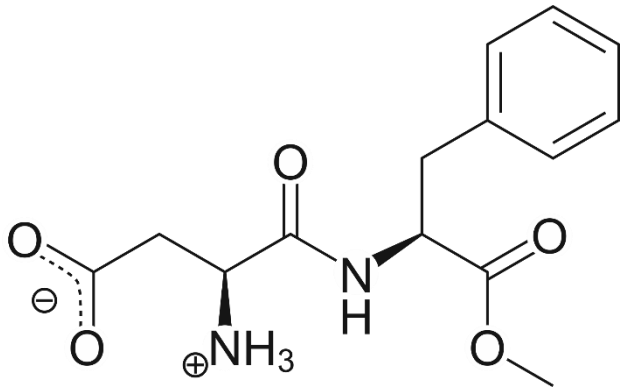

Figure 6.2: *Molecular structure of aspartame, an artificial sweetener.*

stated to be a redetermination of QQQAUJ. Significantly, the presence of multiple unit cells seems to suggest the existence of polymorphism. It should be noted that recently the crystal structure of enantiomerically pure Phe (reported Weissbuch *et al*.[65]) has been called into question.[148] King *et al*. have suggested that the previously reported structure[65] is of too high a symmetry, and propose that the symmetry is described by the primitive space group *P*2 rather than the *c*-centred space group *C*2, based on the fact that the diffraction pattern contains weak peaks that are unaccounted for by the *C*2 structure.

Work by Frey *et al*.,[67] using solid-state ^{13}C NMR, found that two samples of L-Phe, one crystallized from water and the other crystallized from a water/ethanol mixed solvent, had different spectra, indicating that they were different crystalline forms. No identification of these phases was made, other than the report of their ^{13}C NMR spectra and the fact that they contain L-Phe.

The work described here was carried out with the aim of investigating the existence of hydrate phases and the possibility of polymorphism in L-Phe. Any new phases would subsequently be characterized and the crystal structures of these new phases determined directly from powder XRD data. The observation of two distinct crystalline forms by Frey *et al*. was used as the starting point for experimentation.

6.2 - Experimental Details

All experiments were carried out using a sample of L-Phe purchased from Sigma-Aldrich (purity ≥ 98%), without further purification. This material was shown by powder XRD to be a monophasic sample of the known (anhydrous) form of L-Phe. Samples of L-Phe hydrates were crystallized from aqueous solution. Excess L-Phe

(above the solubility of L-Phe in water at 20 °C, *ca.* 50 mg of L-Phe per g of water) was mixed with water and heated, using an oil bath, to 80 °C to allow for complete dissolution, before removing from the bath and allowing to cool to ambient temperature (at which the solution is supersaturated).

Powder XRD measurements were carried out on two Bruker D8 diffractometers: one in transmission mode and one in reflection mode (both using Ge monochromated Cu Kα_1 radiation). For the purpose of "fingerprinting" the solid phases prepared in this work, powder XRD measurements were performed in transmission mode and a hygrometer was used to measure relative humidity (RH) levels within the diffractometer cabinet. The temperature was held constant at 21 °C and the RH was found to vary between 30% and 80% due to changes in atmospheric conditions. These measurements were carried out on samples held flat between two pieces of tape (foil-type sample holder). With this type of sample holder, the sample is not entirely sealed and may be susceptible to changes in atmospheric conditions. High quality powder XRD data, suitable for structure determination, were recorded on samples held within glass capillaries. These capillaries were flame sealed and hence were isolated from the external atmosphere, allowing the relative humidity level within the capillary to remain constant. Powder XRD data were also recorded on a sample in reflection mode. In this case, the sample was held within an indentation in a copper disk, seated in a silver-coated copper cup. The sample was held at 294 K under vacuum, using an Oxford Cryosystems Phenix temperature controller. This set-up allowed powder XRD data for the sample to be measured under entirely anhydrous conditions.

Solid-state NMR measurements were carried out on an 850 MHz Bruker AVANCE III spectrometer at the UK 850 MHz Solid-State NMR Facility (^{13}C Larmor frequency, 213.81 MHz, 12 kHz magic angle spinning frequency). High resolution ^{13}C solid-state NMR spectra were recorded using ramped ^{1}H → ^{13}C cross-polarization. DVS measurements were carried out at 26.5 °C using a DVS Advantage 1 instrument (Surface Measurement Systems Ltd., London, U.K.). The sample was placed in a glass pan and held at a RH of 0% for two hours to allow an equilibrium moisture content to be established. The RH was then changed incrementally in 5% steps every hour from 0 to 90% and then back to 0%. The mass of the sample was recorded as a function of time and RH. TGA measurements were carried out using a Perkin-Elmer Pyris 6 instrument, operated with a scan rate of 10 °C/min and a nitrogen purge gas.

6.3 - Results and Discussion

Visual examination of polycrystalline samples obtained by crystallization of L-Phe from water revealed two distinctly different types of crystal morphology, suggesting the possible existence of two different phases. In one case, the crystals were large and block-like, while, in the other case, the entire solution appeared to crystallize as a single solid mass composed of very fine fibre-like crystallites and containing a significant amount of water. Formation of the fibrous morphology was found to be favoured by crash cooling of the aqueous solution. Slow, controlled cooling using an incubator (e.g., from 85 °C to 25 °C, over twelve hours) was found to produce either the large block-like crystals or the fine fibre-like crystallites (varying between batches) and in some cases, both morphologies concomitantly.

Initially, powder XRD patterns were recorded for samples containing only crystallites with one type of morphology (i.e., the samples either comprised entirely block-like crystals or entirely fibrous crystals). It was found that the two morphologies gave rise to distinct powder XRD patterns. On this basis, the block-like crystals were identified as the known (anhydrous) phase of L-Phe. This phase was found to be indefinitely stable under dry, ambient conditions. In contrast, for samples containing the fibrous morphology, two different powder XRD patterns were observed. When the powder XRD data were recorded using a sample held between two pieces of tape (and, therefore, not entirely sealed from the atmosphere), the pattern observed at a given time was found to correlate with the RH within the diffractometer cabinet and interconversion between the two powder XRD patterns was observed occasionally. A changeover between these two powder XRD patterns was observed at *ca*. 60% RH (at 21 °C). The observation of this change in powder XRD pattern with changing RH indicates a change in solid phase and these phases are termed at this stage as a "low-humidity" form and a "high-humidity" form. No change in the powder XRD pattern of the block-like crystals (i.e., the known form of L-Phe) was observed with changes in RH.

Both the low-humidity and high-humidity forms were found to be stable when sealed in glass capillaries and high-quality powder XRD data were recorded for samples held in this manner (Figure 6.3). The high-humidity form was maintained under high humidity conditions prior to being packed into three glass capillaries with a small

amount of excess water (to ensure a high RH within the capillaries), before flame sealing. The low-humidity form was kept in a desiccator containing silica gel drying agent, before being packed into three glass capillaries and flame sealed. In each case, the powder XRD patterns of the low-humidity form and high-humidity form recorded in this manner matched those recorded below 60% RH and above 60% RH, respectively, using the foil-type sample holder.

High-resolution solid-state ^{13}C NMR spectra were recorded for the low-humidity and high-humidity forms, and for the previously known anhydrous form of L-Phe. The high-humidity form was stored in the presence of excess water until packed into the NMR rotor, while the low-humidity form was stored with silica gel drying agent for several days before packing into the NMR rotor. The NMR rotor was sealed during the measurement on each sample and no evidence for interconversion between the high-humidity and low-humidity forms was observed during acquisition of data. The solid-state ^{13}C NMR spectra are shown in Figure 6.4. From comparison of these spectra with those reported by Frey *et al*.,[67] it is clear that the sample crystallized from water was the known anhydrous form of L-Phe, while the sample crystallized from water/ethanol corresponds to the low-humidity form described in the present work.

The solid-state ^{13}C NMR spectrum acquired for the known form of L-Phe in the present work displays at least three distinct isotropic peaks for the α-carbon environment of the L-Phe molecule (Figure 6.5), suggesting that the crystal structure contains at least three independent molecules of L-Phe. This result contrasts with the crystal structure previously published for this form, which contains two independent molecules of L-Phe. However, as mentioned in Section 6.1, King *et al*.[148] have proposed a new structure of lower symmetry for L-Phe. This structure contains four independent molecules of L-Phe and is, thus, fully consistent with the ^{13}C NMR spectrum recorded in this work, though it cannot be definitively stated that other aspects of the structure proposed by King *et al*.[148] are confirmed by the NMR data (and, consequently, it cannot be stated that this new structure is correct in its entirety). The solid-state ^{13}C NMR data for both the low-humidity and high-humidity forms indicates the presence of at least two independent molecules of L-Phe within each of the crystal structures.

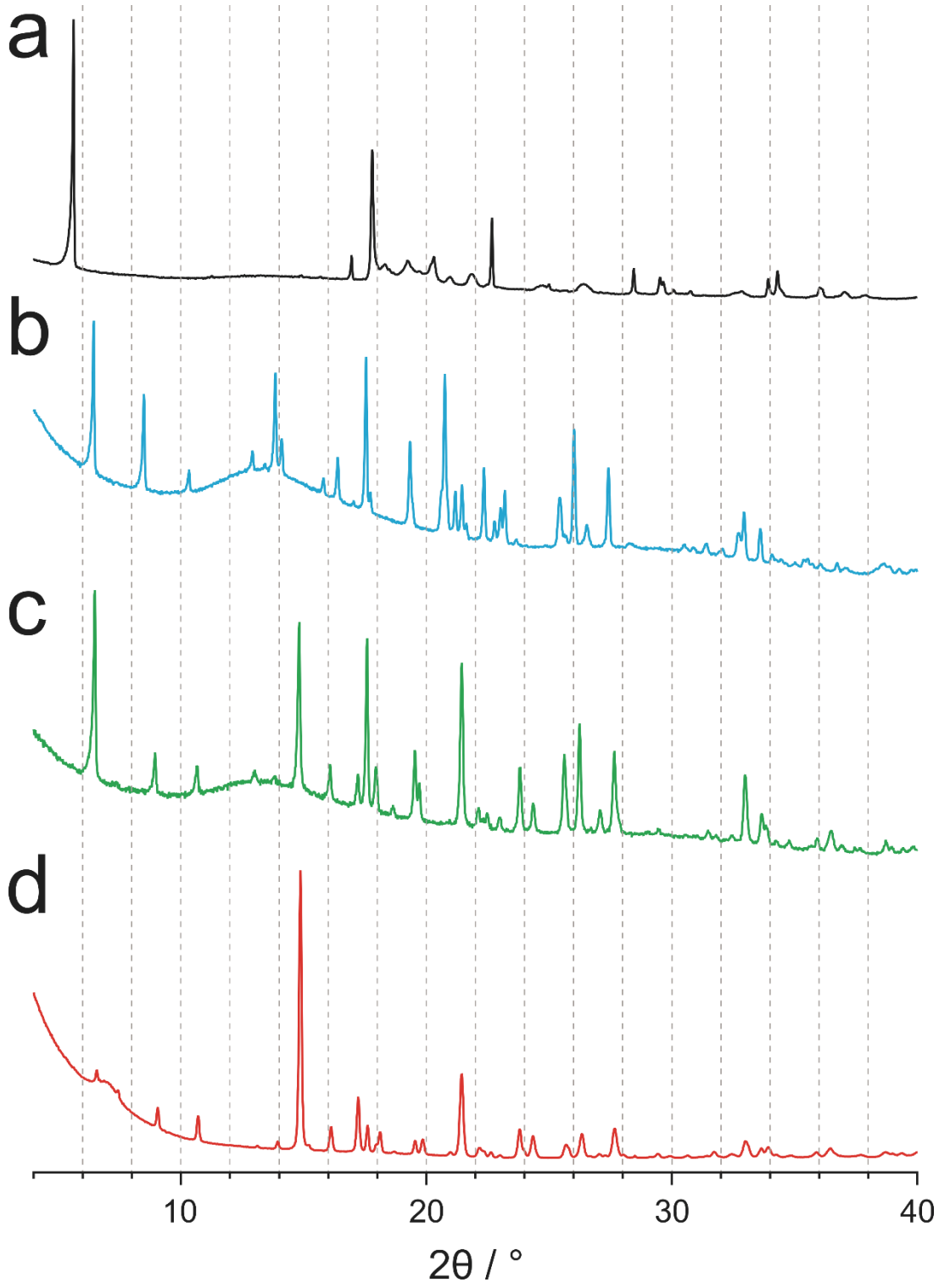

Figure 6.3: *Powder XRD patterns recorded for (a) the previously known anhydrous form (polymorph I) of* L*-Phe, (b) the high-humidity form (monohydrate) of* L*-Phe, (c) the low-humidity form (hemihydrate) of* L*-Phe and (d) the new anhydrous form (polymorph II) of* L*-Phe.*

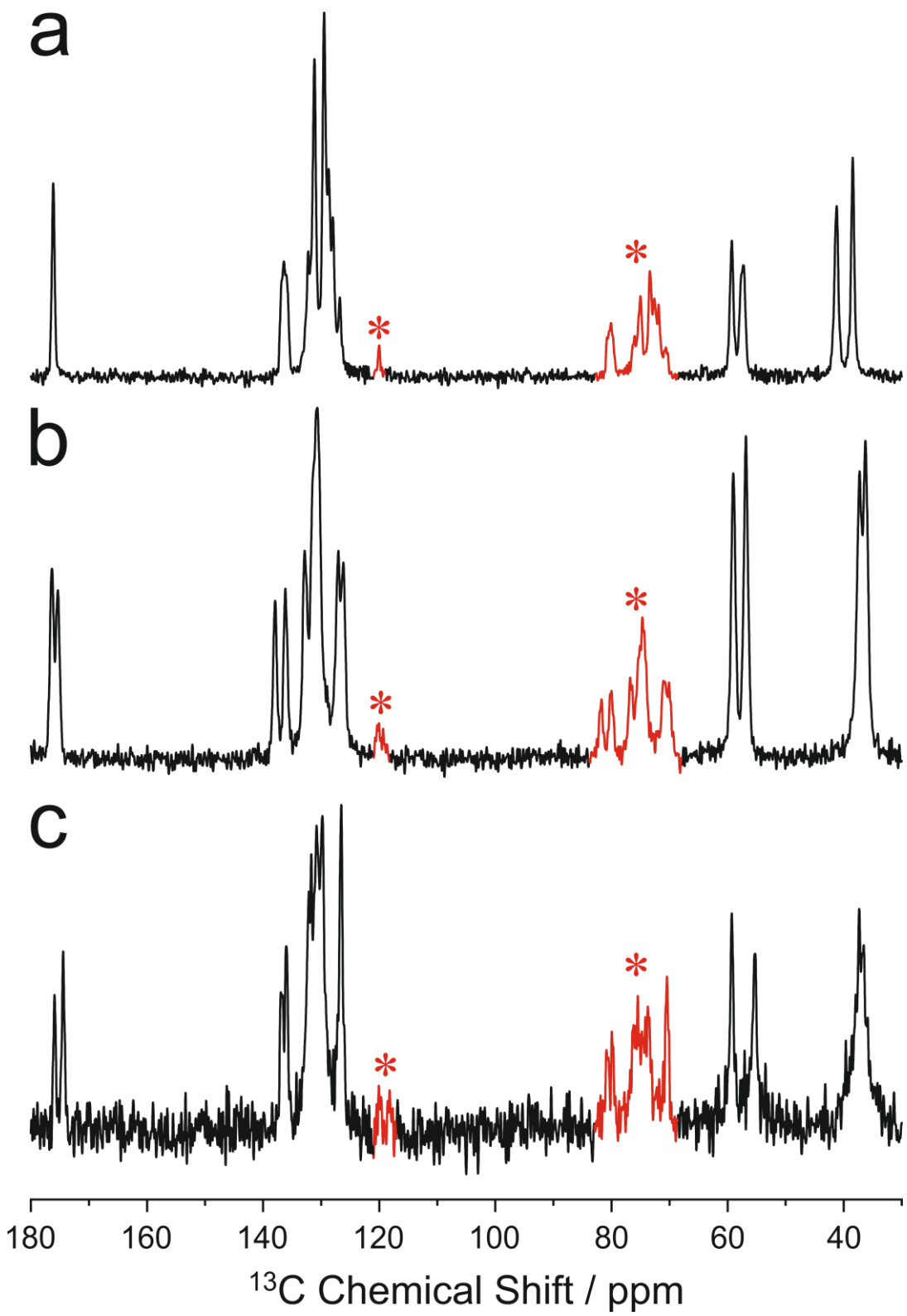

Figure 6.4: *High resolution solid-state ^{13}C NMR spectra of (a) the previously known anhydrous form (polymorph I) of L-Phe, (b) L-Phe hemihydrate and (c) L-Phe monohydrate. Spinning side bands are marked in red.*

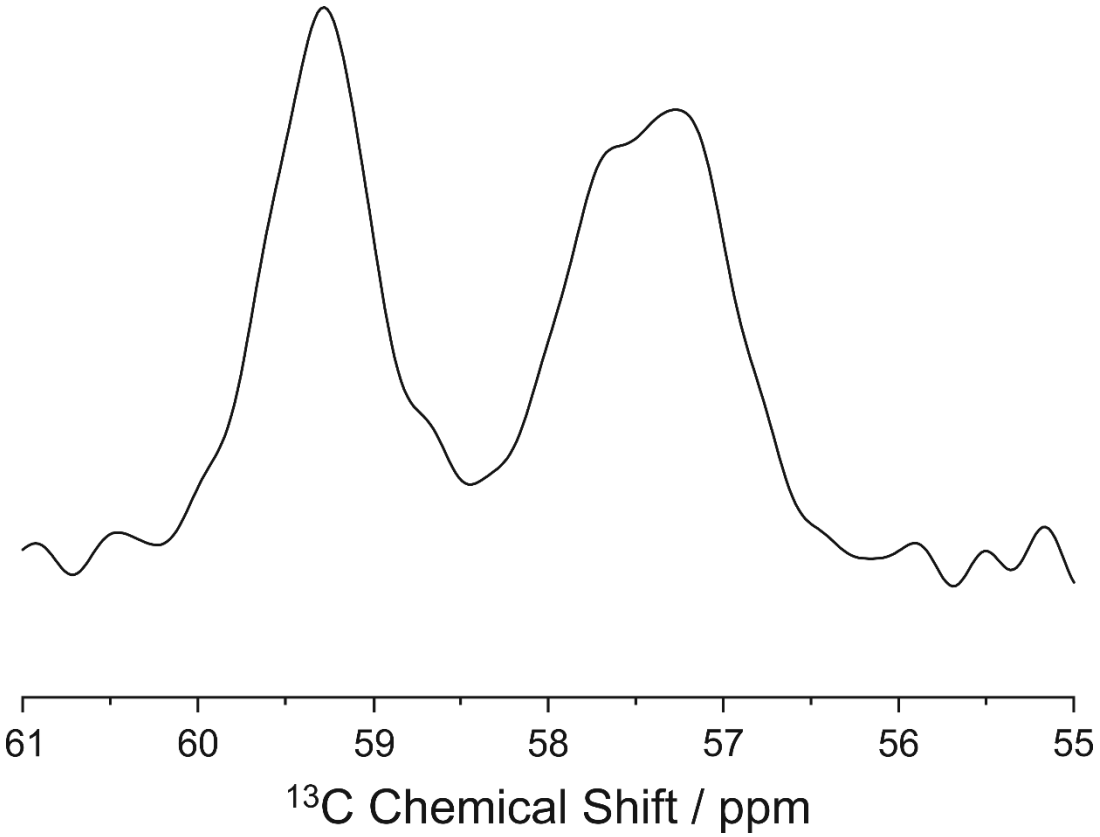

Figure 6.5: *High resolution solid-state ^{13}C NMR spectrum of the previously known anhydrous form (polymorph I) of L-Phe, expanded to show the presence of at least three peaks in the α-carbon region of the spectrum.*

To determine the water content of the high-humidity and low-humidity forms, dynamic vapour sorption (DVS) measurements were carried out. The sample consisting of crystallites of fibrous morphology (crystallized from water) was initially dried, under vacuum, in the presence of phosphorus pentoxide. The results of the DVS experiment are plotted in Figures 6.6 and 6.7. As the RH is increased from 0%, a rapid absorption of water is observed. At *ca*. 5% RH, an uptake corresponding to *ca*. 0.25 equivalents of water has occurred. With further increase in RH, there is a more gradual uptake of water and by *ca*. 60%, close to 0.5 equivalents of water have been absorbed. Increasing the RH further to 65%, a second stage of water absorption occurs, with an abrupt increase in water uptake corresponding to a further 0.5 equivalents of water, i.e., a total increase of 1 equivalent of water, compared to the material at 0% RH. On further increasing the RH from 65% to 90%, there is essentially no further uptake of water.

On decreasing the RH from 90%, the events described previously occur in reverse. It should be noted, however, that hysteresis is observed in the abrupt event that corresponds to a decrease in water content from 1 equivalent to 0.5 equivalents. In the

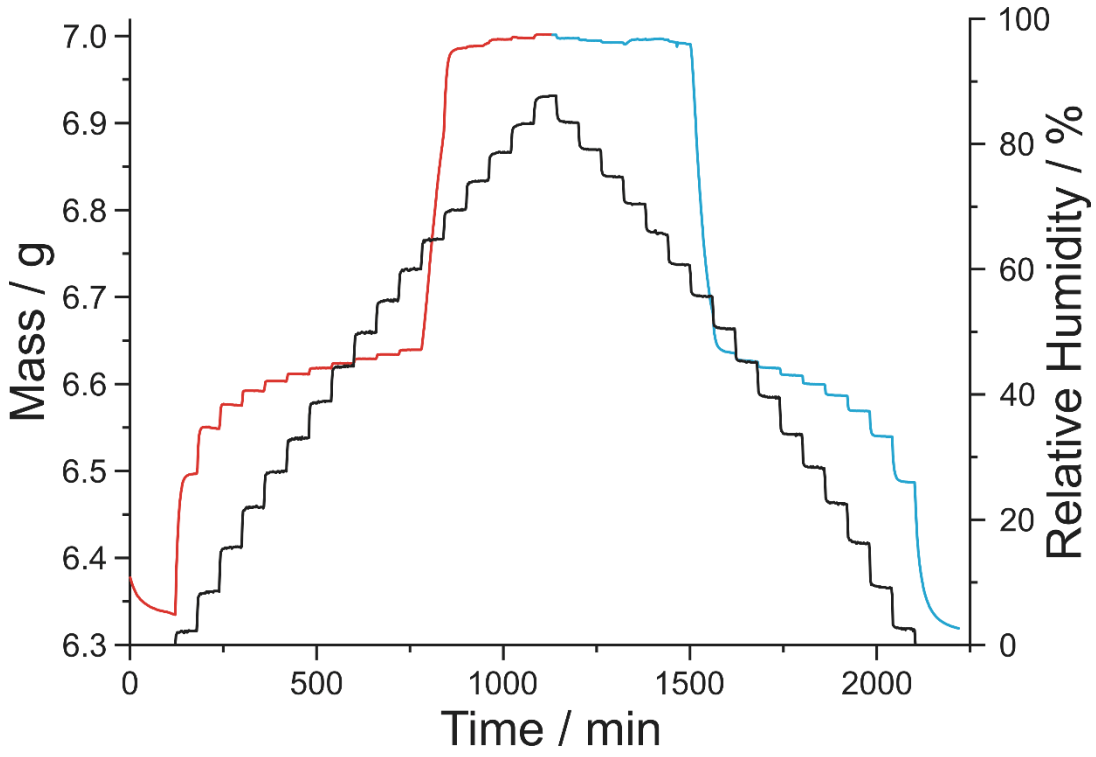

Figure 6.6: *Dynamic vapour sorption (DVS) experiment demonstrating the hydration behaviour of* L*-Phe. Shown in black is the stepwise change in relative humidity over time. Shown in colour is the mass of the sample recorded on increasing (red) and decreasing (blue) the relative humidity.*

desorption cycle, this event occurs at *ca*. 55% RH (compared to *ca*. 65% RH in the absorption cycle).

By defining the stoichiometry of the observed phases as L-Phe$(H_2O)_x$, it is clear from the DVS results that by starting from an anhydrous phase ($x = 0$) at 0% RH, a non-stoichiometric hydrate with variable water content ranging from a quarter-hydrate to a hemihydrate ($0.25 \leq x \leq 0.5$) exists at low RH (lower than 55 to 65% RH), while a stoichiometric monohydrate ($x = 1$) exists at high RH. TGA analysis of the low-humidity form (Figure 6.8) indicates the loss of *ca*. 0.5 equivalents of water upon heating, confirming that the non-stoichiometric, low-humidity form includes a hemihydrate as one end-member of the composition range. Henceforth, the low-humidity form is referred to as the hemihydrate (non-stoichiometric, with actual water content $0.25 \leq x \leq 0.5$) and the high-humidity form is referred to as the monohydrate. As noted above, no change in the powder XRD pattern of the previously known form of anhydrous L-Phe is observed with changes in humidity. Thus, the phase present at 0% RH in the DVS measurements must represent a new polymorph of L-Phe, henceforth

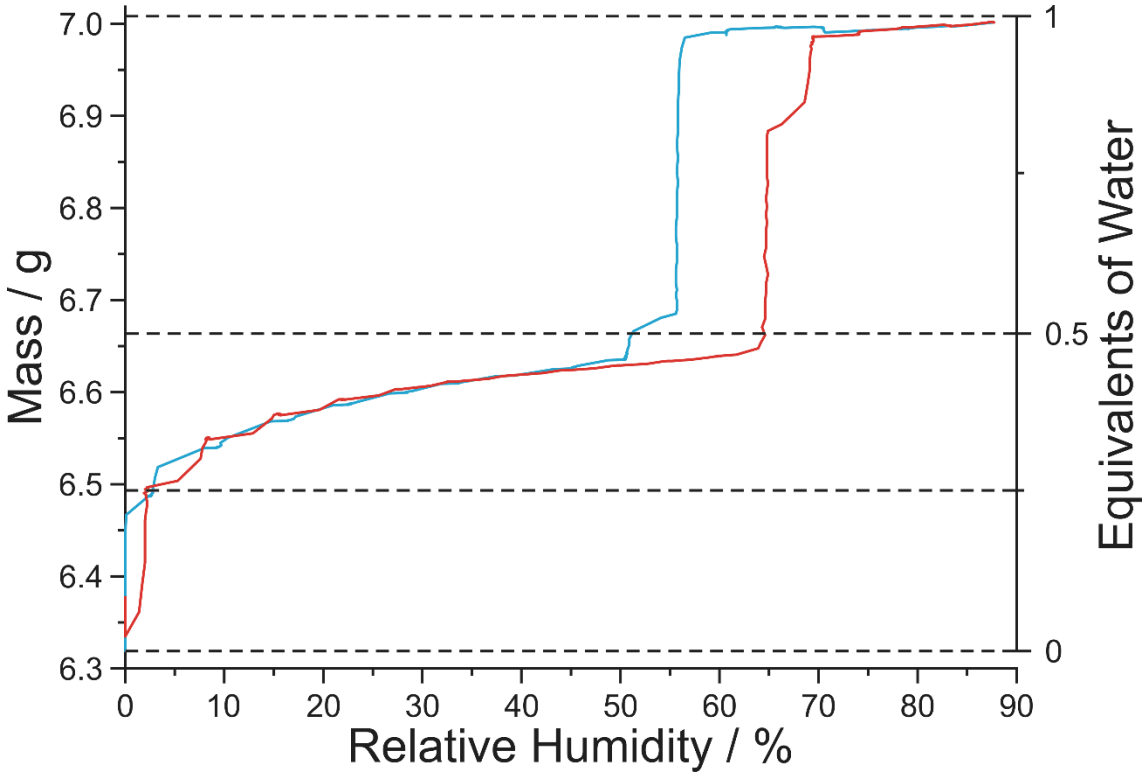

Figure 6.7: *A replotting of Figure 6.6, showing the change in sample mass with relative humidity in the DVS experiment. The data recorded on increasing humidity are shown in red and the data recorded on decreasing humidity are shown in blue. Represented by dashed lines are the mass values for structures containing 0, 0.25, 0.5 and 1 equivalent of water, i.e., anhydrous, quarter-hydrate, hemihydrate and monohydrate forms (taking the lowest mass value during the experiment, 6.319 mg, to represent the anhydrous form).*

designated polymorph II. The previously known anhydrous form of L-Phe is designated polymorph I.

The crystal structures of the hemihydrate and monohydrate were determined directly from the powder XRD data recorded on the samples sealed within glass capillaries. Powder XRD data on polymorph II of L-Phe were recorded by holding a sample of the monohydrate under vacuum, within the Phenix temperature controller on the powder X-ray diffractometer in reflection mode. By subjecting the sample to vacuum (i.e., a very low humidity environment), polymorph II of L-Phe was formed. Details on the structure determination process for the three new phases are given in Section 6.4.

The three new crystal structures (polymorph II of L-Phe, L-Phe hemihydrate and L-Phe monohydrate) share several notable features (Figure 6.9, Table 6.1). All three

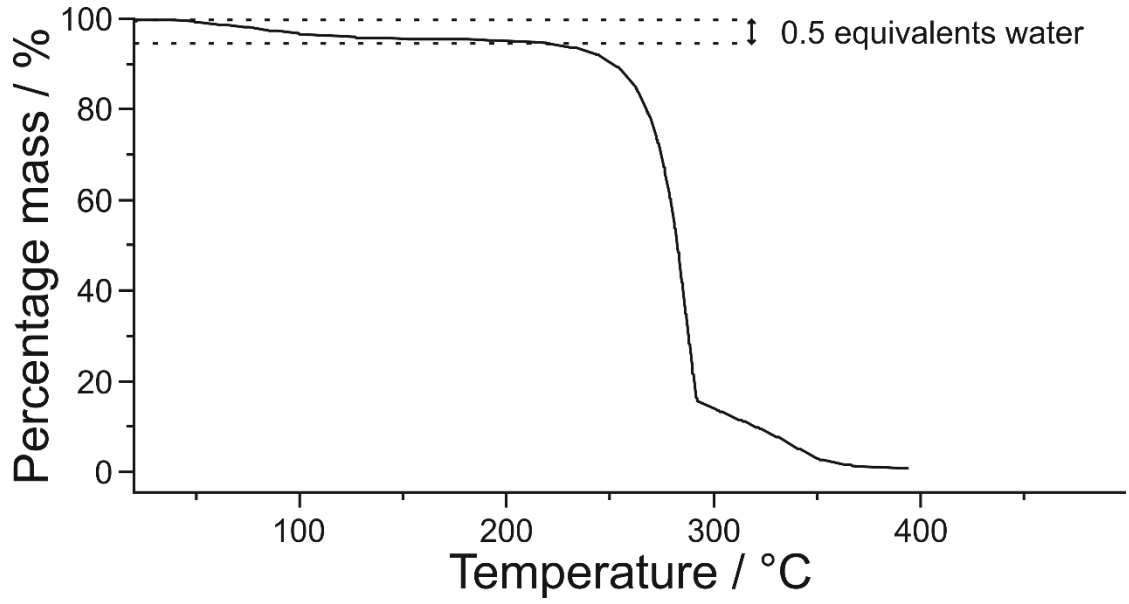

Figure 6.8: *Thermogravimetric analysis (TGA) of the low-humidity form. Dashed lines indicate the percentage mass difference expected for the loss of half an equivalent of water from the structure.*

structures can be described in terms hydrogen-bonded bilayers parallel to the *ab*-plane, containing the carboxylate and ammonium groups of the L-Phe molecules. In addition, in the hemihydrate and monohydrate structures, the water molecules are located within these hydrogen-bonded bilayers. The phenyl rings of the L-Phe molecules are located in the region between adjacent hydrogen-bonded bilayers. In addition, all three structures contain two crystallographically distinct molecules of L-Phe (as corroborated by solid-state ^{13}C NMR), with slightly different molecular conformations (the torsional angles in the two distinct L-Phe molecules in each structure differ by up to *ca*. 20°).

	Space Group	***a* / Å**	***b* / Å**	***c* / Å**	***β* / °**	**V / Å^3**
Monohydrate	$P2_1$	13.0075(4)	5.43017(11)	13.93996(33)	101.1125(14)	966.16(6)
Hemihydrate	$P2_1$	12.1112(5)	5.42130(17)	13.7691(5)	100.0115(35)	890.29(8)
Polymorph II	$P2_1$	12.063(11)	5.412(5)	13.676(13)	99.5976(26)	880.3(24)
Polymorph I	$C2$	8.804	6.041	31.564	96.6	1667.6

Table 6.1: *Unit cell parameters for L-Phe monohydrate, hemihydrate, anhydrous polymorph II and the previously known anhydrous polymorph I.*[65]

L-Phe hemihydrate and monohydrate can be described as channel hydrate structures. In each of these structures, the water molecules are present within channels parallel to the *b*-axis, located within the hydrogen-bonded bilayers. In the hemihydrate,

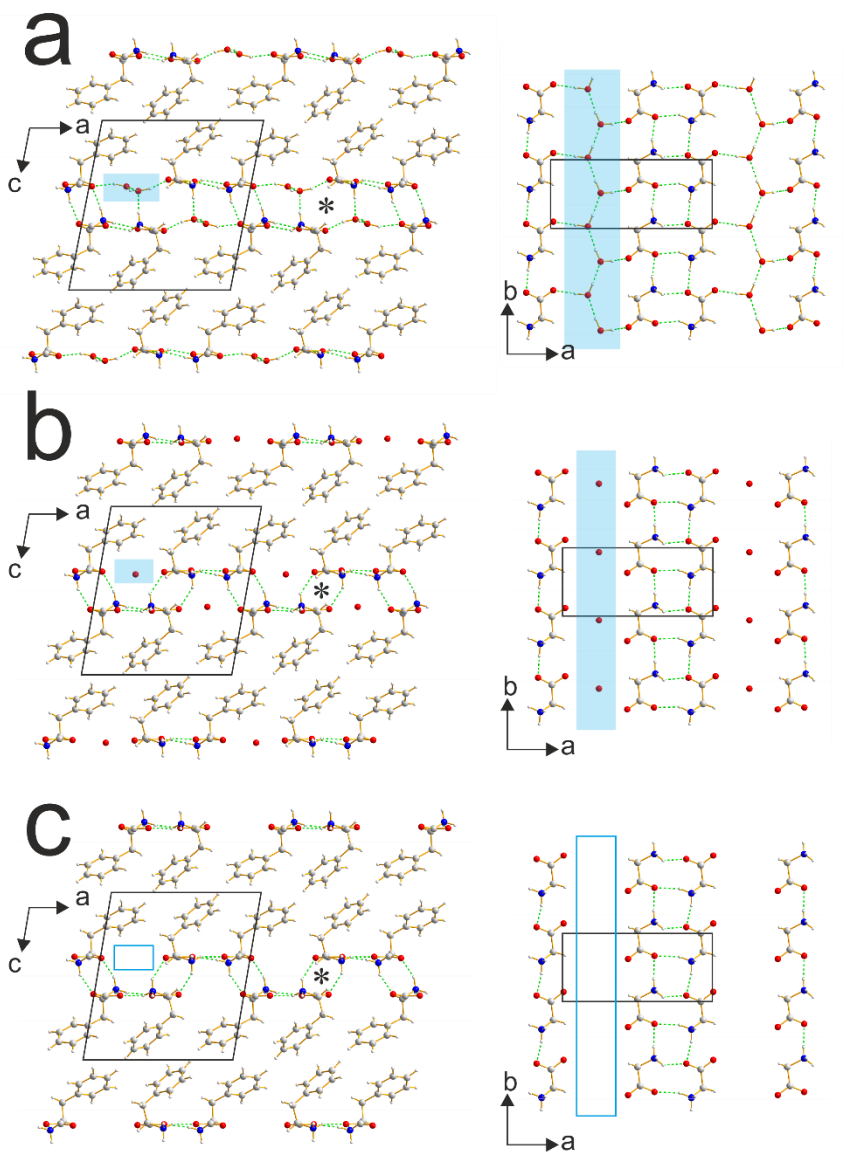

Figure 6.9: *Crystal structures of (a) the monohydrate phase of L-Phe, (b) the hemihydrate phase of L-Phe, and (c) the new anhydrous phase, polymorph II of L-Phe. In each case the view along the b-axis is shown on the left and the view along the c-axis is shown on the right (in this view, only one layer within the hydrogen-bonded bilayer is shown, with the phenyl rings of the L-Phe molecules omitted for clarity). Only one orientation of the hydrogen bonded water chain is shown in (a). In (a) and (b), the water channel (running parallel to the b-axis) is highlighted in cyan, while in (c), the empty channel is outlined in cyan. The helical hydrogen-bonded motif discussed in the text is marked with an asterisk.*

there is only a single crystallographically distinct water molecule. The distance between adjacent water molecules along the channel is too large to give rise to O–H···O hydrogen bonding between them (O···O distance: 5.42 Å, corresponding to the unit cell translation along the *b*-axis). On the other hand, the O···O distances (2.84 and 2.87 Å) between the water molecule and oxygen atoms of carboxylate groups in two different

L-Phe molecules may be interpreted as O–H···O hydrogen bonds. However, the $O_{COO}\cdots O_{water}\cdots O_{COO}$ angle (162.6°) is too large to allow relatively linear O–H···O hydrogen bonds to be formed simultaneously with both L-Phe molecules acting as acceptors. It is therefore likely that at the local level (in both spatial and temporal terms), each water molecule forms a strong and linear hydrogen bond with only one of the two acceptors, with the other hydrogen atom on the water molecule not engaged in any significant hydrogen-bonding interaction. There is likely to be significant disorder in this arrangement and, due to the uncertainty in the time-averaged locations of the hydrogen atoms of the water molecule, these hydrogen atoms were omitted from the final Rietveld refinement. The lack of multiple, simultaneously formed, strong hydrogen bonds involving water in this structure may explain the non-stoichiometry observed for the hemihydrate phase, i.e., the water molecules can escape relatively easily from the channel under low humidity conditions.

The monohydrate, as previously mentioned, also contains water molecules in channels parallel to the *b*-axis. In this case, there are two distinct water molecules in the crystal structure and they lie along the channels. The O···O distances between adjacent water molecules along the channel are 2.82 and 2.98 Å, corresponding to O–H···O hydrogen bonding between the water molecules. Thus, the water molecules form an O–H···O–H···O–H chain along the *b*-axis. These chains may run in either direction along the *b*-axis (i.e., either O–H···O–H···O–H or H–O···H–O···H–O), with the two possibilities only differing in the hydrogen atom positions (the positions of the oxygen atoms are identical in each case). The final Rietveld refinement of the monohydrate invoked disorder of these two orientations of the hydrogen bonded chain, with fractional occupancies of x_H and $1 - x_H$ for the hydrogen atoms in the positive and negative directions of the chain, respectively. During refinement, these occupancies did not depart significantly from the initial value of 0.5, indicating that the populations of each chain orientation are roughly equal. Each water molecule is also engaged in hydrogen bonding to L-Phe molecules. One water molecule is able to act as both the donor in an O–H···O hydrogen bond (O···O distance: 2.61 Å) to the carboxylate group of one L-Phe molecule and as an acceptor within an O···H–N hydrogen bond (O···N distance: 2.79 Å) to the ammonium group of a second L-Phe molecule. The other water molecule, however, only forms a single hydrogen bond to an L-Phe molecule, acting as the donor within an O–H···O bond (O···O distance: 2.81 Å) to an oxygen atom in a carboxylate group.

Another notable difference between the structures of the monohydrate and hemihydrate concerns the nature of the helical hydrogen-bonded motif that follows the 2_1 screw axis (parallel to the *b*-axis) in each structure. In the hemihydrate, this helical motif involves solely N–H···O hydrogen bonds between L-Phe molecules in the two layers of the hydrogen-bonded bilayer while, in the monohydrate, the L-Phe molecules are instead involved in N–H···O–H···O_{COOH} hydrogen bonds, where the O–H bond of an intervening water molecule forms part of the helical motif.

The crystal structure of polymorph II of L-Phe is very similar to that of the hemihydrate and there are only minor displacements in the positions of the L-Phe molecules between the two structures. Due to the fact that differences between the two structures are only minor, polymorph II of L-Phe may be referred to as an "isomorphic desolvate"[149] of the hemihydrate. The presence of channel structures occupied by water in the monohydrate and hemihydrate, and the fact that the empty channels remain without collapse in polymorph II of anhydrous L-Phe, are completely consistent with the facile water absorption/desorption observed within this set of materials. It should be noted that the density of polymorph II of L-Phe (1.25 g cm^{-1}) is significantly lower than that of polymorph I of L-Phe (1.32 g cm^{-1}), which may suggest that polymorph II is less thermodynamically stable than polymorph I. The lower density of polymorph II is related to the presence of the empty channel structure, which is not present in the structure of polymorph I. The conversion of polymorph II to polymorph I has not been observed during this work (on the timescale of several days), indicating a kinetic barrier to the transformation. Exposure of polymorph II to the atmosphere leads to rapid and facile uptake of water (even at low RH, as shown in the DVS experiments), to give the hemihydrate or monohydrate depending on the humidity level.

Channel hydrates are a well-known class of hydrate structure and examples of such materials have been discussed in the literature.[150-153] Particularly relevant is the hydrate crystal structure of another amino acid, DL-proline monohydrate.[154] In this crystal structure, water molecules are located within channels and are hydrogen bonded both to each other and to the carboxylate groups of neighbouring proline molecules, strongly resembling the features of the structure of L-Phe monohydrate.

6.4 - Details of Structure Determination from Powder XRD Data

6.4.1 - Structure Determination of L-Phe Hemihydrate

The powder XRD pattern of L-Phe hemihydrate was indexed using the program TREOR[113], within the CRYSFIRE[106] program suite, with monoclinic metric symmetry and dimensions (following transformation into the standard form with the program PLATON[155,156]): a = 12.13 Å, b = 5.42 Å, c = 13.78 Å, β = 100.1° (V = 892.3 Å^3). From systematic absences, the space group was assigned as $P2_1$ and from density arguments the asymmetric unit was determined to contain two molecules of L-Phe (and therefore one of water). Le Bail fitting was performed on the powder XRD pattern, using the program GSAS,[107] achieving a high quality of fit (Figure 6.10(a), R_{wp} = 2.67%, R_p = 2.01%) and the refined cell and profile parameters were used in the subsequent structure solution calculations.

The program EAGER was used to carry out structure solution with 16 independent GA calculations performed. In total, 200 generations were carried out with a population of 200 structures and a total of 20 mating operations and 100 mutation operations were carried out per generation. One L-Phe molecule was represented by eight structural variables: two positional variables (in the space group $P2_1$, the origin can be fixed arbitrarily along the *b*-axis), three orientational variables and three torsional variables (Figure 6.11); the second L-Phe molecule was defined similarly but with three positional variables, allowing movement along the *b*-axis. The water molecule was defined using three positional and three orientational variables. Both L-Phe molecules were defined as zwitterions during structure solution. After 200 generations, the same good quality fit was found in eight of the 16 calculations and this was used as the starting point for Rietveld refinement.

Rietveld refinement was carried out using the program GSAS.[107] Standard restraints were applied to bond lengths and angles and planar restraints were used to maintain the planarity of the aromatic ring and the carboxylate group. These restraints were relaxed during the refinement procedure. The hydrogen-bonding network between ammonium and carboxylate groups was loosely restrained based on optimum hydrogen-bonding geometries. Intermolecular bond-length restraints were used to orient the ammonium group in order to give the optimum hydrogen-bonding environment. Three separate U_{iso} values were refined (one for each molecule) with the value of U_{iso} for the

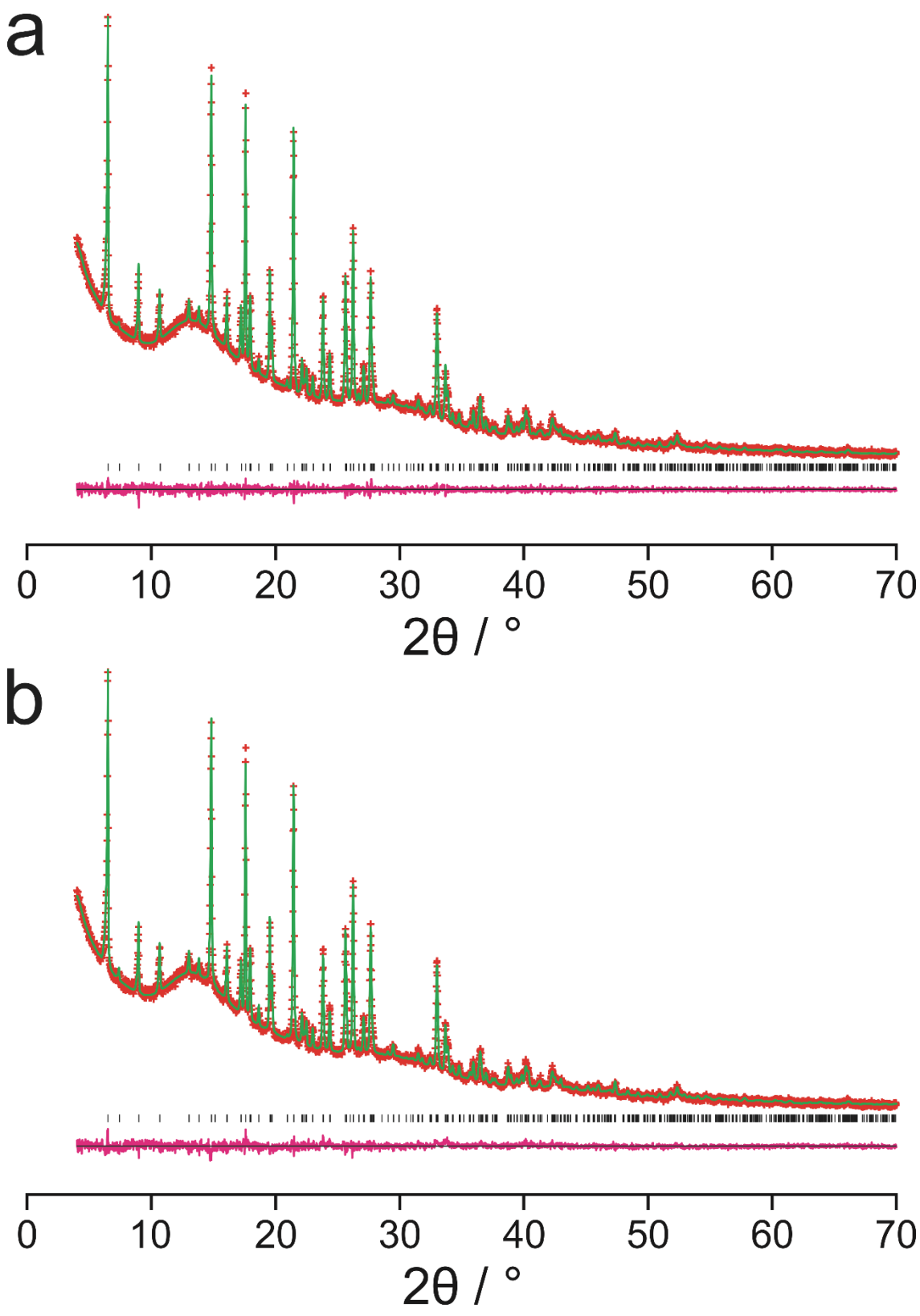

Figure 6.10: *(a) Le Bail fit and (b) Rietveld fit for powder XRD data recorded on L-Phe hemihydrate. The experimental data is shown as red crosses, the calculated fit as a green line and the difference between the two as a magenta line. Peak positions are displayed as black tick marks.*

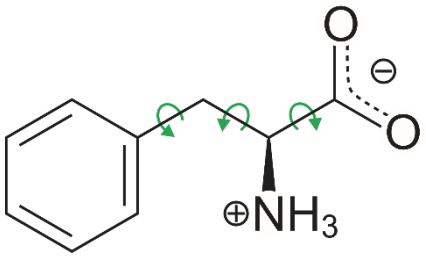

Figure 6.11: *The three torsional angles of L-Phe that were allowed to vary in the structure solution calculations.*

hydrogen atoms set to be 1.2 times that of the non-hydrogen atoms. Due to uncertainty in the time-averaged positions of the hydrogen atoms of the water molecules in this structure (caused by the likelihood of significant disorder), the hydrogen atoms of the water molecule were omitted from the final Rietveld refinement. Due to the non-stoichiometry of the hemihydrate, the occupancy of the water molecule was allowed to vary. However, the occupancy was found to refine to a value very close to 1 and so was fixed at 1 in the final refinement. No correction for preferred orientation was used. The final Rietveld refinement gave a high quality fit to the powder XRD data [Figure 6.10(b), R_{wp} = 2.96%, R_p = 2.21%] with the following refined parameters: a = 12.1112(5) Å, b = 5.42130(17) Å, c = 13.7691(5) Å, β = 100.0115(35)°; V = 890.29(8) Å^3 (space group $P2_1$; 2θ range, 4° to 70°; 3867 profile points; 170 refined variables).

6.4.2 - Structure Determination of L-Phe Monohydrate

The powder XRD pattern of L-Phe monohydrate was indexed using the program DICVOL91[157], within the CRYSFIRE[106] program suite, as a monoclinic cell and dimensions: a = 13.05 Å, b = 5.44 Å, c = 13.98 Å, β = 101.2° (V = 973.5 Å^3). From systematic absences, the space group was assigned as $P2_1$ and from density arguments the asymmetric unit was determined to contain two molecules of L-Phe (and therefore two of water). Le Bail fitting was performed on the powder XRD pattern, using the program GSAS,[107] achieving a high quality of fit [Figure 6.12(a), R_{wp} = 1.41%, R_p = 1.06%] and the refined cell and profile parameters were used in the subsequent structure solution calculations.

The program EAGER was used to carry out structure solution with 16 independent GA calculations performed. In total, 400 generations were carried out with a population of 200 structures and a total of 20 mating operations and 100 mutation

operations were carried out per generation. One L-Phe molecule was represented by eight structural variables: two positional variables (in the space group $P2_1$, the origin can be fixed arbitrarily along the *b*-axis), three orientational variables and three torsional variables (Figure 6.11); the second L-Phe molecule was defined similarly but with three positional variables, allowing movement along the *b*-axis. Each water molecule was defined using three positional and three orientational variables. Both L-Phe molecules were defined as zwitterions during structure solution. After 400 generations, the same good quality fit was found in four of the 16 calculations and this structure was used as the starting point for Rietveld refinement.

Rietveld refinement was carried out using the program GSAS.[107] Standard restraints were applied to bond lengths and angles and planar restraints were used to maintain the planarity of the aromatic ring and the carboxylate group. These restraints were relaxed during the refinement procedure. The hydrogen-bonding network between ammonium and carboxylate groups was loosely restrained based on optimum hydrogen-bonding geometries. Intermolecular bond-length restraints were used to orient the ammonium group in order to give the optimum hydrogen-bonding environment. Four separate U_{iso} values were refined (one for each molecule) with the value of U_{iso} for the hydrogen atoms set to be 1.2 times that of the non-hydrogen atoms. Disorder of the two possible orientations of the O–H···O–H···O–H hydrogen-bonded chain along the *b*-axis was included with fractional occupancies of x_H and $1 - x_H$ for the hydrogen atoms in the positive and negative of directions of the chain, respectively. During refinement, these occupancies were not found to vary significantly from 0.5 and so each occupancy was fixed to 0.5 in the final refinement. No correction for preferred orientation was used. The final Rietveld refinement gave a high quality fit to the powder XRD data [Figure 6.12(b), $R_{wp} = 1.60\%$, $R_p = 1.18\%$], with the following refined parameters: $a = 13.0075(4)$ Å, $b = 5.43017(11)$ Å, $c = 13.93996(33)$ Å, $\beta = 101.1125(14)°$; $V = 966.16(6)$ Å^3 (space group $P2_1$; 2θ range, 4° to 70°; 3867 profile points; 183 refined variables).

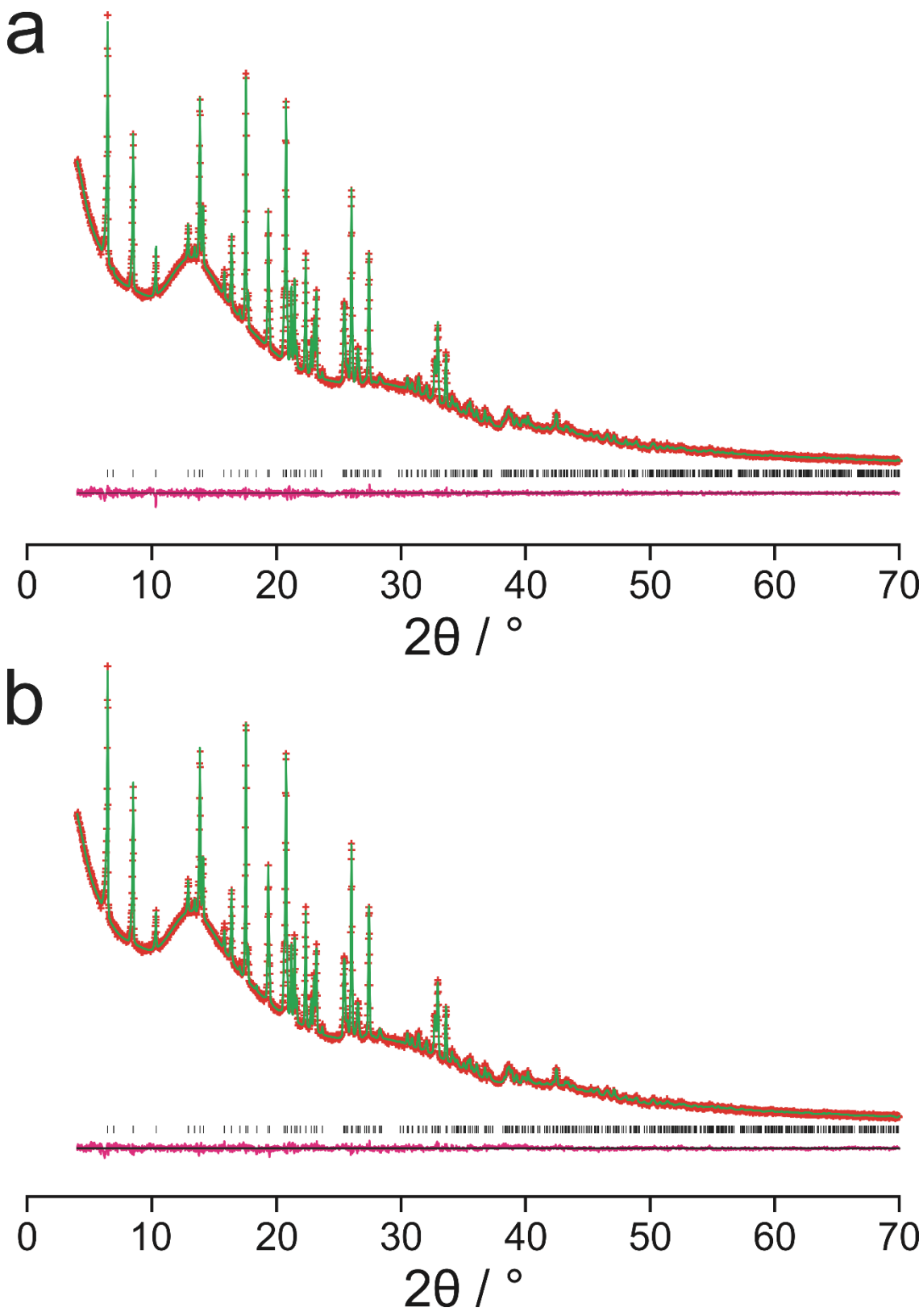

Figure 6.12: *(a) Le Bail fit and (b) Rietveld fit for powder XRD data recorded on L-Phe monohydrate. The experimental data is shown as red crosses, the calculated fit as a green line and the difference between the two as a magenta line. Peak positions are displayed as black tick marks.*

6.4.3 - Structure Determination of Polymorph II of L-Phe

The structure of polymorph II of L-Phe of was determined using the structure of the hemihydrate as a starting point. Le Bail fitting to the powder XRD data gave a good quality of fit [Figure 6.13(a), R_{wp} = 3.38%, R_p = 2.35%]. During Rietveld refinement, the occupancy of the water molecule from the hemihydrate phase was allowed to vary. This occupancy was found to refine to a small, negative value and so was subsequently fixed at zero, corresponding to an anhydrous phase. Preferred orientation was taken into account using the March-Dollase function[114,115] and a correction for surface roughness was included using a normalized form of the function proposed by Suortti.[158] Two separate U_{iso} values were refined (one for each molecule) with the value of U_{iso} for the hydrogen atoms set to be 1.2 times that of the non-hydrogen atoms. The final Rietveld refinement gave a good fit to the data [Figure 6.13(b), R_{wp} = 4.50%, R_p = 3.01%] with the following refined parameters: a = 12.063(11) Å, b = 5.412(5) Å, c = 13.676(13) Å, β = 99.5976(26)°; V = 880.3(24) Å^3 (space group $P2_1$; 2θ range, 6.25° to 41.75°; 2196 profile points; 160 refined variables).

6.5 - Conclusions

The characterization of three new solid phases of L-Phe, including two hydrate forms and a new polymorph of anhydrous L-Phe, along with the rationalization of the transformation processes between them, add clarity to the previously confused topic of the solid-state forms of L-Phe. The monohydrate and hemihydrate structures determined in this work represent the first reported crystal structures of hydrated forms of L-Phe. Analysis of the CSD indicates that, prior to the present work, five of the 20 directly genetically encoded amino acids (arginine,[159] asparagine,[160] aspartic acid,[161] proline[162] and serine[163]) were known to form hydrate structures as the enantiomerically pure amino acid. Four cases (serine,[164] arginine,[165,166] glutamic acid[167] and proline[154,168]) of hydrate structures for the racemic amino acids have been reported (with both a monohydrate[166] and a dihydrate[165] reported for DL-arginine). L-Phe represents the first enantiomerically pure amino acid for which more than one hydrate phase has been discovered and structurally characterized. In addition, the discovery of polymorphism within L-Phe represents the sixth case within the 20 directly genetically encoded amino acids for which polymorphism has been confirmed by crystal structure determination.

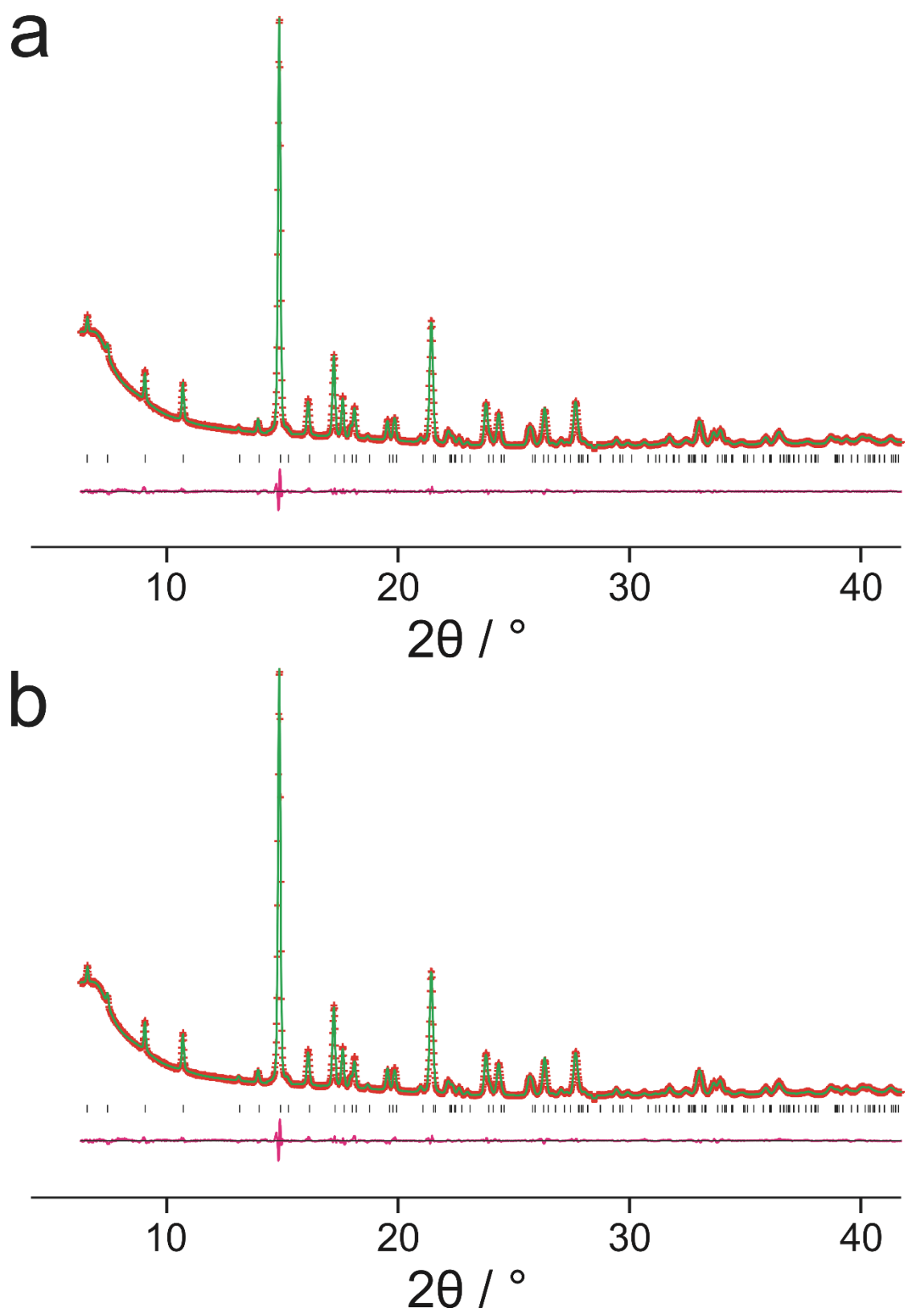

Figure 6.13: *(a) Le Bail fit and (b) Rietveld fit for powder XRD data recorded on Polymorph II of L-Phe. The experimental data is shown as red crosses, the calculated fit as a green line and the difference between the two as a magenta line. Peak positions are displayed as black tick marks.*

Chapter 7: Future Work

While the work in this thesis progresses the current knowledge on several specific organic solid-state systems, many questions are raised which must, in the future, be answered. These issues and the possibilities for future work are now discussed.

In the work conducted on *m*-ABA in Chapter 3, three new polymorphs were discovered and characterized (including crystal structure determination of each of these new polymorphs directly from powder XRD data). However, the crystal structure of the previously reported Form I of *m*-ABA remains unknown. Future work must focus on determination of the crystal structure of Form I, with special attention given to the currently intractable indexing stage. Possible avenues of this study include recording further powder XRD data at different temperatures (with the aim of reducing the high degree of peak overlap found at ambient temperature in the region $20° \leq 2\theta \leq 35°$) and, perhaps, the use of other experimental techniques, e.g., electron diffraction. In addition, the relative thermodynamic stabilities of Form I and Form IV are currently unknown, as slurry experiments result in the formation of Form III, the most stable (currently known) polymorph of *m*-ABA at ambient temperature. The CLASSIC NMR technique developed during the work presented in Chapter 3 represents a powerful new tool in the study of crystallization processes. By allowing the evolution of both the solid and liquid phases to be studied during a single crystallization experiment, changes in both the solid forms present (including the potential to discover novel, transient forms) and in the aggregation behaviour of the solution may be observed. It may be expected that the CLASSIC NMR technique will, in the future, be applied to reveal significant new insights on a range of systems of interest.

In Chapter 4, up to three new solid phases of TPPO were discovered using the CLASSIC NMR method. While a new solid phase of TPPO was subsequently isolated during crystallization experiments conducted within sealed glass capillaries and identified as a new phase by powder XRD, the crystal structure of this phase remains undetermined. Indexing of the powder XRD of this new phase appeared to be successful; however, structure solution using EAGER has not yet progressed to finding a suitable candidate structure for Rietveld refinement. Further work must be conducted to determine the crystal structure of this new phase. A remaining unknown for TPPO is the methods for crystallization of the monoclinic II and monoclinic III polymorphs. To

conclusively rule out the possibility that one or two of the unknown phases observed in the CLASSIC NMR study of the crystallization of TPPO may be the monoclinic II or monoclinic III polymorph, these polymorphs must be crystallized and solid-state ^{31}P NMR spectra acquired. Two previously unknown transient phases of MDPPO were discovered during the crystallization of MDPPO from toluene through use of *in-situ* solid-state ^{31}P NMR. The identity of these new phases is currently unknown and so work must focus on the isolation and characterization of these phases. During the crystallization, only small amounts of these two new phases were formed concomitantly with a large amount of the only previously known phase of MDPPO. New crystallization conditions will likely need to be discovered in order to isolate the two new phases.

During the work described in Chapter 5, it was discovered that, contrary to the prior literature,[22] crystallization of Form II of *rac*-ibuprofen does not require cooling of supercooled liquid *rac*-ibuprofen to a temperature lower than the glass transition, followed by annealing at 258 K. This work has demonstrated that directly cooling liquid *rac*-ibuprofen to 258K (or even 273 K) and maintaining the sample at that temperature for an extended length of time is sufficient for crystallization of Form II. During the DSC experiments, issues with reproducibility can be seen between experiments, i.e., the same temperature regime may produce very different results. This irreproducibility may be caused by a variable lag time before crystallization of Form II of *rac*-ibuprofen, which, as shown in the powder XRD experiments, may be considerably longer than the timescale of the DSC experiments. Further work should be conducted to investigate and explain the problems with reproducibility.

As described in Chapter 6, a new polymorph (polymorph II) of L-Phe and two hydrate phases (a monohydrate and a non-stoichiometric hydrate with quarter-hydrate and hemihydrate end members) were discovered and structurally characterized in the present work. All three crystal structures share similarities, with water molecules present within channels in the structures of the two hydrate phases. Polymorph II of L-Phe also contains these channels, empty of water molecules in this case, and thus polymorph II represents an “isomorphic desolvate”. The existence of these channels appears to be the reason for the facile and completely reversible changes between the monohydrate, hemihydrate and (anhydrous) polymorph II. It would be interesting to attempt the preparation of a single crystal of L-Phe monohydrate to investigate whether

the transformation between the monohydrate, hemihydrate and polymorph II of L-Phe occurs in a single crystal to single crystal manner, without loss of crystal integrity. A question also remains over the thermodynamic stability of polymorph II with respect to the previously known polymorph I of L-Phe. The density of polymorph II (1.25 g cm^{-1}) is significantly lower than that of polymorph I (1.32 g cm^{-1}) which, according to the density rule, may suggest a lower thermodynamic stability. However, no transformation between the two polymorphs was observed over the course of the experiments (a timescale of several days) conducted in this work.

References

[1] L. Yu, G. A. Stephenson, C. A. Mitchell, C. A. Bunnell, S. V. Snorek, J. J. Bowyer, T. B. Borchardt, J. G. Stowell and S. R. Byrn, *J. Am. Chem. Soc.*, **122**, 585-591 (2000).

[2] S. Chen, I. A. Guzei and L. Yu, *J. Am. Chem. Soc.*, **127**, 9881-9885 (2005).

[3] L. A. Yu, *Acc. Chem. Res.*, **43**, 1257-1266 (2010).

[4] G. L. Perlovich, L. K. Hansen and A. Bauer-Brandl, *J. Therm. Anal. Calorim.*, **66**, 699-715 (2001).

[5] E. V. Boldyreva, V. A. Drebushchak, T. N. Drebushchak, I. E. Paukov, Y. A. Kovalevskaya and E. S. Shutova, *J. Therm. Anal. Calorim.*, **73**, 409-418 (2003).

[6] E. V. Boldyreva, V. A. Drebushchak, T. N. Drebushchak, I. E. Paukov, Y. A. Kovalevskaya and E. S. Shutova, *J. Therm. Anal. Calorim.*, **73**, 419-428 (2003).

[7] J. Bauer, S. Spanton, R. Henry, J. Quick, W. Dziki, W. Porter and J. Morris, *Pharm. Res.*, **18**, 859-866 (2001).

[8] D. W. Schacht, M. Hannay and H.-M. Wolff, Patent No. US8246979 (B2); US2005079206 (A1) (14th April 2005).

[9] H.-M. Wolff, L. Quere and J. Riedner, Patent No. US2010311806 (A1) (9th December 2010).

[10] C. R. Groom, *CPOSS*, University College London (2011).

[11] GLAXO INC. v. NOVOPHARM LTD., 830 F.Supp. 869 (1993), United States District Court, E.D. North Carolina, Raleigh Division

[12] GLAXO INC. v. NOVOPHARM LTD., 52 F.3d 1043 (1995), United States Court of Appeals, Federal Circuit.

[13] M. Haïsa, S. Kashino and H. Maeda, *Acta Crystallogr. Sect. B*, **30**, 2510-2512 (1974).

[14] M. Haïsa, S. Kashino, R. Kawai and H. Maeda, *Acta Crystallogr. Sect. B*, **32**, 1283-1285 (1976).

[15] M.-A. Perrin, M. A. Neumann, H. Elmaleh and L. Zaske, *Chem. Commun.*, 3181-3183 (2009).

[16] P. J. Wheatley, *J. Chem. Soc.*, **S**, 6036-6048 (1964).

[17] P. Vishweshwar, J. A. McMahon, M. Oliveira, M. L. Peterson and M. J. Zaworotko, *J. Am. Chem. Soc.*, **127**, 16802-16803 (2005).

[18] A. D. Bond, R. Boese and G. R. Desiraju, *Angew. Chem. Int. Ed.*, **46**, 615-617 (2007).

[19] A. D. Bond, R. Boese and G. R. Desiraju, *Angew. Chem. Int. Ed.*, **46**, 618-622 (2007).

[20] A. D. Bond, K. A. Solanko, S. Parsons, S. Redder and R. Boese, *CrystEngComm*, **13**, 399-401 (2010).

[21] J. F. McConnell, *Cryst. Struct. Commun.*, **3**, 73-75 (1974).
[22] E. Dudognon, F. Danede, M. Descamps and N. T. Correia, *Pharm. Res.*, **25**, 2853-2858 (2008).
[23] V. López-Mejías, J. W. Kampf and A. J. Matzger, *J. Am. Chem. Soc.*, **134**, 9872-9875 (2012).
[24] A. L. Grzesiak, M. D. Lang, K. Kim and A. J. Matzger, *J. Pharm. Sci.*, **92**, 2260-2271 (2003).
[25] J. Anwar, S. E. Tarling and P. Barnes, *J. Pharm. Sci.*, **78**, 337-342 (1989).
[26] F. C. Chan, J. Anwar, R. Cernik, P. Barnes and R. M. Wilson, *J. Appl. Crystallogr.*, **32**, 436-441 (1999).
[27] J. W. Mullin, *Crystallization*. (Butterworth & Co. Ltd., London, 1961).
[28] M. C. Etter, *J. Phys. Chem.*, **95**, 4601-4610 (1991).
[29] R. I. Walton and D. O'Hare, *Chem. Commun.*, 2283-2291 (2000).
[30] R. J. Francis, S. O'Brien, A. M. Fogg, P. S. Halasyamani, D. O'Hare, T. Loiseau and G. Férey, *J. Am. Chem. Soc.*, **121**, 1002-1015 (1999).
[31] I. R. Evans, J. A. K. Howard, T. Sreckovic and M. M. Ristic, *Mater. Res. Bull.*, **38**, 1203-1213 (2003).
[32] M. Berglund and M. E. Wieser, *Pure Appl. Chem.*, **83**, 397-410 (2011).
[33] C. Riekel and R. Schöllhorn, *Mater. Res. Bull.*, **11**, 369-376 (1976).
[34] J. Schöll, D. Bonalumi, L. Vicum, M. Mazzotti and M. Muller, *Cryst. Growth Des.*, **6**, 881-891 (2006).
[35] M. P. Feth, J. Jurascheck, M. Spitzenberg, J. Dillenz, G. Bertele and H. Stark, *J. Pharm. Sci.*, **100**, 1080-1092 (2011).
[36] G. Févotte, *Chem. Eng. Res. Des.*, **85**, 906-920 (2007).
[37] P.-G. Jönsson and Å. Kvick, *Acta Crystallogr. Sect. B*, **28**, 1827-1833 (1972).
[38] Y. Iitaka, *Acta Crystallogr.*, **13**, 35-45 (1960).
[39] Å. Kvick, W. M. Canning, T. F. Koetzle and G. J. B. Williams, *Acta Crystallogr. Sect. B*, **36**, 115-120 (1980).
[40] E. V. Boldyreva, S. N. Ivashevskaya, H. Sowa, H. Ahsbahs and H.-P. Weber, *Z. Kristallogr.*, **220**, 50-57 (2005).
[41] A. Dawson, D. R. Allan, S. A. Belmonte, S. J. Clark, W. I. F. David, P. A. McGregor, S. Parsons, C. R. Pulham and L. Sawyer, *Cryst. Growth Des.*, **5**, 1415-1427 (2005).
[42] C. E. Hughes and K. D. M. Harris, *J. Phys. Chem. A*, **112**, 6808-6810 (2008).
[43] C. E. Hughes and K. D. M. Harris, *Chem. Commun.*, **46**, 4982-4984 (2010).
[44] J. M. Shi, M. W. Anderson and S. W. Carr, *Chem. Mater.*, **8**, 369-375 (1996).
[45] C. Allais, G. Keller, P. Lesieur, M. Ollivon and F. Artzner, *J. Therm. Anal. Calorim.*, **74**, 723-728 (2003).
[46] C. J. Brown and M. Ehrenberg, *Acta Crystallogr. Sect. C*, **41**, 441-443 (1985).

[47] C. D. G. Boone, J. L. Derissen and J. C. Schoone, *Acta Crystallogr. Sect. B*, **33**, 3205-3206 (1977).

[48] H. Takazawa, S. Ohba and Y. Saito, *Acta Crystallogr. Sect. C*, **42**, 1880-1881 (1986).

[49] M. Svärd, F. L. Nordstrom, T. Jasnobulka and A. C. Rasmuson, *Cryst. Growth Des.*, **10**, 195-204 (2010).

[50] T. Yoshida and S. Sawada, *Bull. Chem. Soc. Jpn.*, **49**, 3319-3320 (1976).

[51] J. Voogd, B. H. M. Verzijl and A. J. M. Duisenberg, *Acta Crystallogr. Sect. B*, **36**, 2805-2806 (1980).

[52] T. F. Lai and R. E. Marsh, *Acta Crystallogr.*, **22**, 885-893 (1967).

[53] M. Alleaume, Salascim.G and J. Decap, *C. R. Seances Acad. Sci., Ser. C*, **262**, 416-417 (1966).

[54] R. C. G. Killean, P. Tollin, D. G. Watson and D. W. Young, *Acta Crystallogr.*, **19**, 482-483 (1965).

[55] M. Kuhnert-Brandstaetter and H. Grimm, *Mikrochim. Acta*, 1208-1209 (1969).

[56] M. C. Etter and P. W. Baures, *J. Am. Chem. Soc.*, **110**, 639-640 (1988).

[57] C. P. Brock, W. B. Schweizer and J. D. Dunitz, *J. Am. Chem. Soc.*, **107**, 6964-6970 (1985).

[58] G. Bandoli, Bortoloz.G, D. A. Clemente, U. Croatto and Panatton.C, *J. Chem. Soc. A*, 2778-2780 (1970).

[59] A. L. Spek, *Acta Crystallogr. Sect. C*, **43**, 1233-1235 (1987).

[60] F. Dornhaus, M. Bolte, H.-W. Lerner and M. Wagner, *Eur. J. Inorg. Chem.*, 5138-5147 (2006).

[61] D. H. Ryu and E. J. Corey, *J. Am. Chem. Soc.*, **127**, 5384-5387 (2005).

[62] Z. V. Belyakova, M. G. Pomerantseva, L. A. Efimova, E. A. Chernyshev and P. A. Storozhenko, *Russ. J. Gen. Chem.*, **80**, 728-733 (2010).

[63] R. M. Denton, J. An, B. Adeniran, A. J. Blake, W. Lewis and A. M. Poulton, *J. Org. Chem.*, **76**, 6749-6767 (2011).

[64] P. Derollez, E. Dudognon, F. Affouard, F. Danede, N. T. Correia and M. Descamps, *Acta Crystallogr. Sect. B*, **66**, 76-80 (2010).

[65] I. Weissbuch, F. Frolow, L. Addadi, M. Lahav and L. Leiserowitz, *J. Am. Chem. Soc.*, **112**, 7718-7724 (1990).

[66] R. Mohan, K. K. Koo, C. Strege and A. S. Myerson, *Ind. Eng. Chem. Res.*, **40**, 6111-6117 (2001).

[67] M. H. Frey, J. A. DiVerdi and S. J. Opella, *J. Am. Chem. Soc.*, **107**, 7311-7315 (1985).

[68] W. L. Bragg, *Proc. R. Soc. London, Ser. A*, **89**, 248-277 (1913).

[69] P. A. Doyle and P. S. Turner, *Acta Crystallogr. Sect. A*, **24**, 390-397 (1968).

[70] M. F. C. Ladd and P. R. A. eds., *Theory and Practice of Direct Methods in Crystallography*. (Plenum Press, New York, 1980).

[71] M. M. Woolfson, *Acta Crystallogr. Sect. A*, **43**, 593-612 (1987).
[72] A. L. Patterson, *Phys. Rev.*, **46**, 0372-0376 (1934).
[73] G. Oszlányi and A. Sütő, *Acta Crystallogr. Sect. A*, **60**, 134-141 (2004).
[74] G. Oszlányi and A. Sütő, *Acta Crystallogr. Sect. A*, **61**, 147-152 (2005).
[75] C. Baerlocher, L. B. McCusker and L. Palatinus, *Z. Kristallogr.*, **222**, 47-53 (2007).
[76] K. D. M. Harris, M. Tremayne, P. Lightfoot and P. G. Bruce, *J. Am. Chem. Soc.*, **116**, 3543-3547 (1994).
[77] A. Le Bail, H. Duroy and J. L. Fourquet, *Mater. Res. Bull.*, **23**, 447-452 (1988).
[78] G. S. Pawley, *J. Appl. Crystallogr.*, **14**, 357-361 (1981).
[79] P. Thompson, D. E. Cox and J. B. Hastings, *J. Appl. Crystallogr.*, **20**, 79-83 (1987).
[80] L. W. Finger, D. E. Cox and A. P. Jephcoat, *J. Appl. Crystallogr.*, **27**, 892-900 (1994).
[81] B. M. Kariuki, K. Psallidas, K. D. M. Harris, R. L. Johnston, R. W. Lancaster, S. E. Staniforth and S. M. Cooper, *Chem. Commun.*, 1677-1678 (1999).
[82] E. Tedesco, G. W. Turner, K. D. M. Harris, R. L. Johnston and B. M. Kariuki, *Angew. Chem. Int. Ed.*, **39**, 4488-4491 (2000).
[83] D. Albesa-Jové, B. M. Kariuki, S. J. Kitchin, L. Grice, E. Y. Cheung and K. D. M. Harris, *ChemPhysChem*, **5**, 414-418 (2004).
[84] F. Guo and K. D. M. Harris, *J. Am. Chem. Soc.*, **127**, 7314-7315 (2005).
[85] Z. G. Pan, M. C. Xu, E. Y. Cheung, K. D. M. Harris, E. C. Constable and C. E. Housecroft, *J. Phys. Chem. B*, **110**, 11620-11623 (2006).
[86] F. Guo, J. Martí-Rujas, Z. Pan, C. E. Hughes and K. D. M. Harris, *J. Phys. Chem. C*, **112**, 19793-19796 (2008).
[87] H. M. Rietveld, *J. Appl. Crystallogr.*, **2**, 65-71 (1969).
[88] M. J. Duer ed., *Solid-State NMR Spectroscopy Principles and Applications*. (Blackwell Science, 2002).
[89] A. Pines, M. G. Gibby and J. S. Waugh, *J. Chem. Phys.*, **59**, 569-590 (1973).
[90] B. M. Fung, A. K. Khitrin and K. Ermolaev, *J. Magn. Reson.*, **142**, 97-101 (2000).
[91] T. A. Carlson, *Photoelectron and Auger Spectroscopy*. (Plenum Press, London, 1975).
[92] G. Höhne, W. F. Hemminger and H.-J. Flammersheim, *Differential Scanning Calorimetry*. (Springer, 2003).
[93] B. Shah, V. K. Kakumanu and A. K. Bansal, *J. Pharm. Sci.*, **95**, 1641-1665 (2006).
[94] A. D. Roman-Gutierrez, S. Guilbert and B. Cuq, *J. Cereal Sci.*, **36**, 347-355 (2002).
[95] K. Klokkers, United States Patent No. 6204255 (2001).

[96] C. J. Brown, *Proc. R. Soc. London, Ser. A*, **302**, 185-199 (1968).
[97] A. Théorêt, *Spectrochim. Acta, Part A*, **27**, 11-18 (1971).
[98] M. A. Palafox, M. Gil and J. L. Nunez, *Vib. Spectrosc*, **6**, 95-105 (1993).
[99] G. Reinhard, M. Radtke and U. Rammelt, *Corros. Sci.*, **33**, 307-313 (1992).
[100] A. A. Al-Suhybani, Y. H. Sultan and W. A. Hamid, *Materialwiss. Werkstofftech.*, **22**, 301-307 (1991).
[101] G. C. Levy, A. D. Godwin, J. M. Hewitt and C. Sutcliffe, *J. Magn. Reson.*, **29**, 553-562 (1978).
[102] L. Van Blaricom and E. F. Gilbert, *J. Am. Chem. Soc.*, **61**, 3238-3239 (1939).
[103] L. Gopal, C. I. Jose and A. B. Biswas, *Spectrochim. Acta, Part A*, **23**, 513-518 (1967).
[104] I. Mentré, *Ann. Chim. (Paris)*, **8**, 115-122 (1973).
[105] L. M. Schwartz, R. I. Gelb, J. Mumfordzisk and D. A. Laufer, *J. Chem. Soc., Perkin Trans. 2*, 453-460 (1987).
[106] R. Shirley, *The CRYSFIRE System for Automatic Powder Indexing: User's Manual*. (The Lattice Press, Guildford, U.K., 1999).
[107] A. C. Larson and R. B. Von Dreele, *Los Alamos National Laboratory Report*, LAUR 86-748 (2004).
[108] B. H. Toby, *J. Appl. Crystallogr.*, **34**, 210-213 (2001).
[109] G. Metz, X. L. Wu and S. O. Smith, *J. Magn. Reson. A*, **110**, 219-227 (1994).
[110] M. C. Etter, *Acc. Chem. Res.*, **23**, 120-126 (1990).
[111] M. C. Etter, J. C. Macdonald and J. Bernstein, *Acta Crystallogr. Sect. B*, **46**, 256-262 (1990).
[112] J. Bernstein, R. E. Davis, L. Shimoni and N. L. Chang, *Angew. Chem. Int. Ed.*, **34**, 1555-1573 (1995).
[113] P. E. Werner, L. Eriksson and M. Westdahl, *J. Appl. Crystallogr.*, **18**, 367-370 (1985).
[114] A. March, *Z. Kristallogr.*, **81**, 285-297 (1932).
[115] W. A. Dollase, *J. Appl. Crystallogr.*, **19**, 267-272 (1986).
[116] J. W. Visser, *J. Appl. Crystallogr.*, **2**, 89-95 (1969).
[117] T. Charpentier, *Solid State Nucl. Magn. Reson.*, **40**, 1-20 (2011).
[118] R. K. Harris, R. E. Wasylishen and M. J. Duer, *NMR Crystallography*. (John Wiley & Sons, Chichester, 2012).
[119] D. V. Dudenko, J. R. Yates, K. D. M. Harris and S. P. Brown, *CrystEngComm*, **15**, 8797-8807 (2013).
[120] I. Bertini, G. Gallo, M. Korsak, C. Luchinat, J. Mao and E. Ravera, *ChemBioChem*, **14**, 1891-1897 (2013).
[121] D. Courtier-Murias, H. Farooq, H. Masoom, A. Botana, R. Soong, J. G. Longstaffe, M. J. Simpson, W. E. Maas, M. Fey, B. Andrew, J. Struppe, H.

Hutchins, S. Krishnamurthy, R. Kumar, M. Monette, H. J. Stronks, A. Hume and A. J. Simpson, *J. Magn. Reson.*, **217**, 61-76 (2012).

[122] S. E. Denmark, R. C. Smith and S. A. Tymonko, *Tetrahedron*, **63**, 5730-5738 (2007).

[123] O. Mitsunobu and M. Yamada, *Bull. Chem. Soc. Jpn.*, **40**, 2380-2382 (1967).

[124] H. Staudinger and J. Meyer, *Helv. Chim. Acta*, **2**, 635-646 (1919).

[125] G. Wittig and U. Schöllkopf, *Chem. Ber. Recl.*, **87**, 1318-1330 (1954).

[126] G. Wittig and W. Haag, *Chem. Ber. Recl.*, **88**, 1654-1666 (1955).

[127] Private communication submitted to CSD: A. T. H. Lenstra, Refcode: TPEPHO12 (2007).

[128] P. W. Baures and J. V. Silverton, *Acta Crystallogr. Sect. C*, **46**, 715-717 (1990).

[129] P. W. Baures, *Acta Crystallogr. Sect. C*, **47**, 2715-2716 (1991).

[130] S. W. Ng, *Acta Crystallogr. Sect. E*, **65**, o1431 (2009).

[131] Private communication submitted to CSD: J. Wahl, M. Bolte and D. Franz, Refcode: OBEBAA (2011).

[132] S. Arumugam, C. Glidewell and K. D. M. Harris, *J. Chem. Soc., Chem. Commun.*, 724-726 (1992).

[133] F. Kohlbeck and E. M. Hörl, *J. Appl. Crystallogr.*, **11**, 60-61 (1978).

[134] WHO. Model Lists of Essential Medicines, 18th ed.; 2013.

[135] N. M. Davies, *Clin. Pharmacokinet.*, **34**, 101-154 (1998).

[136] K. D. Rainsford, *Ibuprofen: A Critical Bibliographic Review*. (Taylor & Francis, 2003).

[137] G. Geisslinger, K. Dietzel, H. Bezler, B. Nuernberg and K. Brune, *Int. J. Clin. Pharmacol. Ther.*, **27**, 324-328 (1989).

[138] V. Legrand, M. Descamps and C. Alba-Simionesco, *Thermochim. Acta*, **307**, 77-83 (1997).

[139] F. Paladi and M. Oguni, *Phys. Rev. B*, **65**, 144202 (2002).

[140] N. Okamoto and M. Oguni, *Solid State Commun.*, **99**, 53-56 (1996).

[141] S. F. Chow, M. Chen, L. M. Shi, A. H. L. Chow and C. C. Sun, *Pharm. Res.*, **29**, 1854-1865 (2012).

[142] L. Seton, M. Roberts and F. Ur-Rehman, *Chem. Eng. J.*, **164**, 449-452 (2010).

[143] F. Xu, L.-X. Sun, Z.-C. Tan, J.-G. Liang and R.-L. Li, *Thermochim. Acta*, **412**, 33-37 (2004).

[144] T. Sato and C. Sano, Patent No. EP0703214A2 (1995).

[145] CSD version 5.33, November 2011

[146] B. Khawas, *Acta Crystallogr. Sect. B*, **26**, 1919-1922 (1970).

[147] B. Khawas, *Ind. J. Phys*, **59A**, 219-226 (1985).

[148] M. D. King, T. N. Blanton and T. M. Korter, *Phys. Chem. Chem. Phys.*, **14**, 1113-1116 (2012).

[149] G. A. Stephenson, E. G. Groleau, R. L. Kleemann, W. Xu and D. R. Rigsbee, *J. Pharm. Sci.*, **87**, 536-542 (1998).
[150] P. R. Perrier and S. R. Byrn, *J. Org. Chem.*, **47**, 4671-4676 (1982).
[151] S. Petit and G. Coquerel, *Chem. Mater.*, **8**, 2247-2258 (1996).
[152] H. Nagase, N. Ogawa, T. Endo, M. Shiro, H. Ueda and M. Sakurai, *J. Phys. Chem. B*, **112**, 9105-9111 (2008).
[153] M. O. Okoth, R. M. Vrcelj, D. B. Sheen and J. N. Sherwood, *CrystEngComm*, **14**, 1602-1612 (2012).
[154] S. Padmanabhan, S. Suresh and M. Vijayan, *Acta Crystallogr. Sect. C*, **51**, 2098-2100 (1995).
[155] A. L. Spek, *J. Appl. Crystallogr.*, **36**, 7-13 (2003).
[156] A. L. Spek, PLATON. A Multipurpose Crystallographic Tool (Utrecht University, The Netherlands, 2008).
[157] A. Boultif and D. Louër, *J. Appl. Crystallogr.*, **24**, 987-993 (1991).
[158] P. Suortti, *J. Appl. Crystallogr.*, **5**, 325-331 (1972).
[159] M. S. Lehmann, J. J. Verbist, W. C. Hamilton and T. F. Koetzle, *J. Chem. Soc., Perkin Trans. 2*, 133-137 (1973).
[160] G. Kartha and A. Devries, *Nature*, **192**, 862-863 (1961).
[161] K. Umadevi, K. Anitha, B. Sridhar, N. Srinivasan and R. K. Rajaram, *Acta Crystallogr. Sect. E*, **59**, O1073-O1075 (2003).
[162] J. Janczak and P. Luger, *Acta Crystallogr. Sect. C*, **53**, 1954-1956 (1997).
[163] M. N. Frey, M. S. Lehmann, T. F. Koetzle and W. C. Hamilton, *Acta Crystallogr. Sect. B*, **29**, 876-884 (1973).
[164] S. Chakraborty, A. K. Bera, S. Ghosh, S. Bhattacharya, A. K. Pal, B. P. Mukhopadhyay and A. Banerjee, *Indian J. Phys., A*, **75**, 499-501 (2001).
[165] S. Suresh, S. Padmanabhan and M. Vijayan, *J. Biomol. Struct. Dyn.*, **11**, 1425-1435 (1994).
[166] R. Kingsford-Adaboh, M. Grosche, B. Dittrich and P. Luger, *Acta Crystallogr. Sect. C*, **56**, 1274-1276 (2000).
[167] Z. Ciunik and T. Głowiak, *Acta Crystallogr. Sect. C*, **39**, 1271-1273 (1983).
[168] R. O. Fox, Jr. and R. D. Rosenstein, *ACS Abstract Papers (Summer)*, 50 (1976).

Appendix A: Atomic Parameters for Crystal Structures Determined During This Work

	x	*y*	*z*	U_{iso}
N1	0.56655(26)	0.1471(7)	0.4808(6)	0.0247(10)
C2	0.61825(24)	0.5932(5)	0.1746(5)	0.0247(10)
C3	0.57946(15)	0.4539(7)	0.2708(6)	0.0247(10)
C4	0.60490(22)	0.2876(6)	0.3832(5)	0.0247(10)
C5	0.66909(24)	0.2604(6)	0.3986(5)	0.0247(10)
C6	0.70786(16)	0.3998(8)	0.3026(7)	0.0247(10)
C7	0.68245(23)	0.5662(7)	0.1905(6)	0.0247(10)
C8	0.59109(22)	0.7715(5)	0.0545(6)	0.0247(10)
O9	0.53318(25)	0.8048(8)	0.0773(11)	0.0247(10)
O10	0.62729(23)	0.8885(8)	–0.0712(10)	0.0247(10)
H11	0.5910(7)	0.0555(30)	0.587(12)	0.0346(12)
H12	0.5396(16)	0.1908(23)	0.640(10)	0.0346(12)
H13	0.5434(18)	0.101(5)	0.276(4)	0.0346(12)
H31	0.53433(19)	0.4727(10)	0.2599(8)	0.0346(12)
H51	0.6869(4)	0.1436(8)	0.4776(7)	0.0346(12)
H61	0.75299(20)	0.3810(12)	0.3136(9)	0.0346(12)
H71	0.70974(34)	0.6641(9)	0.1227(7)	0.0346(12)

Table A.1: *Atomic coordinates and isotropic displacement parameters (U_{iso}) for Form III of m-aminobenzoic acid.*

	x	*y*	*z*	U_{iso}
N1	0.16788(32)	0.25994(33)	0.12903(21)	0.0351(9)
C2	0.35922(31)	0.11399(29)	–0.13114(10)	0.0351(9)
C3	0.29725(26)	0.12947(25)	–0.03459(9)	0.0351(9)
C4	0.23251(26)	0.24475(26)	0.02797(17)	0.0351(9)
C5	0.22738(28)	0.34552(32)	–0.00253(26)	0.0351(9)
C6	0.28940(22)	0.3295(4)	–0.09898(29)	0.0351(9)
C7	0.35494(20)	0.2141(4)	–0.16277(23)	0.0351(9)
C8	0.43069(26)	–0.01103(33)	–0.201085(34	0.0351(9)
O9	0.36869(24)	–0.10335(31)	–0.17453(10)	0.0351(9)
O10	0.5471(4)	–0.0164(4)	–0.28128(13)	0.0351(9)
H11	0.3794(27)	0.273(7)	0.16557(33)	0.0420(10)
H12	0.035(13)	0.1896(12)	0.1300(21)	0.0420(10)
H13	0.048(17)	0.326(4)	0.1545(12)	0.0420(10)
H31	0.29950(26)	0.06166(26)	–0.01208(8)	0.0420(10)
H51	0.1824(4)	0.42396(33)	0.04149(31)	0.0420(10)
H61	0.2870(5)	0.3974(5)	–0.1212(5)	0.0420(10)
H71	0.39704(21)	0.2037(4)	–0.22841(25)	0.0420(10)
N11	–0.1392(5)	0.7794(5)	0.64344(26)	0.0351(9)
C12	–0.11783(22)	0.60658(35)	0.37564(20)	0.0351(9)
C13	–0.17950(25)	0.63224(33)	0.47311(19)	0.0351(9)
C14	–0.0754(4)	0.75135(34)	0.54053(23)	0.0351(9)
C15	0.0899(4)	0.84638(33)	0.51314(31)	0.0351(9)
C16	0.15090(34)	0.8203(4)	0.41571(33)	0.0351(9)
C17	0.04729(24)	0.7008(4)	0.34730(26)	0.0351(9)
C18	–0.22873(26)	0.4774(4)	0.30060(19)	0.0351(9)
O19	–0.36092(33)	0.39356(35)	0.32978(24)	0.0351(9)
O20	–0.18280(35)	0.4600(5)	0.21176(22)	0.0351(9)
H111	–0.235(17)	0.8518(35)	0.6660(13)	0.0420(10)
H112	0.070(5)	0.788(6)	0.67947(29)	0.0420(10)
H113	–0.293(11)	0.7161(14)	0.6488(22)	0.0420(10)
H131	–0.29207(25)	0.5686(4)	0.49326(20)	0.0420(10)
H151	0.1598(5)	0.92778(34)	0.5604(4)	0.0420(10)
H161	0.2635(4)	0.8841(4)	0.3958(4)	0.0420(10)
H171	0.08956(24)	0.6834(5)	0.28072(27)	0.0420(10)

Table A.2: *Atomic coordinates and isotropic displacement parameters (U_{iso}) for Form IV of m-aminobenzoic acid.*

	x	*y*	*z*	*Occ*	U_{iso}
N1a	0.81567(35)	0.8863(10)	0.2269(6)	0.602(5)	0.0468(11)
N1b	0.5794(6)	0.9234(11)	0.5392(5)	0.398(5)	0.0468(11)
C2	0.60763(24)	0.50411(34)	0.21252(30)	1.0	0.0468(11)
C3	0.69078(25)	0.5969(5)	0.17642(27)	1.0	0.0468(11)
C4	0.73563(22)	0.7959(6)	0.2608(4)	1.0	0.0468(11)
C5	0.69738(31)	0.9019(4)	0.3812(4)	1.0	0.0468(11)
C6	0.61426(31)	0.8092(5)	0.41732(26)	1.0	0.0468(11)
C7	0.56930(21)	0.6102(6)	0.33296(35)	1.0	0.0468(11)
C8	0.56020(21)	0.2907(4)	0.12113(27)	1.0	0.0468(11)
O9a	0.5977(4)	0.1888(9)	0.01516(32)	0.602(5)	0.0468(11)
O9b	0.48418(22)	0.2109(12)	0.1560(7)	0.398(5)	0.0468(11)
O10a	0.48156(33)	0.2120(10)	0.1534(6)	0.602(5)	0.0468(11)
O10b	0.5992(5)	0.1883(11)	0.0130(5)	0.398(5)	0.0468(11)
H11a	0.8419(18)	0.783(8)	0.1515(33)	0.602(5)	0.0562(13)
H11b	0.572(7)	0.797(6)	0.622(6)	0.398(5)	0.0562(13)
H12a	0.8519(13)	0.950(10)	0.3043(19)	0.602(5)	0.0562(13)
H12b	0.607(5)	1.079(11)	0.567(8)	0.1989(25)	0.0562(13)
H12c	0.523(4)	0.997(28)	0.517(4)	0.1989(25)	0.0562(13)
H31	0.7177(4)	0.5224(8)	0.09185(35)	1.0	0.0562(13)
H41b	0.79407(25)	0.8611(9)	0.2355(6)	0.398(5)	0.0562(13)
H51	0.7289(4)	1.0415(5)	0.4403(5)	1.0	0.0562(13)
H61a	0.5874(4)	0.8838(8)	0.50191(32)	0.602(5)	0.0562(13)
H71	0.51085(25)	0.5449(9)	0.3583(5)	1.0	0.0562(13)
H101a	0.4572(5)	0.0665(10)	0.0845(9)	0.602(5)	0.0562(13)
H101b	0.5612(8)	0.0419(9)	–0.0368(6)	0.398(5)	0.0562(13)

Table A.3: *Atomic coordinates, occupancy (Occ) and isotropic displacement parameters (U_{iso}) for Form V of m-aminobenzoic acid.*

	x	*y*	*z*	U_{iso}
O1	–0.6076(9)	0.1623(18)	–0.38044(16)	0.0401(15)
O2	–0.4298(9)	0.1327(22)	–0.38981(18)	0.0401(15)
C3	–0.5137(6)	0.2613(12)	–0.38219(9)	0.0401(15)
C4	–0.5013(6)	0.5399(13)	–0.37506(13)	0.0401(15)
H5	–0.4510(9)	0.5949(18)	–0.4193(4)	0.0481(18)
N6	–0.6171(9)	0.6537(18)	–0.4086(7)	0.0401(15)
H7	–0.6725(18)	0.566(24)	–0.378(11)	0.0481(18)
H8	–0.616(7)	0.828(9)	–0.389(11)	0.0481(18)
H9	–0.638(7)	0.641(31)	–0.4805(16)	0.0481(18)
C10	–0.4508(7)	0.6117(18)	–0.26885(26)	0.0401(15)
H11	–0.3808(5)	0.5199(33)	–0.2488(4)	0.0481(18)
H12	–0.4339(14)	0.7886(21)	–0.2668(7)	0.0481(18)
C13	–0.5286(5)	0.5570(11)	–0.19674(24)	0.0401(15)
C14	–0.6134(6)	0.7194(11)	–0.1826(4)	0.0401(15)
C15	–0.6842(5)	0.6680(19)	–0.1165(5)	0.0401(15)
C16	–0.6726(7)	0.4521(21)	–0.0621(4)	0.0401(15)
C17	–0.5899(9)	0.2871(14)	–0.0740(4)	0.0401(15)
C18	–0.5172(6)	0.3379(14)	–0.1413(4)	0.0401(15)
H19	–0.6252(10)	0.8722(10)	–0.2211(6)	0.0481(18)
H20	–0.7417(5)	0.7876(27)	–0.1061(9)	0.0481(18)
H21	–0.7185(10)	0.4247(30)	–0.0111(5)	0.0481(18)
H22	–0.5765(13)	0.1417(15)	–0.0313(5)	0.0481(18)
H23	–0.4565(7)	0.2229(21)	–0.1479(7)	0.0481(18)
O24	–0.8367(10)	0.5974(19)	–0.38417(26)	0.0401(15)
O25	–1.0172(9)	0.6181(19)	–0.38758(21)	0.0401(15)
C26	–0.9287(7)	0.4942(10)	–0.37993(13)	0.0401(15)
C27	–0.9336(5)	0.2167(10)	–0.36544(15)	0.0401(15)
H28	–1.0097(6)	0.1576(15)	–0.3905(5)	0.0481(18)
N29	–0.8524(9)	0.0930(19)	–0.4212(6)	0.0401(15)
H30	–0.7788(11)	0.172(8)	–0.404(4)	0.0481(18)
H31	–0.846(4)	–0.082(4)	–0.403(5)	0.0481(18)
H32	–0.8797(24)	0.109(11)	–0.4922(6)	0.0481(18)
C33	–0.9030(7)	0.1591(12)	–0.25516(28)	0.0401(15)
H34	–0.8849(11)	–0.0166(16)	–0.2463(8)	0.0481(18)
H35	–0.8377(6)	0.2577(25)	–0.22616(30)	0.0481(18)

Table A.4: *Atomic coordinates and isotropic displacement parameters (U_{iso}) for L-phenylalanine hemihydrate (continued on next page).*

C36	–1.0007(6)	0.2204(10)	–0.20436(25)	0.0401(15)
C37	–1.0957(7)	0.0719(11)	–0.21524(33)	0.0401(15)
C38	–1.1842(6)	0.1307(16)	–0.1683(5)	0.0401(15)
C39	–1.1792(7)	0.3392(18)	–0.1095(5)	0.0401(15)
C40	–1.0860(9)	0.4872(12)	–0.09814(33)	0.0401(15)
C41	–0.9967(7)	0.4287(13)	–0.1453(4)	0.0401(15)
H42	–1.1012(11)	–0.0741(10)	–0.2578(4)	0.0481(18)
H43	–1.2497(7)	0.0219(23)	–0.1747(7)	0.0481(18)
H44	–1.2390(10)	0.3725(25)	–0.0716(6)	0.0481(18)
H45	–1.0792(13)	0.6264(13)	–0.0520(4)	0.0481(18)
H46	–0.9292(8)	0.5319(20)	–0.1352(6)	0.0481(18)
O47	–1.2420(15)	0.4368(32)	–0.4037(12)	0.071(8)

Table A.4 (cont.)

	x	*y*	*z*	*Occ*	U_{iso}
O1	0.3528(7)	0.1213(17)	0.63877(23)	1.0	0.0671(15)
O2	0.5169(8)	0.0620(20)	0.65024(24)	1.0	0.0671(15)
C3	0.4430(5)	0.2040(12)	0.64641(14)	1.0	0.0671(15)
C4	0.4635(4)	0.4799(13)	0.65113(16)	1.0	0.0671(15)
H5	0.5117(7)	0.5212(17)	0.6074(4)	1.0	0.0805(19)
N6	0.3612(8)	0.6105(19)	0.6168(6)	1.0	0.0671(15)
H7	0.3075(18)	0.540(15)	0.649(6)	1.0	0.0805(19)
H8	0.370(4)	0.786(4)	0.633(7)	1.0	0.0805(19)
H9	0.340(5)	0.591(18)	0.5458(13)	1.0	0.0805(19)
C10	0.5132(6)	0.5558(16)	0.75576(28)	1.0	0.0671(15)
H11	0.5782(5)	0.4627(30)	0.7765(4)	1.0	0.0805(19)
H12	0.5299(12)	0.7318(19)	0.7564(7)	1.0	0.0805(19)
C13	0.4417(5)	0.5085(12)	0.82739(25)	1.0	0.0671(15)
C14	0.4535(5)	0.2966(11)	0.88460(34)	1.0	0.0671(15)
C15	0.3889(7)	0.2508(13)	0.95043(29)	1.0	0.0671(15)
C16	0.3102(6)	0.4156(20)	0.9612(4)	1.0	0.0671(15)
C17	0.2964(6)	0.6274(19)	0.9056(6)	1.0	0.0671(15)
C18	0.3619(7)	0.6756(13)	0.8384(4)	1.0	0.0671(15)
H19	0.5083(7)	0.1771(15)	0.8785(6)	1.0	0.0805(19)
H20	0.3983(11)	0.1006(15)	0.99018(33)	1.0	0.0805(19)
H21	0.2649(8)	0.3812(30)	1.0082(6)	1.0	0.0805(19)
H22	0.2410(7)	0.7443(25)	0.9131(9)	1.0	0.0805(19)
H23	0.3521(11)	0.8261(14)	0.7989(5)	1.0	0.0805(19)
O24	–0.0168(8)	0.5976(18)	0.61102(26)	1.0	0.0671(15)
O25	0.1504(8)	0.5639(18)	0.62153(27)	1.0	0.0671(15)
C26	0.0633(6)	0.4686(10)	0.62439(15)	1.0	0.0671(15)
C27	0.0550(5)	0.1946(10)	0.64418(18)	1.0	0.0671(15)
H28	–0.0166(5)	0.1390(15)	0.6184(5)	1.0	0.0805(19)
N29	0.1283(7)	0.0675(18)	0.5910(6)	1.0	0.0671(15)
H30	0.0997(20)	0.072(9)	0.5206(6)	1.0	0.0805(19)
H31	0.1963(11)	0.151(6)	0.604(4)	1.0	0.0805(19)
H32	0.1371(30)	–0.1040(34)	0.6129(35)	1.0	0.0805(19)
C33	0.0827(6)	0.1396(11)	0.75400(31)	1.0	0.0671(15)
H34	0.0941(11)	–0.0377(13)	0.7641(8)	1.0	0.0805(19)
H35	0.1466(6)	0.2289(24)	0.78310(32)	1.0	0.0805(19)

Table A.5: *Atomic coordinates, occupancy (Occ) and isotropic displacement parameters (U_{iso}) for L-phenylalanine monohydrate (continued on next page).*

C36	–0.0065(6)	0.2215(9)	0.80171(27)	1.0	0.0671(15)
C37	–0.1018(7)	0.0974(10)	0.78349(31)	1.0	0.0671(15)
C38	–0.1834(5)	0.1717(15)	0.8269(5)	1.0	0.0671(15)
C39	–0.1715(7)	0.3705(16)	0.8890(5)	1.0	0.0671(15)
C40	–0.0780(9)	0.4968(11)	0.9083(4)	1.0	0.0671(15)
C41	0.0048(6)	0.4252(13)	0.8656(4)	1.0	0.0671(15)
H42	–0.1115(10)	–0.0453(10)	0.73962(32)	1.0	0.0805(19)
H43	–0.2504(6)	0.0834(22)	0.8131(7)	1.0	0.0805(19)
H44	–0.2301(10)	0.4248(23)	0.9187(7)	1.0	0.0805(19)
H45	–0.0701(14)	0.6405(12)	0.9517(4)	1.0	0.0805(19)
H46	0.0710(7)	0.5168(21)	0.8794(6)	1.0	0.0805(19)
O47	0.7690(8)	0.5281(27)	0.6098(11)	1.0	0.074(7)
H48	0.739(16)	0.688(15)	0.587(6)	0.5	0.089(8)
H49	0.8450(23)	0.55(4)	0.626(4)	1.0	0.089(8)
O50	0.3103(9)	0.5127(30)	0.4167(17)	1.0	0.064(6)
H51	0.3811(27)	0.524(26)	0.403(6)	1.0	0.077(7)
H52	0.280(10)	0.679(13)	0.407(29)	0.5	0.077(7)
H53	0.759(15)	0.355(17)	0.590(20)	0.5	0.089(8)
H54	0.291(10)	0.338(8)	0.411(21)	0.5	0.077(7)

Table A.5 (cont.)

	x	*y*	*z*	U_{iso}
O1	–0.6130(6)	0.1690(15)	–0.38532(13)	0.087(6)
O2	–0.4369(6)	0.1233(18)	–0.39033(14)	0.087(6)
C3	–0.5182(5)	0.2601(12)	–0.38481(7)	0.087(6)
C4	–0.5006(5)	0.5381(12)	–0.37752(10)	0.087(6)
H5	–0.4490(7)	0.5880(16)	–0.42214(28)	0.105(7)
N6	–0.6123(7)	0.6633(17)	–0.4092(5)	0.087(6)
H7	–0.6713(14)	0.569(20)	–0.384(11)	0.105(7)
H8	–0.609(7)	0.831(11)	–0.382(10)	0.105(7)
H9	–0.629(7)	0.671(28)	–0.4817(6)	0.105(7)
C10	–0.4503(5)	0.6111(14)	–0.27103(20)	0.087(6)
H11	–0.3795(4)	0.5217(24)	–0.25122(34)	0.105(7)
H12	–0.4349(10)	0.7890(16)	–0.2689(5)	0.105(7)
C13	–0.5286(4)	0.5519(10)	–0.19855(19)	0.087(6)
C14	–0.6127(5)	0.7162(10)	–0.18332(33)	0.087(6)
C15	–0.6840(4)	0.6619(15)	–0.1171(4)	0.087(6)
C16	–0.6732(5)	0.4416(17)	–0.06431(34)	0.087(6)
C17	–0.5909(6)	0.2749(12)	–0.07755(32)	0.087(6)
C18	–0.5182(4)	0.3266(12)	–0.14399(35)	0.087(6)
H19	–0.6240(8)	0.8694(10)	–0.2219(5)	0.105(7)
H20	–0.7399(4)	0.7835(21)	–0.1041(7)	0.105(7)
H21	–0.7152(7)	0.4165(23)	–0.0097(4)	0.105(7)
H22	–0.5748(9)	0.1338(12)	–0.0325(4)	0.105(7)
H23	–0.4565(5)	0.2129(16)	–0.1501(6)	0.105(7)
O24	–0.8261(7)	0.5891(14)	–0.38431(19)	0.087(6)
O25	–1.0063(6)	0.6426(15)	–0.39248(16)	0.087(6)
C26	–0.9230(5)	0.5022(8)	–0.38181(10)	0.087(6)
C27	–0.93804(32)	0.2270(8)	–0.36585(11)	0.087(6)
H28	–1.0159(4)	0.1798(11)	–0.3916(4)	0.105(7)
N29	–0.8600(5)	0.0880(17)	–0.4205(5)	0.087(6)
H30	–0.7837(8)	0.155(7)	–0.4027(35)	0.105(7)
H31	–0.8600(34)	–0.0873(28)	–0.403(4)	0.105(7)
H32	–0.8851(26)	0.106(9)	–0.4921(4)	0.105(7)
C33	–0.9099(5)	0.1608(10)	–0.25567(21)	0.087(6)
H34	–0.8969(9)	–0.0176(12)	–0.2488(6)	0.105(7)
H35	–0.8417(5)	0.2491(20)	–0.22569(24)	0.105(7)

Table A.6: *Atomic coordinates and isotropic displacement parameters (U_{iso}) for polymorph II of L-phenylalanine (continued on next page).*

C36	–1.0057(4)	0.2324(9)	–0.20306(20)	0.087(6)
C37	–1.1007(5)	0.0836(10)	–0.21167(30)	0.087(6)
C38	–1.1884(4)	0.1483(15)	–0.1637(4)	0.087(6)
C39	–1.1816(6)	0.3621(16)	–0.1070(4)	0.087(6)
C40	–1.0871(7)	0.5103(12)	–0.09837(29)	0.087(6)
C41	–0.9992(5)	0.4467(11)	–0.14605(30)	0.087(6)
H42	–1.1067(8)	–0.0635(10)	–0.25406(34)	0.105(7)
H43	–1.2535(5)	0.0384(21)	–0.1665(6)	0.105(7)
H44	–1.2376(8)	0.3947(22)	–0.0643(5)	0.105(7)
H45	–1.0768(10)	0.6455(12)	–0.05002(32)	0.105(7)

Table A.6 (cont.)

Appendix B: Full Differential Scanning Calorimetry Thermograms for Experiments Performed on *rac*-Ibuprofen

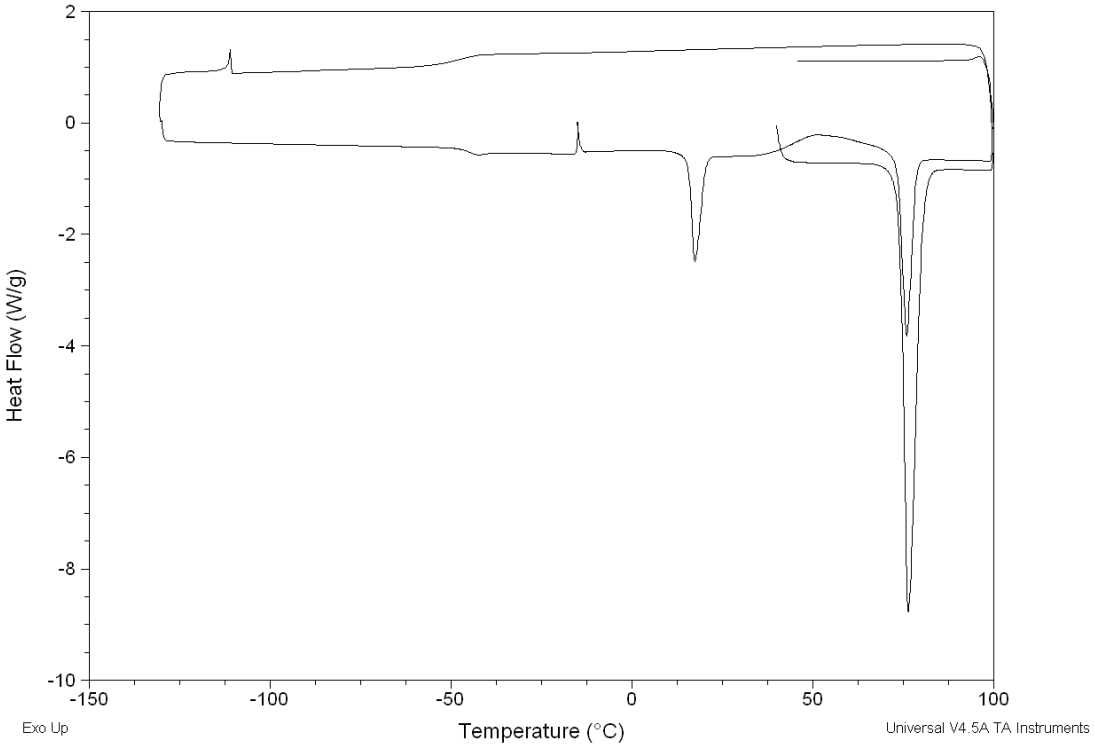

Figure B.1: *DSC data for Experiment A. Mass of sample = 4.9 mg.*

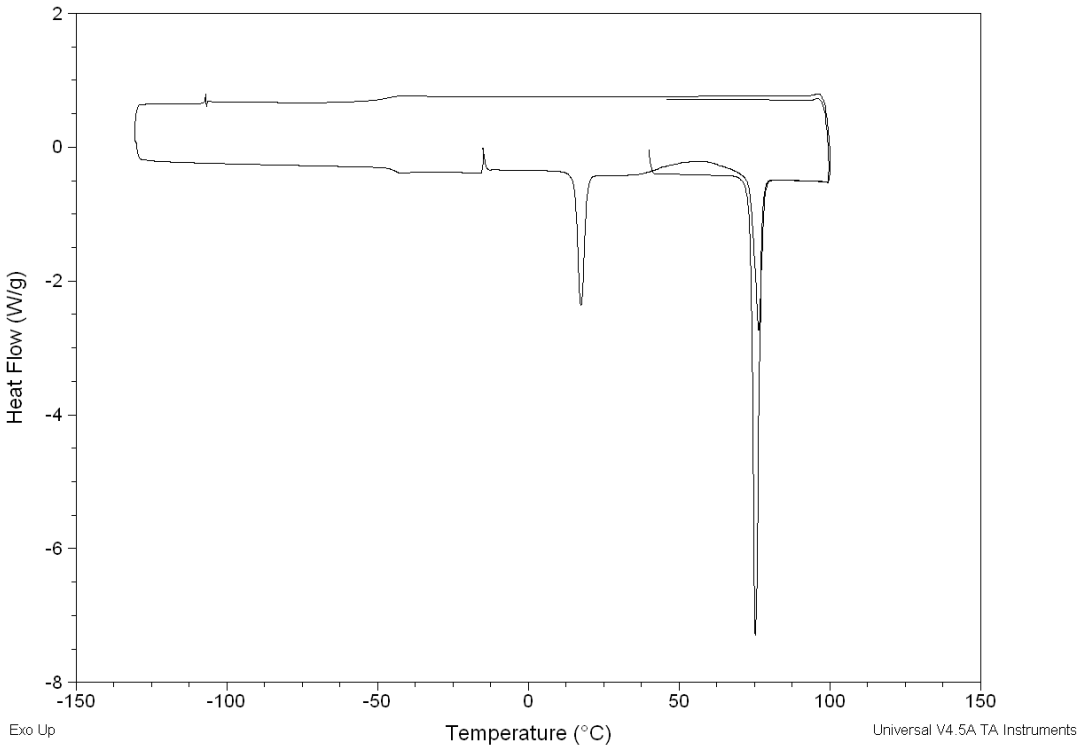

Figure B.2: *DSC data for Experiment B. Mass of sample = 3.5 mg.*

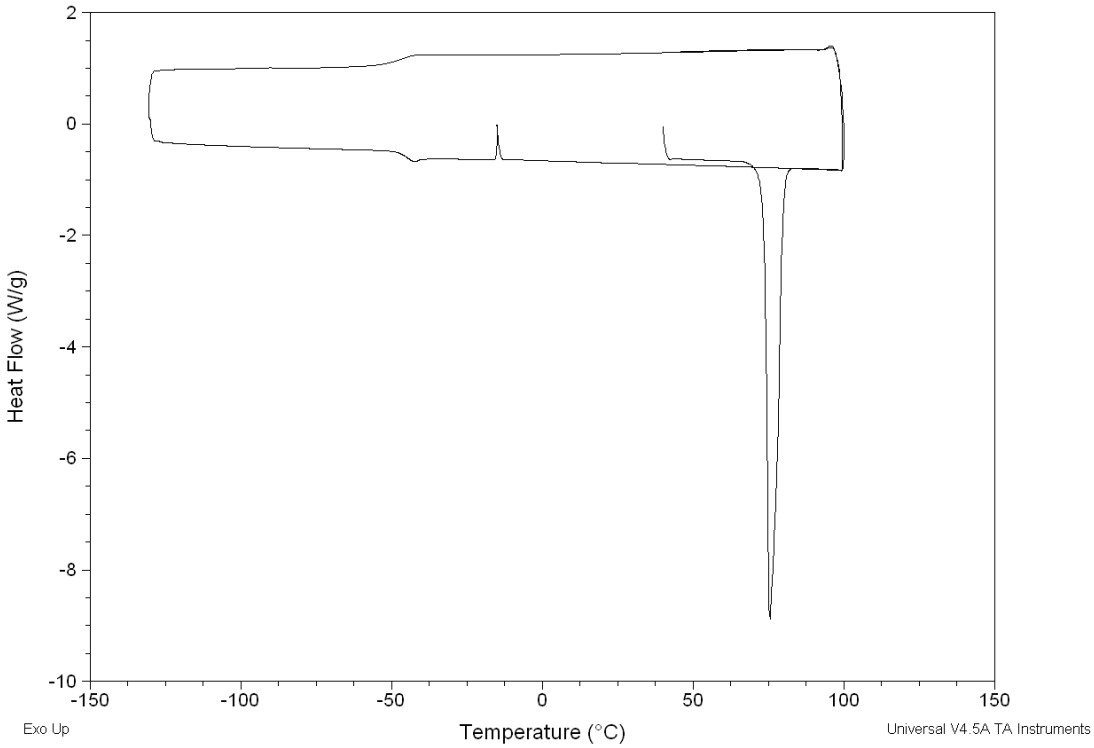

Figure B.3: *DSC data for Experiment C. Mass of sample = 3.4 mg.*

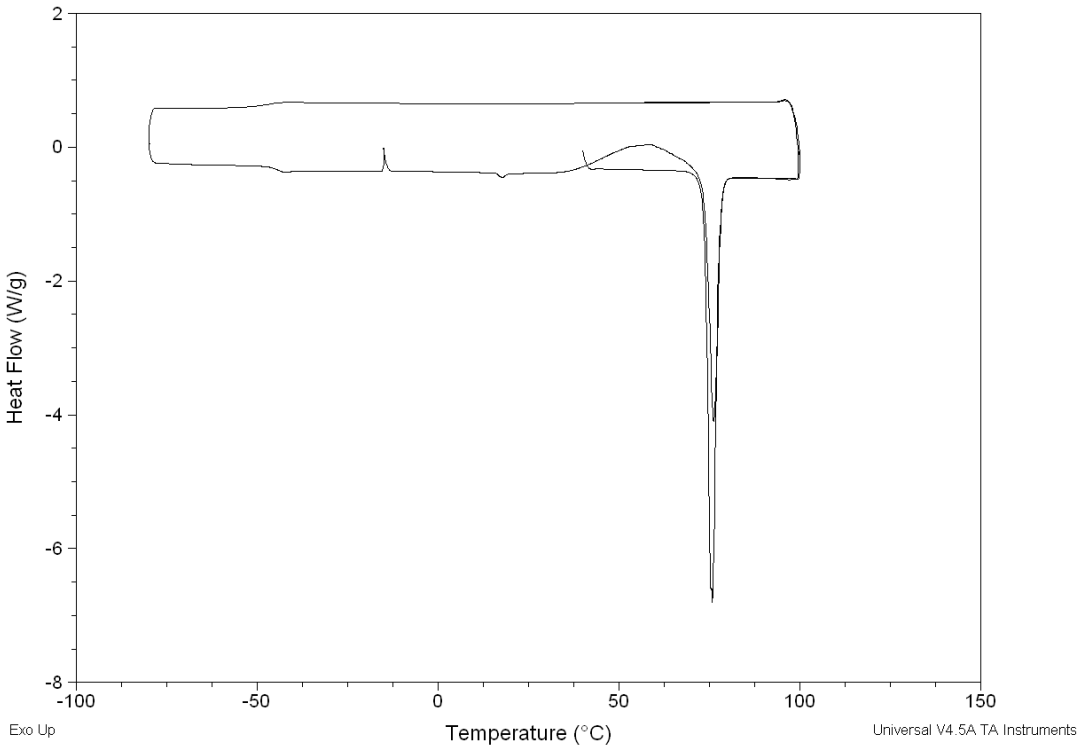

Figure B.4: *DSC data for Experiment D. Mass of sample = 3.6 mg.*

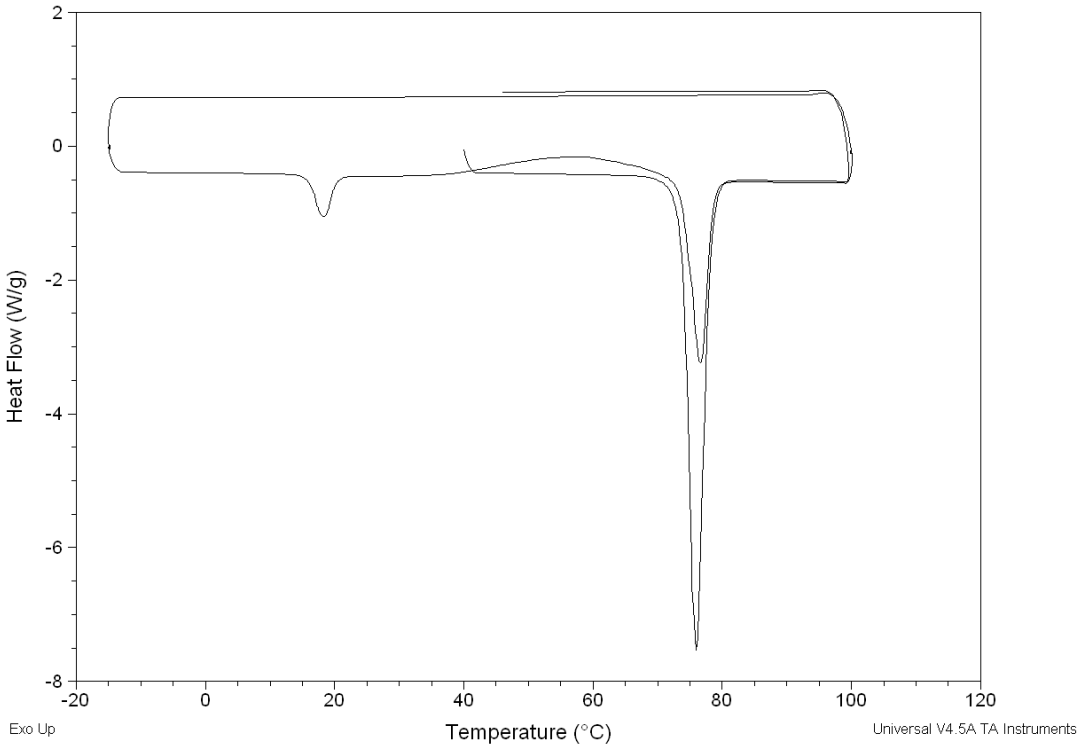

Figure B.5: *DSC data for Experiment E. Mass of sample = 3.7 mg.*

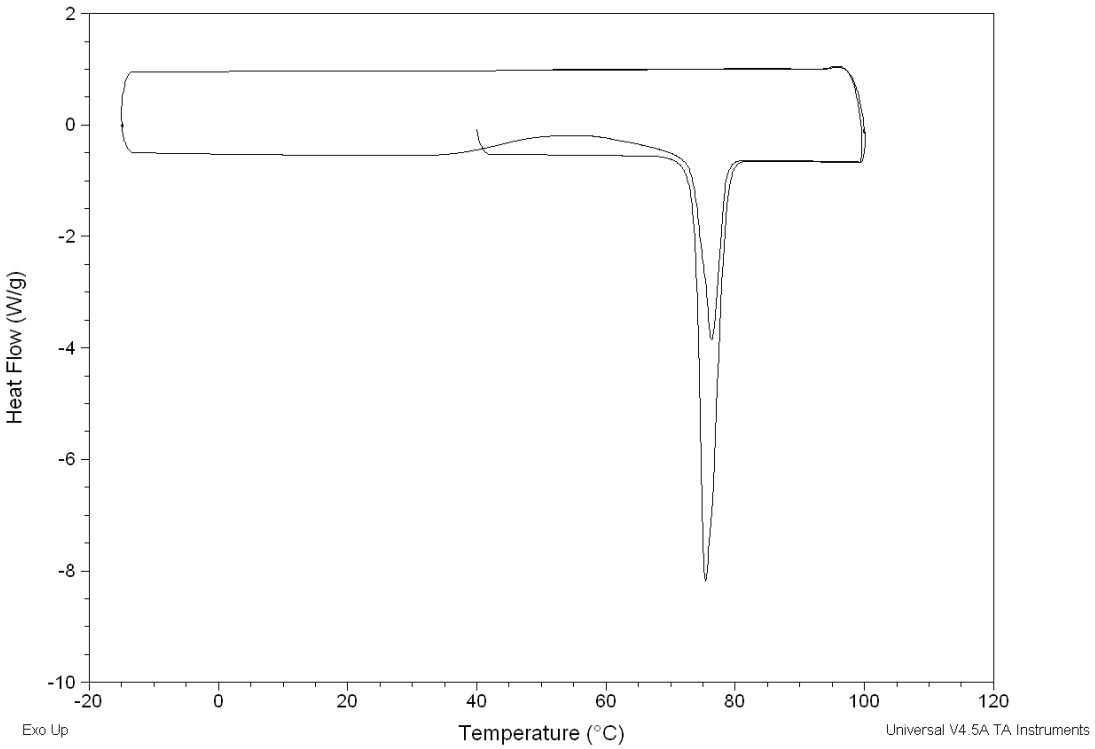

Figure B.6: *DSC data for Experiment F. Mass of sample = 3.4 mg.*

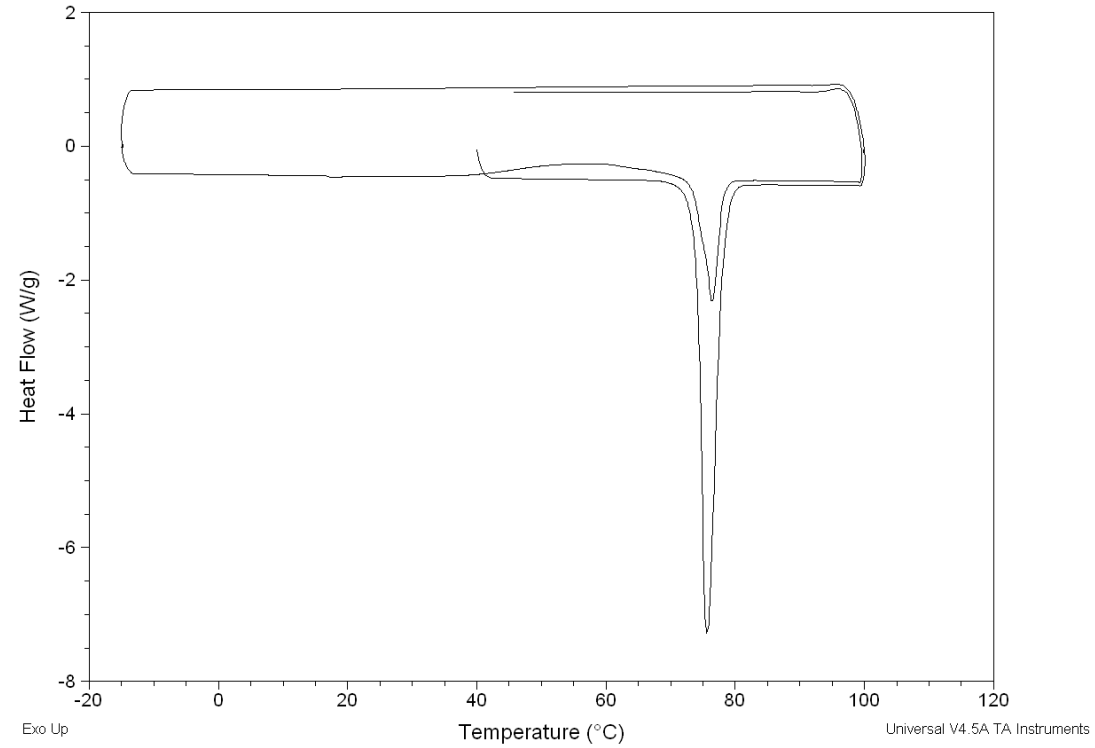

Figure B.7: *DSC data for Experiment G. Mass of sample = 3.9 mg.*

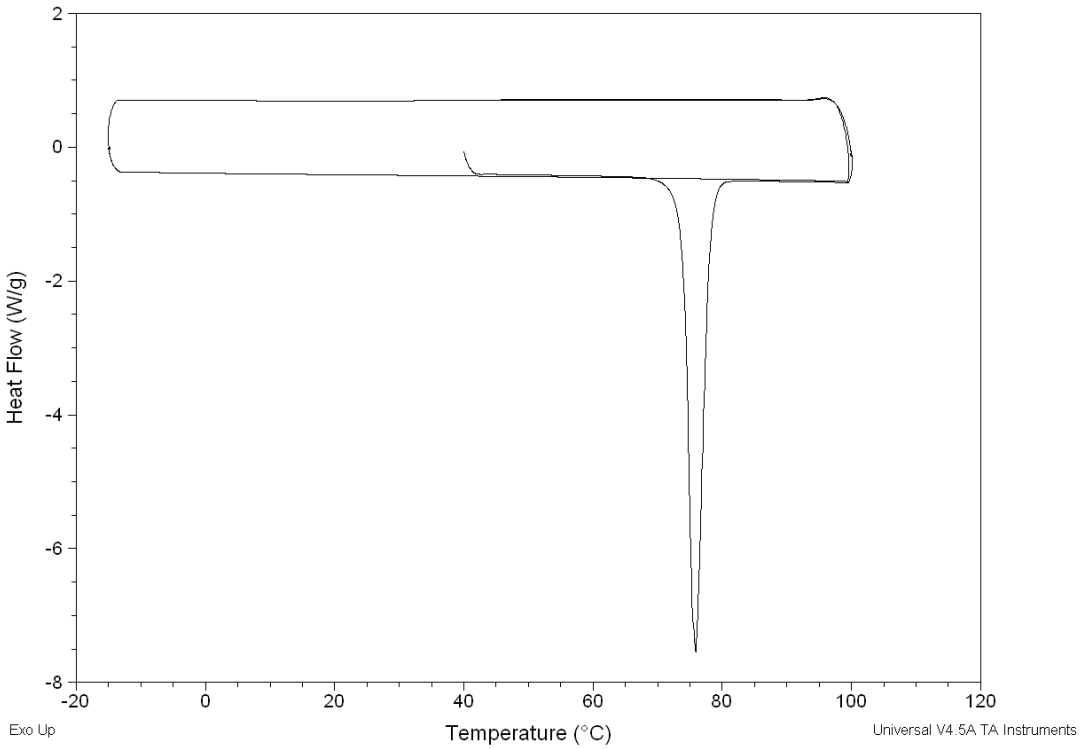

Figure B.8: *DSC data for Experiment H. Mass of sample = 3.2 mg.*

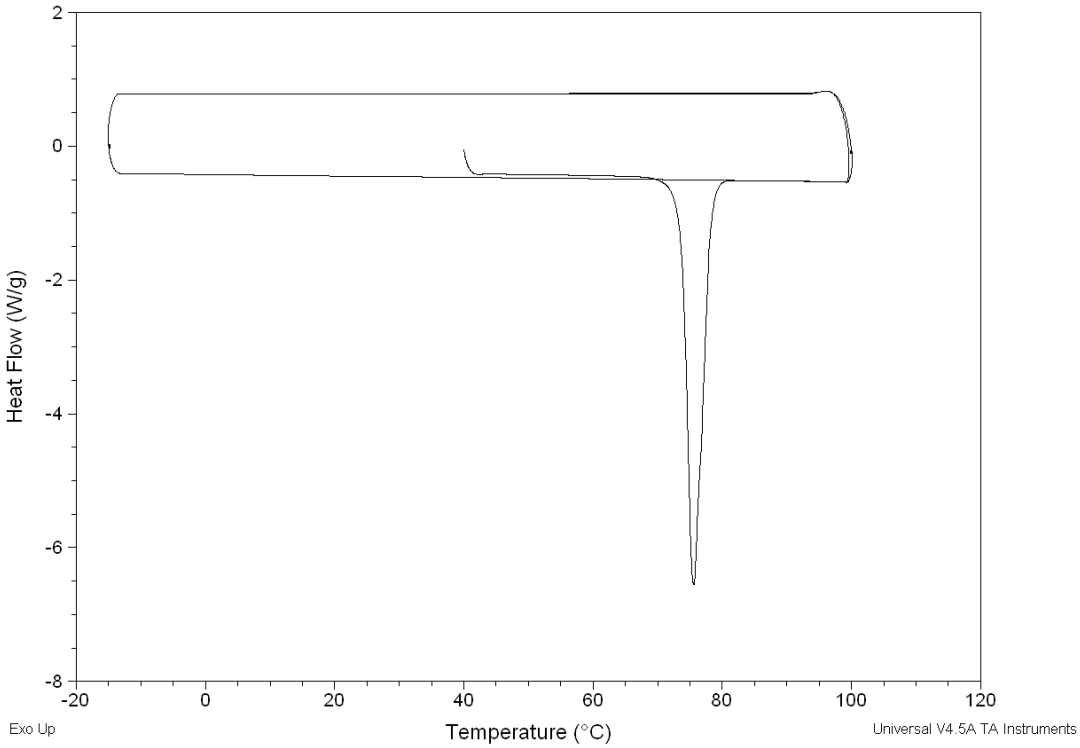

Figure B.9: *DSC data for Experiment I. Mass of sample = 3.4 mg.*

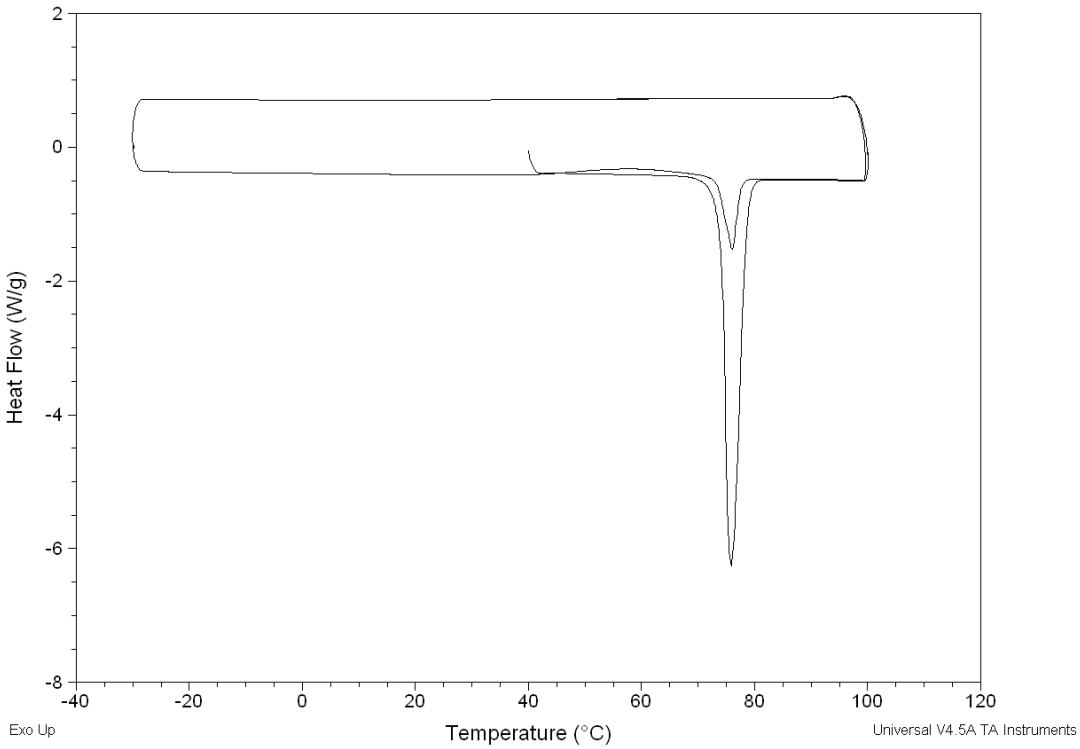

Figure B.10: *DSC data for Experiment J. Mass of sample = 3.5 mg.*

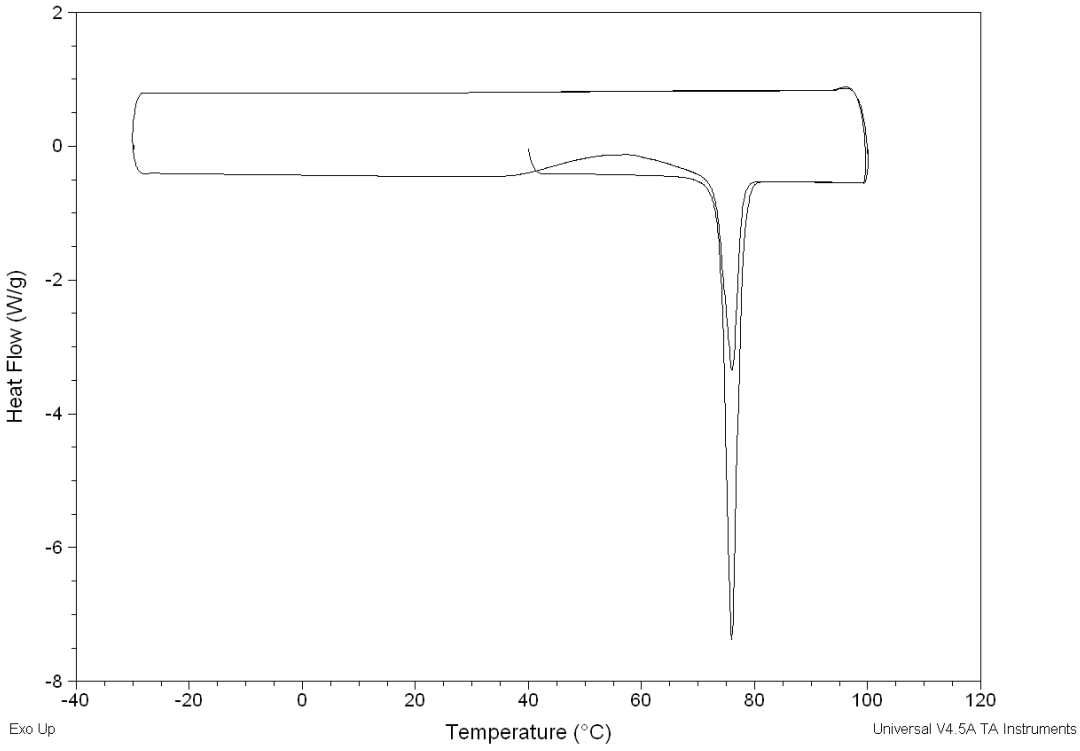

Figure B.11: *DSC data for Experiment K. Mass of sample = 3.7 mg.*

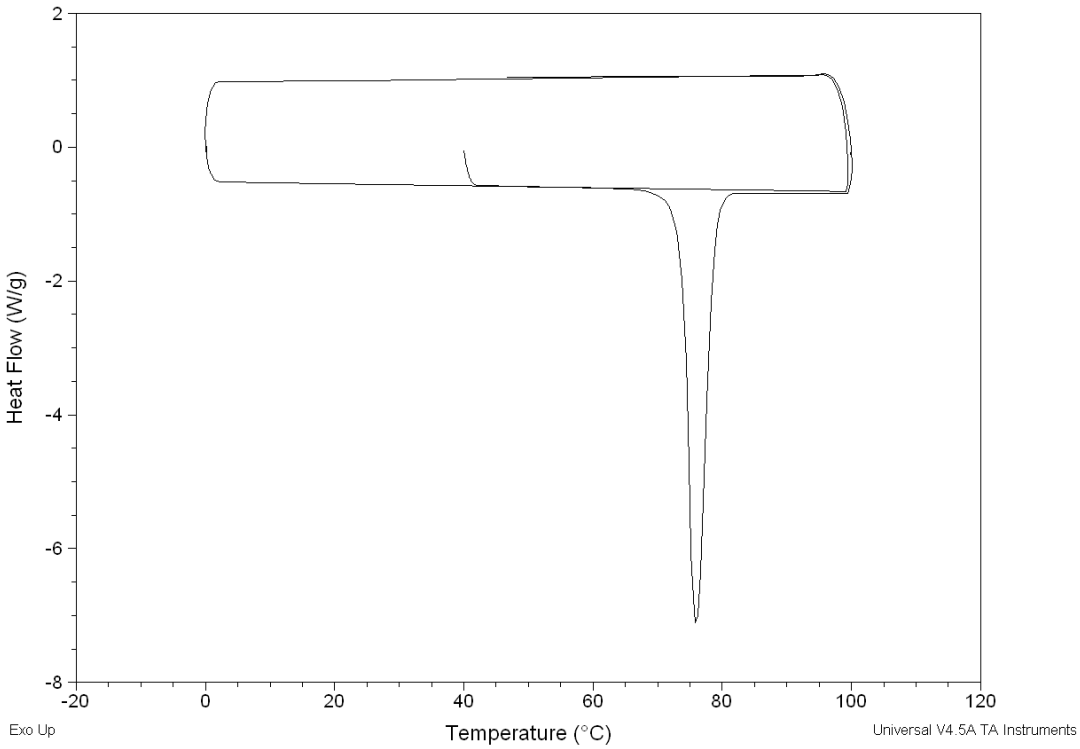

Figure B.12: *DSC data for Experiment L. Mass of sample = 3.7 mg.*

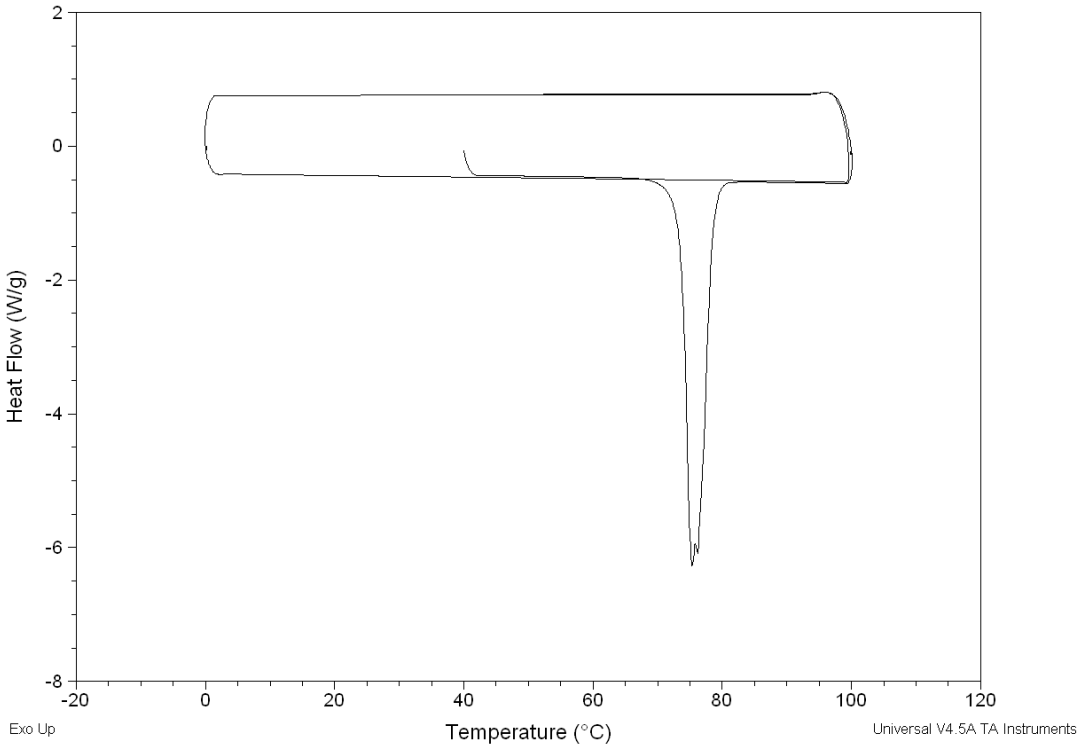

Figure B.13: *DSC data for Experiment M. Mass of sample = 3.7 mg.*

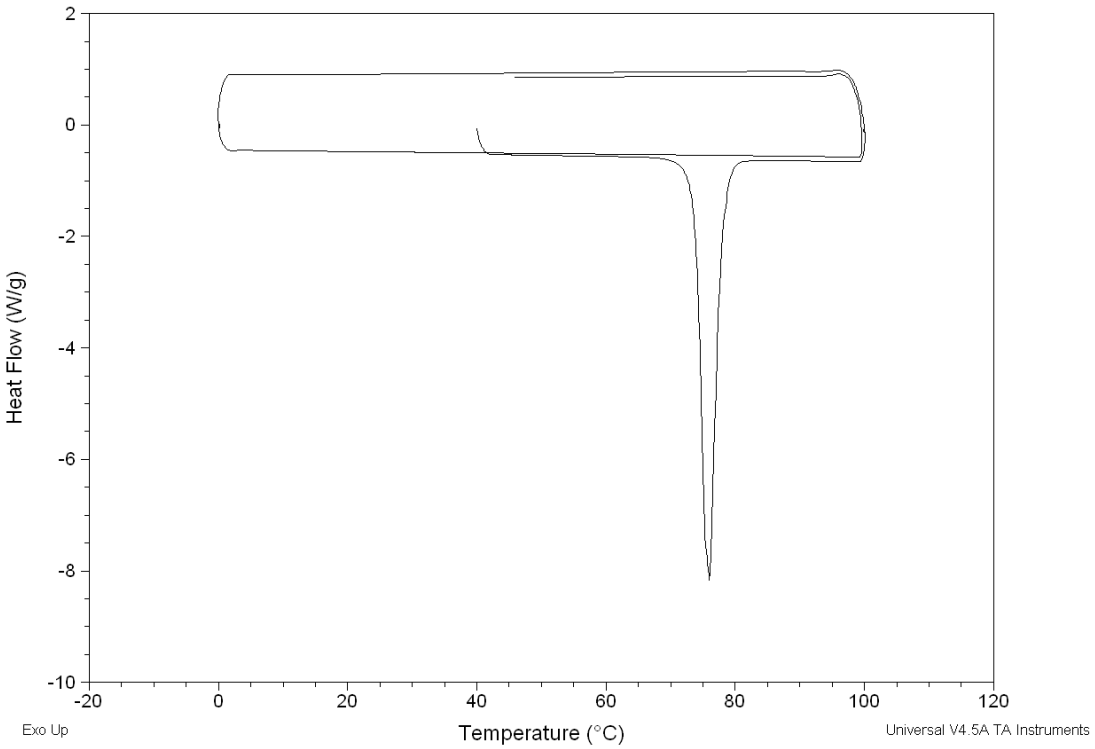

Figure B.14: *DSC data for Experiment N. Mass of sample = 3.5 mg.*

Appendix C: Work Published during this PhD

E. Courvoisier, P. A. Williams, G. K. Lim, C. E. Hughes and K. D. M. Harris; The Crystal Structure of L-Arginine; *Chem. Commun.*, **48**, 2761-2763 (2012).

P. A. Williams, C. E. Hughes, G. K. Lim, B. M. Kariuki and K. D. M. Harris; Discovery of a New System Exhibiting Abundant Polymorphism: *m*-Aminobenzoic Acid; *Cryst. Growth Des.*, **12**, 3104-3113 (2012).

C. E. Hughes, P. A. Williams, T. R. Peskett and K. D. M. Harris; Exploiting In Situ Solid-State NMR for the Discovery of New Polymorphs during Crystallization Processes; *J. Phys. Chem. Lett.*, **3**, 3176-3181 (2012).

P. A. Williams, C. E. Hughes and K. D. M. Harris; New Insights into the Preparation of the Low-Melting Polymorph of Racemic Ibuprofen; *Cryst. Growth Des.*, **12**, 5839-5845 (2012).

D. V. Dudenko, P. A. Williams, C. E. Hughes, O. N. Antzutkin, S. P. Velaga, S. P. Brown and K. D. M. Harris; Exploiting the Synergy of Powder X-ray Diffraction and Solid-State NMR Spectroscopy in Structure Determination of Organic Molecular Solids; *J. Phys. Chem. C*, **117**, 12258-12265 (2013).

P. A. Williams, C. E. Hughes, A. B. M. Buanz, S. Gaisford and K. D. M. Harris; Expanding the Solid-State Landscape of L-Phenylalanine: Discovery of Polymorphism and New Hydrate Phases, with Rationalization of Hydration/Dehydration Processes; *J. Phys. Chem. C*, **117**, 12136-12145 (2013).

K. D. M. Harris and P. A. Williams; *Structure from Diffraction Methods: Inorganic Materials Series* (Eds.: D. W. Bruce, D. O'Hare, R. I. Walton); Chapter 1: Powder Diffraction, Pg. 1-81 (2014).

S. Iwama, K. Kuyama, Y. Mori, K. Manoj, R. G. Gonnade, K. Suzuki, C. E. Hughes, P. A. Williams, K. D. M. Harris, S. Veesler, H. Takahashi, H. Tsue and R. Tamura; Highly Efficient Chiral Resolution of DL-Arginine by Cocrystal Formation Followed by Recrystallization under Preferential Enrichment Conditions; *Chem. Eur. J.*, **20**, 10343-10350 (2014).

C. E. Hughes, P. A. Williams and K. D. M. Harris; “CLASSIC NMR”: An *In-Situ* NMR Strategy for Mapping the Time-Evolution of Crystallization Processes by Combined Liquid-State and Solid-State Measurements; *Angew. Chem. Int. Ed.*, **53**, 8939-8943 (2014).